Fall 2017

A parallelized diffuse interface solver with applications to meso scale simulation of suspensions

Fazlolah Mohaghegh
University of Iowa

A PARALLELIZED DIFFUSE INTERFACE SOLVER WITH APPLICATIONS TO MESO SCALE SIMULATION OF SUSPENSIONS

By

Fazlolah Mohaghegh

A thesis submitted in partial fulfillment
of the requirements for the Doctor of
Philosophy degree in Mechanical Engineering
in the Graduate College of
The University of Iowa

December 2017

Thesis Supervisor:

Professor H. S. Udaykumar

Graduate College
The University of Iowa
Iowa City, Iowa

CERTIFICATE OF APPROVAL

_____

PH.D. THESIS

_____

This is to certify that the Ph.D. thesis of

Fazlolah Mohaghegh

has been approved by the Examining Committee for the thesis requirement for the Doctor of Philosophy degree in Mechanical Engineering at the December 2017 graduation.

Thesis Committee: _____
H. S. Udaykumar, Thesis Supervisor

_____
Ching-Long Lin

_____
Pablo Carrica

_____
James Buchholz

_____
Sarah Vigmostad

To Tahereh, Sarah and Ryan

ACKNOWLEGMENTS

I would like to start by expressing my infinite gratitude to Professor H.S. Udaykumar for all help and support. For me, he was not only a great academic advisor, but also an outstanding teacher and mentor in many aspects of my life. I feel so lucky to have been with him during these years as his level of instruction was far beyond academic levels. This work was not possible without his endless supports.

I also appreciate my respected committee members: Professor Ching-Long Lin, Professor Pablo Carrica, Professor James Buchholz, and Professor Sarah Vigmostad for their time and invaluable help. I also express my especial appreciation to Professor Buchholz and Professor Vigmostad for all the insightful discussions that we had regarding this work.

It has been my pleasure to be a member of a research lab with many amazing scholars. I feel fortunate to have had a chance to work with Mehrdad, Nirmal, Oishik, Alexia, John, Seth, Anil, Liza, Keshav, Sidhartha, Anas, Vishwa, Pratik, Mike, Kayley, Jared, Moustafa, Aaron, Piyusha, and Scott.

Finally, I save my greatest appreciation for my super kind and loving wife, Tahereh, who made many sacrifices to help me in this research. She was always encouraging and supportive, especially in the hard times. She spent tremendous time taking the responsibility of the family alone and had an ample impact to this work. I also sincerely appreciate all the support from my parents and family members in Iran who endured our being parted for many years.

ABSTRACT

The ultimate goal of this research is to develop the capability of direct numerical simulation of a flow containing numerous rigid finite size particles. In order to reach this goal, we have implemented the smoothed profile method (SPM) in the University of Iowa in-house solver, pELAFINT3D and overcame several challenges related to the method. This includes a proposed formulation for the interface thickness and many validations and comparisons with experimental data as well as with a second-order accurate sharp interface method. As one of the issues related to low-density particles is the instability, SPM has been improved by developing to a fully implicit scheme. Moreover, use of higher order integration formulation and implementation of Euler parameters have been shown to be helpful in stabilization of the calculations.

To preserve the efficiency when the number of the particles increases, local mesh refinement is shown to be a very effective tool. A revised version of SPM that has only one projection step is proposed to improve the efficiency of the method. A comprehensive efficiency study is performed and it has been shown that the new method is less expensive in problems with high added mass effect when strongly coupled fluid-structure interaction schemes are used. Moreover, the code is massively parallelized using MPI and PETSc libraries. The parallelization includes I/O, operations leading to construction of the linear solver as well as the solver itself.

Simulation of a particle laden flow involves particles collisions. Two novel collision models are suggested which are able to avoid particle overlapping for arbitrary shape particles. The methods are efficient as they are not involved with extra grid refinement related to implementing lubrication forces. The issue of handling continuously changing number of particles in a particle laden flow is solved by implementation of a linked list data structure for the particles.

By studying a flow over a constricted region we showed that the platelets' activation is more likely to happen for the particles that pass from the middle of the upper bump region

because those particles will have longer exposure time to the high shear flow behind the bump. PDF contour of particles' presence show the more concentrated presence of the particles near the bump. Moreover, the interaction of RBCs and platelets pushes the platelets toward the wall after the bottom wall.

PUBLIC ABSTRACT

This study presents the simulation of multitudes of non-spherical particles which are interacting with a carrier fluid and with each other. This work has a wide range of applications in nature and industry; here we focus on the motion of blood cells in the hinge gap region of the mechanical heart valve to avoid clot formation. While this study gives us new insights about the particle-laden flows, it should overcome many challenging tasks. Due to computationally demanding nature of this simulations, a diffuse interface fluid-structure interaction model i.e. Smoothed profile method (SPM) is developed for the simulations of multitudes of particles. SPM has a smooth transition from solid to fluid and solves the flow equations in the entire domain but applied the effect of the particle using an extra differential equation. We proposed a correlation for the particle interface thickness and showed the importance of implementing an appropriate value for the interface thickness. Moreover, we adapted the model for our use to avoid the numerical instabilities by strong of coupling fluid and solid. In addition, we proposed two new collision methods to model the interaction of non-spherical particles.

The results show that SPM is capable of modeling many complex situations and is more efficient than other methods regarding computational costs. The complex situations include the rotation and the translation of particles with different densities, oscillation of an airfoil subject to free stream flow, flow over particles at different velocities and interaction of particles. Also, the novel collision methods are able to model the collision of non-spherical particles accurately and effectively. The results for flow over the hinge gap of a mechanical heart valve show that red blood cells push the platelets toward the walls behind the constricted region. They show that platelets are more likely to be activated if they are trapped behind the constricted areas.

TABLE OF CONTENTS

CHAPTER 4

CHAPTER 5

CHAPTER 6

CHAPTER 7

LIST OF TABLES

CHAPTER 3

CHAPTER 4

CHAPTER 6

LIST OF FIGURES

CHAPTER 1

CHAPTER 3

CHAPTER 4

CHAPTER 5

CHAPTER 6

CHAPTER 7

CHAPTER 1

INTRODUCTION

1.1. Motivation

Heart disease is the leading cause of death in the US; each year, more than 500,000 Americans die due to cardiovascular complications [2]. One of the most common ones among them, valvular heart disease, is a type of cardiovascular dysfunction that happens as a result of malfunction of any of the heart's four valves. About five million Americans are diagnosed with heart valve problems annually [3]. Approximately 90,000 heart valve replacement surgery is performed in the US and 280,000 worldwide [4]. With an annual expansion rate of 10-12%, the number of procedures in the world is anticipated to reach 850,000 in 2050 [5].

Any heart valve defect affects the hemodynamic performance in either Stenosis (valve narrowing leading to higher pressure drop along the valve) or incompetence or regurgitation (incomplete closure of the valve). Each of these conditions results in various types of diseases such as rheumatic fever, infections or various disabilities [6]. Depending on the conditions if a corrective surgery does not help, a substitute valve should be implanted.

Valve prostheses are categorized as bio-prosthetic-heart valves (BHV) and mechanical heart valves (MHV). Approximately half of the heart valve replacement surgeries are related to MHVs [4] among which St. Jude bileaflet valve (Figure (1-1)) is the most common one [7]. An MHV contains a housing which holds the other parts. Two leaflets mount on a hinge recess on the housing to be able to rotate freely. The housing and the leaflets are made of graphite but they are coated by Pyrolytic carbon, which is a durable and strong material and does not form thrombus. A tenacious Dacron fabric ring attaches the housing to the heart.

When the MHV is fully open, the leaflets are almost parallel to avoid disturbance in the flow. However, the very high velocity of blood in the valve, which can reach 2.2 m/s, causes a turbulence shear stress up to 1500 dyn/cm^2 during the peak systole. At the hinge region, two recirculation zones form [8]. When the valve is closed, there will be small gaps (b-datum gap) between the two leaflets and also between leaflet and the housing (periphery gap). These gaps (Figure (1-2) are designed to prevent blood cells from building up and to reduce the required amount of anticoagulant the patient should receive. With the size of $150\mu m$ for the periphery gap and 1.1 μm for b-datum gap, the gaps are several orders of magnitude smaller than the actual valve size [9] which is about 17mm or more [10]. When the valve is closed, the elevated pressure gradient across the device forms narrow jets, and blood returns to the heart through the leakages in the gaps [8]. Figure (1-3) displays two stages of a bileaflet valve.

Unlike bio-prosthetic-heart valves, mechanical heart valves cause thrombus formation as a result of non-physiological nature of the prosthesis in the pass of blood flow [11]. Contact of blood elements with the hard parts of the valve surface and also exposure of them to the very high fluid stress in the systole leads to damage in the blood elements [12, 13] or platelet activation [14] in the hinge. Platelets are known to be activated in shear stress more than $O(10\ Pa)$ [15]. For constant shear stresses, Hellums criterion [16] represents a precise threshold of platelet activation as the time instant when product of the shear stress and the time duration of it is above 3.5 Pa. Haemolysis, destruction or rapture of red blood cells, threshold is much higher as it happens at 800 Pa. Therefore, activation of platelets are more likely to happen than Haemolysis.

High shear stresses occur during the systole when the valve is closed. This is the time when the imposed large pressure gradient leads to elevated shear stress in the hinge gap region for a long time [6, 9]. Anti-coagulant therapy is the way to prevent thrombus formation; however, it comes with multiple complications such as hemorrhage and infection. Consequently, optimization of the valve design is the best way to avoid the related complications. This optimization could be obtained by using experimental or numerical analysis.

1.2. Numerical Analysis

So far, the performed experimental analysis of the hinge region to understand the blood flow in the MHV and the potential places of platelet activation has many limitations. In addition to the non-physiological conditions related to *in vitro* experiments which can make the study unreliable, only limited information could be achieved because the velocimetries are provided only in 2D and on selected locations [17-21]. Therefore, a possible numerical analysis could be a better choice.

A comprehensive 3D simulation of the flow through the hinge region can be helpful in understanding the thrombus formation. However, this simulation can be highly challenging, because the blood contains a huge number of densely packed deformable blood cells that affect the fluid rheology. Moreover, the simulation is a multiscale study because:

First, the peak of Reynolds number value in a cardiac cycle is at least 6000, leading to minimum length scale of $0.04\ mm$ as Kolmogorov scale [22]. This leads to three orders of magnitude change in the range of length scale from the dissipative length scale to the vessel diameter.

Second, the simulation of flow in the entire valve, including the hinge and the leaflets gaps, requires resolution of the grid in regions with several orders of magnitude difference in size from the gap to the valve diameter. The large cell size variation forced other researchers to increase the central gap from $1.118\ \mu m$ to $98.633\ \mu m$ in [22] and to $140\ \mu m$ in [23]; therefore the high shear stresses and leakage effects were ignored.

Third, in order to analyze the platelet activation mechanism, modeling of blood cells as finite size particles is mandatory. Having particles with sizes of $\mathcal{O}(1\ \mu m)$ necessitates use of a grid with minimum cell sizes or even less.

Consequently, the success in analyzing the blood flow over the constricted geometries depends highly on the accuracy and the efficiency of the numerical schemes in each scale. Figure (1-4) is a schematic of the multiscale simulating through small gaps. A comprehensive numerical study of the thrombus formation needs a combination of several numerical techniques in each scale and the inner

connection among the scales. The scales are separated based on the distance from constriction. They are classified as following:

1.2.1. The Mico-scale subdomain

Inside the gap, where extreme shear stresses can change the cells shape excessively, the micro scale model considers the blood cells as flexible objects with a comparable scale as the constriction. Red blood cells (RBCs) are considered as originally biconcave disks with membranes that deform under the shear stress.

Finite element method in both 2D and 3D (FEM) [24] is widely used in order to capture all deformations as described by [25-32]; however, implementation of other methods is also popular. For example, AlMomani et al. [33] assumed the RBCs as pseudo rigid which means that they deform homogenously under the shear stress. In their study, migration of platelets toward the wall and RBCs to the center was observed. Immersed FEM [34] was used in [35, 36] to model the RBC aggregation and determine the effects on blood rheology. It is shown that with increase of shear stress, the deformation of RBC becomes more significant. At high shear rates the RBC stretches and aligns itself with the flow. Boundary element method [37] was implemented by Ramanujan and Pozrikidis [38] to show the increasing stretch of an RBC with increase of shear stress.

Alongside the above-mentioned methods, use of Lattice Boltzmann method (LBM) [39] is also popular for simulation of blood cells as flexible objects [40-43]. One of the benefits of LBM is the efficiency and simplicity of the implementation. Thus, unlike all of the previously mentioned simulations which are restricted to one or a few particles, LBM is successful in handling tens of particles as described in [40, 41, 44].

Considering RBCs as elastic membranes encapsulating the particle with the Neo-Hookean law, Bagchi et al. [45] and Doddi and Bagchi [46] implemented Peskin's front tracking immersed boundary method (IBM) [47] to find the stresses and then deformations on the particles. Phenomena of tank treading

and tumbling were observed for an RBC. The IBM was also developed to joint with Non-Uniform Rational B-Splines (NURBS) [48]. NURBS generates the geometry of the surface of an individual cell using isogemetries and is capable of generating the surface of various complex shapes with control points [49]. Chivukula's study [50] could capture the deformation of an RBC in a parabolic flow of a microchannel with the help of NURBS.

1.2.2. Meso-scale subdomain

Outside the gap, the number of particles is immensely higher as a result of the much wider domain size. However, the shear stress is lower and thus the deformation of the blood cells is not significant. Therefore, the blood cells can be considered as rigid objects such as disks or ellipsoids. Especially, the RBCs and platelets could be seen as the spheroids and WBCs as spheres. Though, ignoring the flexibility of cells seems to be less computationally demanding, the infinite stiffness assumption can lead to a singular system [51].

Among various meso-scale models, Dissipative Particle Dynamics (DPD) [52] is a coarse graining meso-scale method in which each particle is a substitute for a cluster of smaller particles. The method is capable of modeling the motion of RBCs in a micro channel and various phenomena, such as cell-free layer near the wall, could be observed [53]. Another particle dynamic method was presented by Imai et al. [54] with a 2D mass-spring network for the RBCs, in which by adding the Malaria infected RBCs as rigid objects, possible dramatic increase in the apparent viscosity was discussed.

The other meso-scale methods are more or less the same as micro scale ones. For example, Sun and Munn [55] with a 2D LBM could capture the Fahraeus-Lindqvist and Fahraes effects. Fahraeus-Lindqvist effect [56] is the increase in viscosity as the channel size increases and Fahraeus effect [57] is lower hematocrit in smaller tubes. The finite element model of Tokarev [58] discussed the possibility of finite size particles effect on migration of platelets to the wall.

Many of the studies related to meso scale simulation of the blood as a particulate flow still consider the flexibility of the particles. The 2D LBM of [59] could capture the migration of RBCs from the microchannel wall. Vahidkhan [60] with a front tracking immersed boundary method found that RBCs augment the diffusive motion of platelets in a microtube. In Stokes flow regimes, Zhao et al. [61] with boundary integral approach recognized the higher effective viscosity in a micro-channel due to particle presence.

Perhaps the largest number of RBCs in blood is modeled by Rahimian et al. [62], who performed a DNS simulation on 200 million RBCs using 200,000 cores on Jaguar PF cluster. The boundary integral method in a semi-implicit time stepping scheme was parallelized in distributed and shared memory way as well as by GPU acceleration to achieve maximum concurrency. However, some modeling restrictions that were applied could make the scalability of the run dramatically improve. For instance, limitation of very low Reynolds number of creeping flow in unconfined boundaries made the petascale run possible.

1.2.3. Macro-Scale simulation

The macro-scale simulation is basically the FSI simulation of the valve by assuming the blood as a single phase flow. The pulsatile blood flow through the valve leads to valve closure and opening in each cardiac cycle. The flow peak Reynolds number is 6000 requiring high grid resolution to capture all flow physical phenomena when Direct Numerical Simulation (DNS) is used.

In most arteries, blood as a single phase behaves like a Newtonian fluid [63, 64]; however, in small vessels, the shear thinning behavior is not negligible. In macro-scale in general the Newtonian fluid assumption is valid [65].

Even with the single phase assumption of the blood, no comprehensive solution for the full MHV system is done as they come with simplifications. For example the simulations of [66-68] were in 2D. The other one as mentioned before is increase of the b-datum and the periphery gaps dimensions from the actual dimensions [22, 23, 69]. Borazjani et al. [70, 71] and Ge [72] ignored the periphery gaps and

the related leakages. Other simplifications is symmetric assumption, solving only one quarter of the domain [6] and use of lower Reynolds number to be able to use coarser grids [73].

The main hurdle for simulation of the blood as a single phase is the huge difference among the gap and the valve scales. Adding to the multi-scale complexity, the requirement for new models in the gap region and inclusion of the particles makes the comprehensive study absolutely challenging. Adding to that, use of patient specific data for the MHV inside an actual artery instead of classic shapes demands transfer of geometry from tomographic images to a computational grid.

1.3. Objectives

In this thesis, we establish a framework as the starting point for the meso-scale simulation of blood as a multi-phase flow on the University of Iowa in-house solver, pELAFINT3D. One of the final goals of pELAFINT3D is the computationally challenging multi-scale multi-physics simulation of blood flow in a mechanical heart valve in order to examine the thrombus formation. The code has been developed for moving boundary problems using DNS on a Cartesian grid. The grid can be refined and coarsened wherever needed in the domain using the octree refinement. This local mesh refinement option has improved the efficiency of the code because the user only needs to refine the grid as it needed and thus the applicability of the code is enhanced. The grid is massively parallelized and distributed using MPI and PETSc libraries.

pELAFINT3D was originally set for the sharp interface method using level sets. However, when the number of particles increases it is not efficient to define the particles based on level sets and apply the boundary conditions on each particle. Thus, this research strives to achieve these goals:

1- Implementation, adaptation, and development of the recently introduced smoothed profile method (SPM) [74, 75] in the in the fractional step solver [76, 77] in order to overcome the computational difficulties related to the modeling of non-spherical particles considering the high

added mass effects. This includes implicit stabilizing techniques and use of higher order schemes if necessary.

2- A parallel framework for the simulation to overcome the computationally extensive challenges. This includes reading and writing the data, setting up the grid and solving both particles and the flow in a parallel environment.

3- Modelling particle rotation with Euler parameters.

4- Avoiding particle-particle and particle-wall overlapping by using and developing a collision capturing method.

5- Modelling and analyzing the motion and translation of non-spherical particles.

6- Ability to manage and handle data of high number of particles.

7- To understand and quantify the interaction between RBCs and platelets in blood flow close to a microscale constriction.

8- Applying model to high number of finite size moving.

In the next chapter, we focus more on modeling the particulate flows by introducing various methods for the simulation of finite size particles.

FIGURES

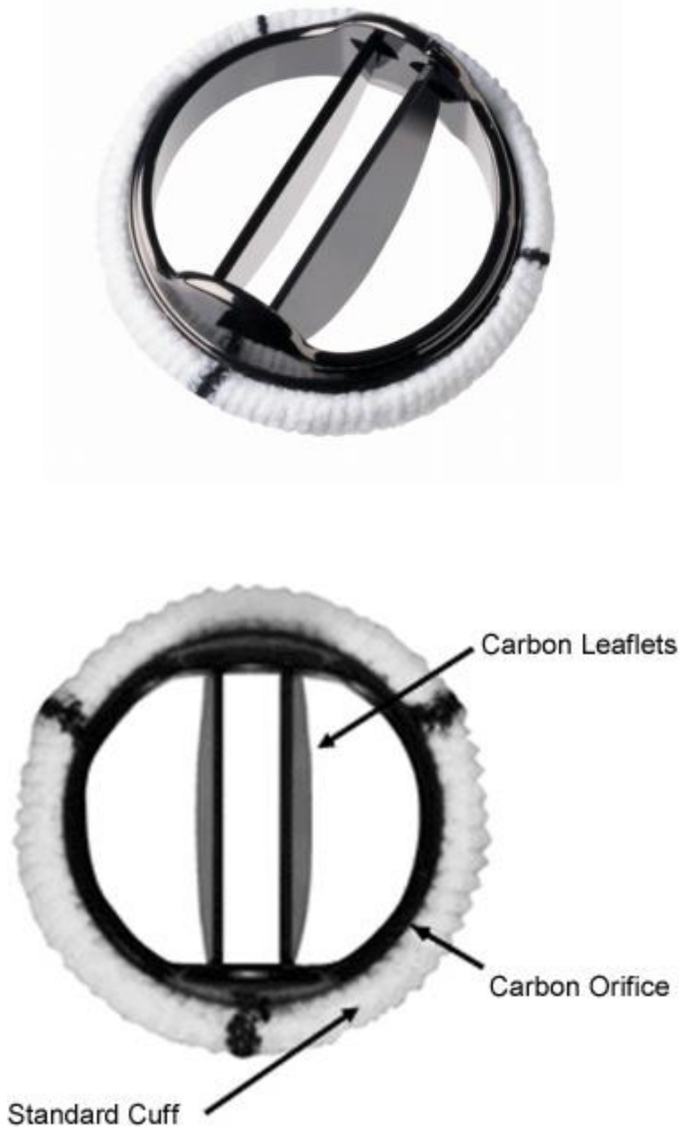

Figure 1-1- St. Jude bileaflet mechanical heart valve [78]

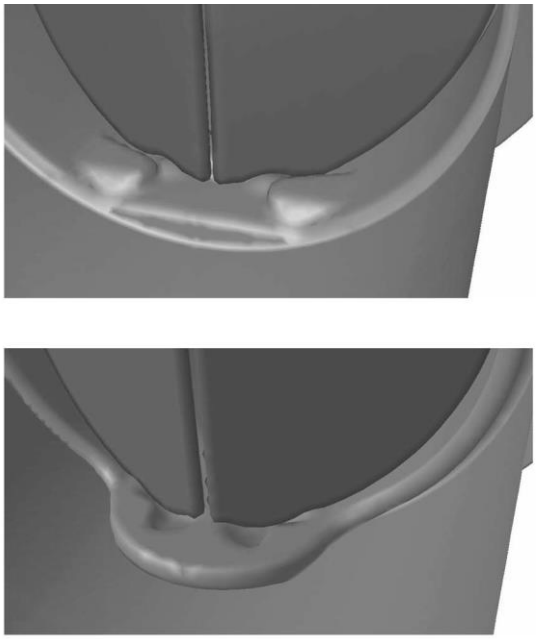

Figure 1-2- **(Top)** Medtronic ATS Medical and **(Bottom)** St. Jude Medical (SJM) bileaflet mechanical heart valve hinge region [23]

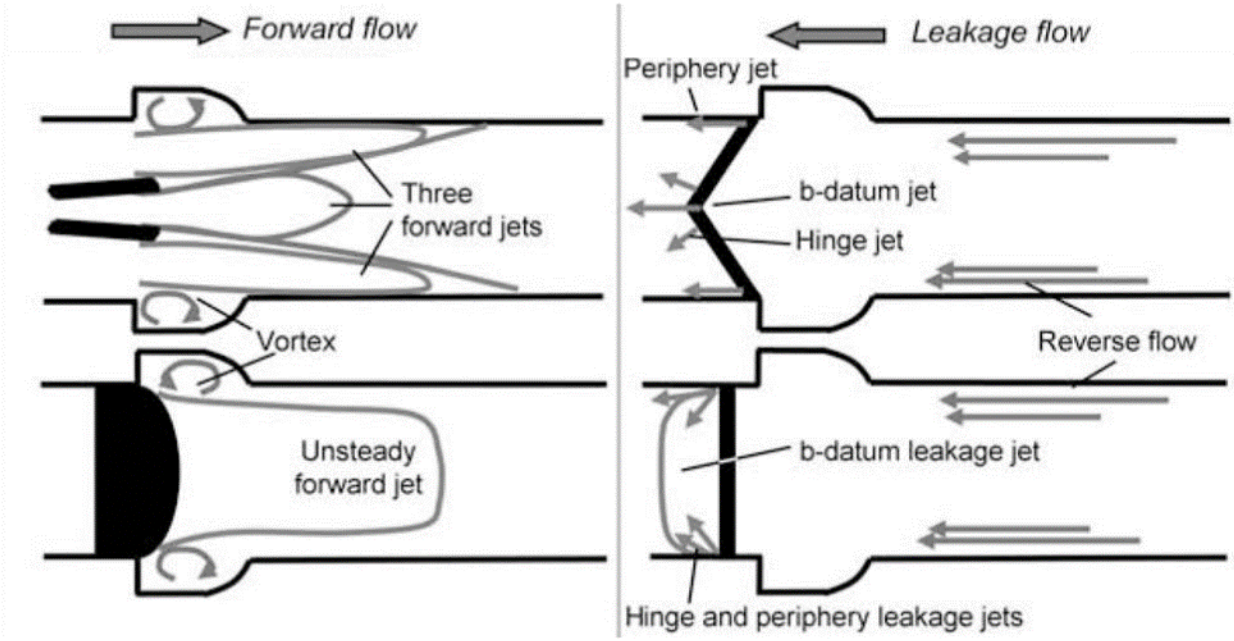

Figure 1-3- Valve operation during systole **(left)** and diastole **(right)** for two different views [8]

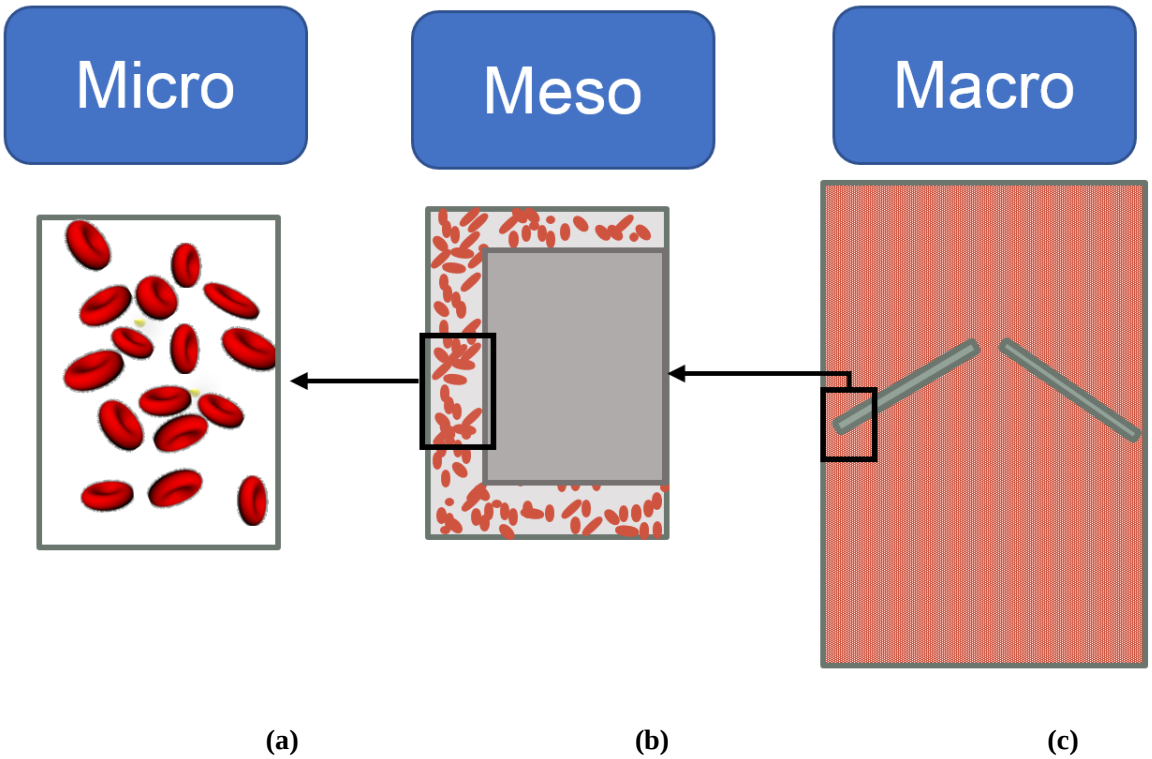

Figure 1-4- Multi-scale simulation of blood: **(a)** Micro scale single phase flow on the right, **(b)** Meso scale particle laden flow and **(c)** Macro scale blood deformable blood cells.

CHAPTER 2

REVIEW OF PARTICULATE FLOW MODELS

Numerical study of blood flow and other particle-laden flows including colloidal dispersion [79, 80], granular flows [81, 82] and aerosols [83, 84] is challenging due to the presence of large numbers of immersed moving boundaries. Simulation of multitudes of finite size particles necessitates efficient and robust simulation methods to capture all physical features of the fluid-structure interaction and to make the meso-scale simulations of particle-laden flows with a high number of particles feasible on current hardware.

In general the numerical analysis of such flows can be categorized into boundary conforming and non-boundary conforming methods which will be described in the next two sections.

2.1. Boundary Conforming Methods

Boundary conforming methods use a body-fitted grid in order to obtain an independent grid from the interface details. While in these methods the interface treatment is easier, the issue becomes how to generate the grid in order to conform to the object boundaries. Among the most popular ways is implementation of mapping from a complex physical space to a computational space. The other way is use of unstructured grids. Both methods come with many complexities that not only make the calculations complicated but also can add to the computational costs extensively.

In the finite volume technique, the grid is constructed to span the fluid field outside a particle. For complex geometries such as when the number of particles is high, a block-structured approach is used to divide the domain into blocks containing particles. The blocks can communicate to each other through their interfaces either in a conforming or a non-conforming way; the latter needs interpolations of data at

the block boundaries. The challenge of this method is to construct the grid and then devise a mapping to shift from the physical domain with a curvilinear system to the computational domain with a Cartesian grid [85, 86].

Spectral methods as higher order schemes have the highest order of accuracy. The flow solution in spectral methods is expanded on functions with global support which means that the spatial derivatives on each point depend globally on all other points as well [87]. Accordingly, the spectral methods are the most accurate due to implementing higher grid resolution. All boundary conditions including the particle boundaries are applied indirectly by filter functions for better stability. The flow variables are discretized based on the Fourier expansion series. The results are able to predict particle-flow interactions at turbulence flows with very high accuracy [88]. With a global nature, instead of a finite volume technique, the spectral methods do not use block structures for the grid around the particles. The consequence is restriction to simple geometries. The Spectral Element Method is the generalization of Spectral Methods for more complex geometries by using a finite element approach. High order piecewise polynomials as the basis functions increase the accuracy of the method. Continuity of the function and all of its derivatives is established through the interface of the particle [89, 90].

In FEM, the fluid and the solid can have separate or combined formulations. The latter is especially useful when stability issues necessitate a fully implicit formulation. In order to couple particles' fluid-structure interaction inside a flow, two techniques can be used: In one technique, at each time step the solution of the flow and particles' dynamical and kinematical variables are iteratively updated to reach a converged value (partitioned approach). When FEM is used, a more stable technique could be implemented, which combines the solid-fluid formulation and considers the fluid and the particles in a single set of formulation, leading to a more robust implicit algorithm (monolithic approach). Therefore, iterative segregation of the hydrodynamic particle-fluid interactions is not mandatory in FEM. While Galerkin finite element scheme is generally used for spatial discretizations, temporal discretization is applied using the finite difference scheme [91]. FEM analysis of Johnson and Tezduyar [92] considered

101 falling spherical particles at Reynolds numbers up to 100 and the overall average particle quantities where monitored.

Arbitrary Lagrangian-Eulerian (ALE) mesh movement [93, 94], which generally is considered as a finite element method, can also be used in the context of finite volume [95] and structured grids [96]. ALE maps the physical domain which varies with time into a computational domain. A body-fitted grid moves with each particle in order to conform the particle interface to the grid. Therefore, geometric conservation laws will be satisfied automatically in the discrete form of the governing equations. Generally, ALE is easy to implement, but it needs re-meshing and interpolation of data to the new grid at each time step when it is applied to moving particles with high displacement. Thus, the mesh should be smoothed by an elliptic solver to avoid skewing [6]. This has made the method inefficient in flows with a broad range of boundary movement due to the requirement of an extensive amount of computations for grid generations. The ALE analysis of particle-fluid interaction is limited to a few particles [97-101].

In conclusion, boundary conforming methods in general are easy to implement, but they need re-meshing and interpolation of data to the new grid at each time step, especially when the particles are moving and have a high displacement. Consequently, boundary conforming methods may become inefficient in flows with a broad range of boundary movement due to the requirement of extensive amounts of computations for grid generations. Modeling Evolution of the grid and assigning initial values to the grid points that are newly joined to the domain by interpolation not only adds to the complexity of the simulation, but also leads to inefficiency of the method when the number of particles increases [91].

2.2. Non-Boundary Conforming Methods

In non-boundary conforming methods the mesh is fixed and the boundary of the solid particle can cut through the grid. The grid is generated much faster and there is also no need to regenerate the grid during the time evolution. This has made these methods generally faster than the boundary conforming methods.

There are two different classes of non-boundary conforming methods. In one group known as continuous forcing approach, the interaction of the solid particles and the fluid is through the interface as immersed boundary and is applied by adding a source term (forcing) to the Navier-Stokes equations. In the other class, the discretization of operators are modified for the grids adjacent to the interface in order to apply the boundary conditions. While in the continuous forcing approach, the forcing is introduced before discretization, in the discrete forcing approach, the forcing is applied after the discretization of the equations. These methods will be discussed in detail in the following sections.

2.2.1. Discrete forcing approach

In the discrete forcing approach the fluid and the solid are separated completely and each medium is solved individually. While the discrete forcing approach depends on the discretization method, this can be a benefit as it controls the numerical stability and accuracy. Moreover, since in this approach the forcing is not defined as specified by user, the associated instabilities are eliminated [102]. It is necessary to mention that the boundary conforming methods described in section 2.1 are essentially discrete forcing approaches. The non-boundary conforming discrete forcing methods are described as following.

Sharp interface method (SIM) [103-107] solves the control-volume based governing equations in the fluid such that the control volumes intersecting the interface are cut to conform to the boundary. The part of each intersecting cell inside the solid is discarded and the remaining reshaped cell is solved as the fluid. In this way, the mass and momentum conservation will be fully satisfied. One of the main challenges in this method occurs in 3D when very small cut cells form which requires extra modifications. For examples, if the cut cell is too small, the cells are merged to bigger cells. The other problem is matching the fluxes and gradients on the boundaries of irregular shaped cells as they do not coincide with the cell centered values of the neighboring cells. When higher order accuracy is required, a multidimensional interpolating polynomial is implemented. Among the applications of SIM are modeling

of bubble dynamics [108, 109], flow over an array of fixed cylinders [110] and motion of a rising immiscible drop under various viscosity and density ratios [111].

In the other approach known as the Ghost Fluid Method (GFM) [112] the computational stencil is preserved by using one layer of the nodes inside the solid, namely, the ghost nodes. The values of the ghost nodes are obtained by using the extrapolation from the adjacent fluid nodes. The method is easy to implement, robust and can handle complex fluid mixtures [113]. One of the great capabilities of GFM is success in simulation of surface tension on discontinuous fluids (multiple fluids) which could lead to simulation of droplets or bubble break up [114-116]. Menard et al. [117] combined GFM with VOF and level set technique to model the primary breakup of a jet. The method is capable of simulation of various applications such as droplet injection in an ink jet printer [113].

2.2.2. Continuous forcing approach

The continuous forcing approach is a "one-fluid" technique which means that the Navier-Stokes equations are solved in the entire domain including the interior of the solid object. Among the advantages of these methods are simplicity and independency from the spatial discretization [102].

The original concept of Immersed boundary method (IBM) of Peskin [47, 118] in the 1970's was the first non-boundary conforming methods with the continuous forcing approach. The term "Immersed Boundary Method" (IBM), known to be suggested by Peskin [118], was first related to a model for simulating the fluid-structure of blood flow in a moving boundary heart valve. Today, the method is well developed in different ways as a consequence of the desire for simpler and faster implementation of multi-phase CFD codes on structured grids. With IBM, particles in particulate flows can slide through the grid in a non-boundary conforming fixed Cartesian mesh. Thus, there is no need for re-meshing of the domain. IBM as a "one-fluid" formulation solves the governing equations in the entire domain. In the IBM, at the interface of particle and fluid, velocity, acceleration and the normal stresses are continuous and without sudden changes. Fluid variables are characterized in Eulerian framework while particles and their

boundaries are tracked in Lagrangian reference frame. The forcing becomes distributed over a narrow band of cells close to the Lagrangian grid points [119] and is a substitution for the transmission of solid stress to the fluid as volumetric force using a mollified Dirac delta function. The way the interface of particle and fluid is treated signifies different methods of IBM [91].

Since invention, various formulations of the IBM concept have enjoyed immense popularity in simulations of particulate flows. The first implementation of the method with the particle-laden flows was by Fogelson and Peskin [120] for the suspension of particles in the Stoke's flow. Each model particle was constructed by a finite number of points on the interface that are linked elastically. Höfler and Schwarzer [121] extended the model by adding inertial terms to the equations. There are many application examples related to IBM for the particulate flows such as computational blood cell modeling [28, 36, 45, 122] and particle sedimentation simulations [123-127].

IBM has been mixed with Lattice Boltzmann (LBM) to use the benefits of both methods [128]. A force density term was added to the LBM equation in order to solve the particles and fluid fields. The particle boundary conditions are applied using the forcing. The technique was validated for various cases of rigid and flexible objects [129, 130]. Due to simplicity and efficiency the application of this method for various particle laden flows are well developed. For example [128, 131] includes the simulation of hundreds of settling 2D and 3D rounded particles. One capability of this method is the simple adaptability for the flexible objects such as RBCs [40, 41, 43, 44].

Distributed Lagrange Multiplier (DLM) or Fictitious Domain (FD) [132, 133] as another extension of IBM maps the time dependent problem with a complex domain into a wider but simpler stationary fictitious domain which spans both inside and outside of the particles domain. Finite element is used for the space discretization and a new operator technique splits the temporal terms. A distributed Lagrange multiplier enforces the rigid-body motion of the several solid multiple 2D and 3D settling particles in the fictitious domain [124, 132]. While the original presentation of Glowinski was with finite element method, finite volume technique also has been implemented with fictitious domain concept

[134]. Singh [135] used the method for the particle-laden flows with collision at low laminar Reynolds numbers.

The Immersed Finite-Element Method (IFEM) [34, 136, 137] uses the same IBM concept as it implements an Eulerian grid for the FEM solver in the entire domain. The Solid grid is tracked in a Lagrangian manner over the background Eulerian grid. Interpolations enforce the continuity between the two grids. Since IFEM uses the benefits of both IBM and FEM, it has been used for the simulation of blood cells [35, 36, 138], especially it has been combined with LBM too [84].

In Immersed Interface Method (IIM) [139-142], in order to have better accuracy and capture the discontinuities near the interface, a jump condition is applied for the velocity and pressure across the interface. In this way the method, like the discrete forcing approach methods, is able to model the dramatic changes in the variables and their derivatives near the interface; however, the stability issues can become serious especially when an explicit time stepping is employed [142]. The examples of studies in this field are limited to flow over fixed spheres or cylinders [143] or the forced oscillation of flow over a hovering wing [144].

Recently, Smoothed profile method (SPM) has been suggested by Nakayama and Yamamoto [74] for the simulation of colloidal suspensions. SPM is applied using a fractional step approach. In the first step, a provisional velocity field is computed as if a single phase incompressible flow existed in the absence of particles. The provisional velocity field is corrected in a second step to account for the presence of rigid particles according to a forcing which smoothly transitions the velocity between the solid and fluid velocities. The forcing is constructed as the sum of a component representing the momentum correction due to the presence of particles and a pressure defect which ensures the divergence free nature of the final velocity. Since SPM applies the boundary conditions implicitly, management of high number of the particles as moving boundaries is easy. Moreover, possibility of implementing an analytical definition for the particles rather than defining level sets for each particle improves the performance of the method. In addition, due to the diffuse nature of the interface it is expected that the pressure

fluctuations related to moving boundaries be alleviated. Details of this method and application will be mentioned in the next chapter as the method might be a proper candidate for the simulation of particle-laden flows.

It is necessary to mention that sometimes the term “sharp interface method” is generalized for the discrete forcing approach, where the interface boundary is sharp, as opposed to diffuse interface method of the original IBM concept [119]. Moreover, the term “immersed boundary” can be employed for the fluid embedded objects on a non-conforming grids or even for the continuous forcing approach [102].

2.3. Conclusions

The efficiency of the simulation of flows containing multitudes particles as rigid object is the essential parameter on choosing a model. While boundary conforming methods are usually easier to implement, the non-boundary conforming methods are faster when the domain contains numerous moving boundaries with high displacement such as blood containing cells as a particulate flow. As mentioned, SPM is supposed to be an efficient method for such problems since there is no need to apply the boundary conditions explicitly and the particles as rigid objects could be defined easily. In the next chapter details of SPM as a continuous forcing approach is expressed.

CHAPTER 3

MESO SCALE MODELING OF PARTICULATE FLOWS

The meso scale simulation of numerous finite size particles such as blood flow is a challenging task as with increase of number of particles, the numerical methods lose their efficiency. Finding an efficient and robust method for this simulations makes the study of such problems feasible in the current clusters. We see the so called "smoothed profile method" (SPM) as a potential candidate for these simulations and present the related features in this chapter.

Nakayama and Yamamoto [74] proposed the SPM as an efficient alternative to various immersed boundary methods such as Arbitrary Lagrangian-Eulerian (ALE) [93], Distributed Lagrange Multiplier (DLM) [124] and Force Coupling Method (FCM) [145] to simulate rigid particulate flows. SPM is a non-boundary conforming diffuse interface method that in the spirit of original immersed boundary method of Peskin [118] constructs a single velocity field spanning the embedded rigid particles and the carrier fluid. In other diffuse interface methods [102] the effect of particles carried by the fluid is modeled through a forcing term in the momentum equations so that the velocity field smoothly transitions between the fluid and solid phases over a finite interface thickness. To distinguish SPM from the traditional diffuse-interface IBM-type approaches, it is noted that SPM applies the fluid-solid interaction forces through an extra projection step in a fractional-step scheme. This leads to the calculation of an extra "particle pressure field" which is used in a second correction step to enforce compatibility between fluid and solid velocities at the transition zone between the two phases. In contrast, in traditional IBM approaches the solid-fluid interaction force is directly included in the momentum equation in the fractional-step scheme [146], so that the "particle pressure" is not computed separately. This is also in contrast to porosity-type formulations [147, 148] where the fluid-to-solid transition zone is treated as a

porous medium with a smoothly varying permeability constant or methods where a mollified Dirac delta function is employed to apply the fluid-solid interaction force directly into the momentum equation.

Nakayama and Yamamoto [74] implemented SPM in the context of Fourier spectral scheme to examine hydrodynamic interactions in colloids. They validated the scheme for drag coefficient, C_D, of a cylindrical rod for $Re < \mathcal{O}(1)$ and then studied sedimentation of 2D colloidal particles in a Newtonian fluid. Luo *et al.* [75] extended the method by adopting a semi-implicit formulation for the flow solver. An time integration scheme based on the fractional-step method was implemented for the fluid phase solver and an explicit scheme was used to update the particle velocity and position. More recently, SPM was advanced to model flows containing charged particles [149-152], Brownian motion [153] and paramagnetic particles [154]. SPM has also is used in turbulent flow modeling [155, 156], multicomponent dispersion of particles [156], and in calculating the diffusion coefficient of multicomponent particles in colloids [157]. The method was modified to model changes in developing boundaries as in in clot formation in aneurysms [158], to simulate wall roughness in flow problems [159], to include the compressibility of flow [160] and to apply appropriate boundary conditions on the surface of self-propelled swimmers [161].

As the various applications mentioned above suggest, SPM is attractive for particulate flow simulations due to several reasons. First, it applies no-slip and no-penetration interface boundary conditions implicitly which greatly simplifies the computational implementation of immersed solid interface conditions. Because SPM does not alter discretization stencils or require interpolations at the solid-fluid interface it is straightforward to implement in existing single-fluid flow solvers and to extend the SPM approach to general mesh topologies. Consequently, SPM also works well with higher-order methods as in spectral element approaches [74, 75]. A potential downside is that because SPM is formulated in terms of a forcing term which is spread over a finite interface thickness, it is necessary to adjust the interface thickness to obtain the correct flowfield and forces on the particle. Specific theory on setting the numerical parameters such as the interface thickness is lacking. The dependency of the results

on the size of interface thickness is addressed in [74] by Nakayama el al. There is a brief discussion on how to choose an integer factor of fluid mesh size for the interface thickness. However, it is limited to one case of drag force for flow over a fixed cylinder. Luo et al [75] showed the dependency of the results obtained on the time step size and suggested an optimum value for the time step size in the Couette flow. Therefore, the success of SPM hinges on appropriate specification of the interface thickness and the time step size and their robustness for a variety of flow conditions needs to be examined.

3.1. Formulation of SPM

The SPM algorithm for fluid-structure interaction starts with updating the flow with a semi-implicit flow solver. Then the interaction of solid and fluid is calculated and the kinematic variables (acceleration, velocity and position) of the solid are updated explicitly using the computed forces and moments from the fluid phase.

3.1.1. Flow solver

For the flow solver, the governing equations are the incompressible Navier-Stokes equations. In non-dimensional form the momentum transport equation is [162, 163]:

$$\frac{\partial \boldsymbol{u}}{\partial t} + \boldsymbol{u} \cdot \nabla \boldsymbol{u} = -\nabla p + \frac{1}{Re} \nabla^2 \boldsymbol{u} \tag{3-1}$$

$$\nabla \cdot \boldsymbol{u} = 0 \tag{3-2}$$

where $\boldsymbol{u}(\boldsymbol{x}, t)$ and $p(\boldsymbol{x}, t)$ are the non-dimensional velocity and pressure fields. The Reynolds number $Re = UD/\nu$, where U and D (particle diameter) are the velocity and length scales, and ν is the constant kinematic fluid viscosity.

Denoting the domain boundary as S, the velocity is required to satisfy a prescribed Dirichlet condition, $\boldsymbol{b}$ on S:

$$\boldsymbol{u}|_S = \boldsymbol{b} \tag{3-3}$$

The value of a variable ζ is set at an outflow boundary by solving the one-dimensional advection equation,

$$\frac{\partial \zeta}{\partial t} + \bar{U}\boldsymbol{n} \cdot \nabla \zeta = 0 \tag{3-4}$$

In Equation (3-4), $\bar{U}$ is a mass-conserving bulk velocity, and $\boldsymbol{n}$ is the outward-directed normal vector to the boundary. In the case that ζ is the component of the velocity normal to the boundary, a uniform correction is added to each grid cell on the outflow boundary after the solution of Equation (3-4) to explicitly enforce mass conservation.

The governing equations are evolved in time using a second order algorithm [164-166] where the use of consistent definitions of the pressure and pressure boundary condition lead to solutions with 2nd-order accuracy. The splitting error can be treated by pressure correction approaches [167, 168] where the pressure is included in an explicit manner in the first step (velocity update) of the fractional-step scheme. In a second step, the pressure is corrected to project the velocity field onto a divergence-free vector subspace. However, pressure correction approaches still carry errors at boundaries due to the pressure boundary conditions, which are typically of Neumann type; a numerical boundary layer persists at the boundary, leading to deterioration of the order of accuracy. The pressure is then only accurate to $\mathcal{O}(\Delta t)$. To recover second-order accuracy Timmermans proposed a rotational correction field [169], which was shown by later works [170] to indeed produce second-order temporal accuracy of velocity and pressure fields in periodic domains. Guermond and Shen [171] showed however that in general domains the velocity and pressure fields show $\mathcal{O}(\Delta t^2)$ and $\mathcal{O}(\Delta t^{3/2})$ accuracy respectively. Note that in the case of the SPM approach the issue of pressure boundary conditions on the interface does not arise since the solid-fluid interface is not treated explicitly, i.e. the no-slip and no-penetration conditions are enforced via source terms in the governing equations. Therefore, the rotational correction for pressure is important mainly for the sharp interface method where boundary conditions at the embedded sharp solid surface are crucial to obtain accurate results.

The current implementation of the fractional-step approach closely adheres to the implementation in Guermond and Shen [171] (also see Shen [172]) with modifications to account for the presence of immersed boundaries in the mesh. As in standard fractional-step approaches, in the first step a provisional velocity field $\boldsymbol{u}^*$ is computed from the momentum equations using an estimation of the pressure gradient from the previous time step, ∇p^n. Here, the index n refers to the time level. Applying a J^{th}-order backward difference scheme for the time-derivative, the provisional velocity is computed according to

$$\frac{\alpha \boldsymbol{u}^* + \sum_{j=0}^{J-1} \beta_j \boldsymbol{u}_{n-j}}{\Delta t_{n+1}} + (\boldsymbol{u} \cdot \nabla \boldsymbol{u})_{n+1} = -\nabla p^n + \frac{1}{Re} \nabla^2 \boldsymbol{u}^* \tag{3-5}$$

$$\boldsymbol{u}^*|_S = \boldsymbol{b}_{n+1} \tag{3-6}$$

Here, $(\boldsymbol{u} \cdot \nabla \boldsymbol{u})_{n+1}$ is an approximation of the non-linear term at time t_n, and the α and β coefficients define the time-integration scheme. In the case of adaptive time-stepping, the coefficients for the 2nd-order backwards differencing scheme are $\alpha = \frac{2r+1}{(1+r)}$, $\beta_0 = -(1+r)$, and $\beta_1 = \frac{r^2}{(1+r)}$ where $r = \frac{\Delta t_{n+1}}{\Delta t_n}$ [173].

In a second step, the pressure gradient estimate used in Equation (3-5) is removed from the provisional velocity,

$$\frac{\alpha \boldsymbol{u}^{**} - \alpha \boldsymbol{u}^*}{\Delta t_{n+1}} = \nabla p^* \tag{3-7}$$

The removal of the pressure estimate introduces additional stability which helps to suppress the pressure checker-boarding experienced for non-staggered grids. Finally, a Helmholtz-Hodge decomposition is constructed to isolate the solenoidal projection of $\boldsymbol{u}^{**}$ which is taken as the physical velocity at t_{n+1}. The final velocity is computed as

$$\frac{\alpha \boldsymbol{u}_{n+1} - \alpha \boldsymbol{u}^{**}}{\Delta t_{n+1}} = -\nabla p_\varphi \tag{3-8}$$

$$\boldsymbol{u}_{n+1}|_S = \boldsymbol{b}_{n+1} \tag{3-9}$$

An equation for the scalar potential p_φ is constructed by taking the divergence of Equation (3-8) which results in the following Poisson equation:

$$\nabla^2 p_\varphi = \frac{\alpha \nabla \cdot \boldsymbol{u}^{**}}{\Delta t_{n+1}} \tag{3-10}$$

The Poisson equation for p_φ is subject to a consistent Neumann condition,

$$\boldsymbol{n} \cdot \nabla p_\varphi = -\boldsymbol{n} \cdot \left(\boldsymbol{a}_S - \frac{1}{Re} \nabla^2 \boldsymbol{u}^* \right) \tag{3-11}$$

where $\boldsymbol{a}_S$ is the acceleration of the immersed solid (particle) surface. Following Timmermans et al. [169], the physical pressure is defined using a rotational correction procedure:

$$p_{n+1} = p_\varphi - \frac{1}{Re} \nabla \cdot \mathbf{u}^* \tag{3-12}$$

Note that the above form of the rotational correction fractional-step method amounts to modification of the procedure from Shen et al. [172] to accommodate immersed boundaries on which the boundary condition, Equation (3-11), is supplied to obtain p_φ from Equation (3-10). The method as presented here also accounts for moving boundary accelerations in Equation (3-11).

3.1.2. Update of particle position

Particle velocity and angular velocity of particles are updated as:

$$\frac{d\boldsymbol{V}_i^{n+1}}{dt} = \left(\boldsymbol{F}_{h_i}^{n+1} + \boldsymbol{F}_{ext_i}^{n+1} \right) / M_i$$

$$\frac{\mathbf{d}\boldsymbol{\Omega}_i^{n+1}}{dt} = \left(\boldsymbol{T}_{h_i}^{n+1} + \boldsymbol{T}_{ext_i}^{n+1} \right) / I_i \tag{3-13}$$

where M_i and I_i are respectively mass and moment of inertia and $\boldsymbol{F}_{ext_i}^n$ and $\boldsymbol{T}_{ext_i}^n$ are external force and moment on the particle. Similarly particle position and orientation is updated by integration of velocity and angular velocity:

$$\frac{d\boldsymbol{X}_i^{n+1}}{dt} = \boldsymbol{V}_i^{n+1}$$

$$\frac{d\boldsymbol{\Theta}_i^{n+1}}{dt} = \boldsymbol{\Omega}_i^{n+1} \tag{3-14}$$

Symplectic Euler integration [173] is used for the time integration of Equation (3-13) and Equation (3-14) which updates the velocity by the first order Euler integral estimation and the displacement is obtained by mid-point (trapezoidal) rule.

The FSI problem of solid particles carried by an underlying fluid is solved in the following using SPM approach, implemented as described in the following section. For better comparison sharp interface method (SIM) is also used to find out what the trade-offs and performance characteristics of sharp and smoothed interface methods are for treating solid particles embedded and transported in incompressible flows. In general, smoothed interface methods are simple to implement when compared to sharp interface methods. For a researcher contemplating the choice between sharp and smoothed (diffuse) methods this leads to the question: Is there sufficient reason to choose sharp interface methods over smoothed (diffuse) ones? To a large extent smoothed or diffuse interface methods are viewed as naturally leading to lower accuracy with regard to the interface treatment and therefore sharp interface approaches are preferred, particularly for flows with thin boundary layers [69, 102]. To what extent this impression regarding smoothed methods is valid and for what Reynolds number regimes it is valid is not *a priori* fully clear. To address these questions on a sound basis it is useful to cast state-of-the-art sharp interface and smoothed interface methods in a unified flow solver framework, with identical nominal order of accuracy and to compare them over a range of flow scenarios. Researchers who intend to pick sharp over smoothed interface methods or vice versa will benefit from having access to a study that clarifies the trade-offs, particularly in the framework of the increasingly popular Cartesian grid methods, or more generally immersed boundary methods [102].

In this chapter, the original semi-implicit formulation of the smoothed profile method [74, 75] is presented and used for several cases in order to characterize and validate the method against a nominally 2^{nd}-order accurate sharp interface method [106, 174]. Both interface treatments are set in the same flow solver that operates on an adaptively refined Cartesian grid [175]. In both methods the interface is represented and tracked by using an analytical representation of particle shape; for communicating the interface location to the SIM the surface representation is converted to a level set function. All computations are performed at cell centers in a regular Cartesian grid in a non-staggered variable arrangement.

3.1.3. Smoothed profile method

The SPM approach implicitly represents the solid particle via a spatial indicator field that smoothly transitions between zero and one in the fluid and solid phases such that the interface is represented as spread over a few grid points. For the i^{th} particle, the indicator field, $\varphi_i(\boldsymbol{x}, t)$, is given by

$$\varphi_i(\boldsymbol{x}, t) = \frac{1}{2}\left[\tanh\left(\frac{d_i(\boldsymbol{x},t)}{\xi_i}\right) + 1\right] \tag{3-15}$$

Here, $d_i(\boldsymbol{x}, t)$ is the signed normal distance to the particle surface and ξ_i is the specified interface thickness; the thickness of the interface is not fixed *a priori* but has to be established through numerical experimentation. By convention, the distance field is positive inside the particle. Figure (3-1) represents a depiction of the SPM indicator function and the variation of the field across the interface. One of the facts about this indicator function is that with a $tanh$ profile, it reaches the saturation points, i.e. zero and one very fast. The other one is that the shape of the profile depends on interface thickness as with increase of ξ_i, the profile becomes smoother. Moreover, due to the diffuse nature of the interface, ξ_i is only a parameter showing the thickness of the interface. In this research the value of ξ_i is fixed for all of the particles and therefore, we always use ξ.

To construct the indicator function field, the indicator function of all particles is summed:

$$\varphi(\boldsymbol{x}, t) = \sum_{i=1}^{N_p} \varphi_i \tag{3-16}$$

The velocity of the rigid particles is convolved with the indicator function field to form the particle velocity field which is defined everywhere in the computational domain:

$$\boldsymbol{u}_p^{n+1}(\boldsymbol{x}, t) = \left[\sum_{i=1}^{N_p}\left(\boldsymbol{V}_i^{n+1} + \boldsymbol{\Omega}_i^{n+1} \times \left[\boldsymbol{x} - \boldsymbol{X}_i^{n+1}\right]\right)\varphi_i\right]/\varphi \tag{3-17}$$

$\boldsymbol{X}_i^{n+1}$, $\boldsymbol{V}_i^{n+1}$ and $\boldsymbol{\Omega}_i^{n+1}$ are the updated i^{th} particle position, velocity and angular velocity, respectively. The total blended velocity field is a weighted combination of fluid velocity and particle velocity fields.

$$\boldsymbol{u}^{n+1}(\boldsymbol{x}, t) = \varphi \boldsymbol{u}_p^{n+1} + (1 - \varphi)\boldsymbol{u}_f^{n+1} \tag{3-18}$$

Since φ is smooth, the resulted blended velocity also will be a smooth blend of particle field velocity and fluid velocity and is stored everywhere in the domain. As shown by Nakayama and Yamamoto [74] and Luo *et al.* [75] two essential characteristics of SPM are obtained by taking the curl and divergence of the total velocity field. Taking the curl of Equation (3-18) demonstrates that the no-slip boundary condition is satisfied over the interface and taking the divergence of Equation (3-18) shows the satisfaction of the no-penetration condition at the particle interface. Thus, the boundary conditions at solid surfaces are implicitly applied in SPM.

In FSI problems SPM updates the provisional velocity and pressure from the particle-free single phase flow solution i.e., $\boldsymbol{u}^*$ and p^* by adding an extra force $\boldsymbol{f}_s$ which represents the particle-fluid interaction through

$$\int_{t^n}^{t^{n+1}} \boldsymbol{f}_s dt = \varphi\left(\boldsymbol{u}_p^{n+1} - \boldsymbol{u}^*\right) \tag{3-19}$$

Then, the blended velocity is updated by

$$\boldsymbol{u}^{n+1} = \boldsymbol{u}^* + \int_{t^n}^{t^{n+1}} \left[\boldsymbol{f}_s - \frac{\nabla p_p}{\rho}\right] dt = \boldsymbol{u}^* + \varphi\left(\boldsymbol{u}_p^{n+1} - \boldsymbol{u}^*\right) - \frac{\Delta t}{\rho}\nabla p_p\,(\boldsymbol{x}, t) \tag{3-20}$$

where, ∇p_p is the extra pressure field due to presence of particles. Taking the divergence of Equation (3-20) to enforce incompressibility constraints $\nabla.\boldsymbol{u}^n = 0$, $\nabla.\boldsymbol{u}^* = 0$ and $\nabla.\boldsymbol{u}^{n+1} = 0$, the following Poisson equation for the particle pressure is obtained:

$$\frac{\Delta t^{n+1}}{\rho}\nabla^2 P_p = \nabla.\varphi\left(\boldsymbol{u}_p^{n+1} - \boldsymbol{u}^*\right) \tag{3-21}$$

Luo et al. [75] presented a semi-implicit version of SPM in which the flow is updated semi-implicitly and the particle kinematic variables (Equations (3-13) and (3-14)) are obtained explicitly. In the first stage, the flow field is evolved in the four-step fractional-step method using Equations (3-5) to (3-10) by ignoring the solid particles. Then, the particle locations and velocities are updated using the previous time step values (Equations (3-13) and (3-14)) based on high-order explicit methods such as Adams-Bashforth scheme. Then, Equations (3-15) to (3-17) are used to create the updated indicator

function field and particle velocity field. The particle-fluid-interaction force and moment are obtained from

$$\boldsymbol{F}_{h_i}^{n+1} = \frac{1}{\Delta t^{n+1}} \int \rho\, \varphi_i \left(\boldsymbol{u}^* - \boldsymbol{u}_p^n\right) d\boldsymbol{x} - \int \varphi_i \rho \boldsymbol{g} d\boldsymbol{x} \tag{3-22}$$

$$\boldsymbol{T}_{h_i}^{n+1} = \frac{1}{\Delta t^{n+1}} \int \boldsymbol{r}_i^{n+1} \times \left[\rho \varphi_i \left(\boldsymbol{u}^* - \boldsymbol{u}_p^n\right)\right] d\boldsymbol{x} - \int \varphi_i\, \boldsymbol{r}_i^{n+1} \times (\rho \boldsymbol{g}) d\boldsymbol{x} \tag{3-23}$$

In Equation (3-23) $\boldsymbol{r}_i^{n+1}$ is the radius vector from center of the particle to any of the grid points.

After finding the particle velocity and angular velocity from Equation (3-13), the particle velocity field is obtained from Equation (3-17) which is updated using the extra particle pressure field computed using a second Poisson equation (3-21). Then, the total velocity field is calculated through the following projection:

$$\boldsymbol{u}^{n+1} = \boldsymbol{u}^* + \varphi\left(\boldsymbol{u}_p^{n+1} - \boldsymbol{u}^*\right) - \frac{\nabla P_p}{\rho} \Delta t \tag{3-24}$$

Finally, the pressure is obtained from summation of the pressure flow solution and the extra particle pressure.

$$p = p_f + p_p \tag{3-25}$$

3.1.4. Sharp interface method

SIM treats the fluid and solid as two separate entities and couples the two fields through the solid-fluid interface by enforcing continuity of normal and tangential velocities as well as tractions for both phases at the exact interface location. The mesh does not change (except for adaptive refinement) and solid boundaries are non-conforming to the mesh [102, 106]. In previous implementations of the SIM, the stencils for differential operators, i.e. ∇ and ∇^2 were modified using a cut-cell [176-179] or finite-difference method [104, 106, 174] to capture the necessary interface conditions. In this work, to simplify implementation of SIM, techniques are adapted from the Ghost Fluid Method (GFM) [112, 180] so that the fluid variables are extended into one layer of solid nodes immediately adjacent to the interface; this set of nodes in the immediate interior of the solid are called “ghost nodes”. By adopting the ghost fluid

approach the regular five-point (in 2D)/7-point (in 3D) discretization stencil is preserved and the discretization in the current central difference scheme is symmetric. The onus then falls on appropriately populating the ghost cell values. Here a least-squares field reconstruction is used that is locally 2nd-order accurate for Dirichlet and Neumann boundary conditions applied on piecewise smooth immersed boundaries. Ghost node values are obtained by constructing a least-squares extrapolation from a cloud of nearby fluid nodes and values on the solid-fluid interface. This approach makes it possible to handle all boundary condition types that may be required by an FSI solver in a unified fashion, and the smoothness of the extrapolation is easily modified by adjusting the least-squares basis functions and cloud radius.

3.1.4.1. Classification of computational nodes

On the Cartesian grid, the immersed boundary is the zero-level of a level set field which encodes the signed normal distance from each grid node to the boundary. The level set field is used to identify different types of computational nodes as explained in Table (3-1). Away from the interface (see Figure (3-2)), standard finite difference techniques may be used to approximate the spatial operators of the governing equations. These grid nodes are called “fluid nodes”, and they are characterized by a positive level set value above a specified threshold. The set of grid nodes immediately inside the solid boundary for which the level set value is negative and a neighboring node in a Cardinal direction has a positive level set value are called “ghost nodes”. For moving solid boundaries a third subset of grid nodes are defined, which are labeled “hybrid nodes”, which form a buffer between the fluid and ghost nodes. A grid node is a hybrid node if it has a positive level set value less than the fluid node threshold value. In this work, the threshold value is set to $\sqrt{2}\Delta x$ if a hybridized treatment is desired. At a hybrid node flow variables are computed using a weighted blending of the treatments applied at fluid and ghost nodes. During the transition from the ghost to hybrid state, computational nodes can emerge from solid to fluid state; such nodes are called “freshly cleared nodes” [106, 174]. A freshly created node does not have a history which satisfies the governing equations. These nodes, which can be identified by a change in level

set value from negative to positive over one time step, are populated using a pure interpolation from the surrounding cells during the solution process. This can be handled in the hybrid node framework by setting the blending to be completely determined by the ghost treatment. After one time step, a freshly cleared node is transitioned to a regular hybrid node. The procedures to discretize the governing equations at each of the four node types above are described in sequence below.

3.1.4.2. Various types of node treatment

In the current moving boundary scheme, the solution of the Navier-Stokes equations is required at fluid nodes, where all neighbors are also in the fluid state and therefore the discretization is straightforward. Operators required for the solution of the Navier-Stokes equations are discretized using standard 2^{nd}-order centered finite differences.

To assign values to ghost nodes, extrapolating functions are constructed such that the function achieves the desired boundary condition value at a specified location on the interface. In multiple dimensions, selecting a unique extension function is not obvious. Two possible approaches are to extrapolate in a dimension-by-dimension manner or to assign a single unique extension for each ghost node which uses a boundary value at the closest point on the interface to the ghost node. Here the second approach is used as it simplifies the interface treatment for Neumann boundary conditions on the immersed boundary.

The extrapolation is constructed from a weighted least-squares treatment which allows for seamless incorporation of both Dirichlet and Neumann conditions into the functional fit. A multi-dimensional polynomial is constructed from a set of cloud points located in a neighborhood of the closest point on the interface to a ghost node. The coefficients of the polynomial are obtained by constructing a linear solver using the known fluid and interface values. Details of the method is described in [69].

Following Luo et al. [181], hybrid cell values are also computed as a weighted average of the fields produced by using the fluid and ghost node solutions. Moreover, the same operators as fluid nodes

are also used at hybrid nodes but the overall discretization at hybrid nodes is then modified by blending with the ghost node operators. The blending coefficients are zero for fluid nodes and one for ghost nodes. For hybrid cells, the blending coefficient α_H is defined in terms of the level set field value as

$$\alpha_H = \text{MAX}(1 - \frac{\phi}{\phi_{fluid}}, 0) \tag{3-26}$$

where ϕ_{fluid} is the level set value at the interface of the fluid and the hybrid nodes. This definition has the property that $\alpha_H \to 0$ as the grid point moves into the fluid and $\alpha_H \to 1$ as the grid point approaches the interface.

For the fresh nodes by setting $\alpha_H = 1$, the value is obtained by a purely implicit interpolation during the solution of the momentum and Poisson equation linear systems.

3.2. Results

SPM and SIM were implemented in a finite volume flow solver called pELAFINT3D [69] that operates on a Cartesian grid. All computations are performed on Helium, the Linux PC Cluster of the University of Iowa, with the number of processors determined based on the grid size and duration for which the flow computations were performed. Processor counts typically ranged between 8 and 64.

In the results presented below the SPM approach is compared with SIM for a variety of particle-fluid coupling problems. The results from SPM and SIM are assessed against benchmarked values for moderate Reynolds numbers in 2- and 3-D and stationary and moving immersed boundaries.

3.2.1. Interface thickness and time step size effect in SPM

3.2.1.1. Specification of interface thickness in the SPM formulation

In SPM a key parameter that determines the accuracy of the interface treatment is the interface thickness. The fact that interface thickness ξ affects the flow results has been reported by Nakayama and Yamamoto [74] who showed that change of ξ affects the calculated drag coefficient C_D of the particle.

They choose an integer factor of grid size for the interface thickness in a creeping flow simulation calibrated to obtaining the correct value of C_D. Kang and Suh [154] also studied similar dependency in a creeping flow over a particle. However, the resultant force varied only a few percent in the limited range of $\xi/\Delta x = 0.2\ to\ 0.5$ for very low Re. In the following, numerical studies are performed to explore the possibility of developing a robust problem-independent correlation for *a priori* setting of the interface thickness parameter. Additionally the interface thickness required for moderate Reynolds numbers is investigated.

In order to avoid rigid object grid generation and also the consequent processes related to level set generation, the analytical approach of Luo et al [75] is implemented. Therefore, instead of defining the indicator function field based on the distance from the particle boundary as in Equation (3-15), when the analytical formulation of the shape is known, the following equation is used:

$$\varphi_i(\boldsymbol{x},t) = \frac{1}{2}\left[\tanh\left(\frac{f_i(\boldsymbol{x},t)}{\xi}\right) + 1\right] \tag{3-27}$$

where $f_i(\boldsymbol{x},t)$ is the surface function of the particle i with respectively zero, negative and positive values on the surface, outside the particle and inside the particle. For an ellipsoid with a, b and c as semi-axes, we have $f_i(\boldsymbol{x},t) = 1 - \left(\frac{x^2}{a^2} + \frac{y^2}{b^2} + \frac{z^2}{c^2}\right)$.

The numerical experiments to determine how to set the interface thickness parameter are performed as follows. A stationary sphere is placed at a position of $(6,5,5)$ in a horizontal channel with a domain of size $24 \times 10 \times 10$ as shown in Figure (3-3a). A uniform unit velocity in the stream-wise direction is specified at all domain boundaries except the right boundary, where a convective outflow condition is prescribed. A uniform grid with $\Delta x = \Delta y = \Delta z = 0.125$ is chosen with $\Delta t = 0.05$ corresponding to the $CFL = 0.4$.

Variation of the C_D with interface thickness is shown in Figure (3-3b). The experimentally determined values of C_D at different Re are obtained from the empirical relation [182]

$$C_D = \frac{24}{Re}[1 + 0.27Re]^{0.43} + 0.47[1 - exp(-0.04Re^{0.38})] \tag{3-28}$$

and displayed as the stars for each Re. As seen in the figure the computed C_D grows with increase of interface thickness but it is almost independent of ξ for ξ values of order one or less. The increase of drag force for higher values of thickness stems from the greater "blockage" of the flow by the somewhat enlarged obstacle presented by the immersed boundary as demonstrated by Figure (3-4). When the interface thickness is greater, the wake is more elongated and the low velocity region near the particle is extended leading to a higher value of form drag. Another observation from Figure (3-3b) is that the experimentally measured drag value is significantly different from the computed one for the lower range of Reynolds numbers and for the range of interface thickness over which the computed drag can be considered to have "converged". As the Reynolds number increases (for $Re = 100$ for example) the experimentally determined C_D value is in agreement with the numerically computed "converged" C_D. However, at the higher Re range the interface thickness at which the drag computation is robust is such that $\xi < \Delta x$. Thus, it is not straightforward to set a specific value of interface thickness that applies over a range of Re and grid sizes.

3.2.1.2. Time step size effect in SPM

Adding more complexity to the method Luo et al. [75] show that there exits an optimum value for the time step Δt which gives rise to minimum error in the computed drag. This can be seen in Figure (3-5). To show this, by fixing the interface thickness at $\xi = 1\Delta x$, the value of the CFL number was varied to quantify the effect of time step size on the computed drag on the particle. The results for the drag at different Reynolds numbers in Figure (3-5) show the decrease of the computed C_D value with increase of CFL (i.e. increase of time step size); this dependency on the CFL number is greater for low Re. With the SPM treatment therefore, the results will depend on interface thickness ξ as well as the time step size (CFL). As is clear in Figure (3-5), the optimum value of CFL decreases with increase of Re, i.e. to obtain accurate results the time step size is increasingly restrictive for lower Reynolds numbers. Therefore,

holding the arbitrary interface thickness parameter fixed, as is commonly the case in diffuse interface methods can lead to incorrect results in the SPM approach.

3.2.1.3 A broadly applicable interface thickness correlation

Luo et al. [75] found that the error produced by SPM is a function of $\sqrt{\nu\Delta t}/\xi$ and suggested some optimum interface thicknesses for different cases using different fractional step schemes combined with a high order spectral element method. However, their suggested values led to high errors in the current finite volume method, especially as CFL and ξ do not affect the present discrete system of equations in the same way as in Luo et al. This necessitates choosing an appropriate value for the Δt and ξ for the particular choice of numerical techniques used, which is not a desirable feature for researchers seeking to use the SPM approach. A possible solution to the problem is to tune the ξ based on Δt, so that the dependency of the results on the CFL can be removed. From a practical standpoint it would be most desirable to develop a general correlation for ξ that the user can employ without having to conduct numerical experiments for various flow situations. It is not clear *a priori* what form such a robust correlation will assume. To attempt to find such a correlation for ξ as a function of the CFL number (the discretization-related parameter) and Re (flow physics-related parameter), the problem of a falling sphere in a stationary fluid was chosen. In this case, the particle terminal velocity depends on the drag force; since from Figures (3-3) to (3-5) the computed drag force is related to the interface thickness parameter the correct terminal velocity will only be obtained if the drag force is computed correctly. Therefore, the accuracy of the final predicted terminal velocity at steady state conditions is used to find a robust value ξ for various grid sizes and Reynolds numbers. At each CFL number, various ξ values are used to find the resulting final velocity (and hence C_D). The optimum value of ξ is obtained provided the correct value of the final velocity is reached. The following correlation is obtained based on the regression of the resulting optimum particle interface thickness from the numerical experiments for $CFL \leq 0.5$ and $Re < 100$:

$$\xi = (\Delta x)^{0.1}\left(0.17 + 1.44Re^{-0.35}\right)(10CFL)^{(0.4+0.1/Re)}Re^{-0.2} \quad (3\text{-}29)$$

Where Re is the particle Reynolds number. Consequently, ξ becomes a fluid and geometry parameter rather than a flow variable. Moreover, similar to [74], it shows that the interface thickness is linearly proportional to the grid size.

To test whether the interface thickness correlation established above is reliable and general, it was employed to compute the flow around a stationary sphere. Figure (3-6) shows the resulting error in drag coefficient for a stationary sphere at different CFL and Re. It shows sensitivity of the results of C_D at a broader range of Re values. It can be inferred that with increase of Re and CFL, the accuracy of the correlation decreases. With increase of Re, the characteristic viscous length scales become smaller and smaller grid sizes are required at the immersed interface. Therefore, the demand for more refined grid to obtain accurate values of drag implies that for higher Reynolds numbers computations of flows using SPM can become computationally expensive. The question then is how the computational demand compares to that for the SIM.

3.2.2. Comparison of SIM and SPM for fixed particles

To compare the performance of SPM and SIM approaches, the methods have been applied to flow around a stationary sphere by implementing SPM with the correlation in Equation (3-29). The geometry is similar to Figure (3-3a). The base mesh grid size is $\Delta x = 0.25$ and two levels of local mesh refinement are used unless otherwise mentioned.

3.2.2.1. Vortex pattern analysis

SPM is compared with SIM for flow around a sphere at $Re = 50$, 100 and 200. The experimental results of Johnson and Patel [183] are used as the benchmark. The minimum grid sizes are respectively $\Delta x = 0.125$, 0.125 and 0.075 for the mentioned Res. For $Re = 200$, a smaller grid size was used to capture the minimum flow characteristic length scale. The results are compared for the vortex

center, separation point angle and the axial length of vortex and are given in Table (3-2). The deviation of the values obtained with SPM from the experiment is very low and overall the values are in good agreement and comparable with that of SIM at $Re = 50$. For $Re = 100$, while SPM predicts the separation point angle better, SIM is more accurate in predicting the center of vortex. At $Re = 200$, SPM predicts the separation angle somewhat better than SIM but SIM results in better values for the vortex length.

Overall, by implementing the suggested correlation based on C_D in SPM, the correct vortex patterns in the coarse grids can be reached and SPM's results are slightly closer to experiments. SPM over-predicts the length of the vortex bubble which is probably due to latency in closure of vortex as a result of a shift in vortex bubble into the backflow due to the diffuse interface.

3.2.2.2. Grid refinement study

Figure (3-7) shows a study of grid dependency of SPM. It is clear that especially for $Re > \mathcal{O}(1)$, the correlation is robust. There is more sensitive dependence on grid size at low Re as ξ is larger for low Reynolds numbers and the effect of particle presence is extended farther from the nominal surface of the particle. The channel size for the next study is $30 \times 20 \times 20$ and $40 \times 12 \times 12$, respectively for $Re = 3$ and 150 and the spherical particle is at (10,10,10) and (6,6,6). In order evaluate the effect of grid refinement, various levels of refinement have been applied on two base grid sizes of 0.33 and 0.24. The resulting C_D related to different Reynold numbers and grid sizes are presented in Figures (3-8) and (3-9), including the variation of the resulting error with refinement of the grid at various Reynolds numbers. Also plotted are the separate components of the drag obtained from SIM. It is clear that for very coarse grids, the results of SPM are better than SIM. It can be seen from the figures that SIM under-predicts the value of C_D on coarse grids but with grid refinement the C_D approaches the correct value. In contrast, the SPM solution appears to give reasonable results even for fairly coarse grids for the lower Reynolds number (Re=3). However, for the higher Reynolds number, Re=150, the error obtained from SPM does

not display a monotonic trend. On the other hand, while SIM produces larger errors relative to SPM on coarse grids the convergence trend of SIM is robust for both Re=3 and Re=150.

Further insight into the rather large variations of error with grid coarsening in SIM relative to SPM is obtained by examining the individual components contributing to the drag on the particle. In the case of SPM, it is not possible to separate out the drag contributions; In contrast, SIM needs to add the traction components at the sharp interface and therefore the contributions of viscous and pressure forces can be separately evaluated. For coarser grids, the viscous component of C_D related to SIM has large variations while the pressure only varies modestly; this is due to the calculation of the viscous stresses at the sharp interface by obtaining normal derivatives of the fluid velocity. This leads to the greater dependency of the total drag on the grid resolution in the case of SIM.

To probe further, the variation of velocity and pressure is examined along the centerline of the axis for the two methods and compared at different Re values. The results are presented in Figures (3-10) to (3-12). The region within the particle is indicated by the box. The positive values of the x-axis indicate the recirculation region. The boundaries of the sphere are located at $x = \pm 0.5$. In general, the velocity at the position of the sphere is not exactly zero in SPM because the indicator function varies smoothly at the nominal surface of the particle. However, with refinement of the grid, the thickness ξ decreases and therefore at the center of the sphere the velocity approaches zero asymptotically. The velocity profiles for both methods are almost identical outside of the particle for refined and moderately coarse grids. The extreme values of pressure in SPM are less than that of SIM as expected. In SIM, the pressure inside the particle is zero except for the points very close to the interface which have some non-zero values due to interpolations related to applying the ghost fluid method. In SIM the pressure and velocity inside the particles are not physical and their values do not participate in the flow solution. The pressure inside the particle for the SPM changes steadily and continuously from positive to negative values and the flow field in computed in the particle as well. As seen in Figure (3-12) for very coarse grids, there are oscillations in both SPM and SIM methods; these oscillations vanish with grid refinement. More

importantly, for coarse meshes the SIM solution (Figure (3-12a)) shows larger differences from the finer mesh solutions than the SPM solution (Figure (3-12b)).

3.2.2.3. Vortex shedding regime

At $Re = 300$, the wake behind the stationary sphere is not stable and vortex shedding occurs [184]. The SPM and SIM solutions are studied on a domain size $50 \times 12 \times 12$ with a sphere of unit diameter whose center is located at (12.5,6.0,6.0). SPM and SIM calculations are performed on a coarse grid with base grid size of 0.3333 with three levels of refinement. The fine grid simulation has a base grid size equal to 0.2 with four levels of refinement.

The results of C_D are shown in Figure (3-13a) which includes the average experimental values [182]. It is seen that SPM overestimates the value but SIM underestimates it. Both methods can capture the vortex shedding phenomenon (Figure 13b)) and the correct Strouhal number of 0.145 ([184, 185]) but only at the finer mesh resolution. Vortical structures for this flow at Re=300 are shown in Figure (3-13b) for fine grid solution of both methods. They are colored based on vorticity on the stream-wise direction. For both SPM and SIM at coarse grid, $St \sim 0.123$; for the fine grid SIM, $St = 0.143$ and the error in the average C_D becomes less than 2%. However, there exist small high frequency fluctuations that do not appear in SPM.

3.2.3. Comparison of SPM and SIM for moving particles

To compare the two methods for moving particles several test cases are considered in the following, viz. the flow around a dropping sphere, impulsively started moving sphere in a horizontal channel and an inline oscillating cylinder in an imposed flow.

3.2.3.1. Dropping sphere

The settling of a sphere in a stationary fluid with the Reynolds number at the final settling velocity $Re_{final} = 30$ is studied. The domain is a vertical channel with dimensions $15 \times 15 \times 50$ and all six walls are considered as fixed. A spherical particle with center located at (7.5,7.5,8.0) settles under gravity. In order to compare the efficiency of SPM and SIM at coarse grids, a mesh with original size $\Delta x = 0.25$ is chosen but two levels of local mesh refinement are applied every five time steps to update the grid with motion of the particle. Using a CFL value based on the maximum velocity in the field and the finest grid size, the time step is adapted to maintain the condition $CFL = 0.2$. For this case the solid to fluid density ratio is 10.0. The Froude number is set to 5.63 to reach the final settling velocity of one.

First, the time history of particle velocity from SPM is compared with that from SIM in Figure (3-14). SIM shows a converging trend towards the correct value of final unit velocity; Note that SPM provides good results even at the coarsest grid. For SIM on the finest grid $V_{final} = 1.045$ but for SPM on the coarse grid $V_{final} = 1.024$. At $t = 30$, Contours of velocity and x-vorticity of SPM for the coarse grid and SIM for fine grid also are shown in Figure (3-15). Both methods have similar flow patterns which verifies the good performance of SPM even at coarse grids. As in the case of the stationary sphere, the error analysis has been performed for the dropping sphere problem at different Re and for varying time step size or CFL parameter (Figure (3-16)). Similar to Figure (3-6), with increase of Re and CFL, the accuracy of the SPM approach decreases because the interface thickness correlation is less robust at high Reynolds numbers for a given grid size. Therefore, for higher Reynolds numbers in the range of $Re > \mathcal{O}(100)$, the SPM approach demands smaller time step sizes and finer grids to produce good results.

3.2.3.2. Moving sphere in horizontal channel

The issues raised above for SPM in the case of moving and stationary spheres are further examined through study of a sphere moving in a channel which is computed using SPM. The spherical particle starts moving from rest in a horizontal channel, under the influence of fluid forces. A uniform

velocity of one is specified in the channel at the start of the calculation. The base grid size for the coarse grid used is $0.3 \times 0.3 \times 0.3$ with two levels of local mesh refinement with a fixed time step size of 0.025. The base grid size for the fine grid used is $0.15 \times 0.15 \times 0.15$ with four levels of local mesh refinement with a time step size of 0.01.

The results are shown in Figure (3-17) for $Re_0 = 10$ where Re_0 is the initial Reynolds Number. The coarse grid SPM solution yields particle velocity trends that are close to the fine grid solution of SIM showing that SPM works well even for coarse grids. Similar to the case of the dropping sphere, SPM shows a small over-estimation of the position in comparison with the fine grid SIM.

3.2.3.3. Inline oscillating cylinder

It is well established that immersed boundary methods suffer from non-physical pressure oscillations in the presence of moving boundaries. Many explanations have been posited as to the source of this numerical artifact. Lee et al. [186] identified two sources contributing to pressure oscillations: the spatial discontinuity of the pressure field as a solid node becomes a fluid node, and the temporal discontinuity of the velocity field as fluid nodes become solid nodes. Through a parametric study, the authors established that pressure oscillations decreased with increasing grid resolution and increasing time-step size. However, pressure oscillations were found to be more sensitive to grid spacing than time-step size. The authors implemented a mass source/sink technique which reduced the pressure oscillation in their indirect discrete forcing approach. Seo and Mittal [107] analyzed the oscillation problem from the perspective of non-conservation of geometric volume which is inherent in most GFM methods. They showed that treating the Poisson equation with a conservative cut-cell technique leads to a significant reduction in pressure oscillations even while retaining the GFM approach for the momentum equation in their fractional step solver. Luo et al. [181] argue that the discontinuous temporal nature of discrete operators induced by switching between ghost and fluid treatments is the source of pressure oscillations. They presented a hybridization strategy that smoothly transitions the numerical scheme between ghost

extrapolation and the discretization of the Navier-Stokes equations as grid nodes move out of the solid and into the fluid. The arguments of Luo et al. [181] show that pressure oscillations depend on grid spacing and time-step size as $\Delta x^2/\Delta t$ for a second-order scheme. Through their analysis of geometric volume conservation, Seo and Mittal predict a dependence of the form $\Delta x^d/\Delta t$, where d is the spatial dimensionality. While consistent for two-dimensional examples, Seo and Mittal [107] predict pressure fluctuations will be much smaller in three-dimensional simulations. Noting that Hartmann et al. [178] observed pressure oscillations in simulations using a strictly conservative cut-cell approach, Schneiders et al. [187] show that the abrupt temporal transitions in numerical stencil is the source of strong pressure oscillations in their conservative scheme. To remedy this, the authors propose a continuously differentiable weighting function to smoothly transition discrete operators near the moving interface.

In this section, the performance of the two approaches is assessed for the moving boundary problem of an inline cylinder which oscillates in a freestream flow. The main focus of this investigation is a characterization of the behavior of the pressure fields for SPM and for SIM with and without hybridized interface treatments. As mentioned, hybridization is utilized at the interface in the SIM approach to suppress spurious pressure oscillations in FSI problems. On the other hand, since SPM is a technique that takes a "one -fluid" approach, the freshly cleared node issue does not arise. In formulating of the SIM hybridized numerical scheme, there are several choices in how to apply hybridization to the fractional step algorithm. One could hybridize the computation of both the intermediate velocity and the pressure, or alternatively, one could hybridize a single step in the algorithm. Through experimentation, it was established that the most significant reduction in oscillation magnitude occurs when hybridization is applied to the Poisson equation. However, utilizing the hybridization technique in all steps of the fractional step method leads to further reduction in oscillation magnitudes.

We examine two alternatives to handling the fresh node condition of GFM. The first is an approach similar to that used in [180, 188], whereby flow variable values are extended into a layer of grid cells of a specified thickness immediately inside the solid domain for each time step of the flow solver.

The extension is carried out using the multi-dimensional partial differential equation approach proposed by Aslam [189]. An alternative approach is implemented very naturally in the current hybridized formulation. The values at fresh nodes are computed by setting the blending coefficient α_H to 1 so the fresh node value is obtained by a purely implicit interpolation during the solution of the momentum and Poisson equation linear systems. This recovers the treatment proposed by Mittal et al. [174]. It should be noted that the pressure field must be extended into the solid for the pressure gradient to be correctly evaluated for fluid cells adjacent to the interface even in the case of stationary boundaries. This is due to the rotational correction of the pressure field imposed in Equation (3-12), which is not incorporated into the GFM treatment.

Following Luo et al. [181] and Seo and Mittal [107], we examine the oscillation characteristics of the proposed interface treatment by considering the flow around a cylinder which is undergoing inline oscillatory motion in an initially quiescent box. The unit diameter cylinder is initially located at the center of a 20×20 domain, and the cylinder centroid and velocity are

$$x(t) = x(0) - \frac{U_{max}}{2\pi f}(1 - cos(2\pi f t)) \tag{3-30}$$

$$u_c(t) = -U_{max}\, sin(2\pi f t) \tag{3-31}$$

where $x(0)$ is the center of the domain, $U_{max} = 1$ in the non-dimensional form and $f = 0.2$ represents the frequency of the oscillation. The Reynolds number, $Re = U_{max}D/\nu$, and the Keulegan-Carpenter number, $KC = U_{max}/fD$, are 100 and 5 respectively.

The effect of grid spacing on oscillation behavior was studied by performing simulations with $\Delta x = 1/16, 1/32, 1/64$, and $1/128$. The CFL number was fixed at a small value of 0.1 in order to generate strong spurious pressure fluctuations. The results of the grid spacing study are shown in Figure (3-18). First, we observe that on a fine enough grid, each of the three schemes converges to the same result. SPM computes smoother solutions on all meshes compared to hybridized SIM and SIM with fresh node interpolation (SIM without hybridization). The hybridized SIM scheme computes significantly

smoother solutions on the three coarsest meshes as well as displaying a more symmetric mean behavior compared to the other schemes.

Next, the effect of CFL number was examined by carrying out simulations with $CFL = 0.1, 0.2, 0.4,$ and 0.8 while fixing the grid spacing at $\Delta x = 1/16$. Here a coarse grid spacing was used to introduce the strongest possible oscillations. The results are shown in Figure (3-19). It is again observed that SPM shows the smoothest trend; the hybridized SIM approach leads to strong suppression of the pressure oscillations at all CFL number values. For all CFL values, the mean behavior of the schemes presented in the SIM with fresh node interpolation displays a strong asymmetry. At small CFL values, the hybridized scheme shows the correct symmetric curve shape. However, at a CFL value of 0.4, the hybridized scheme results show a small asymmetry, and this deviation from the true solution becomes more pronounced at the CFL value of 0.8.

Having ascertained that SPM shows the better pressure suppression and mean trend behavior, we compare the results for the drag coefficient versus time from SPM for the finest grid and smallest time-step size with the results presented by Dütsch et al. [190]; also plotted is the solution obtained from the hybridized SIM scheme (Figure (3-20)). The results of both methods agree well with the benchmark solution.

3.3. Conclusions

In simulating the dynamics of particle-laden flows at the meso-scale one can choose either a sharp or smoothed description of the embedded solid particles. This work compares a sharp interface method implemented with 2nd order discretization of the Navier-Stokes equations and a smoothed particle method. Both methods are built on the same base flow solver; differences in the performance of SIM and SPM are therefore due only to the interface treatment in the two methods. For the SPM approach a robust correlation that applies for a range of Reynolds numbers and resolution is proposed for the interface thickness parameter. This correlation is a function of Re, CFL number and the grid size. The validity of

the correlation has been verified by comparing with experimental data and results from the SIM approach for several problems. SPM results for coarse grids are very close to the ones obtained from fine grids using SIM. The interface thickness parameter used in SPM affects the particle drag force so that larger interface thicknesses lead to higher values of C_D. Also, with increase of the time step size, i.e. the CFL number, the computed, C_D decreases.

Study of the flow around stationary and moving spherical particles shows that the interface thickness correlation in SPM loses accuracy on coarse grids with increase of Re which necessitates decrease of CFL or refinement of the grid when Re increases. It can be inferred that at $Re < 300$ for coarse and moderately fine grids, SPM can predict the value of drag force better than SIM. On the other hand SIM is more reliable and accurate on fine grids. Study of an inline oscillating cylinder demonstrates that SPM shows lower levels of spurious pressure fluctuations and consequently smaller fluctuations in the computed C_D for various grid sizes and CFL numbers. SPM is more successful in suppressing the spurious pressure oscillation field than SIM. However, the hybridized SIM approach is also capable of smoothing the pressure oscillations for fine enough meshes.

In the next section, SPM is further developed to be used in flows containing low particles' density by modifying the method to an implicit scheme. Besides, some necessary steps for better accuracy and stability were performed: Implementation of Euler parameters, introducing a third order variable time step size Backward Euler Formulation for the update of the particle's kinematical variables and implementing the Aitken relaxation technique.

TABLES

Table 3-1- The level set criteria for the four types of computational points in the hybridized ghost fluid method.

Fluid Node	$\phi(\boldsymbol{x}) > \phi_{fluid}$
Ghost Node	$\phi(\boldsymbol{x}) < 0$ and $\phi(\boldsymbol{x})\phi(\boldsymbol{x}_{nbr}) < 0$
Hybrid Node	$0 < \phi(\boldsymbol{x}) \leq \phi_{fluid}$
Fresh Node	$\phi(\boldsymbol{x}^{n+1}) > 0$ and $\phi(\boldsymbol{x}^{n})\phi(\boldsymbol{x}^{n+1}) < 0$

Table 3-2- Comparison of SPM with experiment and SIM for $\Delta x = 0.125$ at $Re = 50$ and $Re = 100$ and for $\Delta x = 0.075$ at $Re = 200$.

Re	**Method**	**Vortex Center**	**Separation Point Angle**	**Vortex Length**
50	Experiment	(0.19,0.21)	139	0.40
	SIM	(0.14,0.25)	143	0.38
	SPM	(0.20,0.23)	137	0.42
100	Experiment	(0.25,0.30)	127	0.88
	SIM	(0.25,0.30)	131	0.89
	SPM	(0.24,0.31)	126	0.89
200	Experiment	(0.91,0.38)	117	1.46
	SIM	(0.87,0.34)	126	1.41
	SPM	(0.95,40)	118	1.71

FIGURES

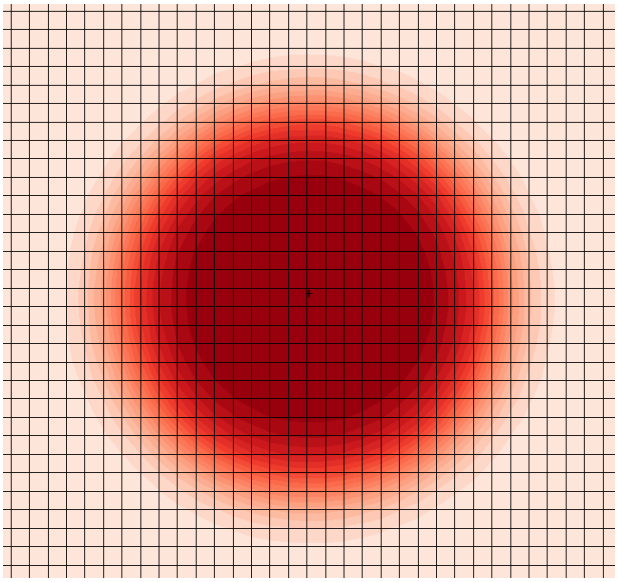

(a)

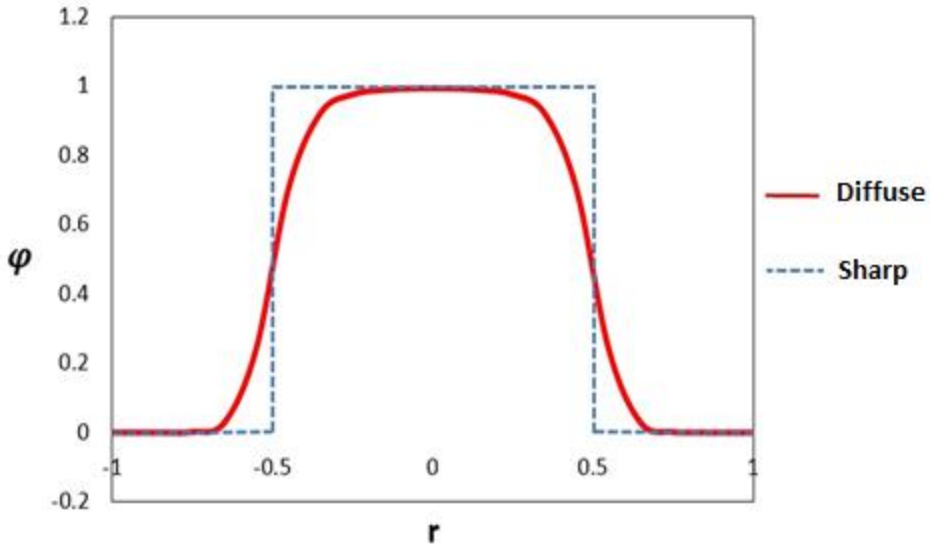

(b)

Figure 3-1- **(a)** An example of generated SPM indicator function for a 2D cylinder case. **(b)** Diffuse and sharp representation of the interface. For the diffuse interface method, SPM indicator function with the $\xi = 5.0$ is used.

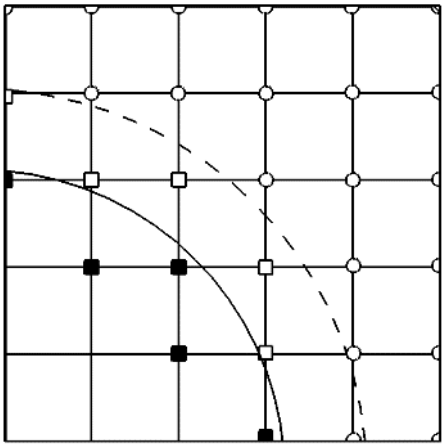

Figure 3-2- The grid node classification of the current sharp interface technique. Ghost and hybrid nodes are represented by filled and open square symbols while fluid nodes are shown as open circles. The ghost nodes complete operator stencils for the white symbols and the hybrid nodes impose a temporal smoothing on the pressure field.

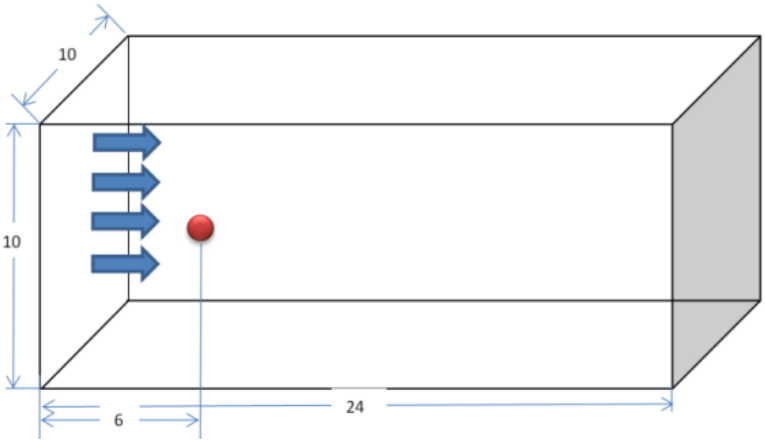

(a)

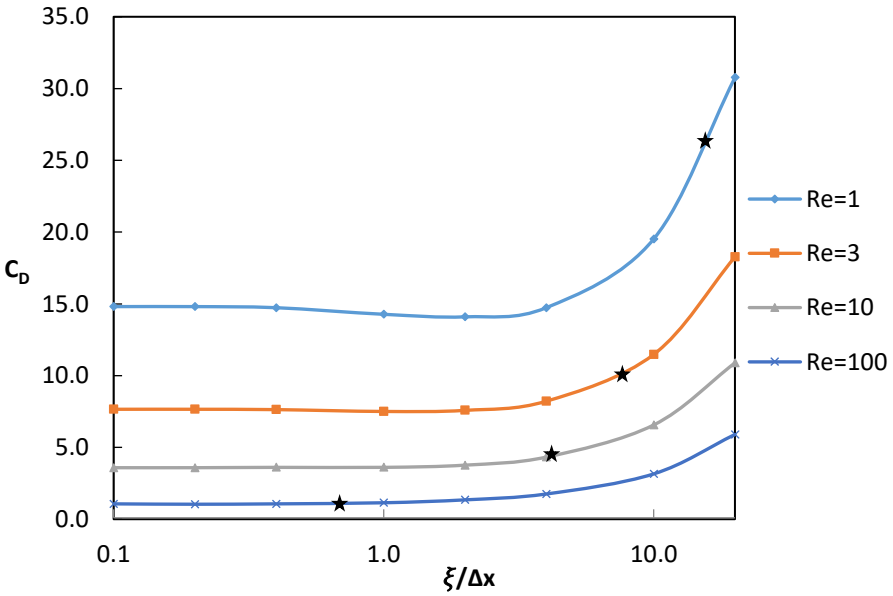

(b)

Figure 3-3- **(a)** A depiction of the simulation domain. The domain has a size of 24×10×10 and the sphere is centered at (6,5,5). A uniform flow condition is prescribed at all domain boundaries except the right boundary where a convective outflow condition is applied. **(b)** Variation of drag coefficient with interface thickness for different Reynolds numbers. The experimental value of C_D for each Reynolds number is marked by a black star.

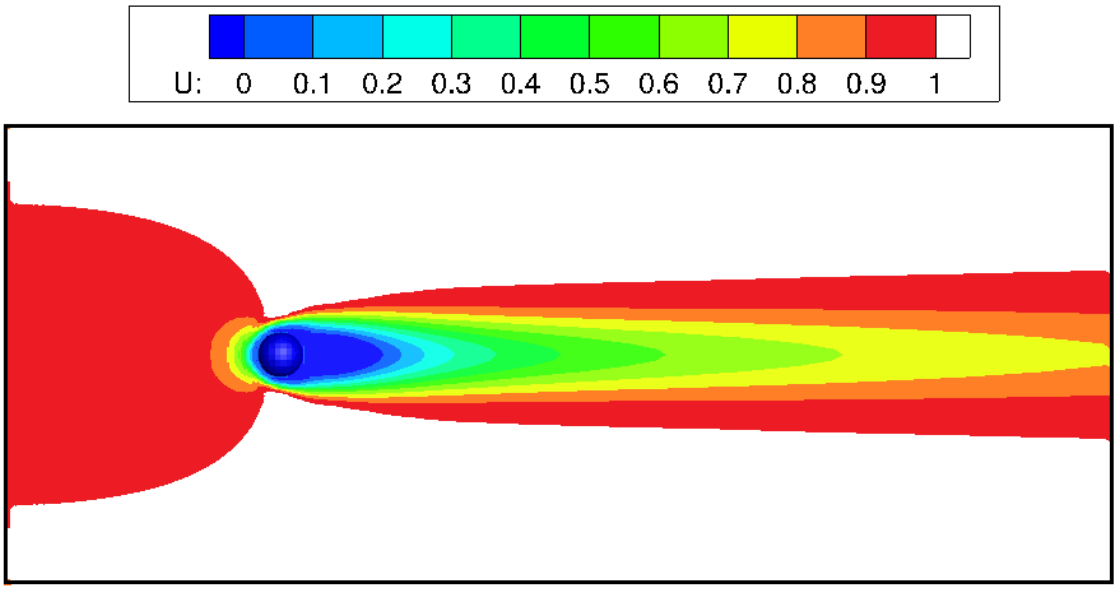

(a)

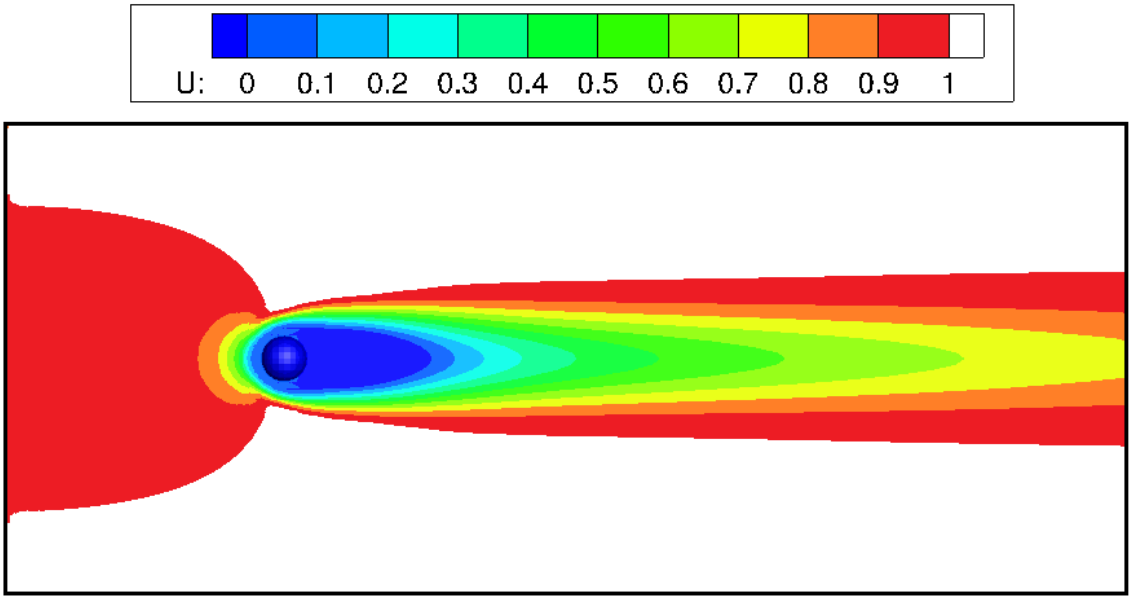

(b)

Figure 3-4- Streamwise velocity contours for flow past a sphere at a Reynolds number of 100 for interface thicknesses of **(a)** $\xi = 0.5$, and **(b)** $\xi = 1.0$. Note the change in the length of the wake bubble associated with the variation of interface thickness.

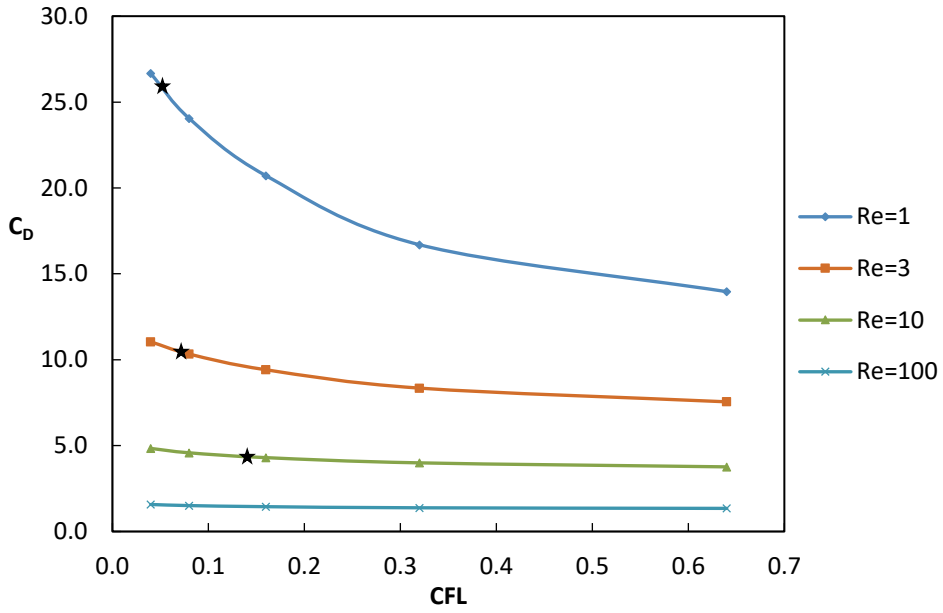

Figure 3-5- Variation of drag coefficient with CFL at different Reynolds numbers at $\xi = 1.0$. The correct drag coefficient for each Reynolds number is marked by a black star.

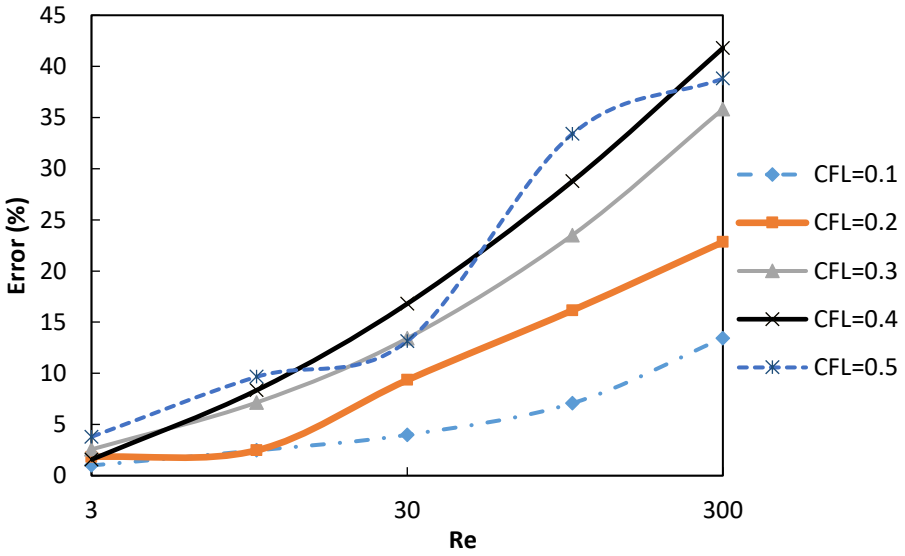

Figure 3-6- The error in adopting the correlation for SPM at various Re and CFL numbers for a stationary sphere.

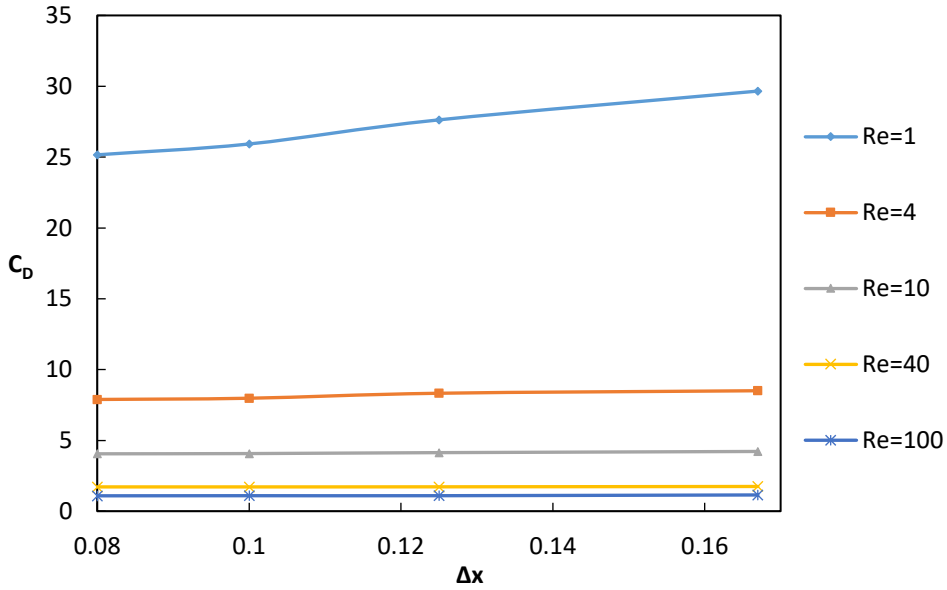

Figure 3-7- Variation of drag coefficient with grid size to show the grid independency of the results when the correlation is applied. Except for very low Reynolds numbers with a mild dependency, the value of drag coefficient does not depend on the grid size.

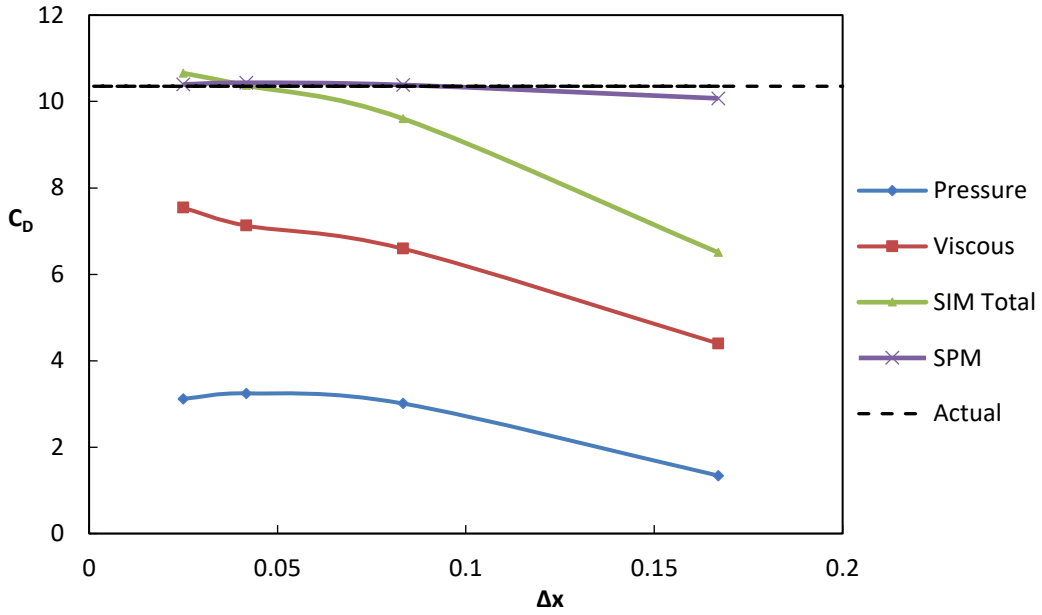

(a)

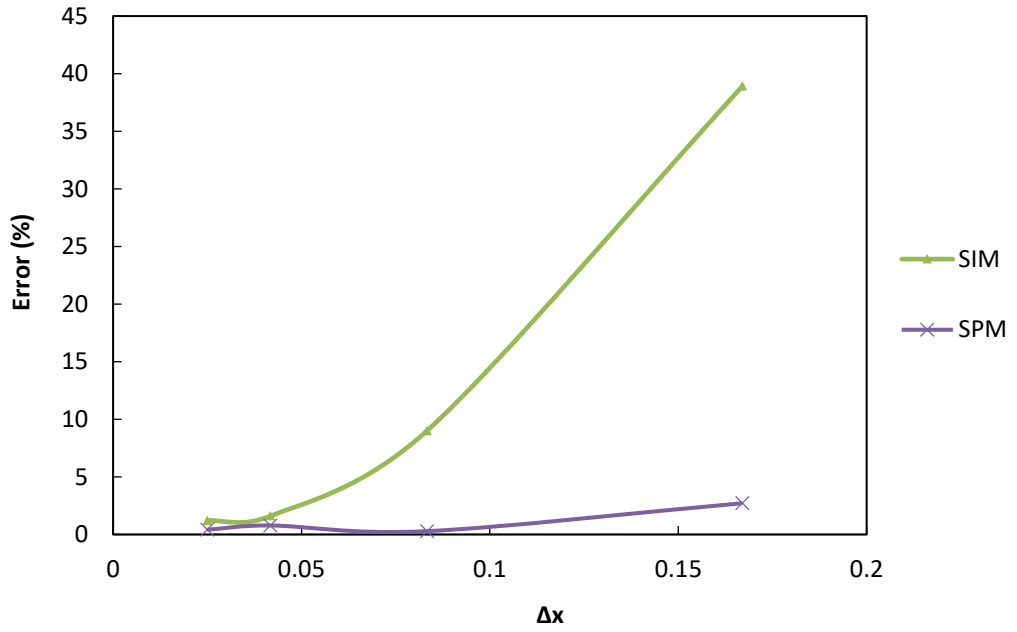

(b)

Figure 3-8- Effect of grid refinement on the drag coefficient: **(a)** Variation of drag coefficient for SPM and SIM at Re = 3. **(b)** Error in drag coefficient with refinement of grid for SPM and SIM at Re = 3.

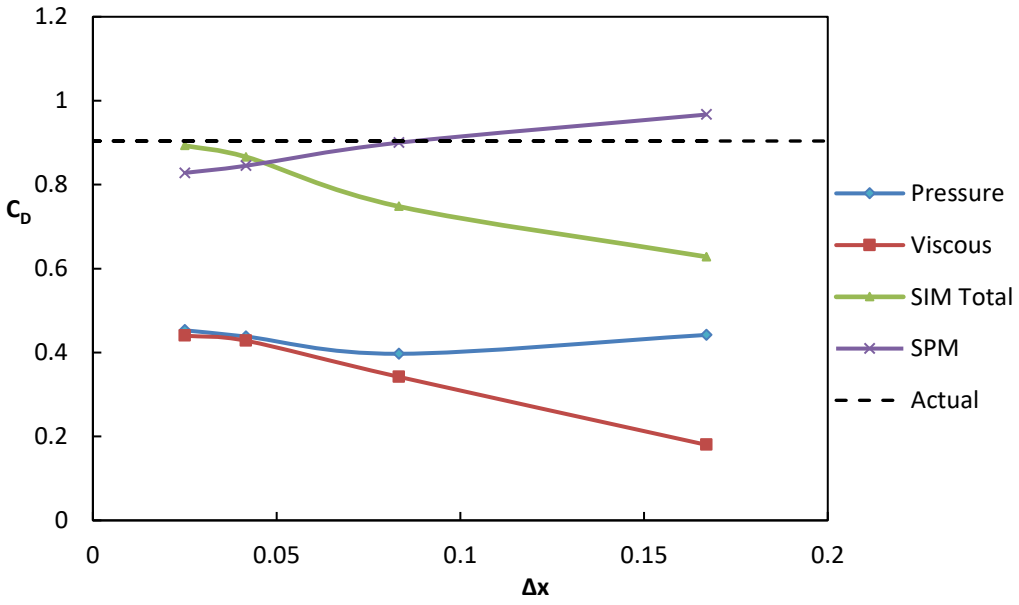

(a)

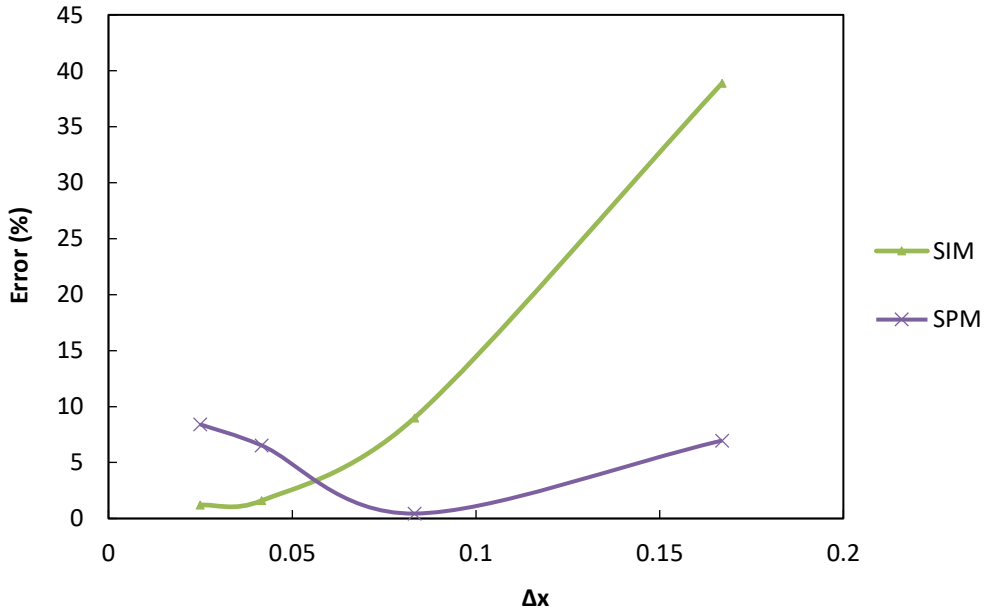

(b)

Figure 3-9- Effect of grid refinement on the drag coefficient: **(a)** Variation of drag coefficient for SPM and SIM at Re = 3. **(b)** Error in drag coefficient with refinement of grid for SPM and SIM at Re = 150.

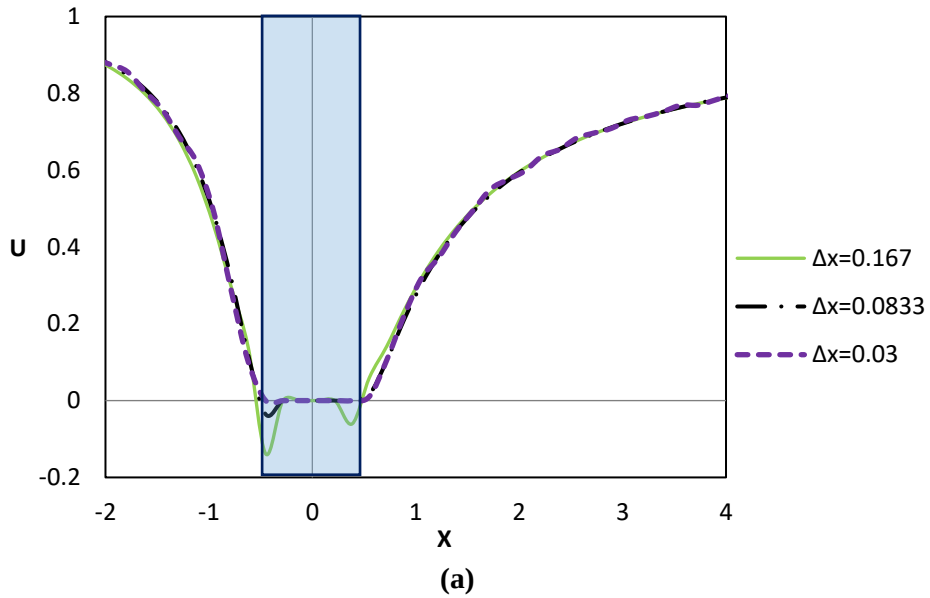

(a)

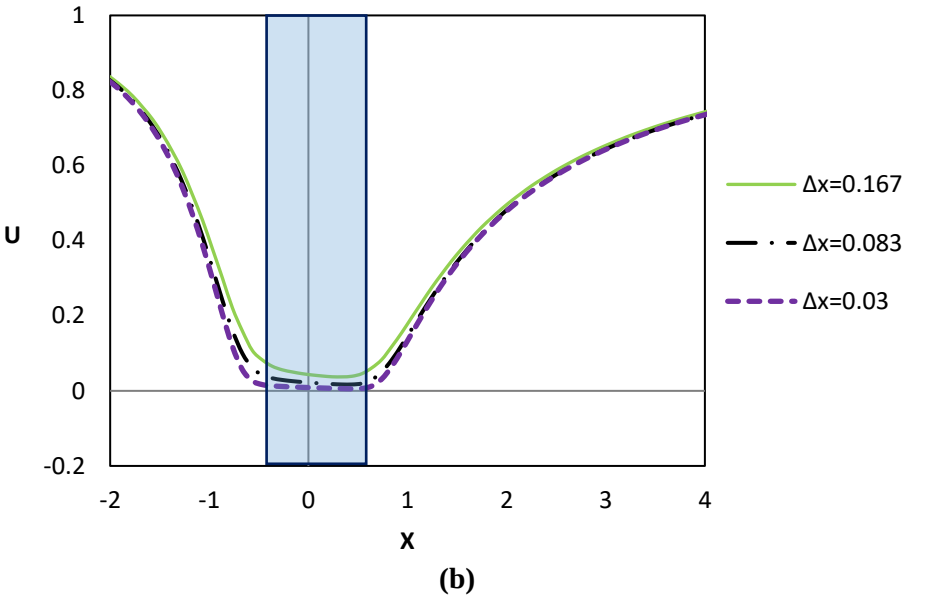

(b)

Figure 3-10- Variation of streamwise velocity for Re = 3 based on **(a)** SIM and **(b)** SPM.

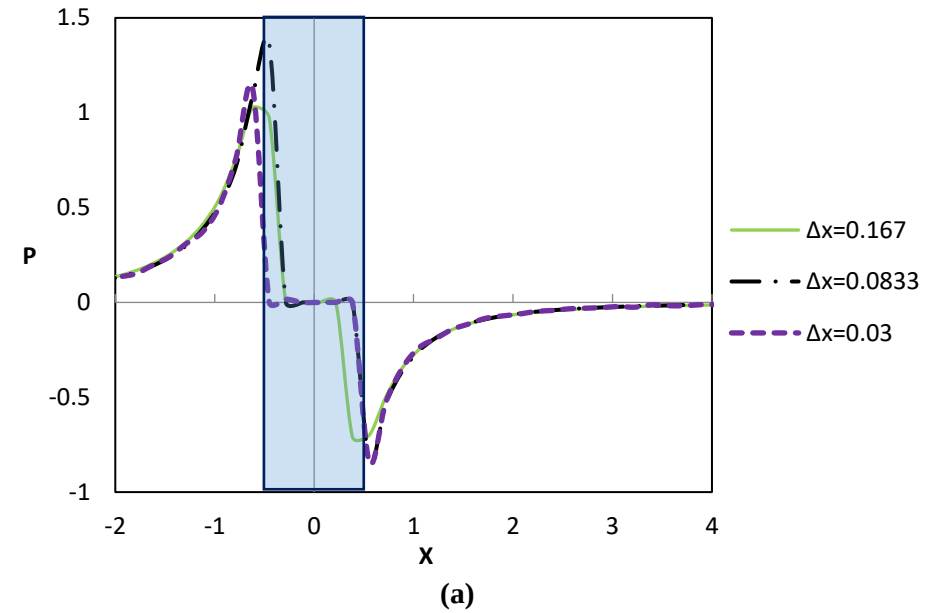

(a)

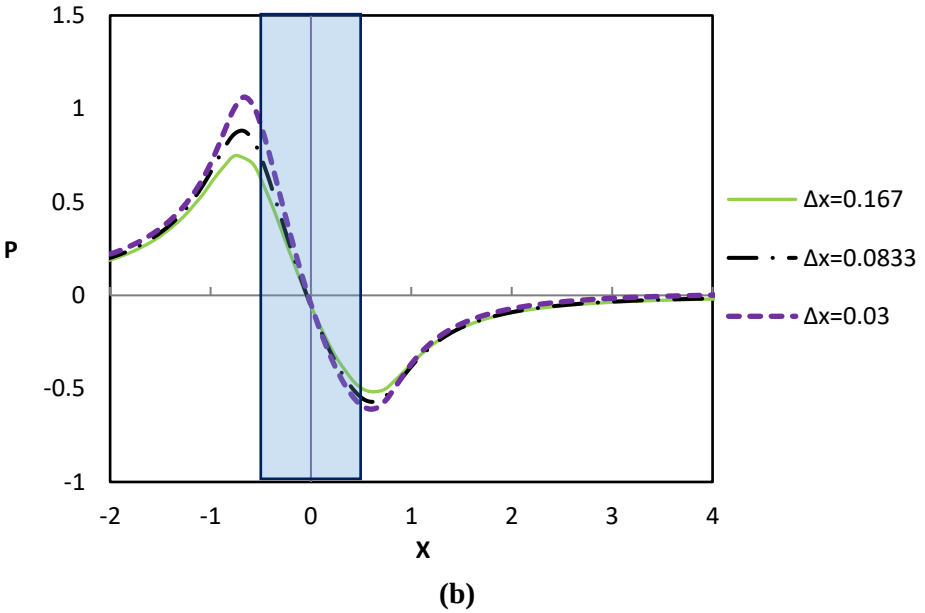

(b)

Figure 3-11- Variation of pressure for Re = 3 based on **(a)** SIM and **(b)** SPM.

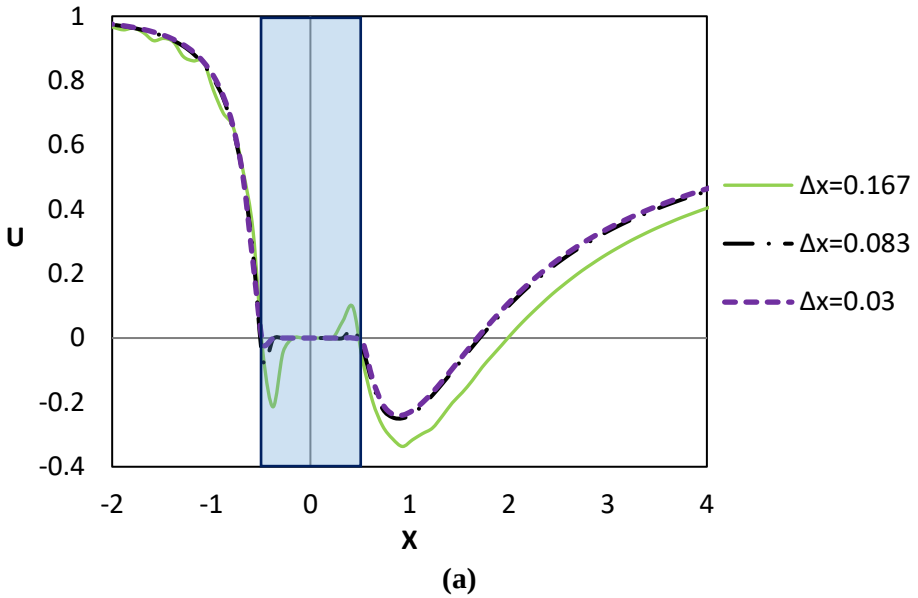

(a)

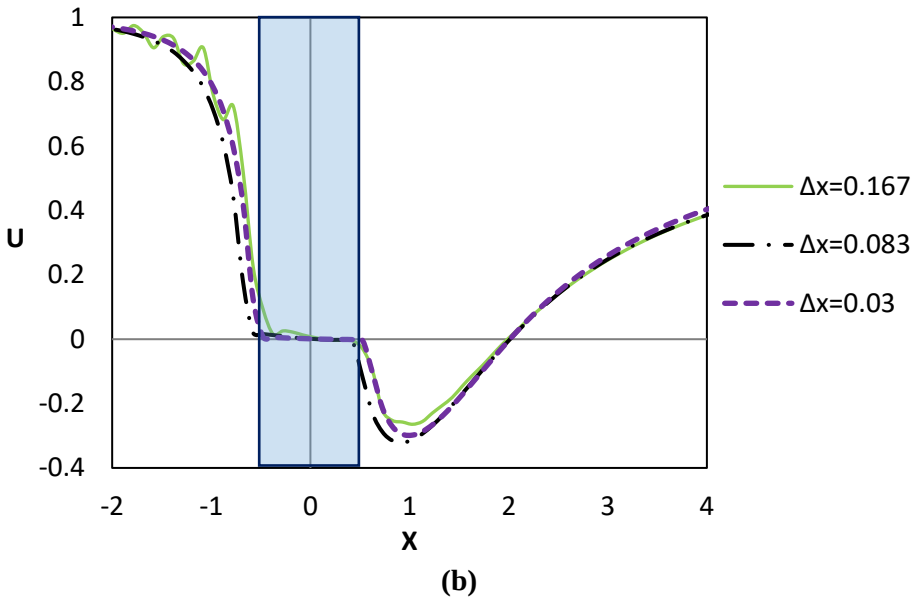

(b)

Figure 3-12- Variation of streamwise velocity for Re = 150 based on **(a)** SIM and **(b)** SPM.

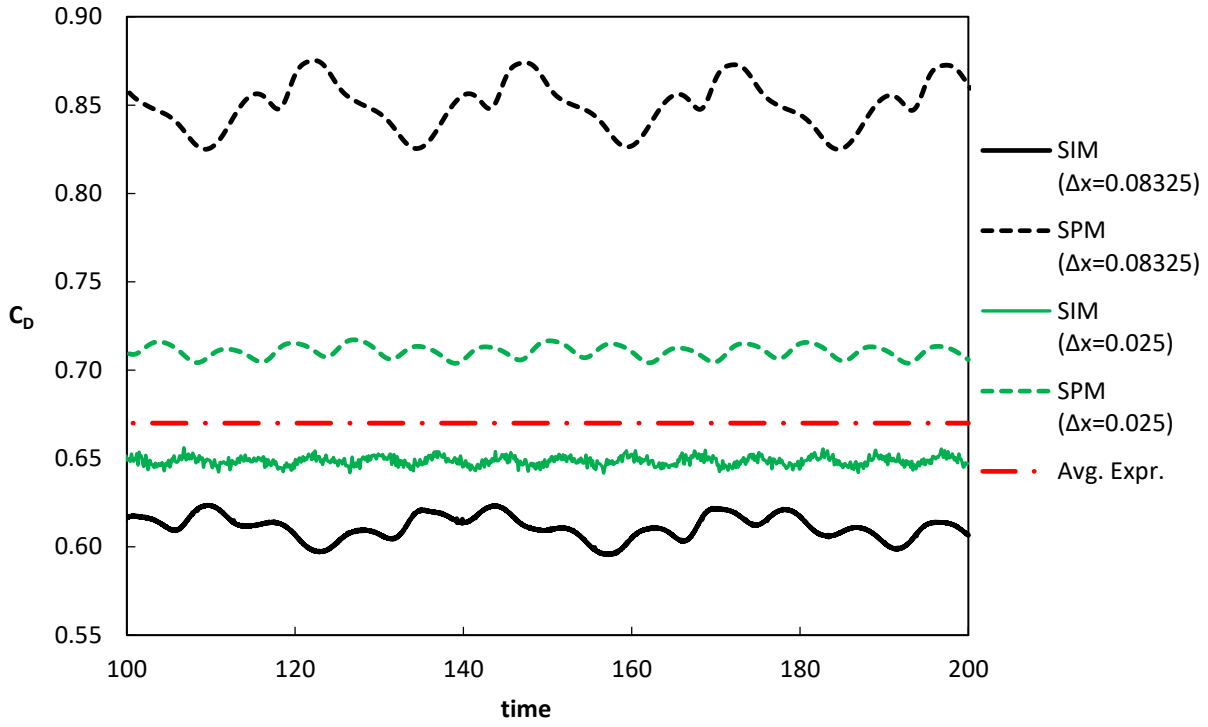

(a)

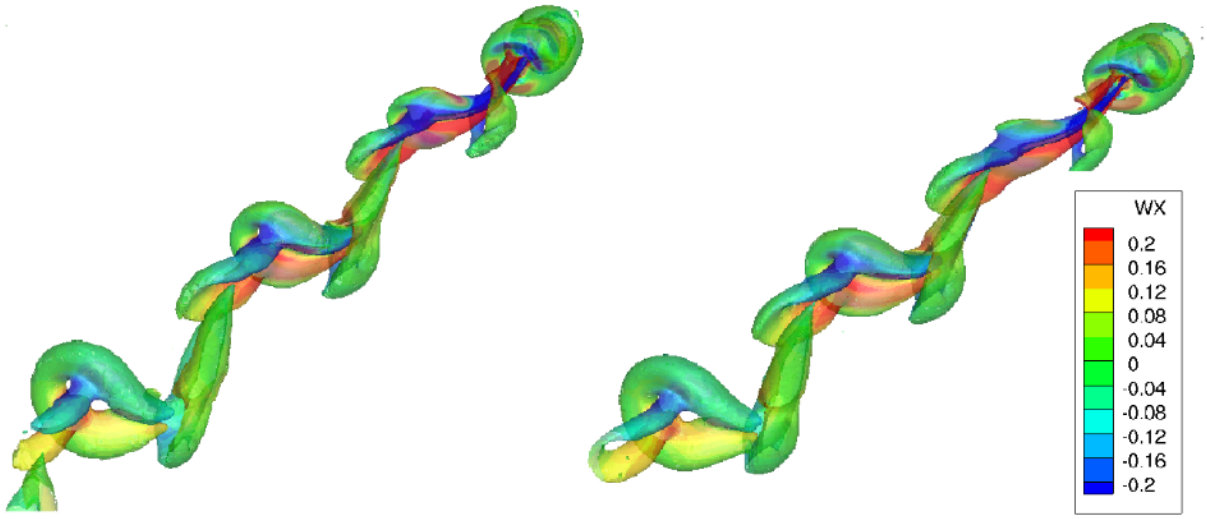

(b)

Figure 3-13- Results for Re = 300: **(a)** variation of drag coefficient as a results of vortex shedding **(b)** vortical structures colored with x-vorticity for SPM (left) and SIM (right).

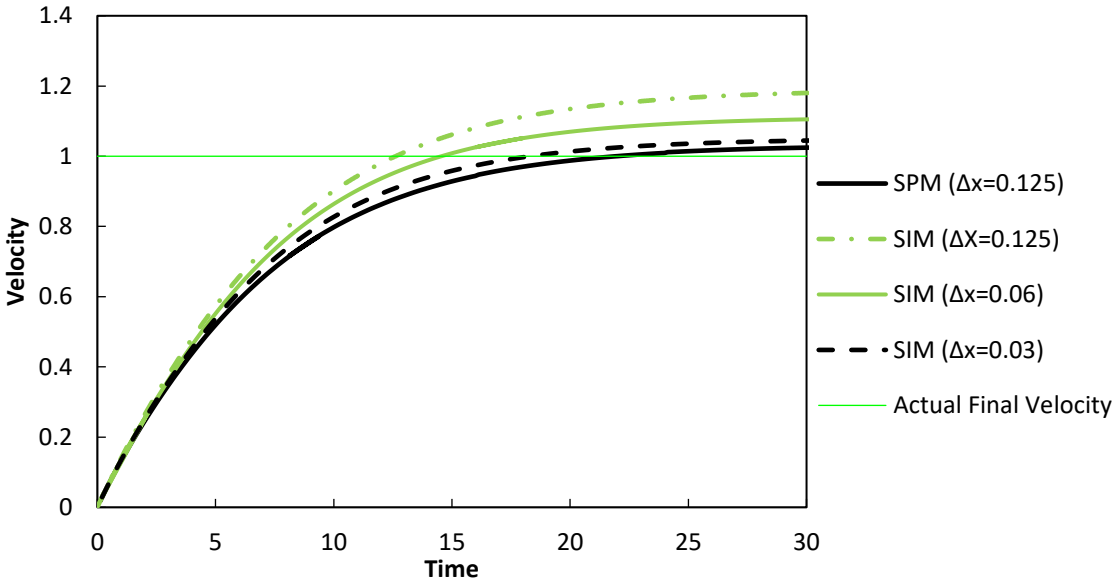

Figure 3-14- Velocity variation of a settling sphere based on the results from SIM and SPM at $Re_{final} = 30$. SPM has the best results for this case.

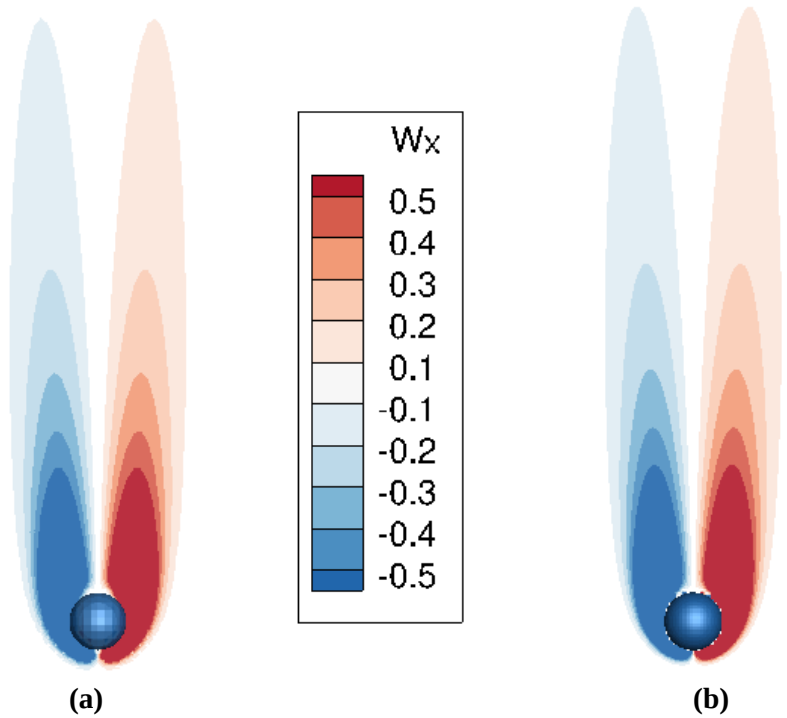

Figure 3-15- The vorticity of flow over a settling sphere based on **(a)** SPM and **(b)** SIM. The final Reynolds number is 30 and the Froude number is 5.63.

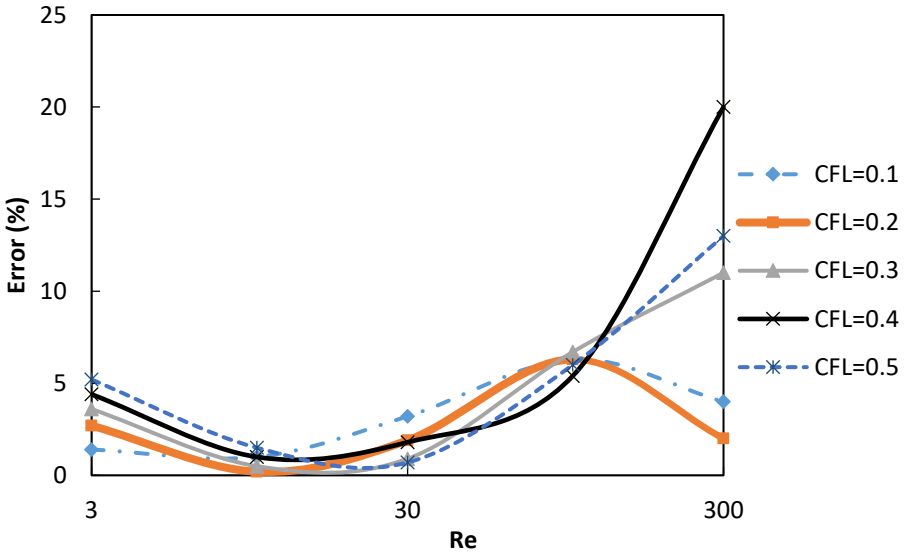

Figure 3-16- The error in adopting the correlation for SPM at various Res and CFL numbers for a dropping sphere.

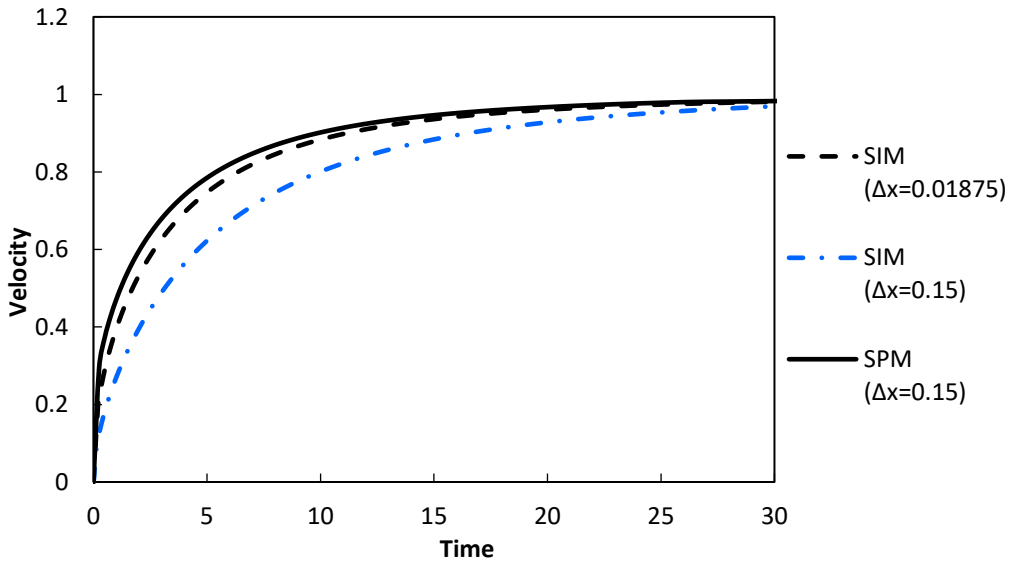

Figure 3-17- Time history of velocity and displacement for a moving sphere at $Re_0 = 10$.

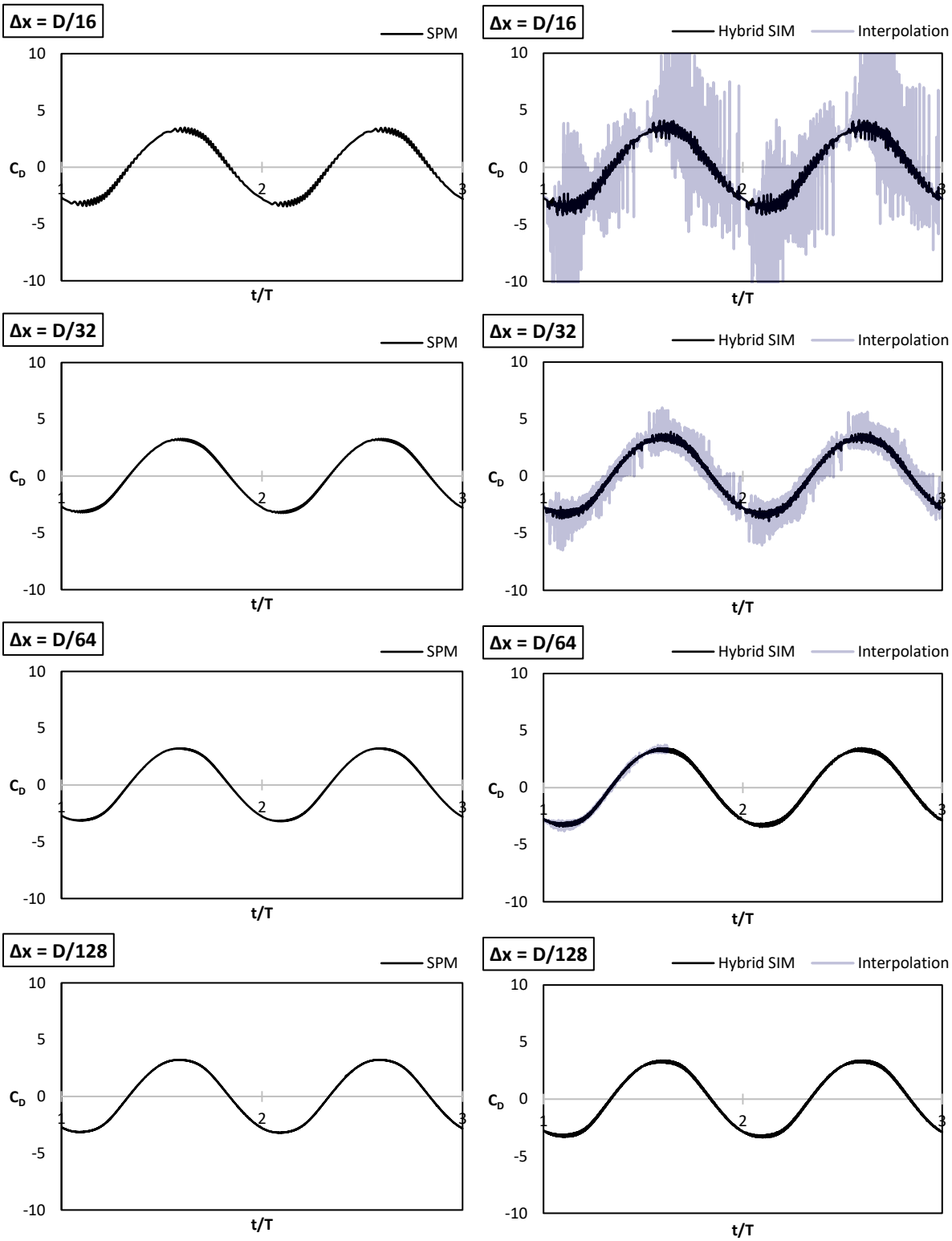

Figure 3-18- Variation of drag coefficient for the inline oscillating cylinder in SPM (left) and SIM (right) at CFL $= 0.1$ and Re $= 100$ for various grid sizes: $\Delta x = \frac{D}{16}, \frac{D}{32}, \frac{D}{64}$ and $\frac{D}{132}$ from top to bottom.

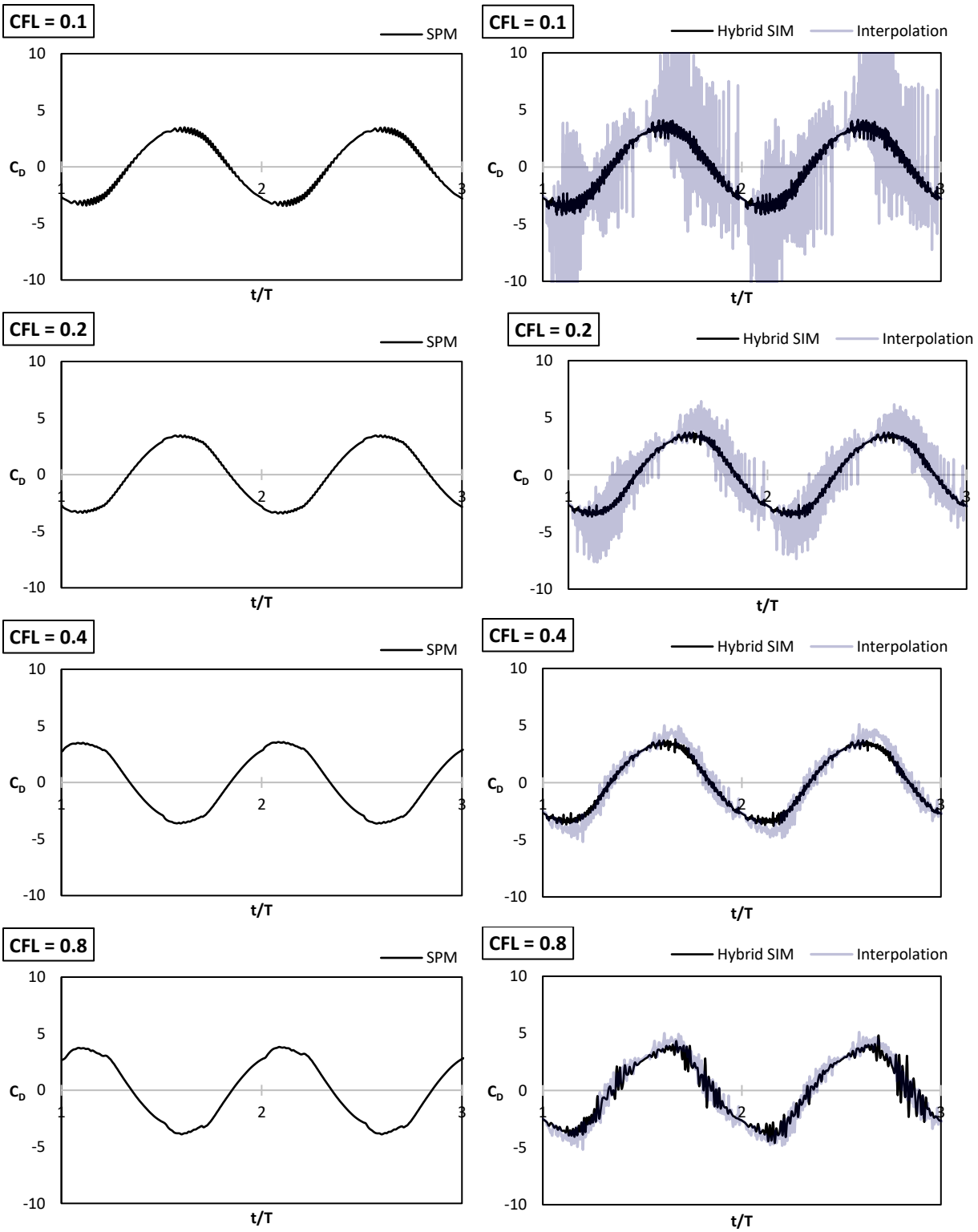

Figure 3-19- Variation of drag coefficient for the inline oscillating cylinder in SPM (left) and SIM (right) for $\Delta x = D/16$ and $Re = 100$ at various CFLs: CFL $= 0.1, 0.2, 0.4$ and 0.8 from top to bottom.

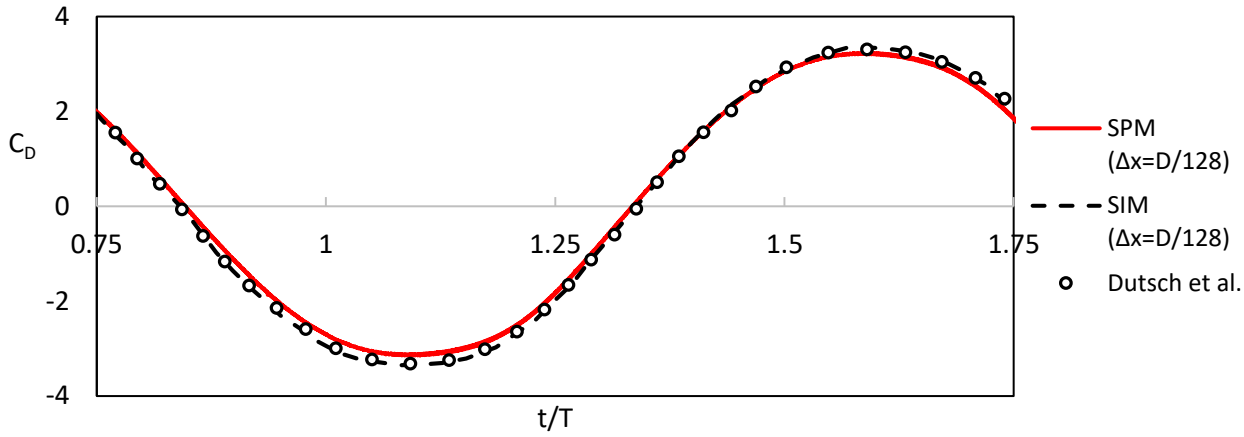

Figure 3-20- Comparison of C_D for $CFL = 0.1$, $\Delta x = D/128$ and $Re = 100$ with Dutsch et al.

CHAPTER 4

UPDATES AND MODIFICATION OF SMOOTHED PROFILE METHOD

This chapter describes a study of the robustness of the Smoothed Profile Method (SPM) in challenging cases when inertia and added mass effects are significant. A 2nd order accurate Sharp interface method (SIM) as described in the previous chapter is used for comparison. SPM was initially constructed for applications involving low Reynolds numbers; this study pushes the envelope towards higher Reynolds numbers, where the boundary layer and wake dynamics will be influenced by the thickness of the solid-fluid interface. The effect of a diffuse interface on this interaction is assessed. Moreover, the validity of implementing a correlation for interface thickness parameter in SPM for unsteady wake flows is also tested.

For cases where high added mass effect can cause FSI calculations to be unstable, particularly for cases where the particles exhibit rotational inertia, the previously mentioned semi-implicit approach becomes unstable and an implicit approach should be implemented. In the next step, SPM and SIM are applied to fluid structure interaction (FSI) problems in an implicit fluid-solid strong coupling treatment using Aitken acceleration to speed up convergence of subiterations.

4.1. Implicit Smoothed Profile Algorithm

4.1.1. Introduction

Computational methods for fluid-structure interaction (FSI) problems with complex geometries and motions can face challenges associated with managing boundary-fitted moving meshes. For this reason, methods based on fixed, simple Cartesian meshes, i.e. the various flavors of the Immersed Boundary Method (IBM) [47, 102, 118] have enjoyed increasing popularity. Cartesian grid based

methods can be particularly useful for the simulation of resolved particulate flows where the large numbers of moving boundaries call for careful numerical treatments to obtain accurate solutions in a computationally tractable manner [28, 36, 45, 79, 80, 83, 84, 122-128]. For Cartesian (i.e. immersed boundary) methods a key issue is the treatment of the immersed boundaries, i.e. whether to adopt sharp or diffuse interface treatments. Additionally, robustness and efficiency of the FSI methods can depend on how the FSI algorithm handles the coupling between the immersed interface and the fluid flow solver.

Typically, Fluid-Structure Interaction (FSI) algorithms are based on the Dirichlet-Neumann strategy in which the flow solver solves for the fluid velocity and pressure using the structural kinematics as boundary conditions and the motion of the structure is solved by enforcing tractions [191] on the solid surface. The simplest method among them constructs a weakly coupling, which involves a time lag between fluid and structure (chapter (3)). The time update related to this coupling is an explicit scheme as the update of fluid is based on the previous time data of the solid and vice versa. This type of coupling is efficient and practical when the solid density is at least one order of magnitude higher than the fluid. For example, explicit schemes are widely used in the aerospace industry [192, 193].

However, the implementation of explicit approaches for many practical particulate flows, such as motion of blood cells in plasma or the motion of thin-walled tubes containing fluids is not advisable. In addition to the difficulties that arise strictly due to the topology and number of moving boundaries, numerical solutions may be further complicated by stability and efficiency issues, particularly for high added-mass situations [194] where two-way fluid-solid coupling leads to associated numerical stiffness. Added mass effects arise because of mass conservation as the solid and the fluid cannot occupy the same space; consequently, whenever a solid moves, the fluid also moves to make space for the solid. The amount of fluid mass that moves in this process is the virtual or added mass and it depends on particle shape and motion as well as flow geometry. In a domain with constraints on mass flux through its boundaries the added mass effect is stronger because the fluid in front of the particle will replace the flow behind it [91]; the overall stability of the flow solution will hinge on the accurate treatment of mass

transport in the domain. In such cases the motion of the solid is intimately coupled to fluid displacements and the disparity of time scales in the movement of solid and fluid lead to a stiff computation. This type of scenario can arise in the case of blood cells carried by plasma, high aspect ratio elastic tubes carrying fluids and in the dynamics of slender structures as in the operation of heart valves and other applications. Fortunately, the Reynolds numbers in these applications are moderate (order of hundreds); However, the stability of numerical solutions is predominated by the added mass effect and therefore the flow calculations are not so much challenged by the need to resolve boundary layers as by the need to stabilize the simulations to added-mass induced divergence of the FSI problem. For such problems, the performance of sharp versus smoothed interface treatments needs to be assessed; there is very sparse work on this issue in the literature [195-198].

To compare sharp and smoothed interface methods in the context of high added mass effect problems, the semi-implicit fractional step algorithm presented in chapter (3) will need to be modified. When the density of the solid is much higher than the fluid, the added mass amount is almost negligible and loosely coupled semi-implicit or explicit schemes are applicable. However, if the density of the fluid is close to the solid, the effect of added mass severely limits the time step size [194]. For incompressible flows, if the solid and fluid densities are at the same order, reduction of time step size can no longer stabilize the solution [199]. Hu et al. [200] showed that that explicit FSI schemes become unstable when the added mass becomes comparable to that of the structure.

In order to reduce added mass instabilities, strongly coupled FSI methods are used. Strong coupling, which makes the FSI scheme implicit, can be performed using either monolithic or partitioned methods. Monolithic methods define the fluid and structure in a single set of discrete equations to consider both fluid and solid sub-domains at once. No domain splitting error is introduced; thus the coupling is robust enough for FSI cases with high added mass effects [201]. However, the resulting system of discrete equations can be poorly conditioned due to stiffness issues related to disparate time scales of the fluid and structure and the solution of the monolithic discrete form can become expensive Therefore, the

efficiency of each monolithic method depends on complicated preconditions such as Krylov sub-space of the iterative solver [191, 202-204]. For a monolithic approach with pressure segregation, non-convergent iterative solutions are possible, as described by Idelsohn et al. [205].

Partitioned approaches [206-210], on the other hand, solve flow and structure equations separately. This makes it convenient to use off-the-shelf or well developed separate fluid and solid solvers and to connect solvers together only in terms of interfacial quantities. The structure does not change while the flow is solved and vice versa. Unlike the monolithic approach, the coupling is not inherent in the discretized equations and implementing a coupling algorithm is mandatory. The previously mentioned explicit schemes can also be categorized as partitioned approaches since fluid and structure are solved independently. By implementing subiterations within each time step, the scheme can be made implicit, i.e. by updating the fluid and structure and their boundary conditions at each time step multiple times to reach a prescribed tolerance as a convergence criterion. The advantage of partitioned methods is that the system of discrete equations is smaller and better conditioned. In addition, modular implementations in the existing codes is possible [204]. However, they become unstable for large time step sizes [211] and to suppress the instability some type of relaxation needs to be applied.

Herein, SPM is implemented in a fully coupled (i.e. implicit) fashion to assess its performance in more challenging cases than it is conventionally applied to, cases such as flows with high added mass effect. An implicit 2^{nd}-order accurate SIM [106, 174] also is used for comparison in most of the cases. Both interface treatments are set in the same flow solver that operates on a Cartesian grid. Adapting the SPM approach to the regimes of higher Reynolds numbers and for high added mass effects involves several measures which are described in this research, including octree based local mesh refinement (will be described in chapter (5)), Aitken acceleration of the fully coupled FSI solver, a third-order backward difference scheme for updating the particle variables and use of Euler parameters for particle rotation calculations; depending on the FSI problem being solved these are all necessary ingredients needed to make the simulation stable and robust.

In the following section, the features of the fully coupled smoothed profile method is described. In the results section, these methods are tested for flows with Reynolds number values of orders up to 10^4. Then the motion of low density particles is studied to analyze the robustness and stability of the methods. Finally, the strengths and limitations of the approach are identified.

The present strongly coupled fluid structure interaction algorithm represents an implicit scheme in a partitioned approach; the update of fluid and structure are done separately by use of subiteration for both fluid and solid variables to reach a final converged state at each time step. The overall algorithm stabilizes the numerical method to overcome the added mass effect and is applied for both SPM and SIM. The implicit algorithm is described below.

4.1.2. Flow solver

The time-splitting algorithm for the strongly-coupled FSI formulation is cast into a subiterative form. The fluid fractional step equations along with the equations of motion for the solid are solved iteratively in an outer loop such that the variables are tightly coupled at convergence. Here, a fractional-step algorithm with rotational pressure correction [169] is implemented to achieve an accuracy more than $\mathcal{O}(\Delta x)$. The current implementation of the fractional-step approach is very close to the implementation suggested by Shen et. al. [172] (See also Guermond and Shen [171]) with some modifications to account for the presence of moving immersed boundaries in the Cartesian grid.

The resulting approximations of the velocity and pressure fields at the end of each subiteration k are denoted as $\boldsymbol{u}_{n+1}^{k+1}$ and p_{n+1}^{k+1}. Using the general formulation of the chapter (3), the subiterative scheme modifies the Equations (3-3) to (3-5) as

$$\frac{\alpha \boldsymbol{u}^* + \sum_{j=0}^{J-1} \beta_j \boldsymbol{u}_{n+1}^{k-j}}{\Delta t_{n+1}} + (\boldsymbol{u} \cdot \nabla \boldsymbol{u})_{n+1}^{k} = -\nabla p_{n+1}^{k} + \frac{1}{Re} \nabla^2 \boldsymbol{u}^* \qquad (4\text{-}1)$$

In Equation (4-1), n is the time step and k is a counter for the number of subiterations at the new time step. The values of coefficients α and β define the time-integration scheme. In the case of adaptive

time-stepping, for the second-order BDF the coefficients are $\alpha = \frac{2r+1}{(1+r)}$, $\beta_0 = -(1+r)$, and $\beta_1 = \frac{r^2}{(1+r)}$, where $r = \frac{\Delta t_{n+1}}{\Delta t_n}$ [173]. Here, $\boldsymbol{u}_{n+1}^{k-j}$ is the fluid velocity at j subiterations before the current one. The non-linear term is treated in the manner proposed by [212]: For $k = 1$, an explicit second-order Adams-Bashforth technique is used to approximate the non-linear term at t_{n+1}. For all $k > 1$, the non-linear term is approximated using $\boldsymbol{u}_{n+1}^{k}$. The boundary conditions for velocity is $\boldsymbol{u}^*|_\Gamma = \boldsymbol{b}_{n+1}$. The rest of formulations are similar to the fractional step method in chapter (3).

In this chapter for simplicity the subscript $n+1$ related to the current time step is dropped. However, at the start of each time step when there is no previous subiterative data available, the last update of the data from the previous time step is used. Similarly, Equations (3-7) to (3-12) are modified to include the subiterative variables by replacing p_n with ∇p^k, $\boldsymbol{u}_n$ with $\boldsymbol{u}^k$ and so on.

4.1.3. Particle variables

Particle velocity and angular velocity of particles are updated as:

$$\frac{d\boldsymbol{V}_i^{k+1}}{dt} = \frac{\Delta t}{M_i}\boldsymbol{F}_i^{k+1} \qquad \text{and} \qquad \frac{d\,{}^L\boldsymbol{\omega}_i^{k+1}}{dt} = {}^L\boldsymbol{\omega}_i^{k} + \frac{\Delta t}{{}^L\boldsymbol{I}_i}\,{}^L\boldsymbol{T}_i^{k+1} \tag{4-2}$$

where M_i and ${}^L\boldsymbol{I}_i$ are respectively mass and moment of inertia of the i^{th} particle. Superscript L denotes the inertial reference frame and $\boldsymbol{F}_i^n$ and ${}^L\boldsymbol{T}_i^n$ are total force and moment on the particle. Similarly, particle position and orientation is updated by integration of velocity and angular velocity:

$$\frac{d\boldsymbol{X}_i^{k+1}}{dt} = \boldsymbol{V}_i^{k+1} \qquad \text{and} \qquad \frac{d\boldsymbol{\Theta}_i^{k+1}}{dt} = \boldsymbol{\omega}_i^{k+1} \tag{4-3}$$

A third-order backward differencing scheme with non-uniform time step size capability is used for time integration of Equations (4-2) and (4-3) as discussed in the following section.

4.1.2.1 Third order Backward Differencing Formulation

Since backward difference formulas (BDF) for time discretization use the latest update of flow variables in the time derivative and are implicit methods and they have fewer stability issues [213]; in the present case they are found to be essential for time-stepping the high-added mass effect cases attempted in this work; in fact, as will be shown later, a third-order BDF method is necessary in more sensitive cases. For uniform time step sizes the BDF methods are well developed for any order [214, 215] but few studies exist for the cases with variable time step sizes. Emmrich [173] proposed a second-order BDF with variable time step sizes as well as a comprehensive study of stability. The method was developed by Heard [216] for a third-order but there is a restriction of constant uniform time step expansion ratios. Because of the time adaptive solver, the scheme is extended herein for varying time step sizes. Considering t^{k+1} as the last time step, $h_j = t^{k+1} - t^{k-j+1}$, the third-order scheme for the time derivative of the variable $\boldsymbol{\phi}$ is used to find $\boldsymbol{\phi}^{k+1}$ which is the desired update of the variable $\boldsymbol{\phi}$.

$$\frac{d\boldsymbol{\phi}^{k+1}}{dt} = \sum_{j=0}^{3} c_j \, \boldsymbol{\phi}^{k-j+1} + \varepsilon_T \tag{4-4}$$

In the above relation

$$c_0 = \frac{1}{h_1} + \frac{1}{h_2} + \frac{1}{h_3}$$

$$c_1 = -\frac{h_2 h_3}{h_1(h_1 - h_3)(h_1 - h_2)}$$

$$c_2 = -\frac{h_1 h_3}{h_2(h_2 - h_3)(h_2 - h_1)}$$

$$c_3 = -\frac{h_1 h_2}{h_3(h_1 - h_3)(h_2 - h_3)} \tag{4-5}$$

The leading truncation error of the scheme shows the third order accuracy:

$$\varepsilon_T = \frac{\left(c_1 h_1^4 + c_2 h_2^4 + c_3 h_3^4\right)}{24} \frac{d^4 \boldsymbol{\phi}^{k+1}}{dt^4} \tag{4-6}$$

When the step sizes are equal, $h_3 = 3h_1$ and $h_2 = 2h_1$, the standard BDF will be recovered:

$$\frac{d\boldsymbol{\phi}^{k+1}}{dt} = \frac{\left(-\frac{1}{3}\boldsymbol{\phi}^{k-2} + \frac{3}{2}\boldsymbol{\phi}^{k-1} - 3\boldsymbol{\phi}^{k} + \frac{11}{6}\boldsymbol{\phi}^{k+1}\right)}{\Delta t} \tag{4-7}$$

and thus $\boldsymbol{\phi}^{k+1}$ is obtained from

$$\boldsymbol{\phi}^{k+1} = \frac{1}{11}\left[6\frac{d\boldsymbol{\phi}^{k+1}}{dt}\Delta t + 18\boldsymbol{\phi}^{k} - 9\boldsymbol{\phi}^{k-1} + 2\boldsymbol{\phi}^{k-2}\right] \tag{4-8}$$

At the start of the simulation when only the initial data is available, a first order scheme is implemented as:

$$\boldsymbol{\phi}^{k+1} = \boldsymbol{\phi}^{k} + \frac{d\boldsymbol{\phi}^{k+1}}{dt}\Delta t \tag{4-9}$$

At the second time step, a second order BDF is applied [173]:

$$\frac{d\boldsymbol{\phi}^{k+1}}{dt} = \frac{1}{\Delta t}\sum_{j=0}^{2} c_j\, \boldsymbol{\phi}^{k-j+1} + \varepsilon_T \tag{4-10}$$

Considering $r_n = \frac{\Delta t_{k+1}}{\Delta t_k}$,

$$c_0 = \frac{1+2r_n}{1+r_n}$$

$$c_1 = -(1+r_n)$$

$$c_2 = \frac{r_n^2}{1+r_n} \tag{4-11}$$

Thereafter at the 3rd-order BDF takes over the time-stepping.

4.1.2.2 Particle rotation

Equations (4-2) and (4-3) for particle rotation are straightforward in 2D cases. However, in 3D these equations become complicated as the moment of inertia in the inertial reference frame ${}^{L}\boldsymbol{I}_i$ is a 3×3 matrix that has six independent components varying with time as the particle rotates [217]. Use of a body-fixed principal reference frame solves this problem as the moment of inertia in this system does not change and only has three components. Therefore, rather than $\boldsymbol{x} = [x, y, z]$ as the inertial frame, $\hat{\boldsymbol{x}} = [\hat{x}, \hat{y}, \hat{z}]$ and $\hat{\hat{\boldsymbol{x}}} = [\hat{\hat{x}}, \hat{\hat{y}}, \hat{\hat{z}}]$ reference frames are used which describe, respectively, the coordinate system attached to the particle center of mass and the co-moving frame with an origin at the particle center of mass but with axes parallel to the inertial frame. Denoting $k+1$ as the latest update, $\boldsymbol{\omega}_i^{k+1}$ can be obtained by integration of the following equations in the principal frame:

$$\frac{d\omega_{i,\hat{x}}^{k+1}}{dt} = \frac{1}{I_{\hat{x}}}\left[T_{i,\hat{x}}^{k+1} + \omega_{i,\hat{y}}^{k}\omega_{i,\hat{z}}^{k}\left(I_{\hat{y}} - I_{\hat{z}}\right)\right] \tag{4-12}$$

$$\frac{d\omega_{i,\hat{y}}^{k+1}}{dt} = \frac{1}{I_{\hat{y}}}\left[T_{i,\hat{y}}^{k+1} + \omega_{i,\hat{z}}^{k}\omega_{i,\hat{x}}^{k}\left(I_{\hat{z}} - I_{x}\right)\right] \tag{4-13}$$

$$\frac{d\omega_{i,\hat{z}}^{k+1}}{dt} = \frac{1}{I_{\hat{z}}}\left[T_{i,\hat{z}}^{k+1} + \omega_{i,\hat{x}}^{k}\omega_{i,\hat{y}}^{k}\left(I_{\hat{x}} - I_{\hat{y}}\right)\right] \tag{4-14}$$

Integration of the above equations in time leads to Euler angles (θ, ϕ, ψ) which are based on the elemental rotation in a 3D Euclidean space [218, 219]. Transformation between the particle frame and the co-moving coordinate is given by

$$\hat{\boldsymbol{x}} = \boldsymbol{A}\hat{\hat{\boldsymbol{x}}} \tag{4-15}$$

$\boldsymbol{A}$ is the transformations matrix which is defined in the x-convention of Goldstein [218] as

$$\begin{bmatrix} \cos\psi\cos\phi - \cos\theta\sin\phi\sin\psi & \cos\psi\sin\phi + \cos\theta\cos\phi\sin\psi & \sin\psi\sin\theta \\ -\sin\psi\cos\phi - \cos\theta\sin\phi\cos\psi & -\sin\psi\sin\phi + \cos\theta\cos\phi\cos\psi & \cos\psi\sin\theta \\ \sin\theta\sin\phi & -\sin\theta\cos\phi & \cos\theta \end{bmatrix} \tag{4-16}$$

In the representation of the particle angles, the superscript $k+1$ related to subiteration and the subscript i related to the i^{th} particle have been dropped; the Euler angle values are computed over each subiteration. The Euler angles are updated by integrating the angular velocity according to [220]

$$\begin{bmatrix} \frac{d\theta}{dt} \\ \frac{d\phi}{dt} \\ \frac{d\psi}{dt} \end{bmatrix} = \begin{bmatrix} \omega_{i,\hat{x}}^{k+1}\cos\psi - \omega_{i,\hat{y}}^{k+1}\sin\psi \\ \left(\omega_{i,\hat{x}}^{k+1}\sin\psi + \omega_{i,\hat{y}}^{k+1}\cos\psi\right)/\sin\theta \\ \omega_{i,\hat{z}}^{k+1} - \left(\frac{d\phi_i^{k+1}}{dt}\right)\cos\theta \end{bmatrix} \tag{4-17}$$

However, Euler angles can lead to singularities and ill-posed conditions [218, 220-222]. The general remedy for these problems is the use of Euler parameters [218, 220-222] which extends the definition of elemental rotation to a set of four quaternions. Using similar coordinate systems as the Euler angles for the particle's rotation, Equations (4-12) to (4-13) can still be used. The Euler parameters are defined as [220, 222, 223]

$$\varepsilon_1 = \cos\frac{\phi-\psi}{2}\sin\frac{\theta}{2} \tag{4-18}$$

$$\varepsilon_2 = \sin\frac{\phi-\psi}{2}\sin\frac{\theta}{2} \tag{4-19}$$

$$\varepsilon_3 = \sin\frac{\phi+\psi}{2}\cos\frac{\theta}{2} \tag{4-20}$$

$$\eta = \cos\frac{\phi+\psi}{2}\cos\frac{\theta}{2} \tag{4-21}$$

Euler parameters as quaternions as subject to the identity

$$\varepsilon_1{}^2+\varepsilon_2{}^2 + \varepsilon_3{}^2 + \eta^2 = 1 \tag{4-22}$$

The transformation matrix for the Euler parameters is

$$\boldsymbol{A} = \begin{bmatrix} 1-2(\varepsilon_2{}^2+\varepsilon_3{}^2) & 2(\varepsilon_1\varepsilon_2+\varepsilon_3\eta) & 2(\varepsilon_1\varepsilon_3-\varepsilon_2\eta) \\ 2(\varepsilon_2\varepsilon_1-\varepsilon_3\eta) & 1-2(\varepsilon_3{}^2+\varepsilon_1{}^2) & 2(\varepsilon_2\varepsilon_3+\varepsilon_1\eta) \\ 2(\varepsilon_3\varepsilon_1-\varepsilon_2\eta) & 2(\varepsilon_2\varepsilon_3-\varepsilon_1\eta) & 1-2(\varepsilon_1{}^2+\varepsilon_2{}^2) \end{bmatrix} \tag{4-23}$$

Euler angles are used to define the Euler parameters at the start of the simulation. After finding the Euler parameters there is no need for the Euler angles since the Euler parameters can be calculated by integrating:

$$\begin{bmatrix} \frac{d\varepsilon_1}{dt} \\ \frac{d\varepsilon_2}{dt} \\ \frac{d\varepsilon_3}{dt} \\ \frac{d\eta}{dt} \end{bmatrix} = \frac{1}{2}\begin{bmatrix} \eta\omega_{i,\hat{x}}^{k+1} - \varepsilon_3\omega_{i,\hat{y}}^{k+1} + \varepsilon_2\omega_{i,\hat{z}}^{k+1} \\ \varepsilon_3\omega_{i,\hat{x}}^{k+1} + \eta\omega_{i,\hat{y}}^{k+1} - \varepsilon_1\omega_{i,\hat{z}}^{k+1} \\ -\varepsilon_2\omega_{i,\hat{x}}^{k+1} + \varepsilon_1\omega_{i,\hat{y}}^{k+1} + \eta\omega_{i,\hat{z}}^{k+1} \\ -\varepsilon_1\omega_{i,\hat{x}}^{k+1} - \varepsilon_2\omega_{i,\hat{y}}^{k+1} - \varepsilon_3\omega_{i,\hat{z}}^{k+1} \end{bmatrix} \tag{4-24}$$

In this research, the third order BDF as described in the last section is used to preserve the solution accuracy and stability of the particle variables. In order to avoid instabilities related to Euler parameters [221], a normalization condition as in Equation (4-22) is applied after each update of the Euler parameters.

4.1.4. Fluid-structure interaction

The FSI formulation for both SPM and SIM is the same as chapter (3) except that the time updated variables are replaced with the subiterative updated variables (Equations (3-15) to Equation (3-21)). The time update happens when the convergence occurs at the end of subiterative outer loop. For faster convergence rates, the relaxation as Aitken scheme is applied as following.

4.1.4.1 Aitken acceleration for strongly coupled FSI

Convergence acceleration schemes improve the performance of strongly coupled partitioned FSI. Methods such as Aitken acceleration [224], steepest descent relaxation [225, 226], Newton-Krilov [227] or vector extrapolation [228] can be used in an iterative scheme designed to avoid instability issues related to high added mass effects. Here, Aitken acceleration is chosen because of its simplicity and proven performance in FSI cases [70, 71, 229]. Aitken acceleration is a fixed point relaxation scheme for the strong coupling of nonlinear systems [230]. In this scheme, the equilibrium interface condition is reached by iterative update of the fluid and structure and by considering their mutual interaction using the last updated value in the subiteration. The update of variable $\boldsymbol{\phi}$ at subiteration $k+1$ will be [231]

$$\boldsymbol{\phi}^{k+1} = (1-\lambda_{k+1})\boldsymbol{\phi}^{k+1} + \lambda_{k+1}\boldsymbol{\phi}^{k} \tag{4-25}$$

The variable $\boldsymbol{\phi}$ can stand for velocity or pressure of fluid or the velocity or angular velocity of the solid particle. λ_{k+1} is the relaxation parameter, which is obtained from Aitken Δ^2 method ([70, 212, 229]) as

$$\lambda_{k+1} = \lambda_k + (\lambda_k - 1)\frac{(\boldsymbol{Q}_k - \boldsymbol{Q}_{k+1})\cdot Q_{k+1}}{\|\boldsymbol{Q}_k - \boldsymbol{Q}_{k+1}\|^2} \tag{4-26}$$

where $\boldsymbol{Q}^{k+1} = \boldsymbol{\phi}^{k} - \boldsymbol{\phi}^{k+1}$ is the difference of the $\boldsymbol{\phi}$ in one subiteration.

The subiteration process is carried out until the norms of the differences between the iterations for the fluid velocity, pressure, and solid velocity and angular velocity are all smaller than a set of prescribed tolerances:

$$\left\|\boldsymbol{\phi}^{k+1} - \boldsymbol{\phi}^{k}\right\| < \varepsilon_{\boldsymbol{\phi}} \tag{4-27}$$

Then the algorithm proceeds to the next time step and the subiteration counter is reset to $k = 1$.

4.2. Results

The fully coupled algorithm for SPM and SIM is implemented to study the behavior of fixed and moving boundaries related to flows with embedded solid objects such as particles. The flow solver uses

a finite-volume method on octree-refined Cartesian grids. In this context, all variables are in non-dimensional form and the particle diameters are set to unit length. An octree-based local mesh refinement scheme is used to enhance resolution in flow regions containing high velocity gradients (chapter (5)). The solution is considered as converged at each subiteration if the norm of the velocity and pressure change within the linear solver iteration is less than 10^{-8} and 10^{-9}, respectively. Moreover, the subiterations are considered as converged if the changes between two subiteration in flow velocity and pressure, and also particle velocity and angular velocity are less than $\varepsilon \Delta t^2$. Based on tests performed, the value of 0.01 is chosen for ε to satisfy both safety and efficiency. For all of the cases, $\rho_f = 1$.

4.2.1. Flow past cylinder at moderately high Reynolds numbers

So far, use of SPM as a DNS approach for particulate flows has been limited to very low to almost moderate laminar Reynolds number values [74, 75, 149-154, 156, 157, 161, 195] but study of the application for higher laminar Reynolds number values with significant vorticity confinement at the solid surface, would be helpful in many applications such as blood flow in the arteries [64, 232]. For comparison purposes, a 2nd-order accurate SIM approach based on a least-squares Ghost Fluid Method (GFM) [112, 180] also is used. The key issue addressed is how the spreading of the interface in an SPM approach, which coincides spatially with the region of generation and confinement of vorticity, affects the results obtained with SPM at high laminar Reynolds numbers.

In order to test the ability of the flow solver to accurately simulate the flow characteristics over a solid surface at moderately high Reynolds numbers, SIM and SPM are applied to solve for flow over a stationary cylinder. The flow impulsively starts in a quiescent fluid to achieve Reynolds number values of 1000 and 9500 where $Re = U_\infty D/\nu$. The time history of drag coefficient, contour plot of vorticity and values of surface vorticity are compared with benchmark values [233], which are based on the Lagrangian vortex method. This reference provides a good benchmark case as the temporal evolution of

the vorticity field reflects a strong interaction between boundary-layer vorticity and the localized wake features and thus can test the capability of the SPM to capture all relevant physics in an adequate manner.

The cylinder with unit diameter is located at 6×6 in a channel of dimension 18×12. All boundaries except the outflow have unit velocity and the initial fluid velocity is 1.0 in the x-direction. In order to have at least ten grid points inside the boundary layer, the most refined grid is chosen to satisfy $\Delta x < 1/10\sqrt{Re}$. The mentioned equation assures resolved solution for the higher Reynolds number values, as a finer grid is required to capture all length scales. Consequently, the approximate minimum required fine grid spacings for $Re = 1000$ and $Re = 9500$ simulations are 0.0032 and 0.001, respectively. In the context of the octree refinement, to achieve this resolution, a base grid size of 0.025 and 0.02 with respectively four and six levels of refinement is used for $Re = 1000$ and $Re = 9500$. The CFL number is set to 0.3 and the time variable is normalized based on the radius of cylinder as $T = Ut/R$.

First, the drag coefficients (C_D) from SPM and SIM are compared (Figure (4-1)). Since it is an integrated quantity, the calculated C_D from SPM and SIM are in excellent agreement with [233] at $Re = 1000$. For $Re = 9500$, the results are also in good agreement provided that the grid for SPM is fine enough. The discrepancy between SPM and SIM is significant for coarse SPM simulations.

The effect of grid refinement on C_D for SPM is shown in Figure (4-2) with using different grid spacing. It is clear that at $Re = 1000$, having 2.52 grid points along the boundary layer related to $\Delta x = 0.0125$ is enough for having a similar trend for C_D. However, at $Re = 9500$, there should be at least ten grid point along the boundary layer. This is because at $Re = 9500$, the flow is very close to have transition from laminar to turbulence and use of boundary layer thickness criterion does not lead to the smallest length scale.

Vortex patterns also are presented in Figure (4-3). The results are qualitatively in good agreement; however, there is a noticeable discrepancy in the rollup of the shear layer coming off the cylinder among the methods at $Re = 9500$; this may be due to the greater dependency of the boundary layer profile and subsequent shear layer instability on the grid at higher Reynolds numbers. The separation

point for the different methods is in good agreement however. For the $Re = 9500$, the history of the vortex is shown in Figure (4-4) using SPM. The evolution of the vortex and how they are generated at the surface and the detachment of the boundary layer from the surface is noticeable.

Figure (4-5) shows the vorticity values along the surface of the cylinder using the same grid spacing for SIM and SPM at $Re = 1000$. The surface vorticity obtained from the two methods at $Re = 1000$ are in good agreement with the benchmark. However, as seen in Figure (4-6), at $Re = 9500$, the values of surface vorticity from SPM are lower than that for the SIM and the vortex method. This is because of the diffuse interface of SPM that has smoothed the velocity gradient at the interface leading to lower vorticity values. As noted above this leads to discernible differences in the vorticity contours downstream of the cylinder. However, the values of the drag on the cylinders are in fairly good agreement for SPM, SIM and the benchmark even for Re=9500, as shown in Figure (4-1).

For a closer study of surface vorticity in the case of SPM, the effect of grid refinement is examined (Figure (4-7)). With grid refinement, the surface vorticity approaches that of the vortex method [40] at $Re = 1000$. However, as seen in Figure (4-7), at $Re = 9500$ there exist sharp peaks in the values of surface vorticity obtained from the benchmark solution and the SIM, which are not always captured even at the finest grid attempted with SPM although the rest of the surface vorticity is well represented. Therefore, SPM can present difficulties in capturing surface features adequately as the Reynolds numbers become large, due to the interaction of the boundary layer with the inherent thickness of the diffuse interface.

In summary, this section demonstrates that while SIM and SPM are able to resolve the evolution of complicated interplay among surface vorticity and the formed coherent wake structures, as the Reynolds numbers become large SPM cannot capture details on surface vorticity unless very fine meshes are used.

4.2.2. Solid object interacting with a wake flow

The interface thickness of SPM depends on the value of the Reynolds number, the time step and grid resolution; the interface thickness correlation determined in Equation (3-29) is designed to provide a robust parameter that can apply to flows containing particles under a wide range of inertia and grid resolution. However, that correlation was determined for the single flow type, i.e. pertaining to a uniform far field flow navigating a single particle. It is important to establish that the correlation holds under conditions where the incoming flow is vorticity laden and for the situation of particles interacting with each other. To study this aspect, the problem of flow over two spheres with unit diameters in a channel flow is chosen for study. The spheres are fixed and the interaction between the particles is quantified by finding their drag coefficients when a uniform inlet velocity (non-dimensional value of 1.0) passes over the spheres. The channel size is $50 \times 15 \times 15$; the first spherical particle is located at $8 \times 10 \times 10$. The second sphere is placed at different axial gap distances Δ from the first (upstream) sphere where the gap distance $\Delta = 0$ means that the spheres are in contact.

The study is done at $Re = 30$ and the results are presented in Figure (4-8) for SPM and SIM. There are two cases for SIM, the first with the same coarse grid as for SPM and the second for a fine grid which is considered as the "exact" solution to compare with SPM. The base mesh size for SPM and the coarse grid solution of SIM is 0.3333 with three levels of local mesh refinement. The base mesh size for the refined grid solution of SIM is 0.2 with four levels of local mesh refinement. As seen in Figure (4-8a), there is an increasing trend for the drag coefficient ($C_D = 8F/\pi\rho U^2 D^2$) for both methods when the distance among the particles increases and consequently the wake effect on the second particle decreases. The second particle obviously experiences lower drag than the first. It should be mentioned that when two spheres touch (i.e. the gap between the particles goes to zero), SIM cannot be applied as it leads to non-invertible matrixes but it is still possible to use SPM. It can also be seen that for this Reynolds number SPM provides good solutions even on the coarse mesh while a finer mesh is required for SIM. Figures (4-8b) and (4-8c) shows the contour plots of stream-wise velocity and vorticity for SPM when $Re = 30$

and gap distance $\Delta = 1$. Extension of the wake at the rear of the spheres is noticeable. SPM is able to simulate the wake flows and in this case displays better accuracy than SIM when it is applied with the same coarse grid.

This study was extended to the higher Reynolds number of 300 (Figure (4-9)). The channel size is $36 \times 10 \times 10$; the first spherical particle is located at $(5,10,10)$. The base mesh size for all cases is 0.3333 with three and five levels of local mesh refinement to reach minimum grid sizes of 0.08333 and 0.02083 for coarse and fine grids respectively. The results are compared with Prahl et al. [234]. As shown in [234], at $Re = 300$, the wake is unsteady and vortex shedding occurs at Strouhal number $St = 0.135$. Therefore, a time-averaged value for C_D is obtained by taking values over several shedding cycles within the simulation time interval $[10.0 < T < 200.0]$.

As seen in Figure (4-9a), there is an increasing trend in the drag coefficient for both methods when the distance between the particles increases and consequently the wake effect on the second particle decreases. As expected, the second particle experiences lower drag than the first one. It can also be seen that for this Reynolds number SPM provides good solutions for the first particle even on a coarse mesh while SIM requires a finer mesh. For the second particle, the coarse grid result obtained from SPM is less accurate than SIM when the two particles are close, i.e. when the wake effect is higher. However, SPM provides better results than SIM when the distance between the two particles increases. The fine grid solution obtained using SIM however is very close to the benchmark showing that with fine grids SIM provides more accurate results. This behavior of SPM and SIM, where SPM produces good results for the drag coefficient for moderate Reynolds numbers even on coarse meshes, while SIM performs poorly for coarse meshes but produces accurate results for fine meshes is consistent with the findings in the case of a single immersed boundary in [195, 235, 236].

Figure (4-9b) shows the contour plots of streamwise velocity and vortical structures of the flow using SPM when $Re = 300$ and the gap distance $\Delta = 2.5$. SPM is able to simulate the wake flows and in this case displays better accuracy than SIM when both methods are employed on the same coarse grid.

4.2.3. Moving disk in a horizontal channel with high added mass effects

When the density of the moving object is of the same order as the carrier flow, the added mass effect becomes important and necessitates implementation of fully coupled methods. In this section, a cylindrical disk that is free to move at $Re = 400$ is considered in a 2D channel. The ratio of density of solid to the flow is $\rho_s/\rho_f = 1.5$ representing a case with potentially high added mass effect. The particle is placed at (6,6) in a channel of size 50×12 and is released at $T = 0$ in a uniform flow in the entire channel including the boundaries. It starts to move due to the imposed flow to reach the final flow velocity. A third-order backward differencing scheme is used to update the particle velocity and its position. The scheme with variable time step size makes the time adaptive solution possible and therefore the efficiency of computations is managed with $CFL = 0.3$. Two grid sizes are chosen to test the grid independency. The base grid spacing is 0.25 units and three and five levels of grid refinement are applied.

The results, as displayed in Figure (4-10), show that at the start of the motion there is a transient in the particle motion where the relative velocity between particle and the flow is high. This leads to the highest drag force and as a result the particle acceleration is the highest and relaxes to zero when the particle eventually asymptotes to its final steady velocity. There is a discrepancy between the results from SPM and SIM for the particle velocity (Figure (4-10a)) in the transient period which occurs because SIM and SPM predict the drag force in different ways. SPM obtains a higher value for the drag force. The discrepancy decreases quickly and the final results approach each other. The history of the position of the particle (Figure (4-10b)) does not show a significant difference between two methods. Since the position of the particle is calculated by integrating the velocity and the initial discrepancy is short-lived, the final results of the particle position are in agreement.

It is interesting to examine how SPM compares with SIM in terms of computational effort. The wall-clock time required for the particle to reach the end of channel is used to make the comparison between the two approaches. Each run was performed on a shared memory cluster on an eight core node

with 24 GB of memory. To reach the end of the channel (at non-dimensional time $T = 45.0$) SIM needed 1675s and 19181s for the coarse and fine grids respectively, while SPM required 950s and 6710s for the coarse and fine grids. This shows a significant reduction in the simulation time with SPM over SIM for the problem computed. . Note that SPM [74, 75] solves two Poisson equations which should make it less efficient when a loosely coupled FSI formulation with only one subiteration is used. On the other hand, at low particle densities, when subiterations are used to make the solver implicit, SPM converges with fewer subiterations per time step than SIM. The average number of subiterations per time step for coarse and fine grids are respectively 12 and 14 for SIM and 6 and 7 for SPM. This is because of the inherent smoothing present in the SPM approach which makes it less sensitive than the SIM approach for FSI problems with strong added mass effects. Therefore, SPM in the implicit formulation presented here turns out to be less expensive for low particle density (high added mass) cases.

For freely moving objects, even with the strongly coupled scheme the FSI simulation may become unstable at low solid to fluid density ratios, for reasonable values of time step size and relaxation factors. In the above case the critical solid density is found to be 0.009 for SPM and 0.025 for SIM showing that SPM is inherently more stable that SIM. The reason again is that the diffuse nature of the SPM mollifies the pressure fluctuations near the particle when compared to SIM [235]. Even with the strongly coupled FSI scheme such fluctuations can adversely impact stability of the FSI solver for very low solid densities, i.e. for very high added mass effects.

4.2.4. Settling particle

As a second, perhaps more challenging test case, the sedimentation of a cylindrical disk in an otherwise quiescent fluid is simulated. In this FSI problem, as in the previous moving particle in the horizontal channel, the motion of the particle is not forced but evolves as a response to flow solution. However the fluid motion is induced by the solid itself and therefore the coupling between the settling solid and fluid is more intimate in the present case. In confined domains, this intimate coupling leads to

a stronger added mass effect and thus more unstable solutions [91]. Thus, this problem provides a stronger assessment of the accuracy and robustness of different methods.

Glowinski et al. [124] used a Lagrange multiplier fictitious domain approach in the context of finite elements to simulate the dropping disk problem defined as follows : A 2D 2×6 vertical channel with solid walls contains a cylindrical disk at $(1,4)$ which is released and settles. The disk diameter is 0.25 and $\rho_s = 1.5$. The fluid viscosity is $\nu = 0.01$ leading to maximum Reynolds number value of 300 and Froude number of 0.588. The base grid size in 0.2 and is refined four times to reach the minimum grid size of 0.0125.

As shown in Figure (4-11), the velocity calculated by SPM is at first slightly less than that obtained by Glowinski et al. but as the particle settles, it increases to reach agreement with their result. On the other hand, SIM at first predicts the drag better than SIM but under-predicts it at later time leading to a discrepancy; the grid for SIM is possibly not fine enough towards the high Re part of the motion. The history of particle position also shows that, for the resolution used, SPM is more accurate than SIM in predicting the position of the particle with time. It is notable that in this case, when no subiteration is used, namely with the semi-implicit approach, SIM diverges at very early time; however, SPM converges to a result that exhibits higher errors than the fully coupled SPM. Therefore the implicit smoothing present in SPM leads to a stabilization of the FSI calculations and the total error is comparable with SIM with subiteration.

Figure (4-12) displays the contour plots of vorticity for the falling disk at $\mathrm{T} = 0.0625$, T=0.1875 and $\mathrm{T} = 0.3125$. As the resulting particle velocity from SIM is higher than for SPM, the vorticity contours are different and the position of the particle is different for each method. Besides, the wake for SIM is more extended and shows higher vorticity values in comparison with SPM.

4.2.5. Elliptical particle pure rotation

The above cases concerned spherical/cylindrical particles. To characterize the methods for cases where particle rotation comes in to play the dynamics of ellipses embedded in flows are studied. The first case involves an ellipse that is held fixed at its centroid but free to rotate due to forces exerted by an oncoming flow. An ellipse with major axis =2.5 and minor axis=0.7 is placed at $(5.0, 5.0)$ in a channel of size 30.0×10.0 as shown in Figure (4-13a). The initial angle of the particle is $\theta_0 = \pi/4$ with respect to the horizontal and it starts to rotate around its center in an initially uniform flow. Uniform velocity value of 1.0 is supplied to all boundaries except the outlet, where the zero gradient condition is applied. Minimum grid size $\Delta x = 0.083$ is obtained by refining the base grid of size 0.3333 with two levels of refinement. The Reynolds number value is 100.0 which is based on the major diameter of the ellipse. The particle density is of the same order as the fluid density, leading to a strong added mass effect. Subiteration with Aitken acceleration is applied to make the coupling between solid and fluid strong. In this study $CFL = 0.2$ and the particle starts to rotate from its initial angle to align itself with the flow. However, because of inertia, it overshoots the equilibrium position and oscillates back to the final equilibrium. Damping due to viscosity causes the particle to finally stop oscillating and reach the final horizontal condition.

First, the high added mass effect due to low solid density $\gamma = \rho_s/\rho_f = 0.1$ is considered to study the effect of order of the time integration scheme by using the first, second and third order backward differencing schemes for the rotational update. As shown in Figure (4-13), with increase of order of time integration, the stability increases. The first order scheme becomes unstable at $T \cong 0.38$ and the second order at $T \cong 0.71$. Only the third order scheme is stable during the whole range of simulation. Therefore, for the rest of study, the 3rd order BDF is always used for computing cases with particle rotation.

Figure (4-14) shows contours of streamwise velocity and vorticity for $\rho_s = 1$ after the particle reaches a quasi-steady state at $T = 10.0$. The asymmetry in the vorticity contours arises at the start of the rotation; these vortical structures move downstream with the flow.

To see the impact of subiterations on this high added mass problem, three different cases are considered: one without subiteration, i.e. the semi-implicit method, the second with subiterations with a constant relaxation parameter and the third with Aitken acceleration of the subiteration process. Using a third order BDF scheme and $\gamma = \rho_s/\rho_f = 1.0$, the dynamics of the ellipse is computed; the orientation of the ellipse with time is shown in Figure (4-15). The results show that in this case the subiteration approaches with and without Aitken acceleration yield identical results; however, use of Aitken relaxation accelerates the solution; in order to reach $T = 10.0$, the simulation times were 137.83 CPU sec and 171.11 CPU sec for the subiteration process with and without acceleration, respectively. When no subiteration is used, a discrepancy exists in the behavior of the ellipse which is small for the momentum but noticeable in the accumulated angular velocity and orientation behaviors. In the present case, the semi-implicit approach remains stable albeit deviating from the implicit solution.

The effect of solid density on rotation of the ellipse is shown in Figure (4-16) for density ratios $\rho_s/\rho_f = 10^{-6}, 0.1, 1,$ 10 and 100. Aitken acceleration is applied in order to relax the results at each subiteration. The minimum density ratio for which stable calculations were possible for the present problem is 10^{-6}. As expected, with increase of density ratio the time to settle into a quasi-steady mode is delayed. Therefeore, particles with higher values of moment of inertia will reach a final orientation parallel to the flow later in time. When the density ratio is less than one, the observed behavior of the particle does not show significant differences as the solid density decreases. However, the current subiterative scheme works adequately for the entire range of density ratios for this problem. It is also noted that for $\rho_s/\rho_f \leq 1.0$, the simulation becomes unstable if a first order BDF is used in the integration of rotation variables. The third order BDF performs better than second-order BDF and reduces the computational time from 963.91s to 463.53s at $\rho_s/\rho_f = 1.0$; this is a result of reducing the average number of subiterations from 14 for the second-order BDF to 6 for the third order BDF. Thus, the order of the BDF approach for time-stepping has a significant impact on the efficiency and stability of the computations in such sensitive FSI cases. Therefore, a combination of strong coupling, Aitken relaxation

and third-order BDF scheme allows for extension of the FSI calculations in the high added mass regimes to very low values of ρ_s/ρ_f.

4.2.6. Motion of an elliptical particle in a channel

Here the ability of the SPM approach to simulate the dynamics of an elliptical particle free to translate and rotate while interacting with the carrier fluid is studied. Using similar conditions as in the previous section for a rotating elliptical particle but for $\rho_s = 2.0$, the domain has been expanded to 80.0×15.0 for $Re = 1000$ based on the particle's major diameter at the start of motion. The particle is released at $t = 0$ and the uniform velocity of the flow leads to very strong forces on the particle at the start of the motion. Different grid sizes have been chosen for grid independence study with minimum grid size of $\Delta x = 0.05$, $\Delta x = 0.0313$ and $\Delta x = 0.0186$, which has been obtained by using a base cell size of 0.2, 0.25 and 0.3 but with three, four and five levels of local mesh refinement, respectively.

The snapshots of the particle rotation in time are displayed in Figure (4-17). The particle orientation finally settles down to the horizontal configuration. For more detailed study, the rotational motion of the particle is shown in Figure (4-18). The initial particle angle of attack is $\pi/4$ which results in asymmetric flow. This asymmetry will lead to a moment and also a lift force. While the lift force pushes the particle upward, the particle accelerates along the channel length.

Translational motion in the channel shows two behaviors as represented in Figure (4-19): one is the streamwise displacement which follows close to a linear trend as the particle reaches the fluid velocity quickly due to its low density. The other is the drift from the center of the channel as is clearly observable in the lateral displacement, which is because of the lift at the start of the motion. The lift force becomes negligible after the particle almost reaches the flow velocity. The convergence of the particle orientation and position with grid refinement is shown in Figures (4-18) and (4-19). There is stronger convergence of the orientation angle and displacement along the y-direction than of the particle's position in the y-direction. Overall, the SPM algorithm with subiteration appears to be able to handle the motion of

particles in moderate Reynolds number flow in the presence of both translational and rotational degrees of freedom.

For better clarification, a parametric study is done to observe the effect of particle density and the Reynolds number.

4.2.6.1. Particle density effect

Similar conditions are implemented here for various particle densities to observe the motion of the elliptical particle in an initially uniform flow with $Re = 100$ with respect to major particle diameter. Due to differences in density, the particles would have different velocities in the channel. The simulation is performed till $T = 55.0$ with time lapses of $T = 3.0$ for writing the data. As shown in Figure (4-20), with increase of density, the delay in the translation of the particle causes the rotational motion to be more apparent at the start of the motion. when the particle becomes more inertial, the characteristic time of the particle increases leading to an increase in the value of the Stokes number ($St = \tau_p u_f / l_f$ where $\tau_p$is the particle relaxation time, and u_f and $l_f$are the flow characteristics velocity and length). When the value of the particle Stokes number rises, the higher inertia of the particle leads to more independent particle motion from the flow and a lag in the motion.

The delay in the stream-wise direction of the flow is studied quantitatively in Figure (4-21a). However, in the counter stream-wise direction (Figure (4-21b)), there is not such a simple pattern. The drag force in the stream-wise particle velocity is significantly higher than the lift. Moreover, the lift force highly depends on the particle angle which as shown in Figure (4-22) does not show a straightforward dependency to the particle density. The dependency of both particle angle as well as the relative velocity has made the moments' behavior complicated.

4.2.6.2. The Reynolds number effect

Considering the same case as the previous section, we change the particle Reynolds number for $\rho_p = 1.0$. The snapshots of the particle motion are shown in Figure (4-23) and the center of particle displacement results are displayed in Figure (4-24). It can be inferred from the results that with increase of the Reynolds number value, the particle stream-wise displacement would be higher as a result of faster approach to the final velocity. For the counter steam-wise displacement, the more the Reynolds number value, the more drift toward the upper wall.

As can be seen in Figure (4-25a), when the Reynolds number value is low, the particle angle change is not significant. The reason is that in low Reynolds numbers, with characteristic of reaching the flow velocity very fast, the rotational moment will be very low (Figure (4-25b)).

4.2.7. Motion of an ellipsoidal particle in a channel

An ellipsoid is placed in a 3D channel of size $60 \times 15 \times 15$ with the initial angle of $(0.0, \pi/4, 0.0)$ from position (5.0,7.5,7.5). A uniform flow is applied on all of the side walls and at the entrance. The particle with $\rho_p = 1.0$ and diameter of (2.5,0.7,2.5) starts to move when the simulation starts. The particle Reynolds number based on the major diameter of the particle at the start of the simulation is 100. Minimum grid size is 0.0625 and $CFL = 0.25$.

The results are shown in Figure (4-26) for the stream-wise and counter stream-wise displacement of the particle and in Figure (4-27) for the particle angles. Due to symmetry the first two Euler parameters are almost zero during the entire simulation; thus, only two Euler parameters are shown. The resulted Euler angle also has been added.

4.2.8. Investigation of a plunging airfoil

As another example of a flow at very high Reynolds numbers, in the section we describe a study of the flow over a plunging airfoil at $Re = 10000$ where the interaction of vortices with each other and

with the surface generates highly complex flow patterns. As the airfoil is oscillating, the unsteady motion of the airfoil adds to the complexity of the flow. The results of this study have numerous applications in nature and industry. For example, the flapping wings of a bird produces unsteady vortices that helps the animal generate enough lift to hold its height and give it the desired thrust to move forward [237-239]. The impact on the airfoil can be detrimental when flutters are induced or favorable when a lift force is generated [240].

The study of vortex dynamics shows that the leading edge vortex (LEV), which is the strongest vortex generated from the body surface, has a great influence on aerodynamic characteristics. Moreover, the interaction of secondary vorticity generated from the airfoil surface determines the stability and strength of the LEV [241]. The unsteady motion of the body produces a lift which is specific to unsteady aerodynamics. Consequently, the study of LEV formation can illustrate several important features that helps us thoroughly understand the physics.

While the formation of LEVs happens at the leading-edge of the airfoil, they appear with a delay. In a plunging or rotating airfoil, an adverse pressure gradient (APG) develops on the airfoil's surface due to the flow dynamics [242]. A sufficiently high APG ejects the vorticity from the attached boundary layer leading to boundary layer roll-up and separation from the surface. If the vorticity flux continues to form at the shear layer of the leading-edge, LEV circulation increases. Thus, the LEV's strength will increase and more interaction with the neighboring surfaces and vortices occurs. The interaction with the nearby surfaces leads to the production of secondary vorticity which is in the opposite direction to the LEV vorticity. The secondary vorticity will eventually detach the LEV from the surface [243-245] and gradually annihilates the vorticity flux of the shear layer [241].

While, research in this area has been predominantly experimental, several simulations have been performed to explore the phenomena. For example, Lewin and Haj-Hariri [243] characterized the flow and the thrust at low Reynolds numbers for heaving airfoils in 2D. Visbal [244] studied the entrainment of secondary vorticity into an LEV using large eddy simulations. The main benefit of performing these

simulations is that many detailed insights that are not shown by experiment, are revealed by simulations. As an example, a simulation can show the distribution of stress and surface pressure which helps the study of vorticity production, thrust and lift forces. Consequently, this section describes the simulation for such cases.

In this part of the research we studied the DNS of LEV formation, stability and transition for a flow over an oscillating flat plat at $Re = 10000$. Because of the high computational cost of 3D simulations, only 2D simulations are performed. This does not affect the accuracy of the overall results significantly as the span of the plate ($304.8\ mm$) is significantly greater than the cord length ($76\ mm$). Moreover, as shown by Eslam Panah et al. [241] using a nominally 2D flat plate, the three dimensional vorticity fluxes are less important in comparison with the vorticity diffusion from the surface. Therefore, the 3D effects on a similar flat plate used in this research has a minimal effect in the flow characteristics. Instead, the transport of LEV and secondary vorticity control the LEV's stability.

The simulations are set up so that the results could be compared with Akkala [246] who studied an airfoil similar to Figure (4-28) with the chord length of $c = 76.2\ mm$ and a thickness of $t = 3.175\ mm$. In this 2D simulation we ignore the effect of span size of $s = 304.8\ mm$.

Figure (4-29) shows the simulation domain and the initial position of the plate. The flat plate airfoil is located in a $9c \times 6c$ channel and is subject to a uniform inlet velocity of water with $U_\infty = 0.13\ m/s$ at the inlet and the top and bottom walls. The reduced frequency is equal to $\kappa = \frac{\pi f c}{U_\infty} = \frac{\pi}{2}$ and the Strouhal number to $St = \frac{2fh_0}{U_\infty} = 0.3$. The flat plate airfoil has a prescribed sinusoidal oscillation in counter-streamwise direction represented as

$$h = h_0 \sin(2\pi f t) \tag{4-28}$$

where $h_0$stands for motion amplitude, f for frequency and t for time. The velocity and acceleration of the airfoil will have the following relations

$$h = 2\pi f h_0 \cos(2\pi f t) \tag{4-29}$$

$$h = -(2\pi f)^2 h_0 \sin(2\pi f t) \tag{4-30}$$

We used the non-dimensional form of the equations based on Table (4-1). The main parameters are non-dimensionalized as

$$h_0{}^* = \frac{h_0}{c}$$

$$f^* = \frac{f U_\infty}{c}$$

$$t^* = \frac{tc}{U_\infty} \tag{4-31}$$

The relation $C_L = \frac{2L}{\rho U_\infty^2 cs}$ calculates the lift coefficient for 3D simulations, while in the 2D simulation the lift coefficient is calculated as $C_L = \frac{2L}{\rho U_\infty^2 c}$. Based on the reduced frequency, the frequency for the experiment is $f = 0.853$ and in the non-dimensional form is $f^* = 0.5$.

To avoid sudden spikes at the start of the motion, at first the plate is fixed for one cycle ($T^* = 2$). After the boundary layer develops, it starts to oscillate with an amplitude equal to

$$\overline{h_0} = h_0\,(1 - \exp(-9.2\,t^*)) \tag{4-32}$$

The above exponential function saturates very fast and reaches 99% of h_0 in $t^* = T^*/4$. Thus, it only can affect the first cycle of the motion.

The minimum grid size $\Delta x = 7.8 \times 10^{-4}$ is achieved by refining the base grid 0.025 five times. Moreover, CFL=0.35 and the strongly coupled solver is used to reach the final converged FSI solution.

Figure (4-30) represents the vorticity results from SPM for one cycle. The results are for the 5th cycle from the start of the oscillation when the transient effects are negligible and they are compared with the experiment of Akkala [246]. Because of the PIV shadow affect, the experimental results for the bottom surface is not available. Therefore, this discussion only compares the top surface of the airfoil.

At $\theta = 0°$, when the plate is in the middle of its range and at its maximum downward velocity, LEV develops a substantial region of secondary vorticity. During the downward motion of the airfoil the LEV continues to grow and gains strength. However, when the airfoil approaches the bottom LEV starts to detach from the surface. During the upward motion of the flat plate, LEV is washed down the airfoil

and no new LEV is generated. The results show the overall good agreement between the SPM results and the experiment.

The history of lift coefficient C_L (Figure (4-31)) shows the sinusoidal behavior of C_L with time. The phase average results from the experiment for a half cycle also has been added for comparison and it shows the overall agreement of the simulation with the experiments. The maximum C_L with a small shift in the phase (oscillation angle) follows the oscillations of plate. The shift in the phase and even the amplitude of the motion could be explained using the Theodorsen theory which is based on the assumption of having an inviscid incompressible flow. Theodorsen Lift force for pure plunge is [247]:

$$C_L = \frac{\pi}{2}\ddot{h} + 2\pi\dot{h}C(\kappa) \tag{4-33}$$

With the reduced frequency of $\kappa = \frac{\pi}{2}$, the Theodorsen function value becomes $C(\kappa) = 0.520 - 0.071\,i$. Using the complex functions to represent the oscillations instead of sine function leads to

$$\dot{h} = 0.122ie^{i5.36t} \tag{4-34}$$

$$\ddot{h} = -0.654e^{i5.36t} \tag{4-35}$$

Substitution of Equation (4-34) and (4-35) into Equation (4-33) results in

$$C_L = (-4.22 + 2.94\,i)e^{i\pi t} \tag{4-36}$$

For better comparison, the results for the variation of C_L with phase from the simulation, theory and the experiment [246] are compared in Figure (4-32). It shows that the results from the SPM simulation are very close to the experimental outcomes and the predictions of Theodorsen theory. Specially, all methods predict the phase shift in the maximum C_L which is almost -0.39 $(-22.3°)$. For the amplitude of C_L, the discrepancy between the Theodorsen theory and the experiment stems from the fact that the Theodorsen theory is based on inviscid flow. The difference between the simulation and the experiment is because SPM is more accurate for low and moderately high Reynolds numbers.

4.3. Conclusions

This chapter investigated the applicability of the smoothed profile method to various FSI problems of the type that are encountered in particle-laden flows where the particles are resolved during the computations. Several cases were considered to study SPM in more challenging conditions than it has hitherto been applied, where the Reynolds number value is high enough that significant inertia effects exist, for wake flows and FSI problems with high added mass effect. The 2nd-order accurate SIM was used to compare the performance of and validate SPM.

For flow over a cylinder at high Reynolds number values, SIM and SPM are shown to be capable of capturing the interplay between the boundary layer, the coherent structures in the wake and to adequately calculate the surface vorticity generation. Time histories of drag coefficient as an integrated variable are in agreement for SPM and SIM with the benchmark [233]. However, the resulting surface vorticity for SPM is lower than for SIM and the Lagrangian vortex method of [233]; since SPM is a diffuse interface method it does not capture the vorticity values on the surface with great fidelity. The deviation of SPM from the sharp methods increases as the Reynolds numbers increases even in moderate locally refined meshes at the solid surface.

Use of SPM in vorticity-bearing far field flows was determined to be adequate as demonstrated in the study of two spheres where one of them is placed in the wake of the other. For lower Reynolds numbers, in fact SPM provides better accuracy on coarse grids in comparison with SIM. Furthermore, limitations imposed by the level set based ghost fluid implementation in SIM does not allow contact of the two particles, while SPM does not carry such a restriction.

At low solid densities, when high added mass effects arise, use of fully coupled solution becomes necessary. In such cases, SPM is found to be more efficient as it needs fewer subiterations that SIM. Study of the rotational motion of particles, in particular of an ellipse free to rotate in an oncoming flow showed that higher order time integration schemes leads to better converged results. The role of Aitken acceleration on efficiency is decisive when subiterations are implemented in the implicit solutions. The

translational and rotational motion of an elliptical particle show the capability of the SPM to capture the complex motion of particles in the moderate Reynolds number range ($0 < Re < 1000$). Then, a parametric study is performed on tilted elliptical particles based on the particle density and particle Reynolds number. A delay to the particle motion in inertial particles and higher rotation rates at higher Reynolds number values were observed.

Finally, we investigated the capability of SPM in prediction of the flow at $Re = 10^4$ for an airfoil subject to prescribed oscillation. The development of the leading edge and secondary vorticity for the moving boundary problem was studied and the lift coefficient results were compared with the Theodorsen lift force theory and the experiments. The results showed the overall agreement of all methods in prediction of lift coefficient.

Overall, the current study shows that SPM can be used for particulate flows at high laminar Reynolds numbers and may be a more efficient choice that sharp interface schemes for $Re \ll \mathcal{O}(10^4)$; for the cases tested, SPM provides more robust and accurate calculations for problems with low solid density values where high added mass effects can lead to instabilities.

In the following chapter we extend our investigation toward more efficient simulations. First, we express the local mesh refinement technique to improve the efficiency. Next, we propose a new SPM formulation which has only one Poisson equation and finally, compare the efficiency of different models for different problems.

TABLES

Table 4-1- The original and non-dimensional parameters used in this study.

Variable	Formulation	Experiment	Simulation
Chord length	c	0.0762	$c^* = 1.0$
Amplitude	h_0	0.0227	${h_0}^* = 0.3$
Inlet Velocity	U_∞	0.13	1.0
Time	t	t	$t^* = 1.706t$
Frequency	$f = \frac{kU_\infty}{\pi c}$	$f = 0.865$	$f^* = \frac{1}{T^*} = 0.5$
Lift Coefficient	$C_L = \frac{2L}{\rho U_\infty^2 cs}$	$5.06L$	$2L$

FIGURES

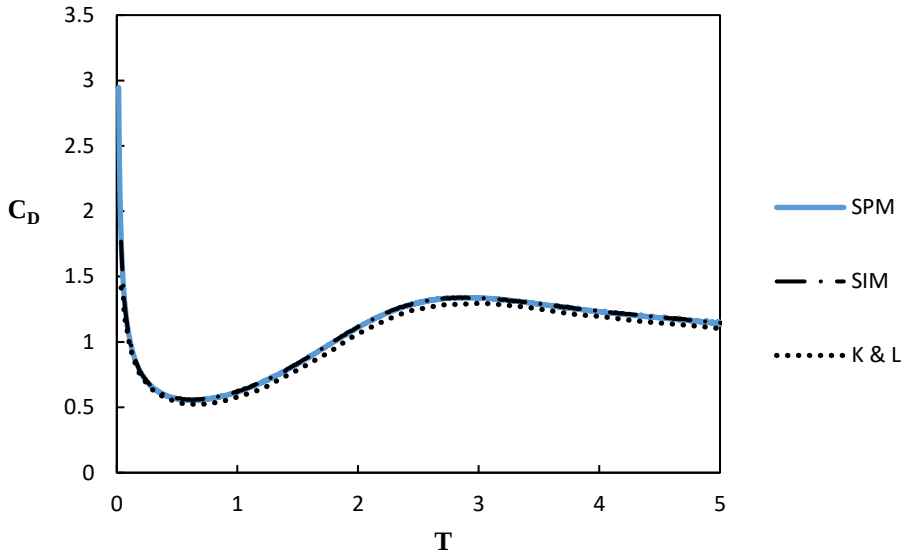

(a)

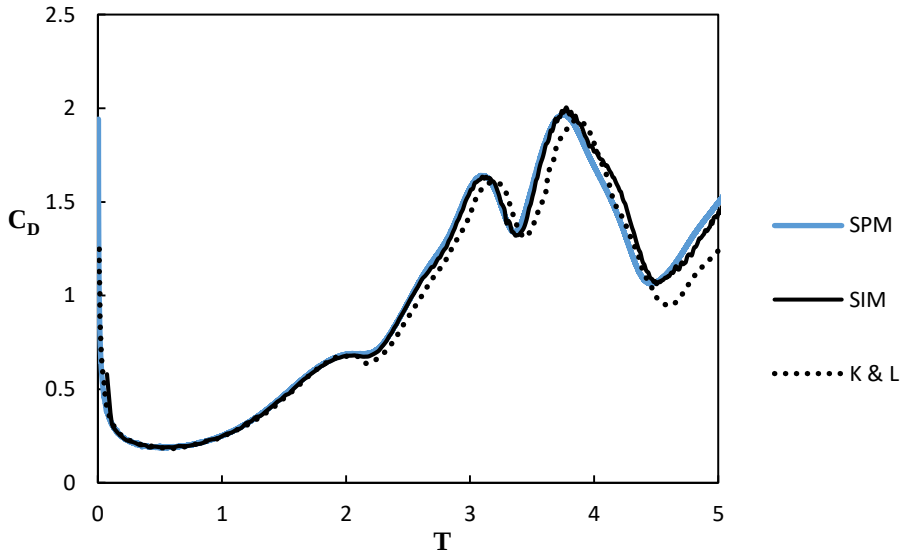

(b)

Figure 4-1- Comparison of time history of drag coefficient for flow over a stationary cylinder in an impulsively stating flow at **(a)** $Re = 1000$ and **(b)** $Re = 9500$ for different methods.

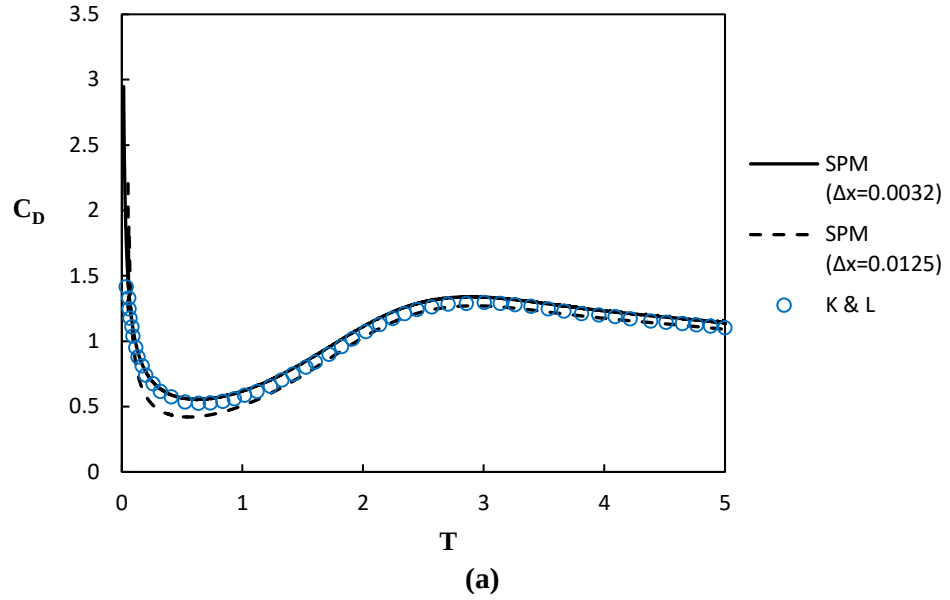

(a)

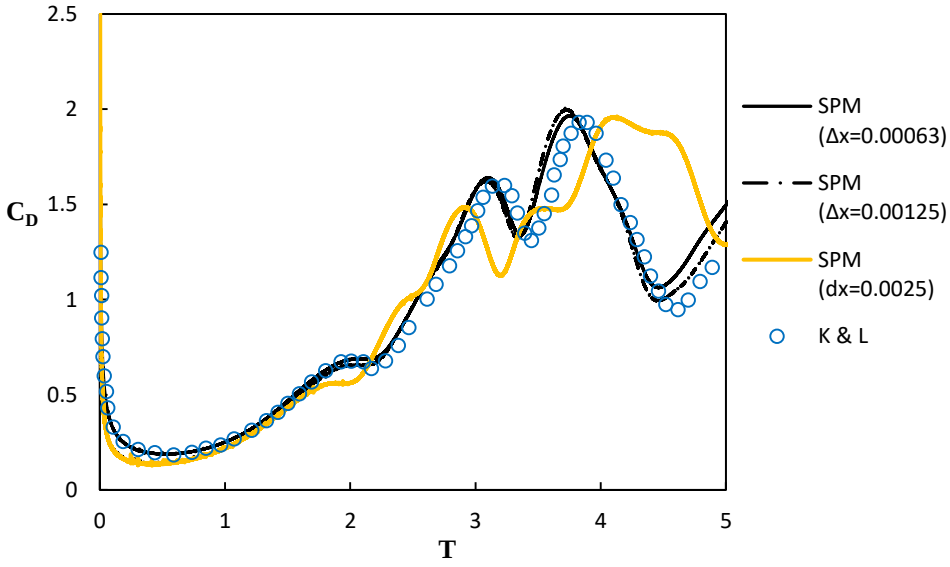

(b)

Figure 4-2- Comparison of time history of drag coefficient for flow over a stationary cylinder in an impulsively stating flow at **(a)** $Re = 1000$ and **(b)** $Re = 9500$ at different grid sizes.

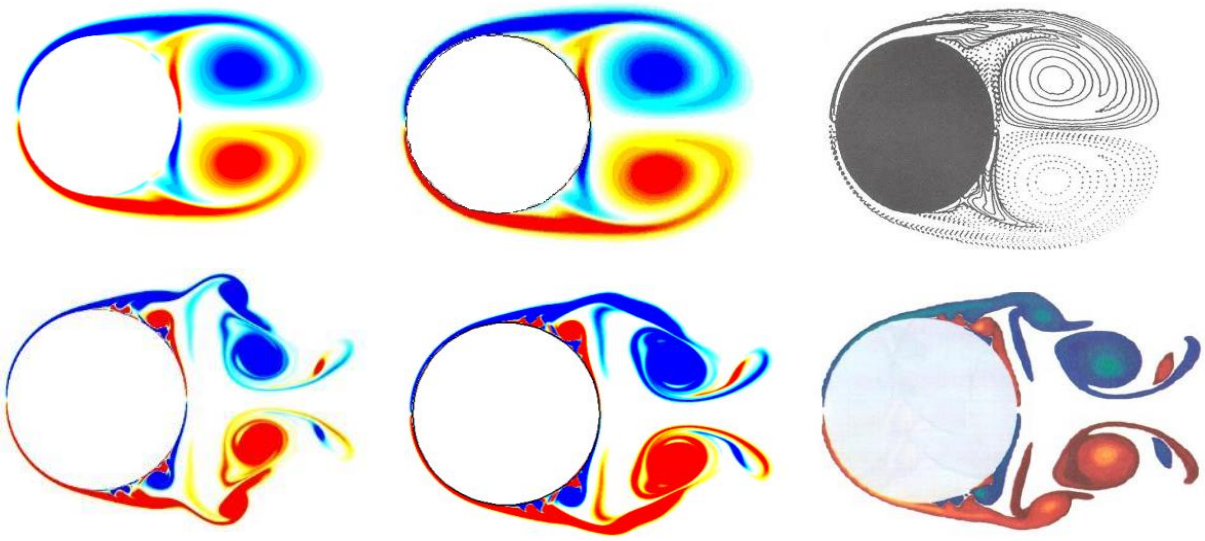

Figure 4-3- Comparison of vorticity results for flow over a stationary cylinder at **top)** $Re = 1000$ and **bottom)** $Re = 9500$ at $T = 6$ for **Left)** SPM, **Middle)** SIM and **Right)** Koumoutsakos and Leonard.

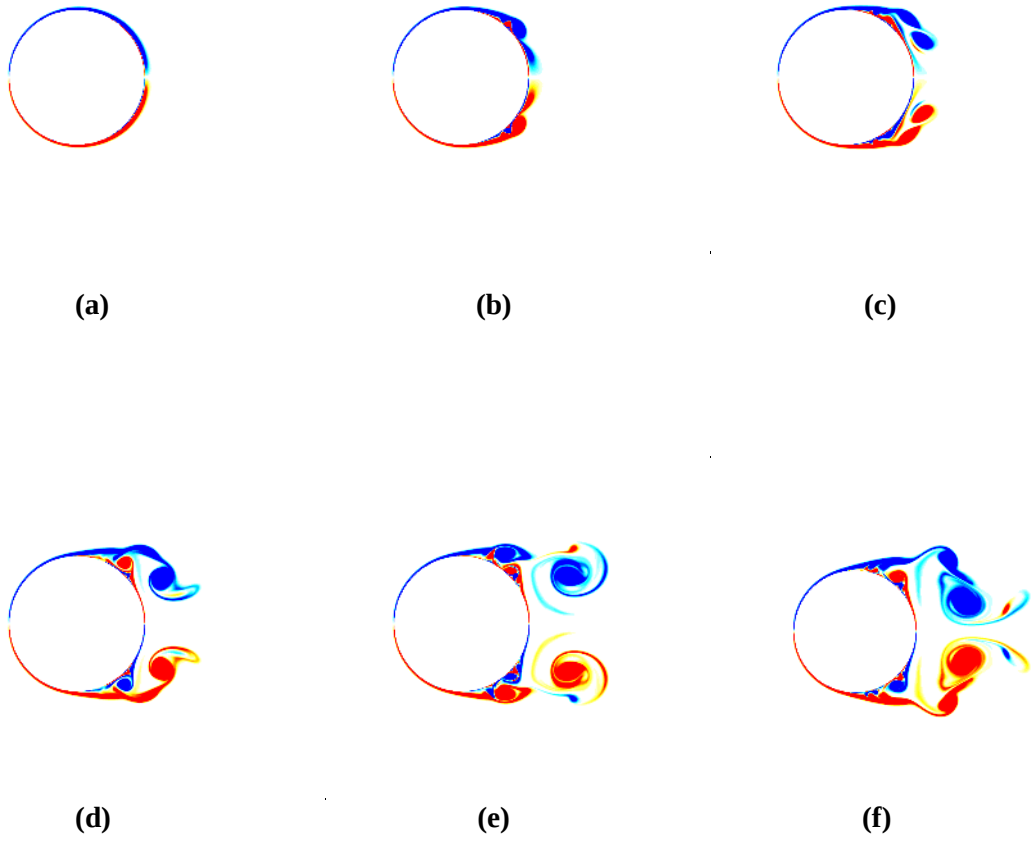

Figure 4-4- Evolution of vorticity contours for impulsively started flow over cylinder at $Re = 9500$ using SPM at **(a-f)** $T = 1.0$ to $T = 6.0$.

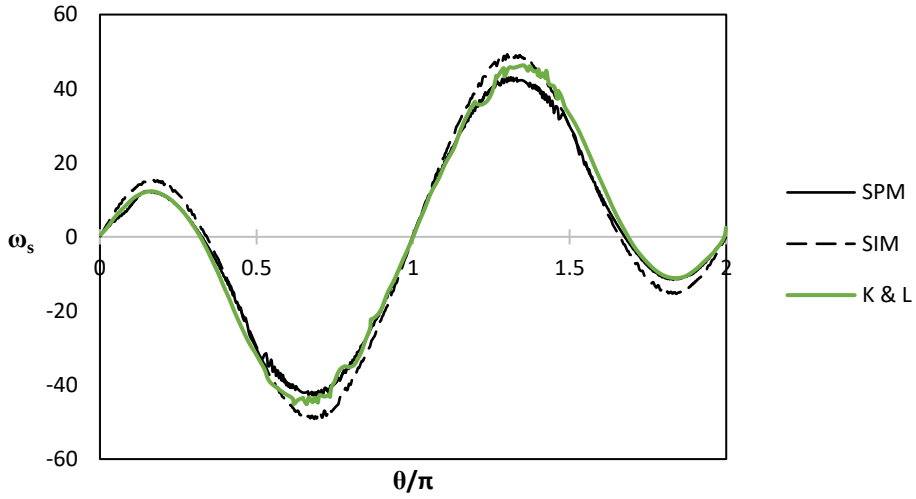

(a)

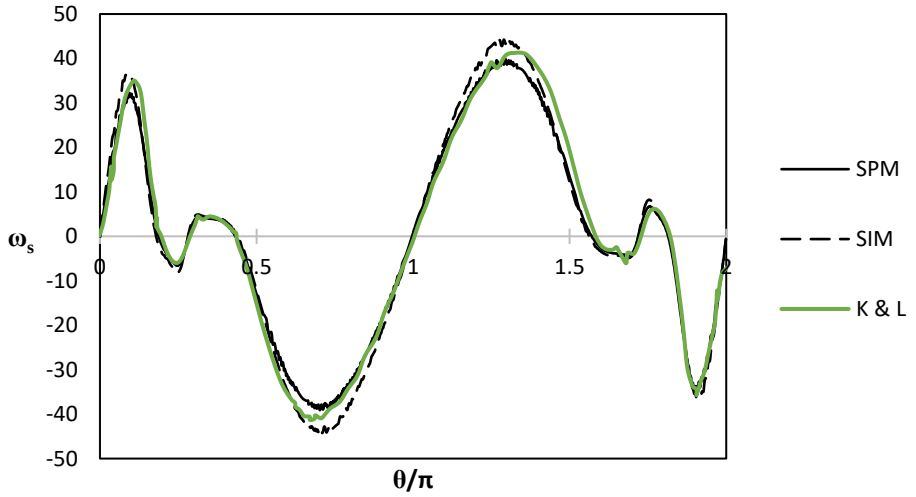

(b)

Figure 4-5- Comparison of surface vorticity results for flow over a stationary cylinder for $Re = 1000$ at **(a)** $T = 1.0$ and **(b)** $T = 3.0$.

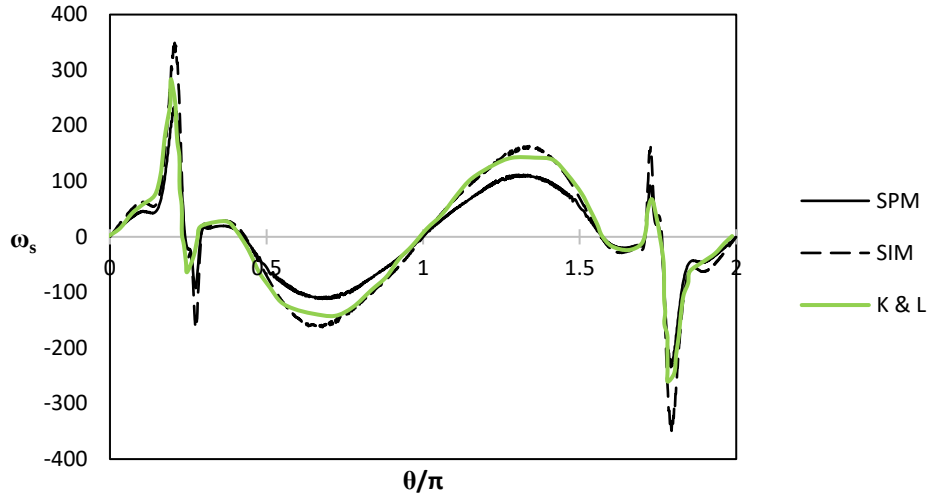

(a)

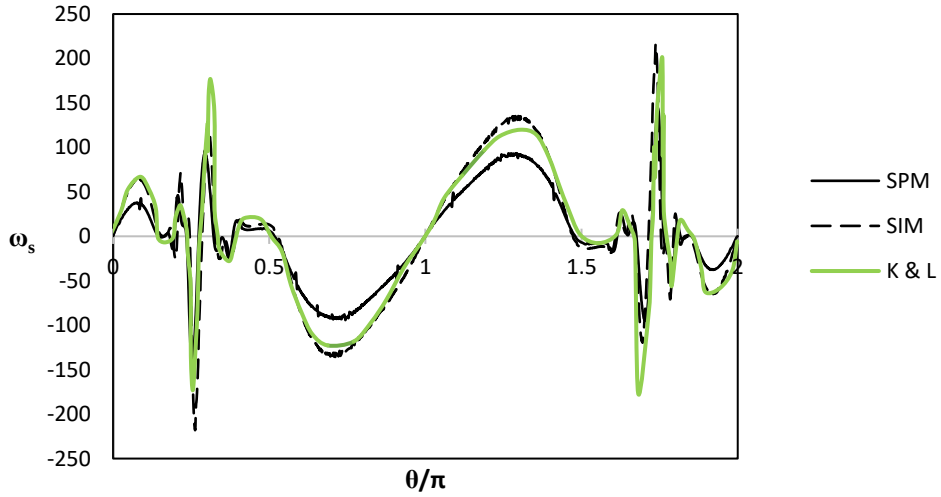

(b)

Figure 4-6- Comparison of surface vorticity results for flow over a stationary cylinder for $Re = 9500$ at **(a)** $T = 1.8$ and **(b)** $T = 5.0$.

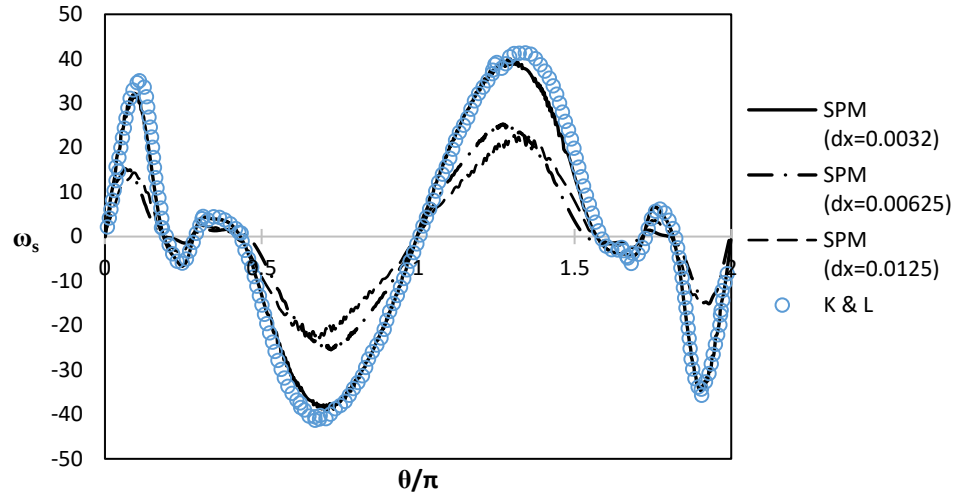

(a)

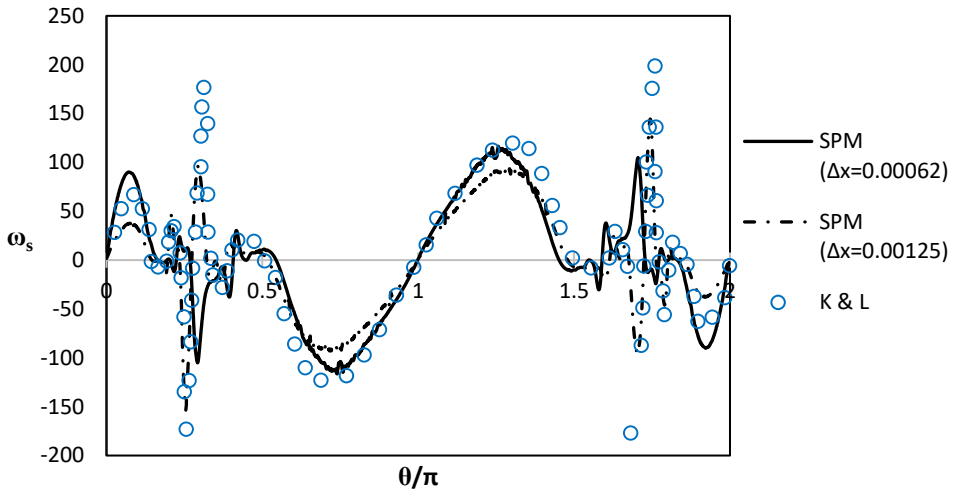

(b)

Figure 4-7- Effect of grid refinement on surface vorticity for flow over a cylinder for **(a)** $Re = 1000$ at $T = 3.0$ and **(b)** Re=9500 at $T = 5.0$.

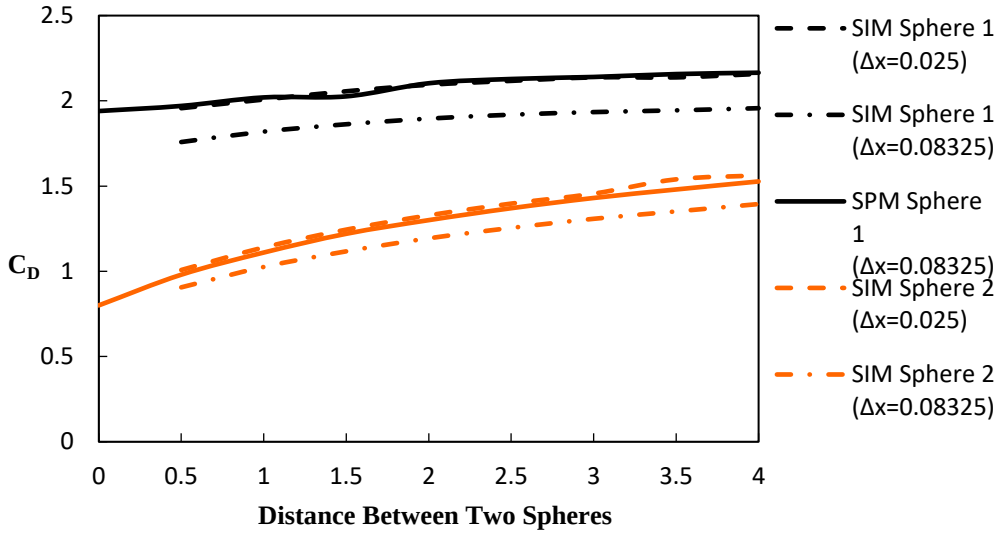

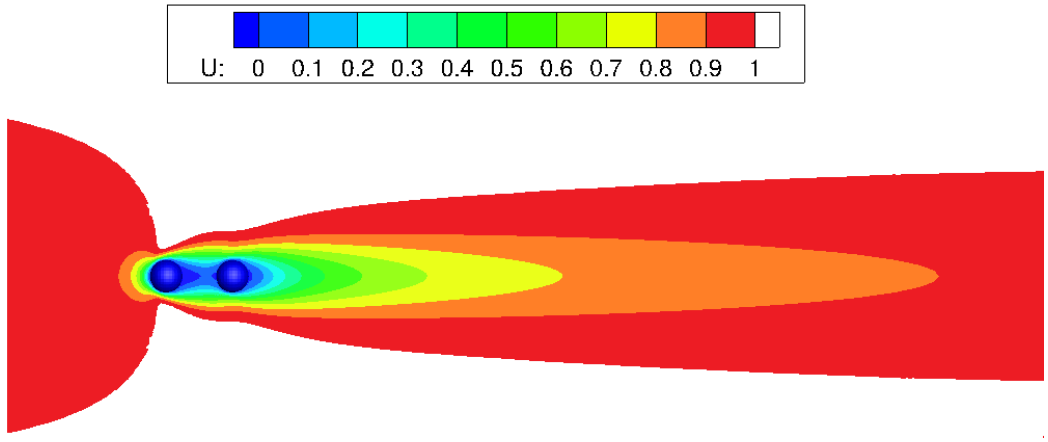

(b)

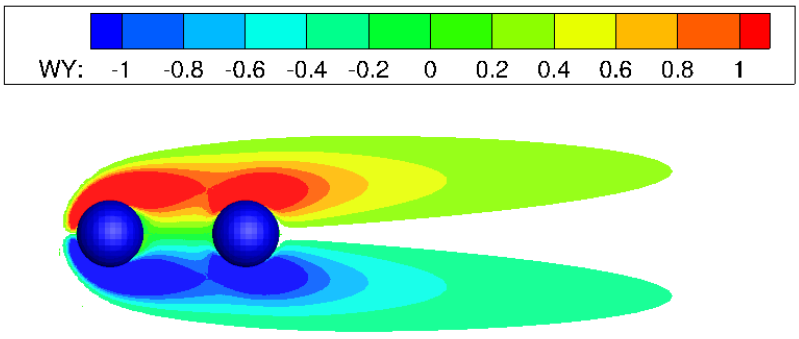

(c)

Figure 4-8- **(a)** Comparison of the resulted drag coefficient of two spherical particles in a channel flow at $Re = 30$. The second particle is located at different distances from the first one. The SPM Contour plots for $Re = 30$ and $\Delta = 1$. **(b)** streamwise velocity and **(c)** vorticity.

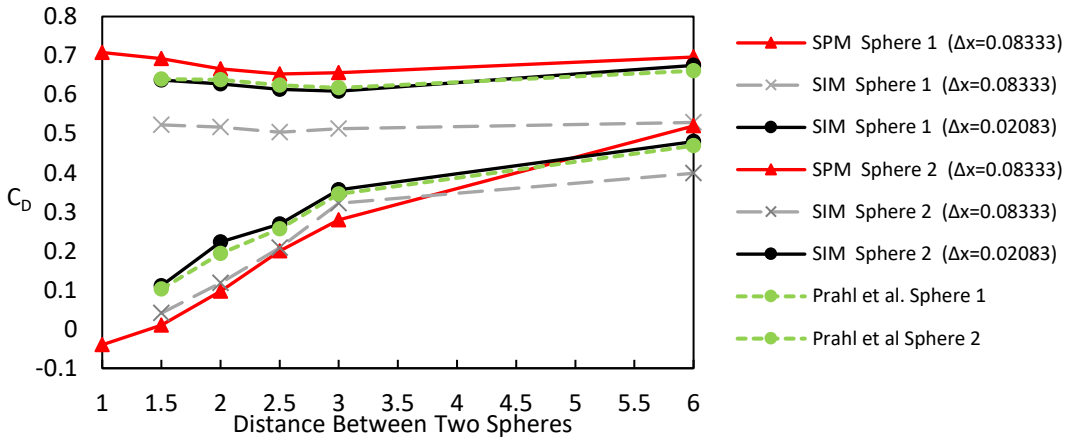

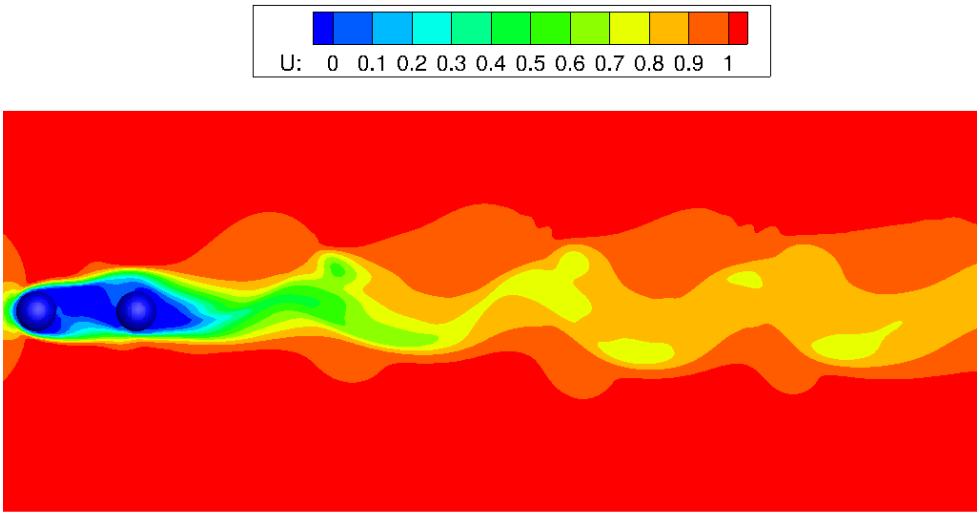

(b)

(c)

Figure 4-9- **(a)** Comparison of the resulted drag coefficient of two spherical particles in a channel flow at $Re = 300$. The second particle is located at different distances from the first one. The SPM Contour plots for flow over sphere at Re = 300 and Δ= 2.5. **(b)** streamwise velocity and **(c)** vorticity. The view of the vortical structures is shown at a 30° rotation around the channel axis.

(a)

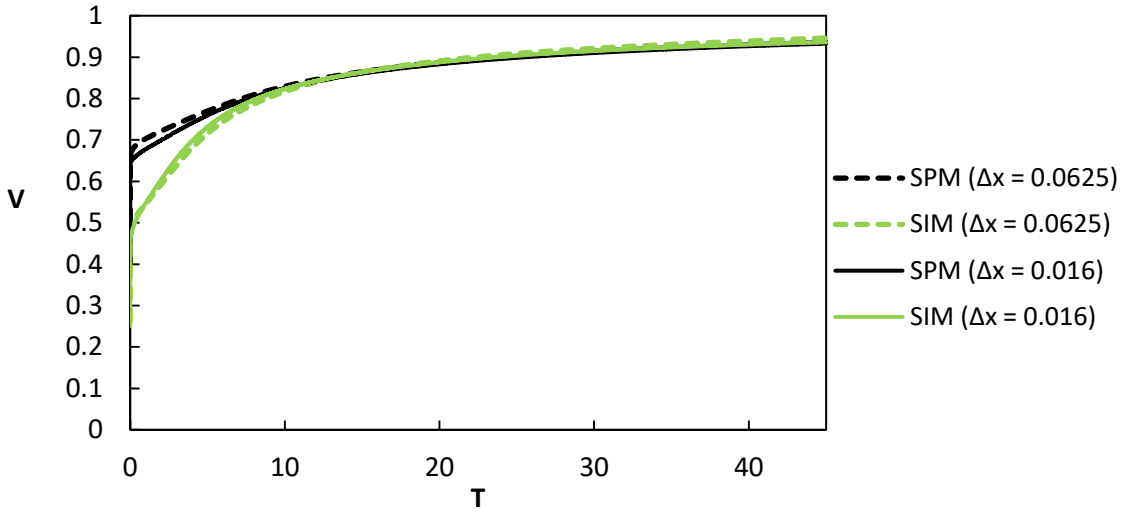

(b)

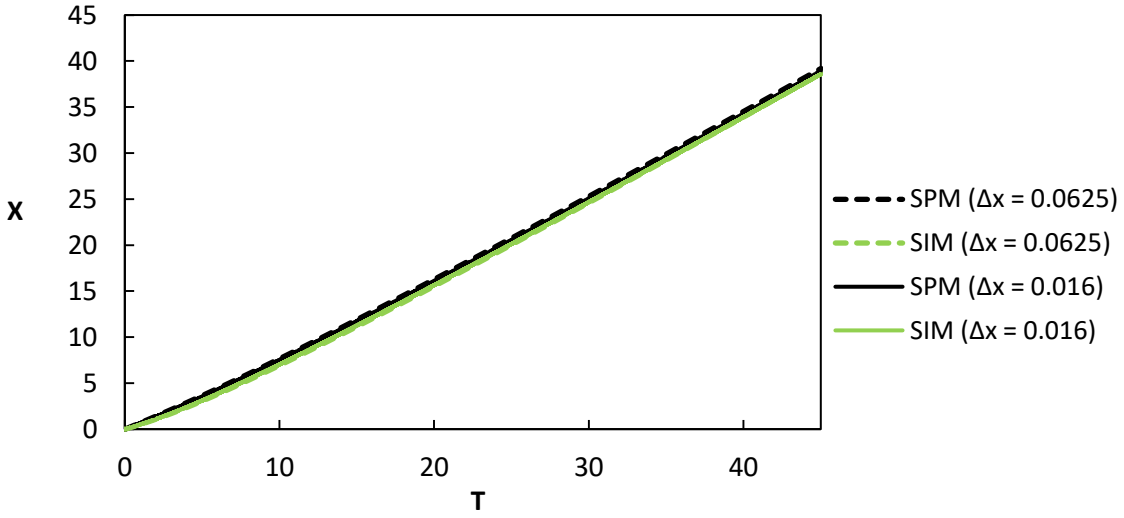

(c)

Figure 4-10- **(a)** The schematic for a moving disk with $\rho_s/\rho_f = 1.5$ in a horizontal channel. **(b)** Variation of velocity with time **(c)** Position history.

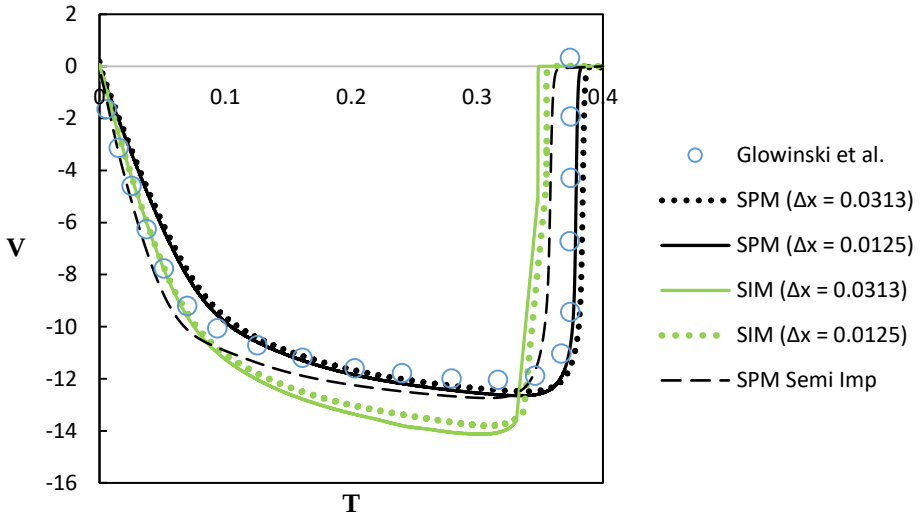

(a)

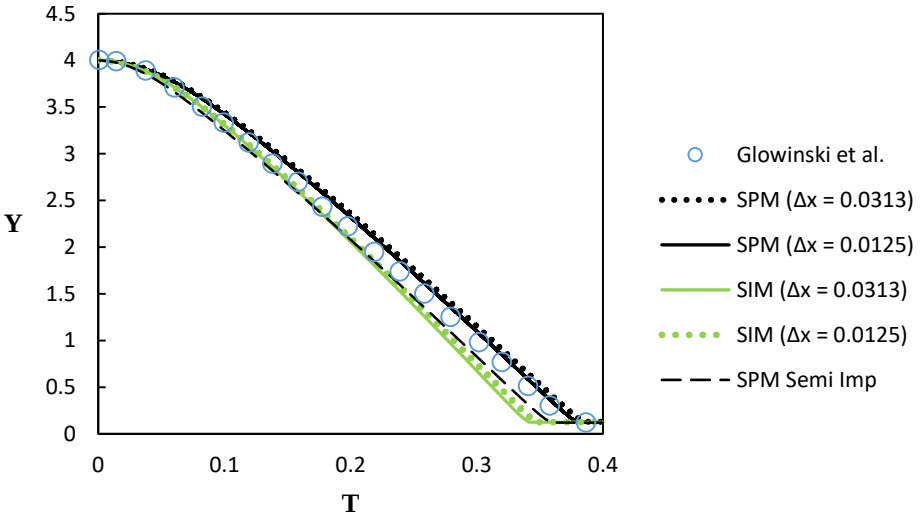

(b)

Figure 4-11- Time history of **(a)** vertical velocity and **(b)** vertical position of a falling disk with $\rho_s/\rho_f = 1.5$ from SIM and SPM and comparison with Glowinski et al.

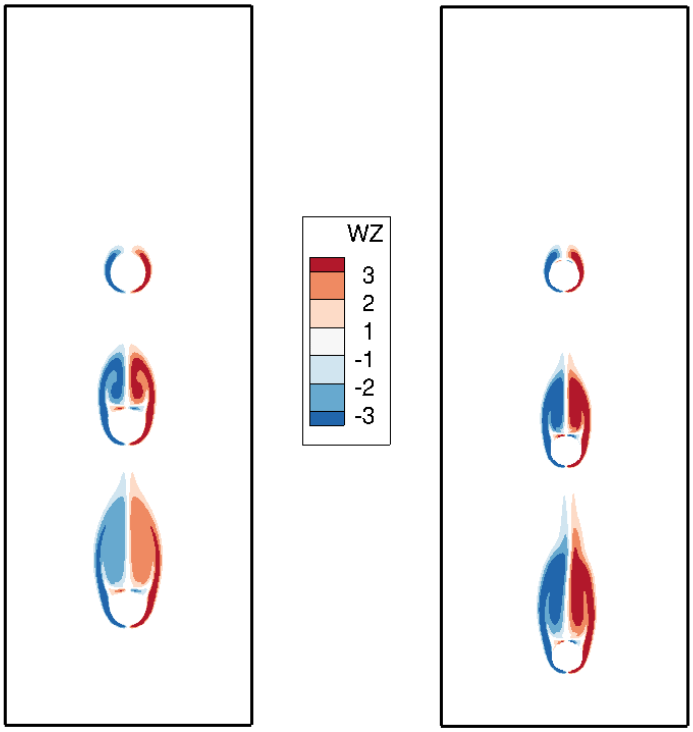

Figure 4-12- Contour plots of vorticity for a falling disk for **(left)** SPM and **(right)** SIM from top at $T = 0.0625$, T=0.1875 and $T = 0.3125$.

(a)

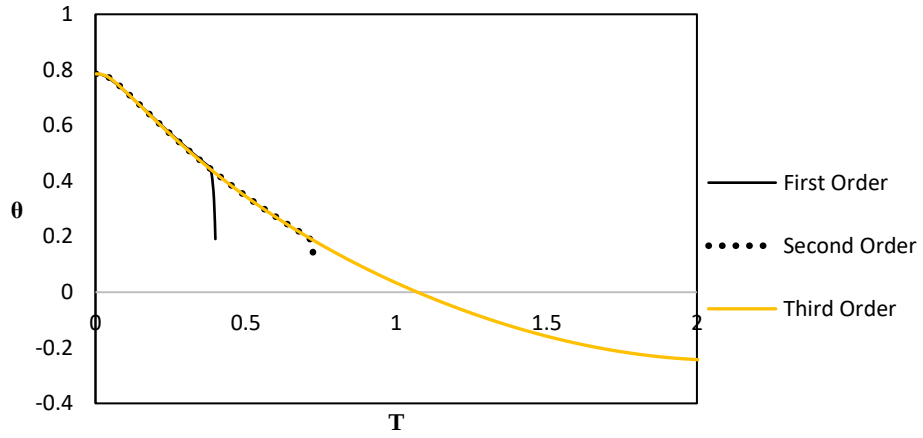

(b)

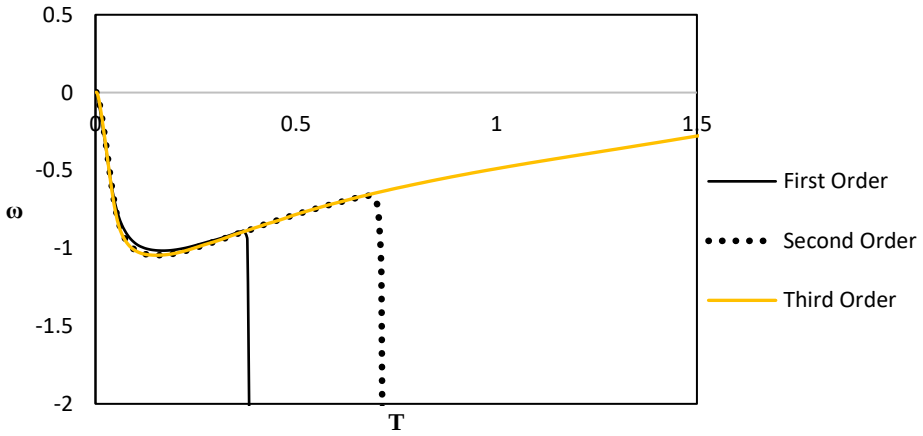

(c)

Figure 4-13- Effect of time integration scheme on variation of angular velocity and angle with time for an ellipsoid with $\theta_0 = \pi/4$ for $\rho_s = 0.1$. **(a)** The schematic of the problem. **(b)** Particle angle. **c)** Particle angular velocity.

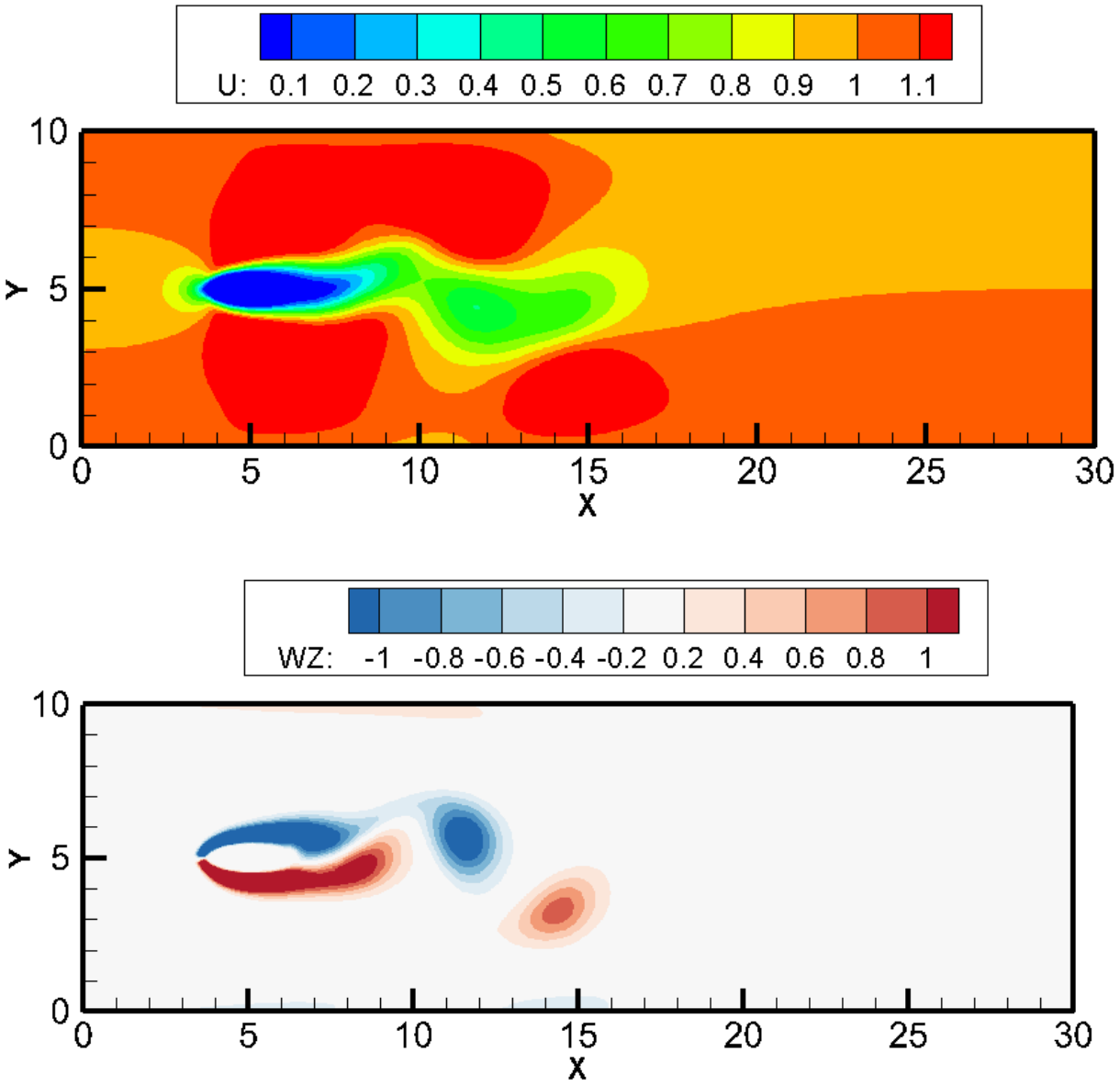

Figure 4-14- Contours of streamwise velocity and vorticity after reaching the final position for $\rho_s = 1$ at T=10.0.

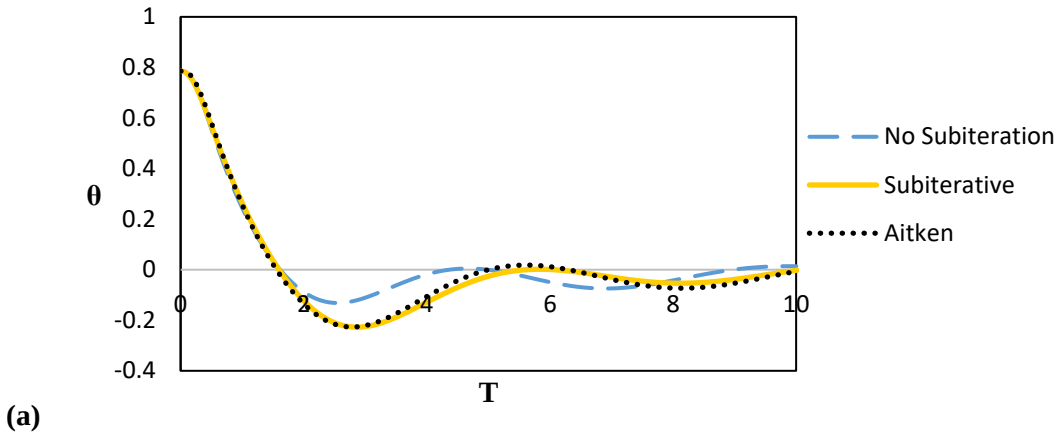

(a)

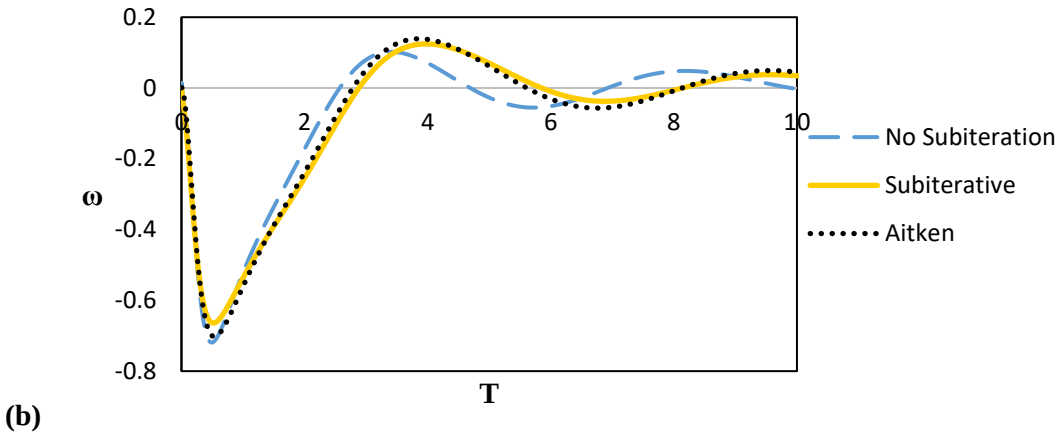

(b)

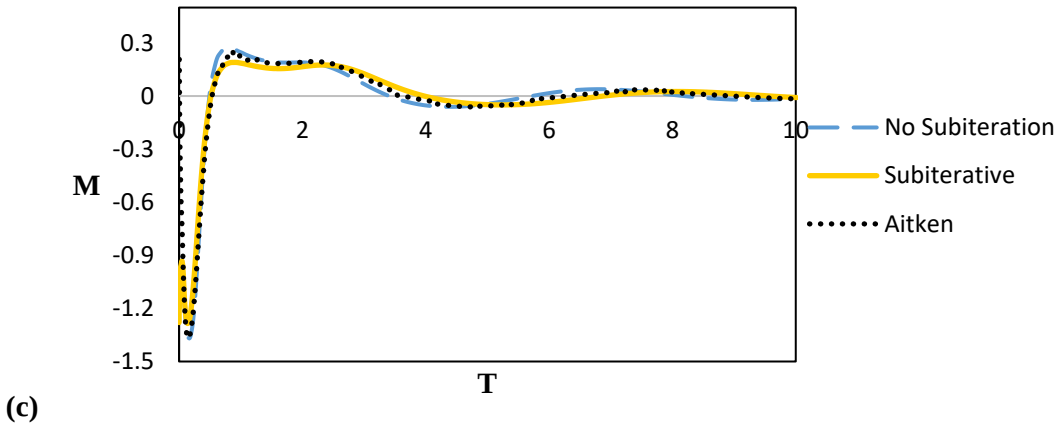

(c)

Figure 4-15- Variation of **(a)** angle, **(b)** angular velocity and **(c)** moment with time for an ellipsoid with $\theta_0 = \pi/4$ using different subiteration conditions for ρ_s = 1.0.

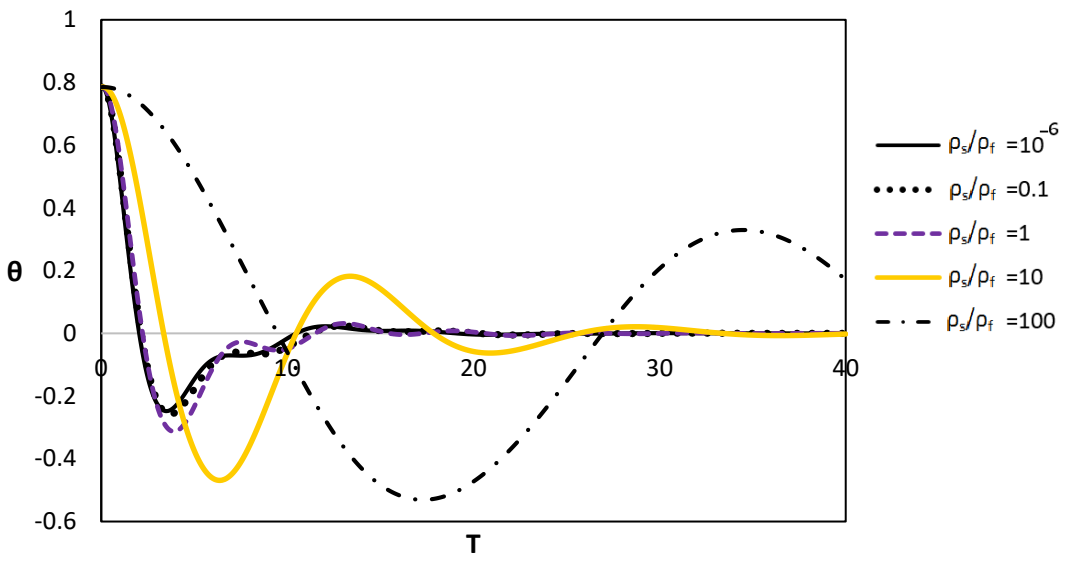

Figure 4-16- Variation of angle with time for an ellipsoid with $\theta_0 = \pi/4$ for different particle densities.

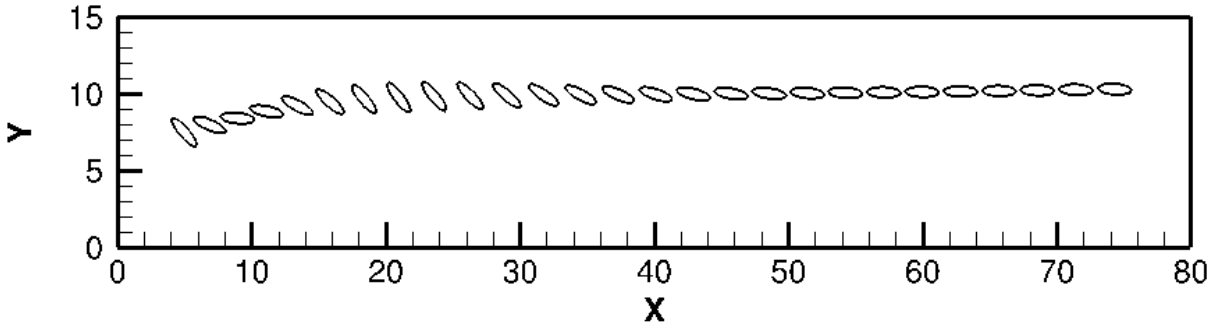

Figure 4-17- Snapshots of the particle rotation by time for $\theta_0 = \pi/4$ with $\rho_s = 2$.

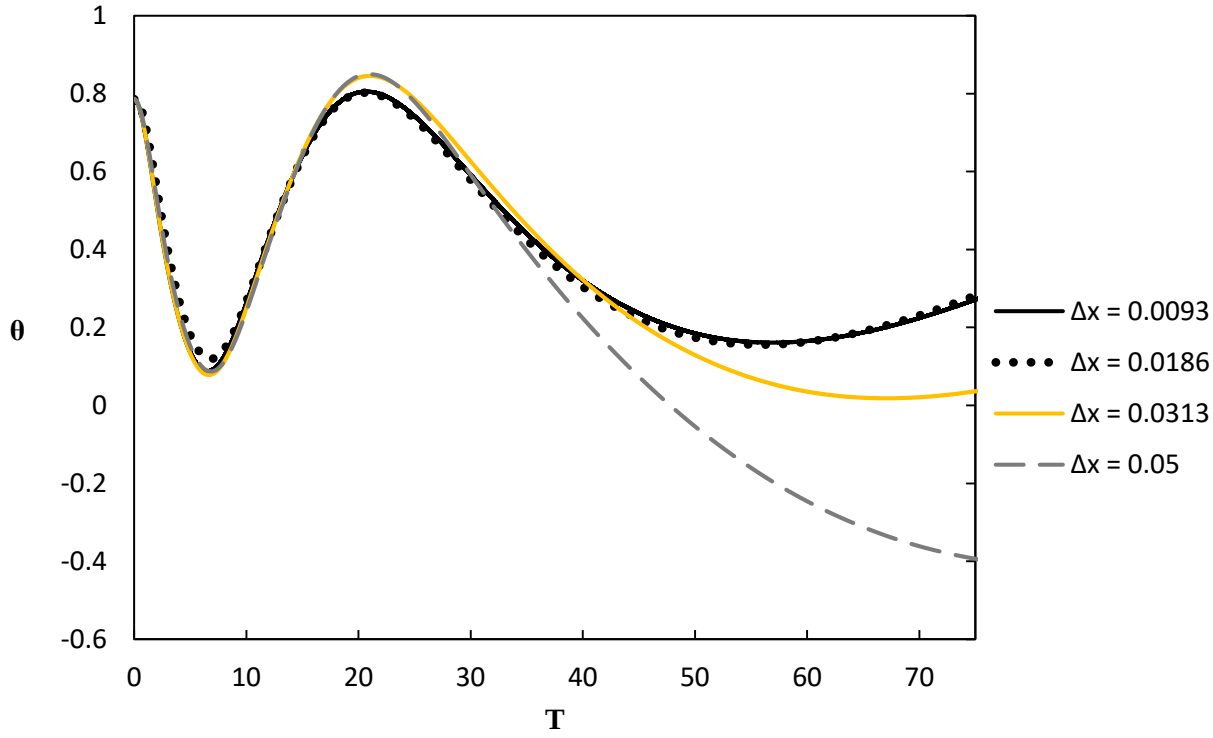

Figure 4-18- Variation of angle with time for a particle at $\theta_0 = \pi/4$ and $\rho_s = 2$ which moves freely in the channel.

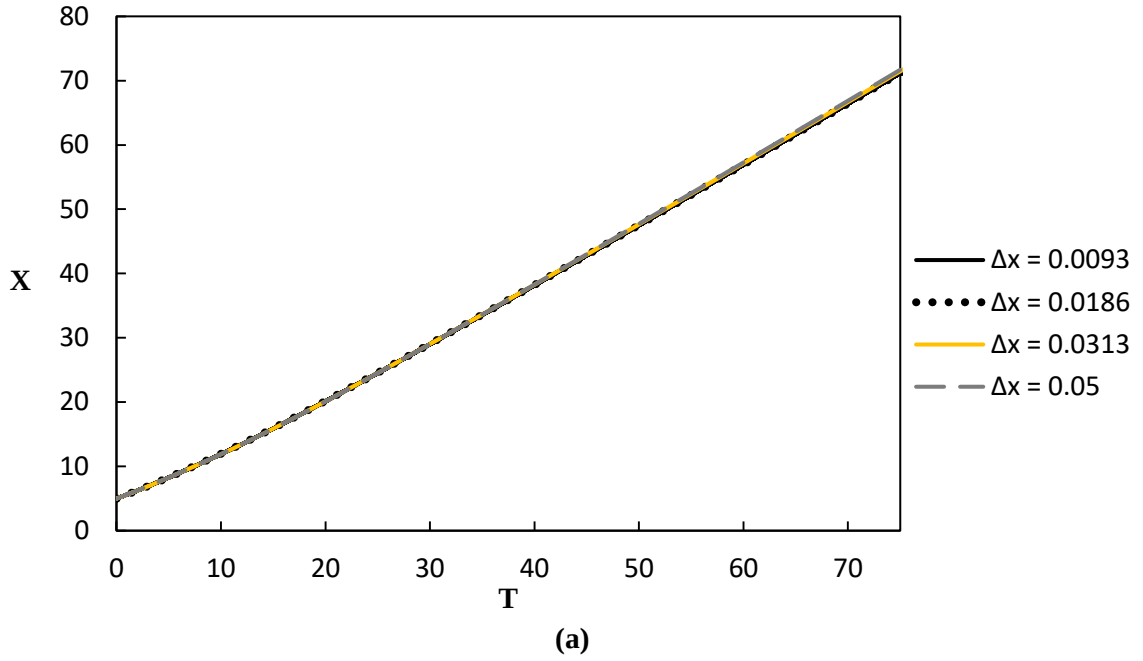

(a)

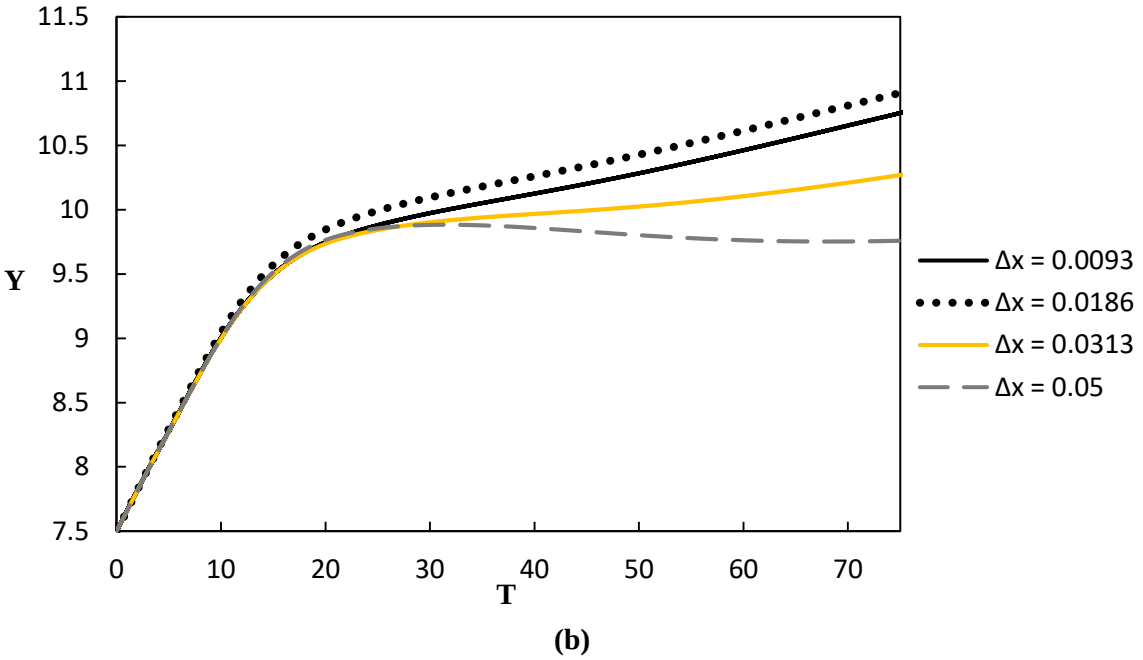

(b)

Figure 4-19- Displacement of a particle for a particle at $\theta_0 = \pi/4$ and $\rho_s = 2$ which moves freely in the channel. **(a)** Stream-wise displacement; **(b)** Counter Stream-wise displacement.

(a) $\rho_p = 1$

(b) $\rho_p = 10$

(c) $\rho_p = 100$

(d) $\rho_p = 1000$

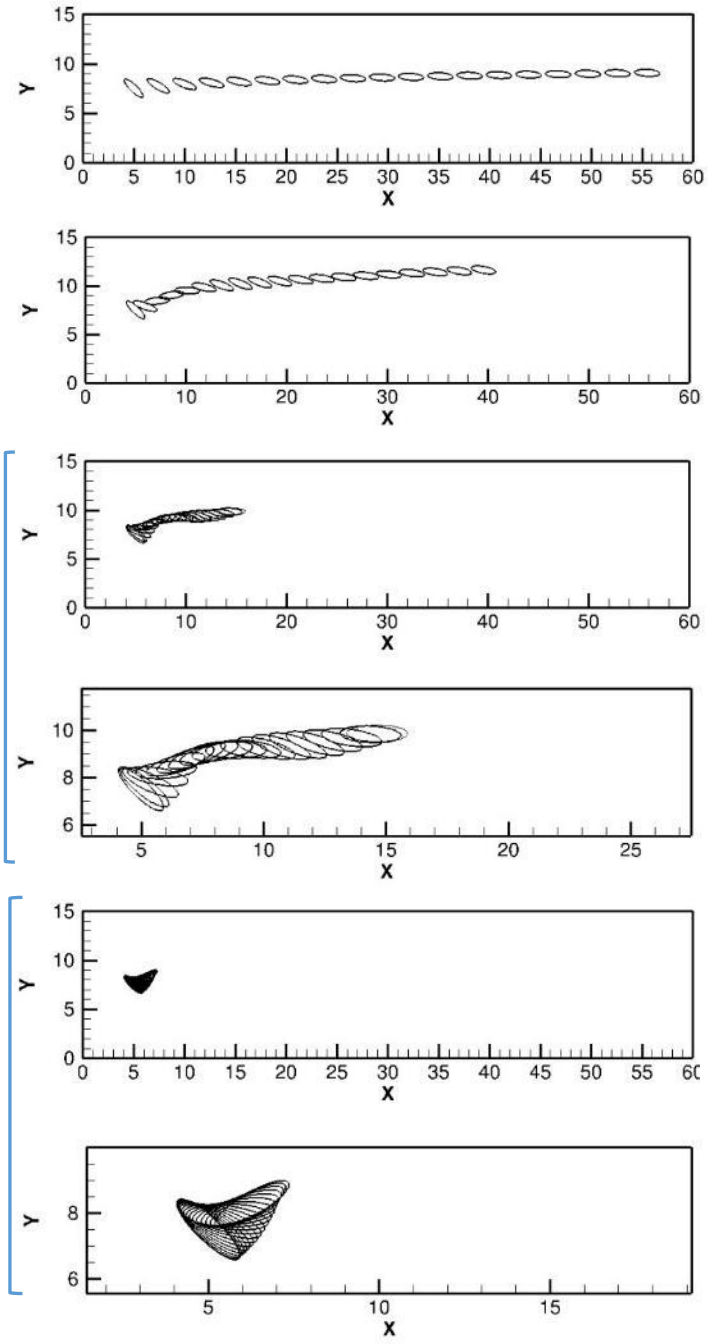

Figure 4-20- Snapshots of the particle motion for **(a)** $\rho_p = 1$, **(b)** $\rho_p = 10$, **(c)** $\rho_p = 100$ and **(d)** $\rho_p = 1000$. In (c) and (d), the zoomed view of the snapshot also is shown.

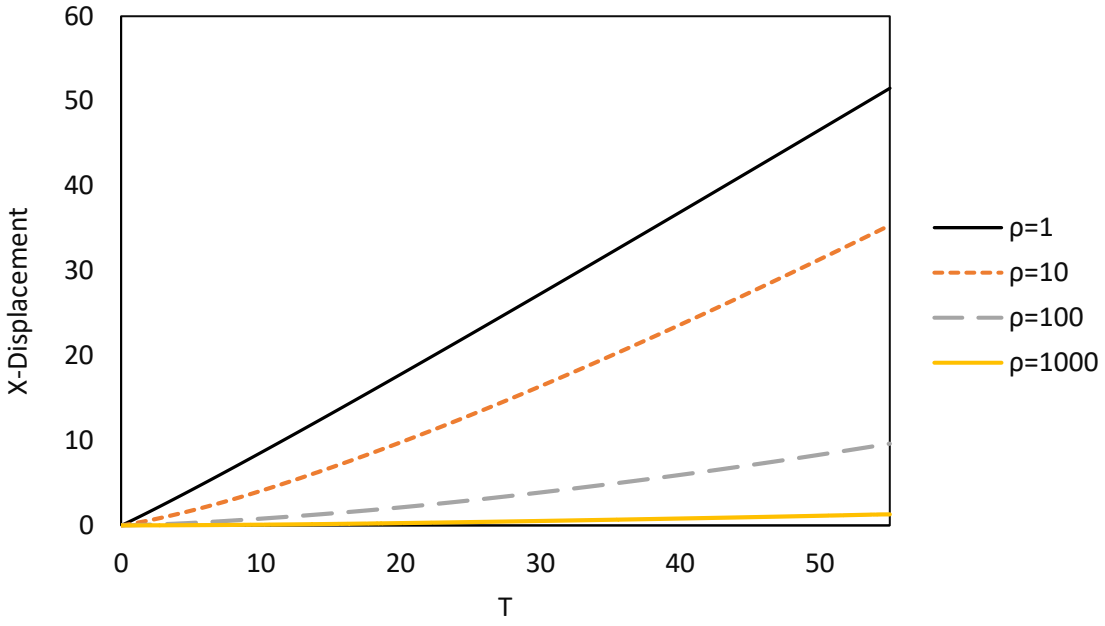

(a)

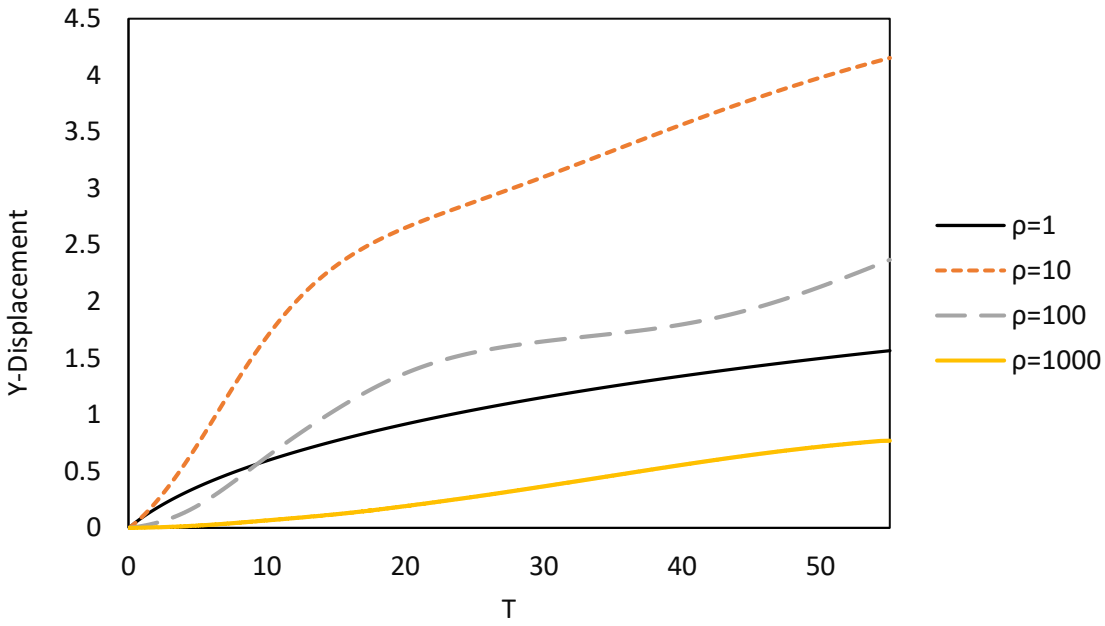

(b)

Figure 4-21- The displacement of an elliptical particle in **(a)** stream-wise **(b)** counter stream-wise direction at $Re_p = 100$ and $\theta_0 = \pi/4$.

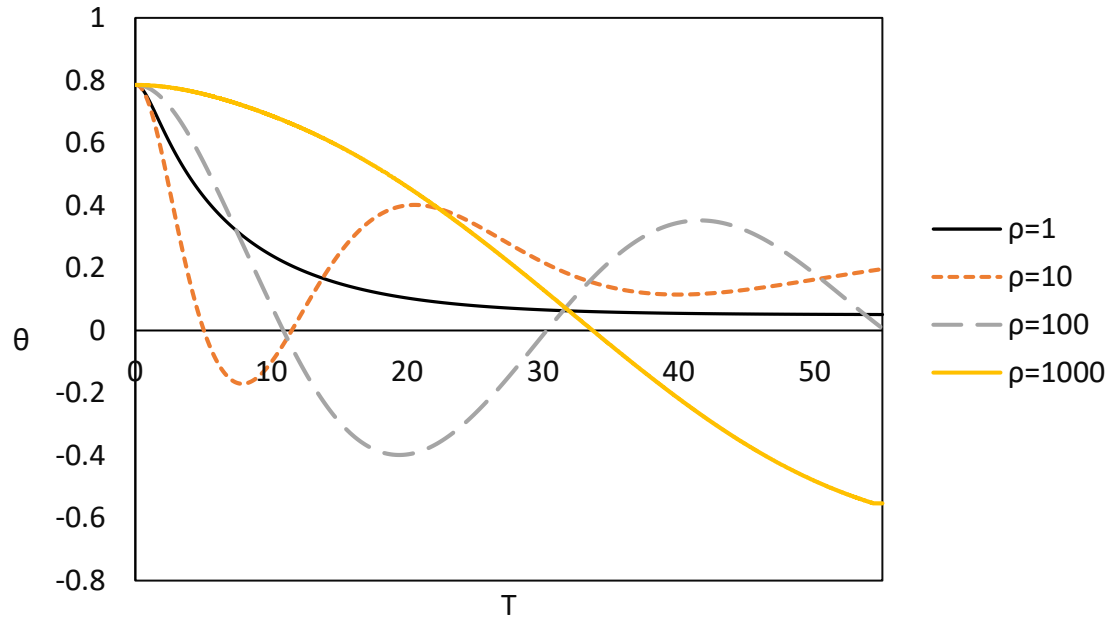

(a)

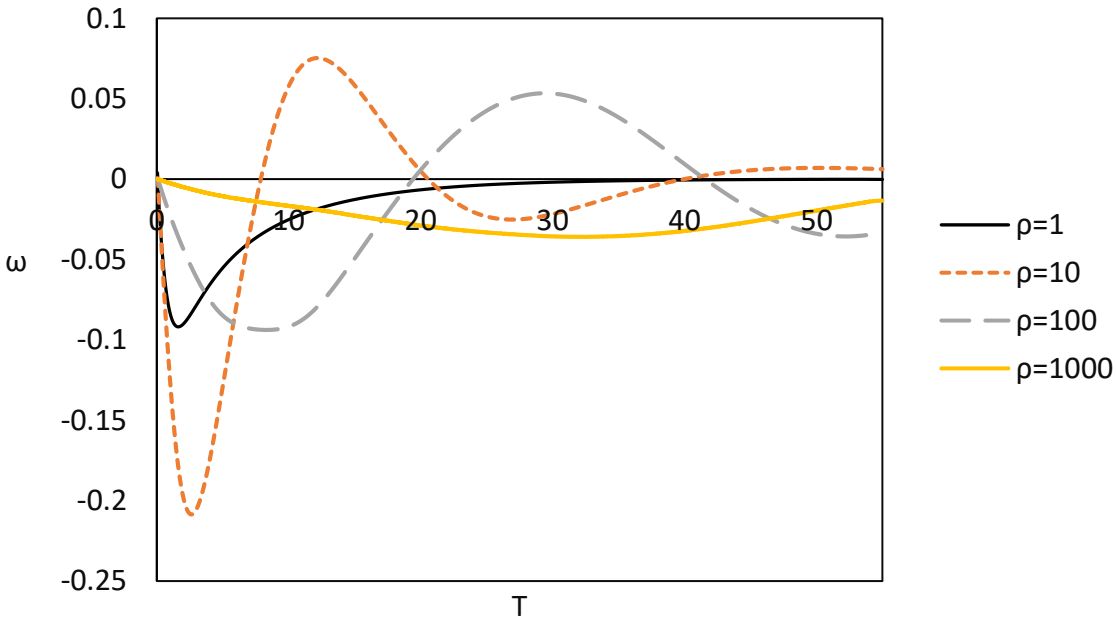

(b)

Figure 4-22- **(a)** Rotation angle and **(b)** angular velocity of an elliptical particle at $Re_p = 100$ and $\theta_0 = \pi/4$.

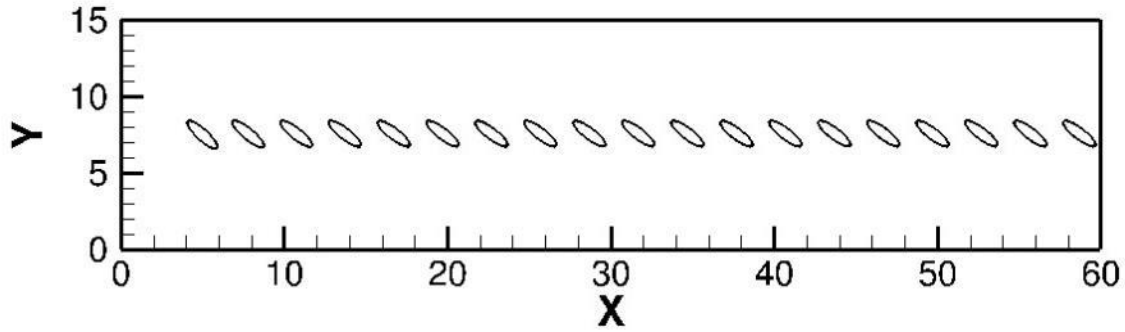

(a)

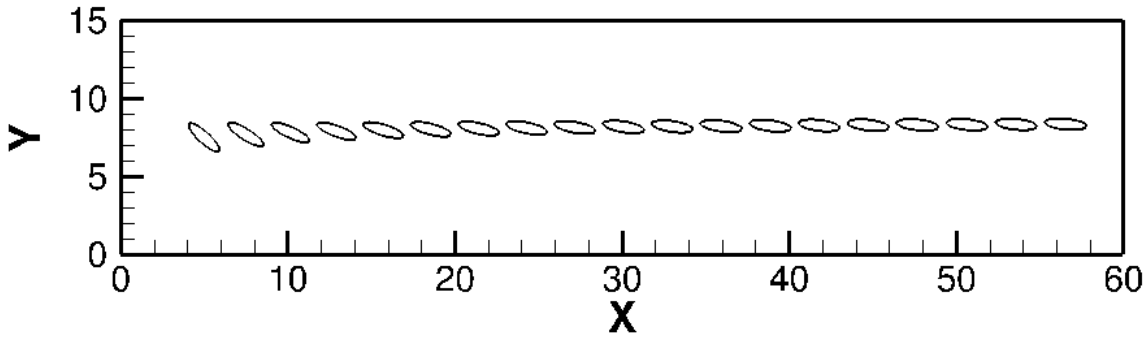

(b)

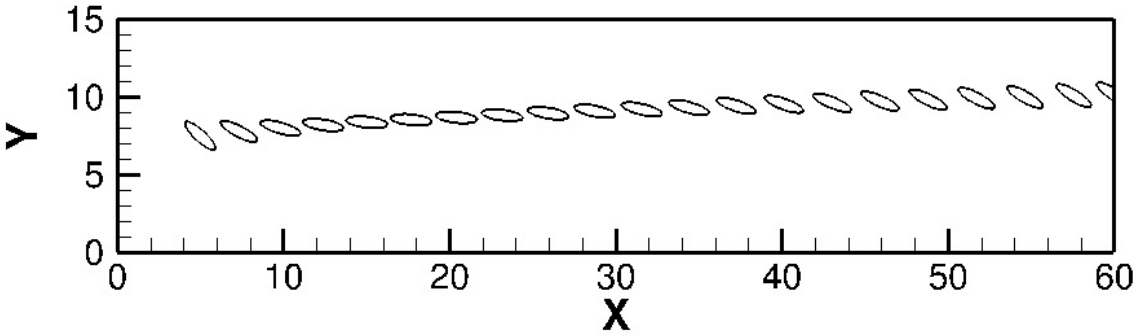

(c)

Figure 4-23- Snapshots of the particle motion for **(a)** $Re_p = 5$, **(b)** $Re_p = 50$ and **(c)** $Re_p = 200$ for $\rho_p = 1$ and $\theta_0 = \pi/4$.

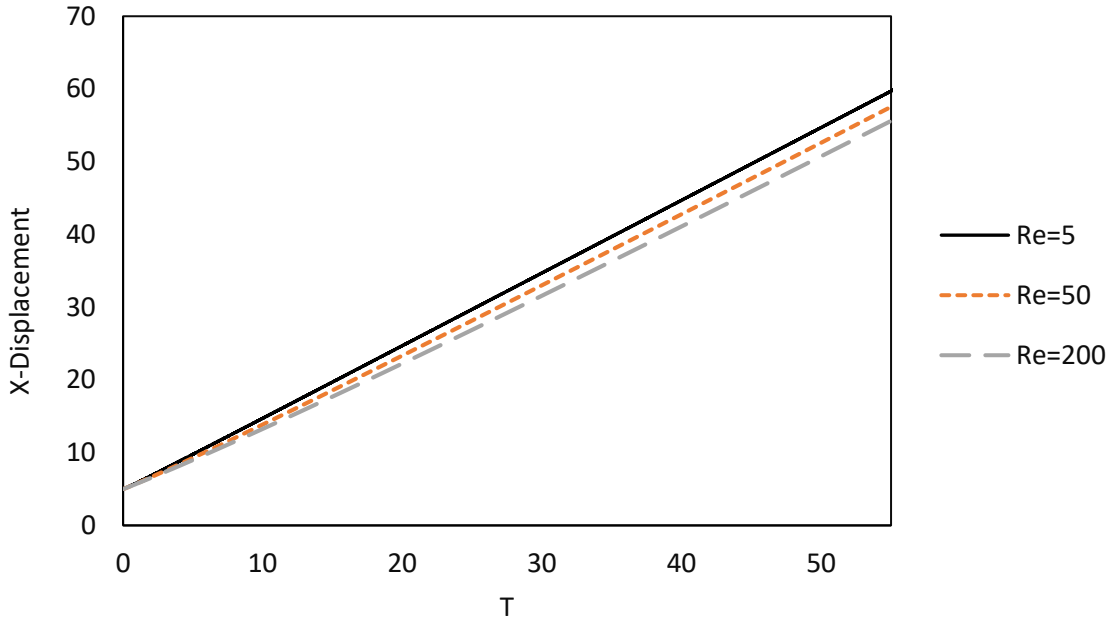

(a)

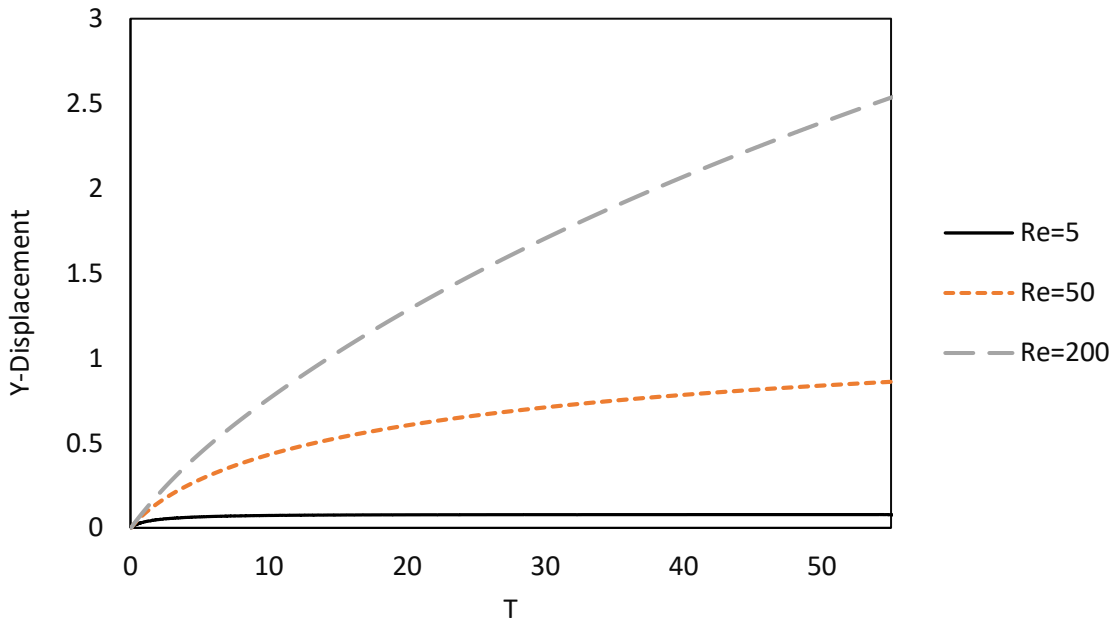

(b)

Figure 4-24- The displacement of an elliptical particle in **(a)** stream-wise **(b)** counter stream-wise direction for $\rho_p = 1.0$ and $\theta_0 = \pi/4$ at different Reynolds number.

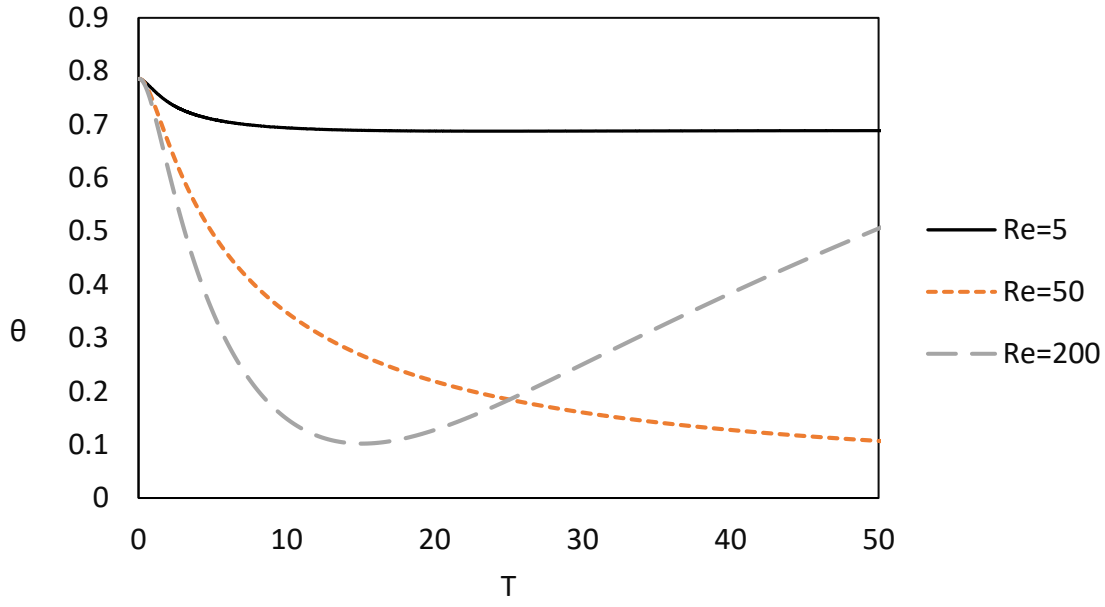

(a)

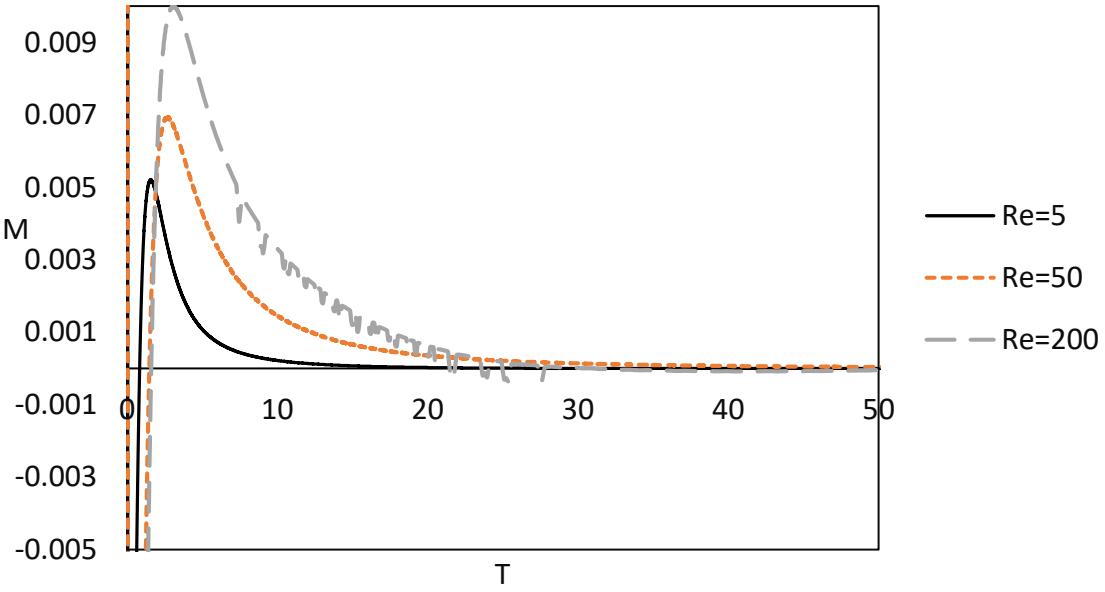

(b)

Figure 4-25- **(a)** Rotation angle and **(b)** angular moment of an elliptical particle for $\rho_p = 1$ and $\theta_0 = \pi/4$ at different Reynolds numbers.

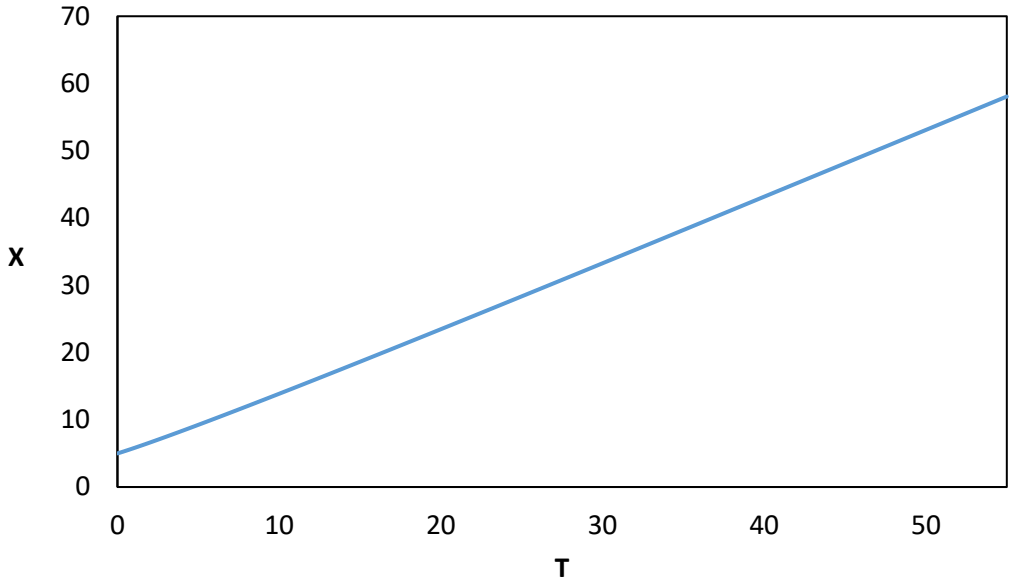

(a)

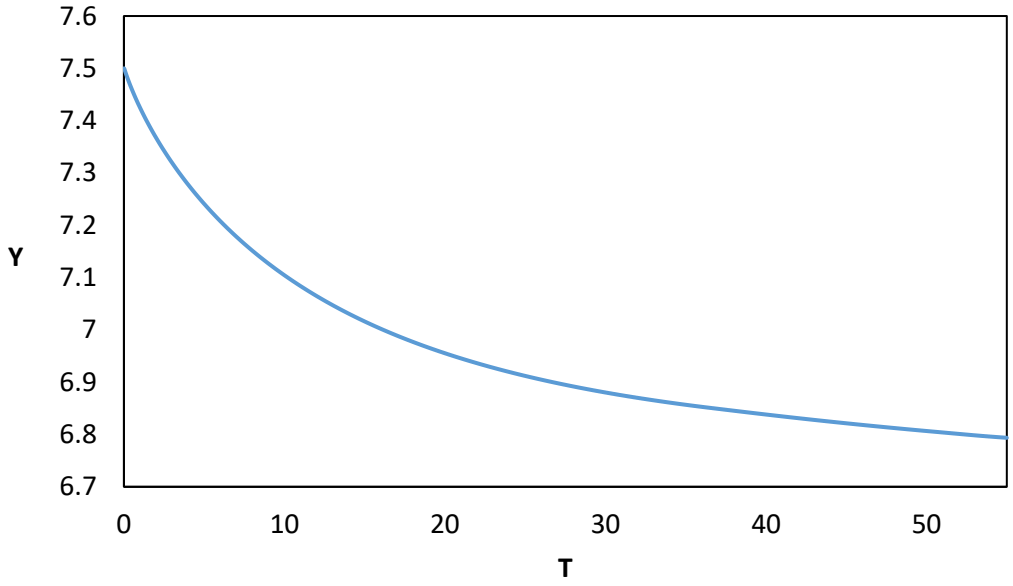

(b)

Figure 4-26- Displacement of an ellipsoidal particle with $\rho_p = 1$, $Re_0 = 100$ and $\theta_0 = (0.0, \pi/4, 0.0)$ in **(a)** stream-wise **(b)** counter stream-wise direction.

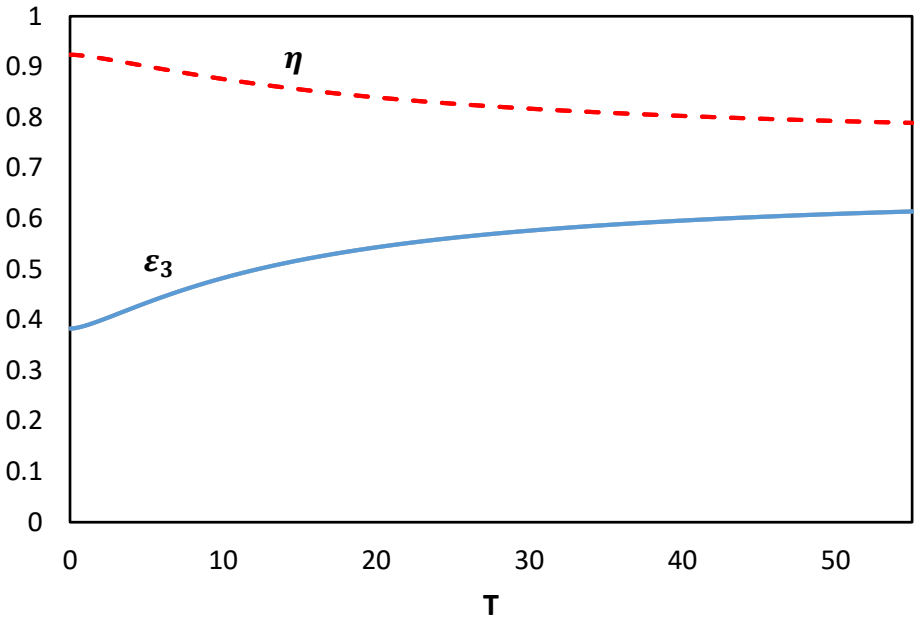

(a)

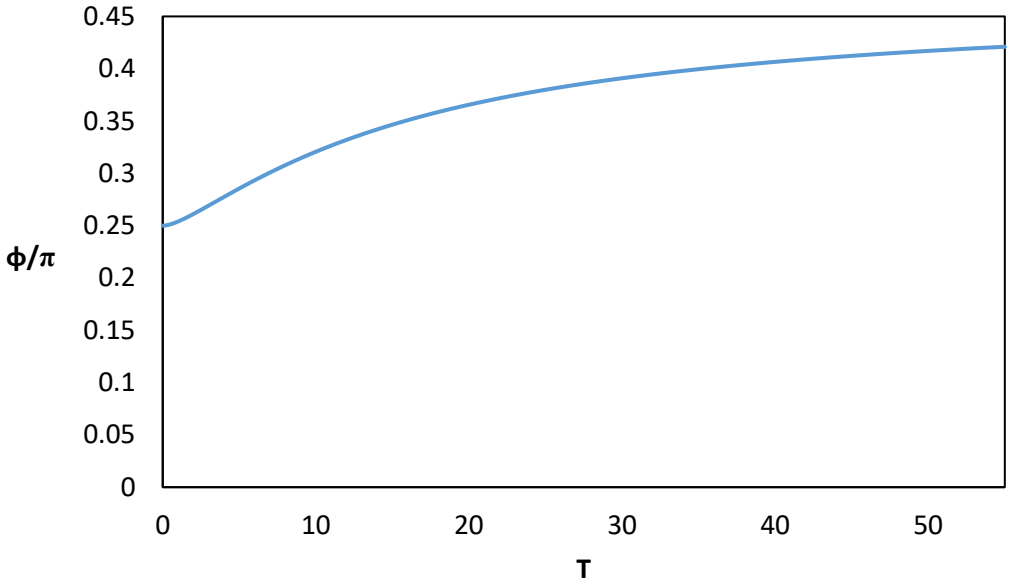

(b)

Figure 4-27- Time history of **(a)** Euler parameters and the **(b)** Euler angle of an ellipsoidal particle with $\rho_p = 1$, $Re_0 = 100$ and $\theta_0 = (0.0, \pi/4, 0.0)$.

Figure 4-28- The schematic of the simplified 2D airfoil shape.

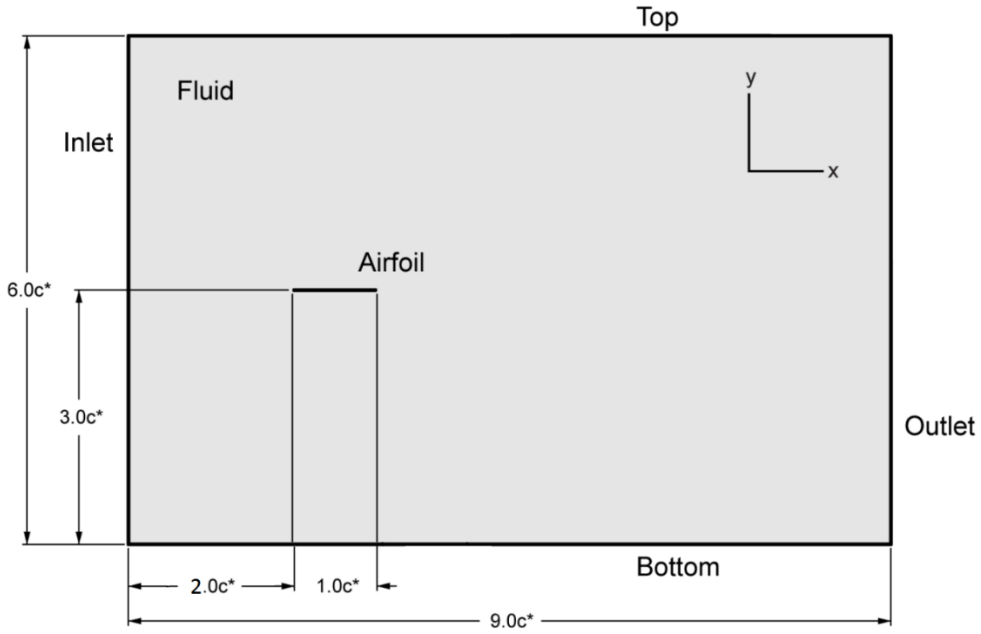

Figure 4-29- A depiction of the simulation domain showing the dimensions, boundaries and the location of the airfoil.

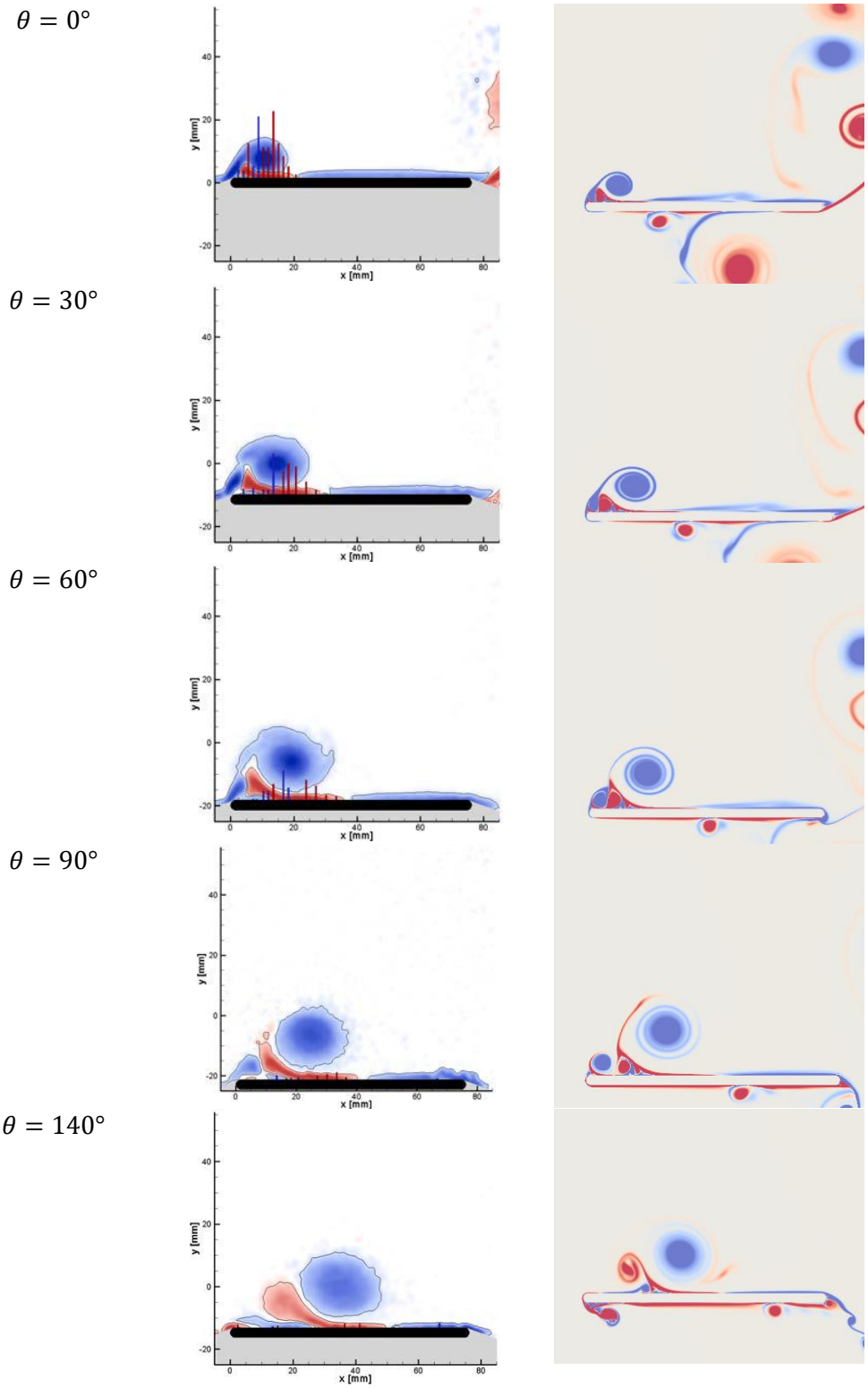

Figure 4-30- Vorticity results for flow over an oscillating flat plate at $Re = 10000$ using SPM for different phases of oscillation.

$\theta = 180°$

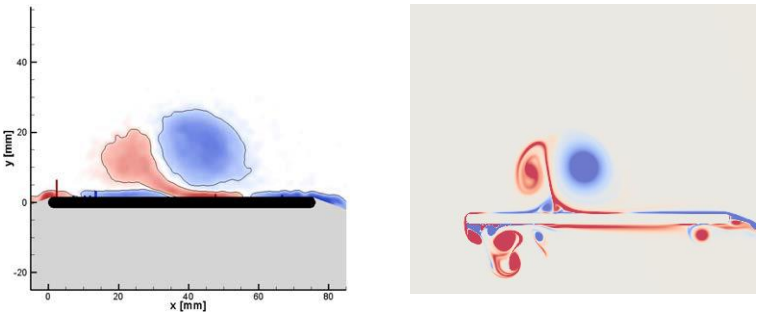

Figure 4-30 (continued)- Vorticity results for flow over an oscillating flat plate at $Re = 10000$ using SPM for different phases of oscillation.

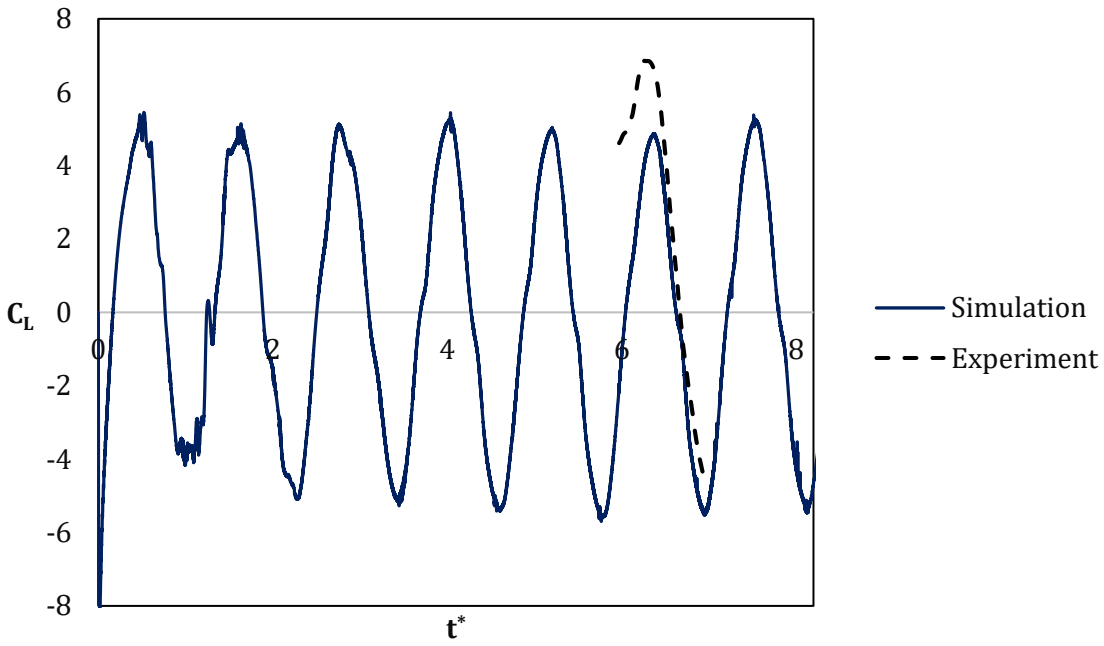

Figure 4-31- History of lift coefficient obtained from the experiment and SPM simulation for flow over an oscillating flat plate at $Re = 10000$.

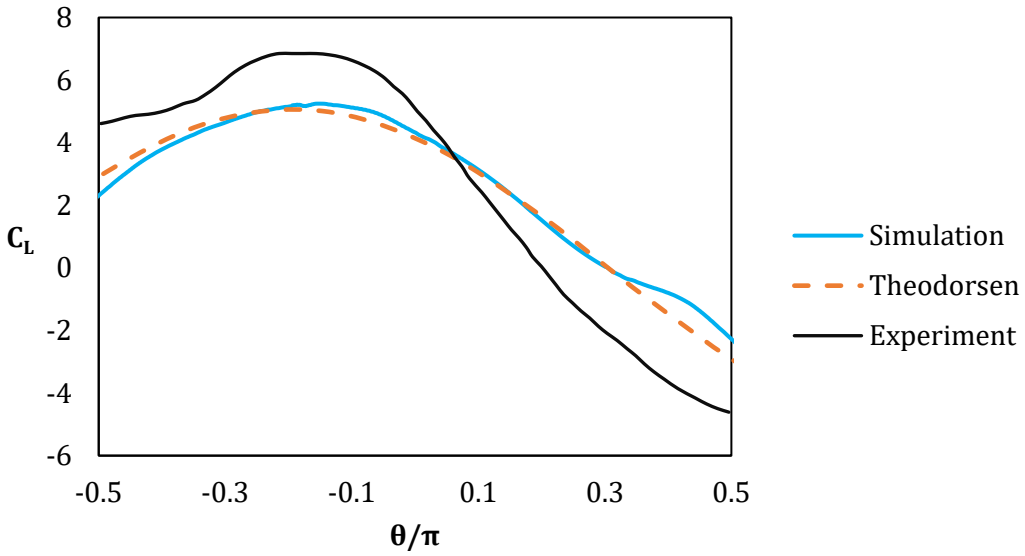

Figure 4-32- Variation of lift coefficient with phase obtained from the experiment, simulation and theory for flow over an oscillating flat plate at $Re = 10000$.

CHAPTER 5

EFFICIENCY OF SMOOTHED PROFILE METHOD

As mentioned before, due to limitations of the current hardware for the simulation flows laden with multitude of finite size particles, it is very important to use an efficient model. The purpose of this chapter is to improve and quantify the efficiency of the smoothed profile method for cases with high added mass effect when use of implicit methods as strongly coupled schemes is inevitable. One improvement of the implicit subiterative scheme is use of Aitken acceleration, as described in chapter (4). The other way is use of the higher order schemes such as 3rd order BDF for the FSI (chapter (4)) which alleviates the requirement for extra number of subiteration.

In this section at first the local mesh refinement (LMR) process for grid management is described first. Then, a new formulation for the SPM is proposed to increase the efficiency of the original SPM formulation. Finally, the efficiency of the two SPM versions are compared to SIM in order to determine the least expensive method.

5.1. Local Mesh Refinement

An octree-based local mesh refinement scheme is used to enhance resolution in flow regions containing vorticity concentrations as described in [248]. In these regions, adaptive mesh refinement is applied using an approach called forest of octrees [249, 250]. It is constructed by decomposing the domain into cells which are either base cells or leaf cells (parent vs. child). The base cells are geometrically uniform grid cells that span the whole computational domain. Wherever needed, each cell is allowed to divide recursively to reach the final fine cell size which is called leaf cells (Figure (5-1)). A pointer-based data structure facilitates handling the grid changes within each time step. The connectivity of the

neighboring cells is integer based and thus topological errors are avoided. All cells other than base cells are modified to satisfy the 1:1 or 2:1 size relation which means no neighboring cell is allowed to be coarser or finer by more than one level.

The grid should evolve to preserve computational efficiency and accuracy through refinements based on the motion of the objects and the flow physics. Three different refinement criteria are considered [251]:

Interface: A refinement at the interface and nearby area in which high velocity gradients typically exist due to solid object boundary conditions. This refinement is made not only at each time step, but also is used at the start of calculations before any flow solution. It is applied to a narrow band around the interface defined by $|\psi| < n\Delta x$ in SIM, where n is the number of base grid cells to which refinement will be applied. For SPM the band has a minimum and maximum indicator function of $\varepsilon < \varphi_i < 1 - \varepsilon$. ε is a case-dependent variable with values very close to zero. For $Re < \mathcal{O}(100)$, where the interface is thick, $\varepsilon = \mathcal{O}(0.01{\sim}0.1)$ and with increase of Reynolds number value, ε decreases.

Velocity gradient: If the related velocity gradients in each cell are more than a certain threshold, the cell is marked to be refined.

Vorticity gradient: If the 2nd-order central finite difference derivative of the velocity is greater than a certain threshold, that cell will be refined.

In each time step the grid is checked for coarsening as well. If none of the specified criteria are satisfied, the grid is coarsened by replacing the eight leaf cells with the immediate parent cell. Then the 2:1 and 1:1 size relation among the neighboring octants is checked and if required refinement is re-applied to satisfy the constraint.

The evolution of the grid for the flow over a cylinder that impulsively starts to move with $Re = 9500$ as described in section 4.2.1 is presented in Figure (5-2). At the start of the simulation the refinement is solely based on the interface (Figure (5-2a)). Then the mesh is refined according to vorticity and vorticity as well. The results are sensitive to the evolution of the adaptively refined grid with time. A

close-up view of the boundary layer is presented in Figures (5-2b) and (5-2c). The mesh is fine enough that the boundary layer is well resolved even for SPM as a diffuse interface approach.

To determine the effect of local mesh refinement on the efficiency of the code, the problem of flow over a stationary sphere at $Re = 3$ is considered. The channel size is $24 \times 10 \times 10$ and a spherical diameter with $D_p = 1.0$ is located at (8.0,5.0,5.0). The minimum grid size, $\Delta x = 0.075$, is reached in two ways: by implementing a uniform grid of size 0.075 or by refining the grid twice from the base grid size of 0.3. The run is performed until $T = 15.0$. The simulations are performed on the Helium cluster of the University of Iowa, on three 8-core nodes (24 cores) with 24 GB of memory.

The results do not show a notable difference on the drag coefficient and the contours, for example, for the uniform grid case $C_D = 11.67953$ but the case with LMR has $C_D = 11.64328$. However, the wall clock time of the simulation is significantly different. When no refinement is used $t_{run} = 1376.12$ CPU sec while with refinement $t_{run} = 11539.55$ CPU sec, which is one order of magnitude longer. This stems from the fact that the number of cells is significantly different in the two approaches. With no refinement, there are 5781832 computational cells, while with refinement the number of cells increases from 274183 at the start of the calculations to 451878 at the end.

5.2. Smoothed Profile Method with One Projection

The original algorithm of smoothed profile method as introduced by Nakayama and Yamamoto [74] has two projections: one projection is for the flow update and the other one is to add the effect of particles to the fluid. Before applying each projection, a Poisson equation should be solved for the pressure field. The Poisson equation solution time is the most expensive operation in the fractional steps method and can consume up to 90% of the computational time as reported in [69]. Consequently, if the SPM can be modified to have only one projection, it probably will lead to a huge saving in computational expenses.

In this section we propose a new SPM formulation with one projection step (SPM1P) as opposed to the original two projection SPM (SPM2P). The difference is how to implement the forcing. In general for the continuous forcing approach, the forcing is added to the Navier Stokes equation as

$$\frac{\partial \boldsymbol{u}}{\partial t} + \boldsymbol{u} \cdot \nabla \boldsymbol{u} = \frac{1}{Re} \nabla^2 u - \nabla p + \boldsymbol{g} + \boldsymbol{f} \tag{5-1}$$

Here $\boldsymbol{f}$ is the forcing, which in SPM2P is applied using the extra projection in the fractional steps method in the subiteration $k+1$. At the first state of SPM2P, the forcing is dropped. Then it is added by defining

$$\boldsymbol{f}^{k+1} = \frac{\varphi_i^k(\boldsymbol{x},t)(\boldsymbol{u}_p^k - \boldsymbol{u}^*)}{\Delta t_{n+1}} \tag{5-2}$$

where $\boldsymbol{u}^*$ in SPM2P is the provisional velocity obtained from the last step of the fractional steps method. Adding forcing to the equations is postponed until all steps of the fractional steps have been completed by ignoring the particles at first.

In the SPM1P formulation, the presence of particles is always considered as the forcing is not dropped in the first step of the fractional steps method. In the discrete formulation of SPM1P, the forcing is substituted in Equation (5-1) directly. Thus, the first step of the fractional steps method in the discrete form becomes:

$$\frac{\alpha \boldsymbol{u}^* + \sum_{j=0}^{J-1} \beta_j \boldsymbol{u}_{n-j}}{\Delta t_{n+1}} + (\boldsymbol{u} \cdot \nabla \boldsymbol{u})_{n+1}^k = \frac{1}{Re} \nabla^2 \boldsymbol{u}^* - \nabla p^k + \frac{\varphi^k(\boldsymbol{x},t)(\boldsymbol{u}_p^k - \boldsymbol{u}^*)}{\Delta t_{n+1}} + \boldsymbol{g} \tag{5-3}$$

By separating the implicit and explicit parts we have:

$$\left[\frac{\alpha}{\Delta t_{n+1}} + \frac{\varphi^k(\boldsymbol{x},t)}{\Delta t_{n+1}} - \frac{1}{Re}\nabla^2\right] \boldsymbol{u}^* = -\frac{\sum_{j=0}^{J-1} \beta_j \boldsymbol{u}_{n-j}}{\Delta t_{n+1}} - (\boldsymbol{u} \cdot \nabla \boldsymbol{u})_{n+1}^k - \nabla p^k + \frac{\varphi^k(\boldsymbol{x},t)\boldsymbol{u}_p^k}{\Delta t_{n+1}} + \boldsymbol{g} \tag{5-4}$$

In the Equation (5-4), the term $\frac{\varphi^k(\boldsymbol{x},t)\boldsymbol{u}_p^k}{\Delta t_{n+1}}$ on the right hand side of the equation uses $\boldsymbol{u}_p^k$ which is the last update from the previous subiteration as there in no calculated value in the present subiteration like SPM2P.

The algorithm of the SPM1P proceeds by calculating the particle variables using $\boldsymbol{u}^*$ and then the rest of the general fractional step method as Equations (3-7) to (3-12). At the end, the particle field velocity is updated. In Figure (5-3), the concise algorithms of SPM1P and SPM2P are shown.

SPM2P uses two different values of particle field velocity in each subiteration. The first time after the flow solution, $\boldsymbol{u}_p^k$ is used for calculating the forcing in order to find the forces on the particle, and the second time it is used in the second projection. On the other hand SPM1P at each subiteration only uses one value of $\boldsymbol{u}_p^k$ from the previous subiteration.

5.3. Efficiency Study of SPM and SIM

To determine the most efficient numerical method of the available frameworks on pELAFINT3D, an efficiency study is conducted by measuring the time required to finish a simulation. SPM1P, SPM2P and SIM are compared for similar cases and identical grids as follows. In all of the cases the refinement criteria is 0.01 for both vorticity and vorticity gradient.

The linear solver uses PETSc library [252] which implements Enhanced BiCGStab(L) (BCGSL) [253] and Geometric-algebraic multigrid (GAMG) [254] algorithms respectively for the Helmholtz and the pressure Poisson equations. The libraries are known to reduce the solution time significantly and are massively scalable in parallel. It is necessary to mention that solution time for the Helmholtz equation is significantly shorter than Poisson equation as the related Helmholtz equation linear solver matrix is diagonally dominated. Here, $\xi_{SPM1P} = 1.3\ \xi_{SPM2P}$ is considered and the accuracy of the relation will be examined. Regarding the efficiency study, various cases were chosen and are represented as following:

5.3.1. Explicit FSI solution of a fixed object

A stationary sphere located at (6.0,5.0,5.0) in a channel with $24.0 \times 10.0 \times 10.0$ dimensions is subject to a uniform flow at all boundaries except the outflow (Figure (5-4a)). The diameter of the particle

is $D_p = 1.0$ and $Re = 50.0$. The base grid line is 0.25 and different levels of local mesh refinement are applied in order to study different grids. The simulation is performed until $T = 20.0$ when the steady condition is achieved. Here $CFL = 0.2$.

First, the flow streamlines and vorticity contours of SPM1P at the cross section of the channel are presented in Figures (5-4b) and (5-4c). The results show the qualitative agreement with the experiment as the extension of wake, the recirculation zone behind the object and the generation of vorticity from the solid boundary is noticeable. Due to diffuse nature of the immersed boundary method, some of the streamlines can enter the particle where the value of φ is close to zero and thus the particle rigidity is not strictly satisfied.

For quantitative comparison, the results of velocity and pressure on the channel's major axis is shown in Figure (5-5). The place of the particle is represented with a box. The SPM and SIM outcomes are different, especially close to the sphere as the diffuse interface of the SPM results in deviation from the practical values of velocity and pressure. Moreover, the pressure spike in the SIM is mollified in SPM. Considering the solution of SIM as the correct result, the results of SPM1P are less accurate in comparison with SPM2P.

The other validation is the grid independency study by considering the drag coefficient as the criterion (Figure (5-6)). Local mesh refinement based on the vorticity and vorticity gradient is employed to achieve the desired minimum grid size. While with grid refinement all methods approach an asymptotic value close to the experiment, the SPM methods are slightly more accurate than SIM. SIM underestimates the value of the drag coefficient but SPM1P and SPM2P overestimate it.

To study the efficiency of the method, wall clock time is used to measure the time required to achieve the simulation. The running times are based on the simulations which were performed on the Helium cluster of the University of Iowa, on three 8-core nodes (total number of 24 cores) with 24 GB of memory. As shown in Figure (5-7), even though at coarse grids the running time of all methods are almost the same, with refinement of the grid, the differences among different methods becomes significant. SIM

is the fastest method for the simulation of flow over fixed boundaries. SPM1P is faster than SPM2P for these cases as it has only one pressure Poisson equation. However, SPM1P is slower than SIM even though SPM1P does not need level sets in order to generate the object and does not require extra interpolations like SIM. The longer running time for SPM1P stems from the fact that the resulted linear solver matrix from SIM is better conditioned in comparison with SPM1P.

5.3.2. Implicit solver of the moving objects with low added mass effect

When the density of the solid is significantly greater than the fluid, the added mass effect is low. In this section motion of a disk (2D circular cylinder) with $\rho_p = 20.0$ in a horizontal channel is considered to neglect the high added mass effect. The particle with unit diameter starts moving in a channel 24×12 at $Re = 10$. We use an implicit solver for this problem. For a fair comparison, the simulation is performed until $T = 28.0$ when all of the models show the particle is still in the channel.

Due to high density of the particle, the added mass effect is not significant. We use a fully implicit solver for this problem. For a fair comparison, the simulation is performed until $T = 28.0$ when all of the models show the particle is still in the channel. Setting $CFL = 0.3$, two to four levels of grid refinement are applied on the base grid sizes of 0.2, 0.25 and 0.3. The results are presented in Figure (5-7) and show that even though in coarse grids the speed of all methods are comparable, with grid refinement SPM1P becomes the fastest method in comparison to the other two methods. Even SPM2P is also faster than SIM. Consequently, for the fully coupled simulation of moving objects, SPM is faster than SIM. This is because the number of subiterations required to reach the convergence in each subiteration is different among the methods. For example, at $\Delta x = 0.025$ the average number of subiterations are 7.72, 7.01 and 8.16 for SPM1P, SPM2P and SIM, respectively.

5.3.3. Implicit solver of the moving objects with high added mass effect

When the density of the solid object is at the same order as the fluid or lower, the added mass effect becomes important. A standard case of Glowinski [124] for a dropping disk is considered to study a case with high added mass affect. A cylindrical particle (2D disk) with a density close to fluid i.e., $\rho_p = 1.5$ is dropped in a stationary fluid and moves under gravity. The domain is a 2×6 2D channel and the initial location of the particle with $D_p = 0.25$ is (1.0,4.0). The kinematic viscosity of the fluid is $\nu = 0.01$ and the results for different methods are shown in Figure (5-8).

The SPM1P and SPM2P results are very close to Glowinski's [124] and are better than the SIM. SIM underestimates the value of the drag coefficient leading to higher velocities. Accordingly, the particle reaches the end of the channel earlier. For this reason the efficiency study is performed until T=0.35 when all models show the particle has not reached the bottom wall yet (Figure (5-9a)). SIM is the most expensive method in this case with high added mass effects, as the running time is significantly longer than SPM1P and SPM2P. This is because the average number of subiterations required to reach the converged solution is notably higher in SIM. The strongly coupled SIM converges more slowly than SPMs, as shown in Figure (5-9b). It is clear that the number of required subiterations has a key role in the running time of each method. SPM1P and SPM2P have almost the same average number of subiterations. Hence, their running times are all of the same order. Unlike the explicit algorithm, SPM1P is slightly faster than SPM2P even though the number of subiterations is greater for SPM1P. Unlike SPM2P, SPM1P has only one Poisson equation which leads to faster solution due to having only one Poisson equation.

5.4. Conclusions

Local mesh refinement was implemented in the pELAFINT3D based on the interface, vorticity and vorticity gradient and shown to improve the efficiency of the simulation significantly. An efficiency study has been performed for different types of FSI problems using smoothed profile method (SPM) and

sharp interface method (SIM). At first the original formulation of SPM with two pressure Poisson equations (SPM2P) is modified by revising the formulation to an algorithm with only one pressure Poisson equation (SPM1P). This novel formulation is validated for several cases and is used for comparison alongside SPM2P and SIM for different types of flows.

Study of flow over a fixed object reveals that if no subiteration is used, namely for a loosely coupled FSI, SIM becomes the fastest method. After SIM, SIPM1P is faster than SPM2P showing that the new formulation actually has made the SPM faster. Even though SPM1P solves only for one Poisson equation, the resulted linear solver matrix is stiffer in comparison with SIM. Therefore, SPM1P running time is not shorter than SIM when no subiteration is applied.

When a subiterative scheme is applied, both SPMs become faster than SIM in cases with and without high added mass effect. The number of subiterations has a key role in efficiency of each method. SIM with a meaningful difference in the convergence rate has the highest number of subiterations, and consequently is the least efficient method. SPM1P for implicit cases is the fastest method and after it SPM2P is faster than SIM. These conditions are still valid for problems with high added mass effect. In overall, SPM is faster when a strongly coupled scheme is implemented and SIM is faster in loosely coupled schemes. SPM1P is more efficient and less accurate that SPM2P.

If a flow contains more than one particle, some other parameters become important such as data management of large ensembles of the particles and the particle-particle collision. We will discuss the perquisites for the simulation of flows containing several particles in the next chapter and test these parameters with some particle laden flows.

FIGURES

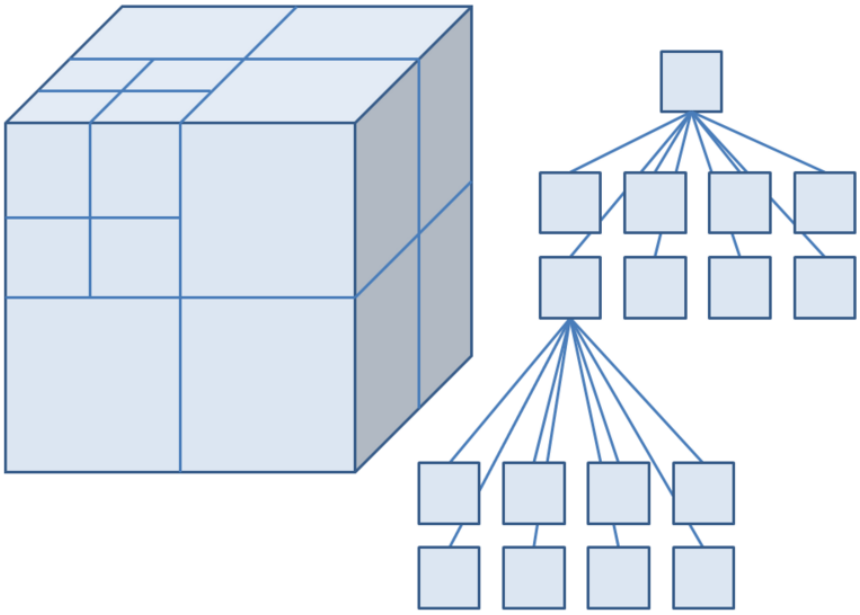

Figure 5-1- A schematic of an octree subdivision in space and the base cell and leaf cell structure after the refinement [255].

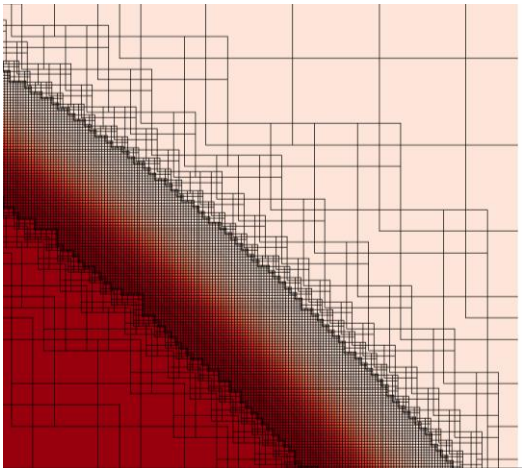

(a)

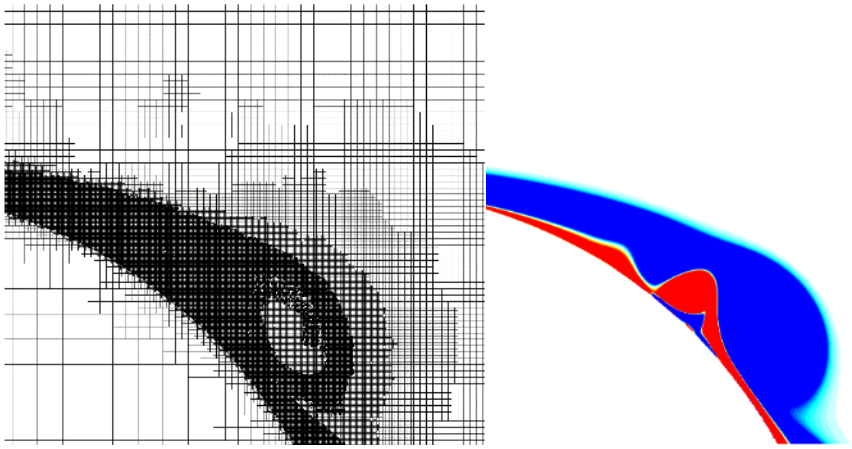

(b)

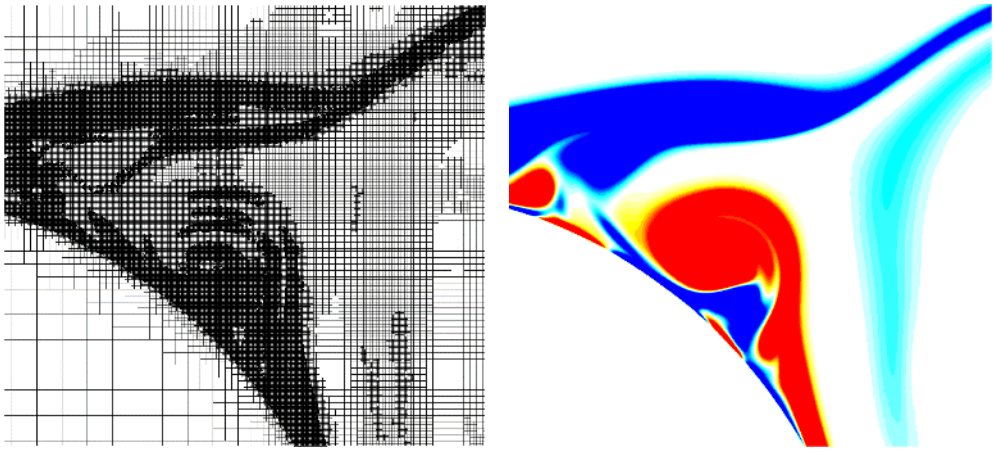

(c)

Figure 5-2- Evolution of the grid for impulsively started flow over cylinder using SPM at **(a)** $T = 0.0$ (The interface refinement at the start of the simulation). **(b)** $T = 2.0$ and **(c)** $T = 6.0$ for $Re = 9500$. **(Left)** grid **(Right)** vorticity contours using SPM.

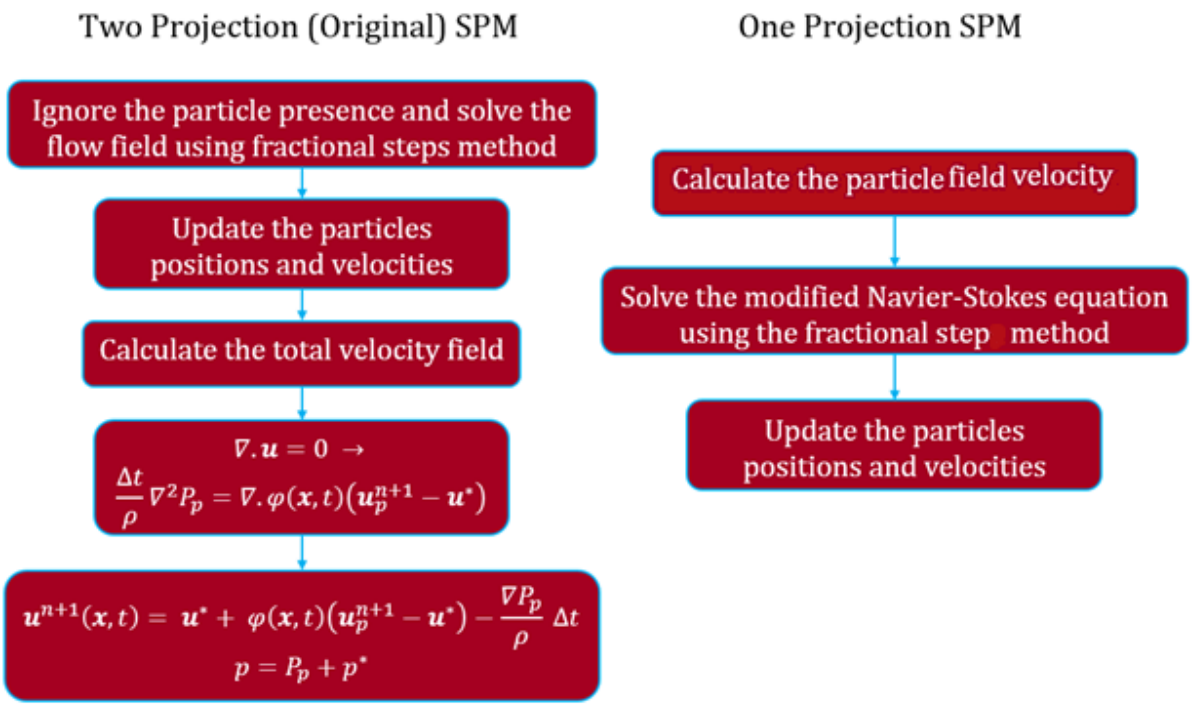

(a) **(b)**

Figure 5-3- A brief depiction of two versions of smoothed profile method. **(a)** SPM2P or the original SPM formulation with two projection and **(b)** SPM1P the modified SPM formulation with only one projection.

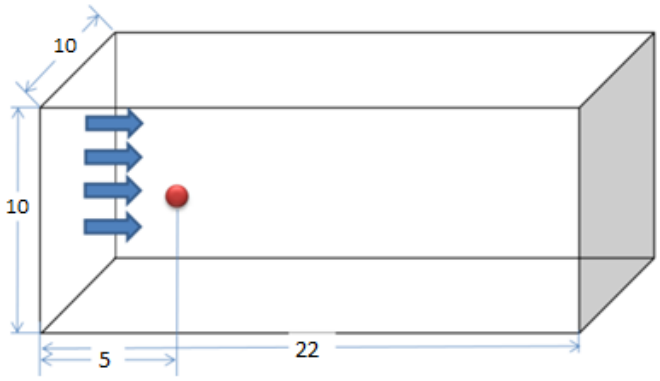

(a)

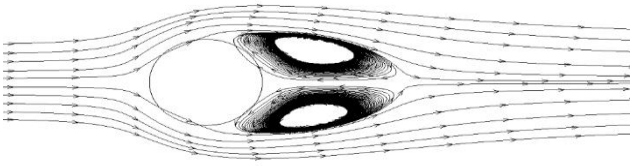

(b)

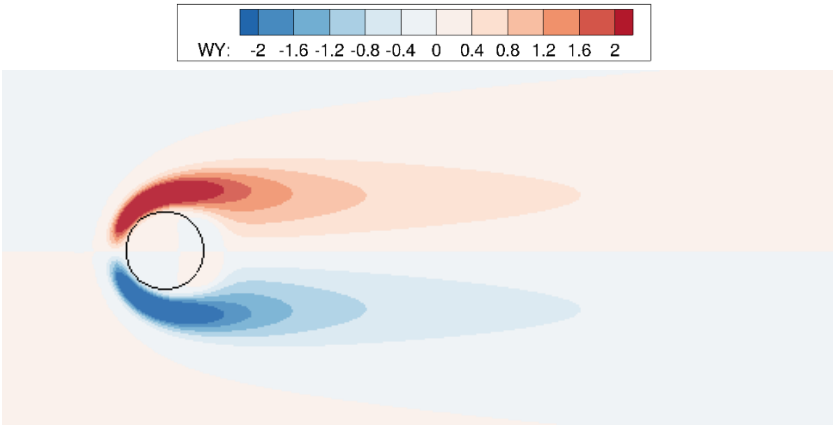

(c)

Figure 5-4- Flow over a sphere at Re = 50. **(a)** The simulation domain. **(b)** and **(c)** The flow streamlines and vorticity contours on the cross section of the flow at the middle of the 3D channel.

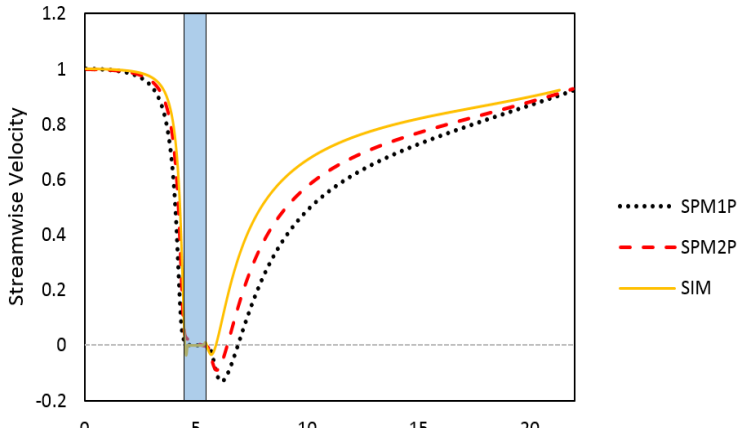

(a)

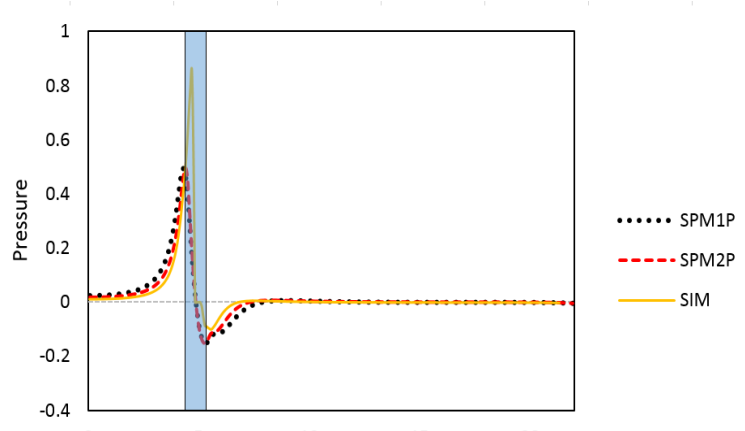

(b)

Figure 5-5- Variation of **(a)** Streamwise velocity and **(b)** Pressure on the centerline of the channel for flow over sphere at Re = 50.

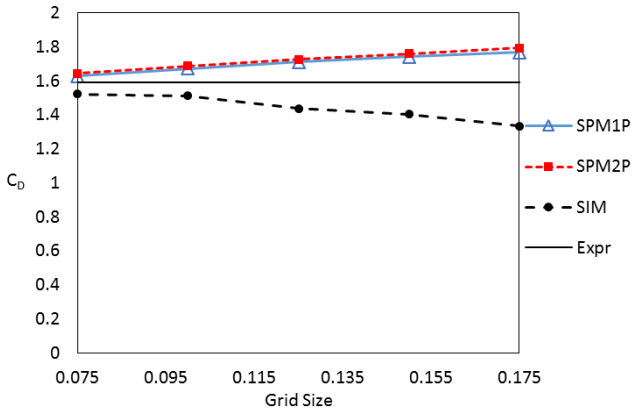

(a)

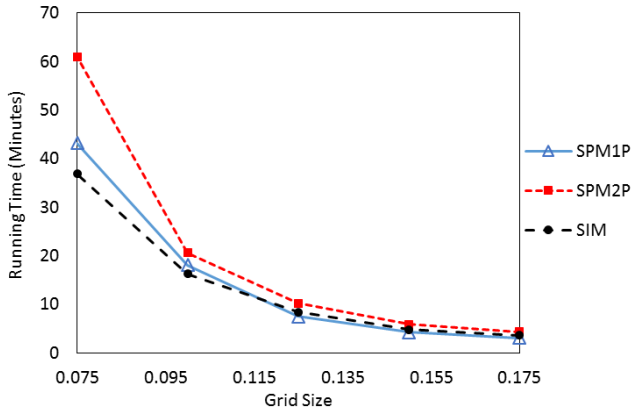

(b)

Figure 5-6- Simulation of flow over a stationary sphere at $Re = 50.0$. **(a)** The drag coefficient and **(b)** the running time.

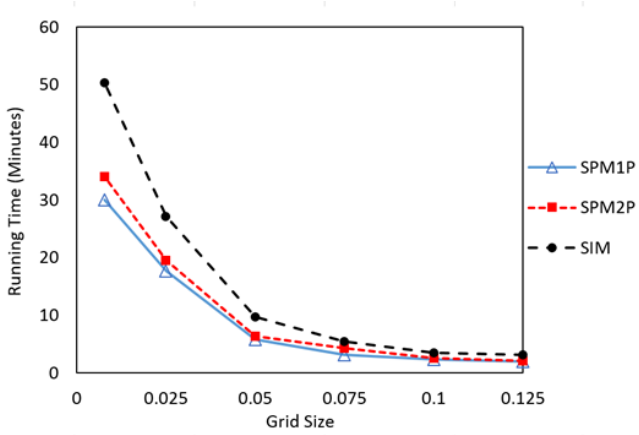

Figure 5-7- The running time for the simulation of a moving cylinder with $\rho_p = 20.0$ at $Re = 10$.

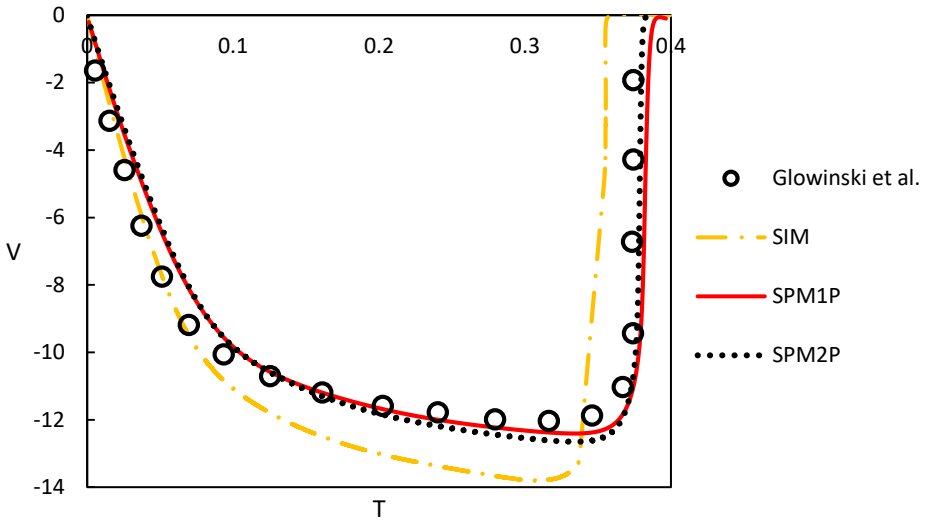

(a)

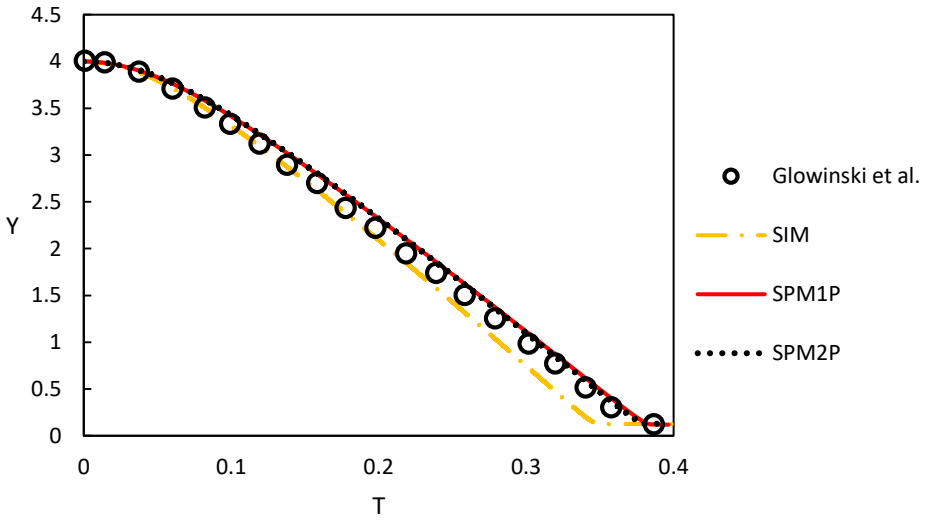

(b)

Figure 5-8- Time history of **(a)** vertical velocity and **(b)** vertical position of a falling disk with $\rho_s/\rho_f = 1.5$ from SIM, SPM1P, SPM2P and comparison with Glowinski et al.

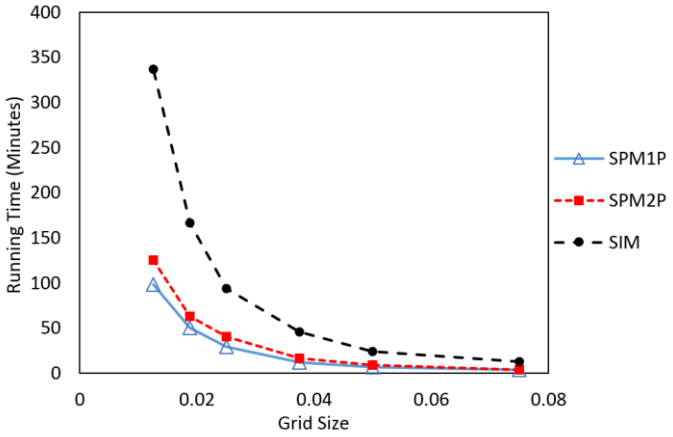

(a)

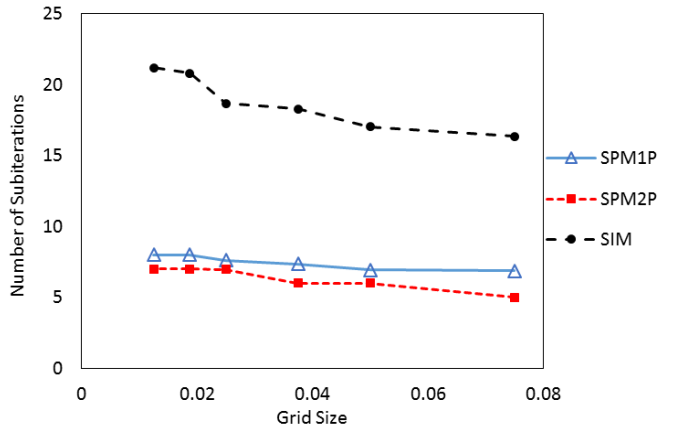

(b)

Figure 5-9- **(a)** Running time and **(b)** number of subiteration for a falling disk with $\rho_s/\rho_f = 1.5$ from SIM, SPM1P and SPM2P.

CHAPTER 6

PARTICLE COLLISION

When the number of particles is more than one, new effective parameters can change the flow physics. Particle-particle interaction and sometimes particle-wall interaction become important in flows containing large numbers of particle suspensions. This requires particle collision capturing methods in particle-laden flows. These flows appear in both nature and industry such as fog drops, blood, sediments, pharmaceutical processing, and fuel injection systems. While numerical study of these flows is challenging due to fluid-structure interaction of several particles with the carrier fluid, the interaction of particles with each other and with the enclosing surfaces adds to the complexity of the simulations.

When two solid objects are very close in a Newtonian fluid, they cannot have physical contact if the surfaces are smooth [256]. For an actual collision between smooth surfaces, the fluid film between the two solids should rupture which is not possible in finite time within the limits of Navier-Stokes equations. In other word, based on classical lubrication theory, when the distance between two surface approaches zero, the lubrication force becomes singular. However, when surfaces are rough, the bumps of different objects can reach and van der Waals forces attract them [257]. The surface roughness related to the lipid bi-layer, the RBC membrane, is $\mathcal{O}(1nm)$ which is significantly lower than the cell size $\mathcal{O}(1\mu m)$. Therefore, in this research surface roughness is ignored and the lubrication forces are valid.

The straightforward approach for the numerical simulation of the collision is refinement of grid when the gap size is decreasing. In addition, the time step size should decrease to keep the CFL number less than one. The consequence is a huge computational cost as the gap shrikes to a size several orders of magnitude than the original size [93]. It is evident that the calculation is very expensive and sometimes

impossible to implement. Therefore, fluid-structure interaction study of a flow containing multitude of particles requires models capable of capturing the effect of particles of each individual particle.

The literatures studying various collision models span very diverse approaches [258-262] and includes different approaches. One approach is the two fluid model which by considering the particles as a continuous phase requires empirical relations to couple the two phases [263]. The uncertainty of the empirical data related to most of the problems and also the non-physical nature of the modeling can result in high errors in this approach.

The other approach, the Discrete Element Method (DEM) or Granular Dynamic (GD), directly calculates the motion of each individual particle [264] based on more realistic assumptions. However, when calculating the motion of the particles, the collisions become important as no material overlapping can happen due to mass conservation law. A collision can be among two or more particles at the same time or between a particle and a wall. The current collision models mostly include definition of case dependent parameters which can affect the results. Moreover, the modeling becomes challenging when the particles have non-spherical shapes. This includes particles with arbitrary shapes such as sediments and dust storms or particles with non-spherical standard shapes such as biconcave shape of red blood cells, or the cylindrical shape of fibers. Thus, this study presents a simplified collision model for handling the contact of spherical and non-spherical particles within large clusters. It shows an efficient and robust model with parameters easily obtainable from the flow and particle motion.

DEM collision capturing methods are categorized in two groups: hard sphere and soft sphere models. The hard sphere model (HSM) is a solid-body collision model which is basically a particle binary and quasi instantaneous model that ignores carrier fluid at the time of collision. It means the particles velocities change instantly and without any dependency on time. HSM solves the integration format of the particles i.e., Newtonian motion equations used as conservation laws to determine post collision translational and rotational velocities [265]. A soft sphere model (SSM) instead is based on differential format of particle motion and conservation laws as the particles' velocities and positions are updated in

time [266, 267]. Since SSM needs to track collision phenomenon at smaller length scales, time step size should be reduced dramatically. However, it is possible to reduce the material stiffness to avoid extra small time scales [268]. When the solid particles undergo plastic deformation, Elastic-plastic collision models are used [269, 270]. In the following we determine the important parameters in detail for the the wet collision based on SSM. No plastic deformation happens in this study.

6.1. Collision Forces

The simplest implementation of SSM obtains the collision forces by defining a repulsive potential for each particle. Glowinski et al [132] and also Wan & Turek [271] suggested that the collision force between two particles is proportional to the square of the amount of overlapping. The overlapping is a parameter representing how much the two particles are neighboring. A similar approach uses a Lenard-Jones type potential to define a potential [74]. For example, Nakayama and Yamamoto [74], used a Lenard-Jones soft sphere potential for each particle as

$$E = 0.4 \sum_{i=1}^{N-1} \sum_{j=i+1}^{N-1} \left[\left(\frac{2a}{d_{ij}} \right)^{12} - \left(\frac{2a}{d_{ij}} \right)^{6} \right] \theta \left(2^{\frac{7}{6}} a - d_{ij} \right) \quad (6\text{-}1)$$

where $\theta(\dots)$ is the step function and d_{ij} is the distance between two particles i and j which both have the diameter a. The force on particle i is obtained from $F = \frac{\partial E}{\partial d_{ij}}$.

Glowinski et al [132] suggested a repulsive by defining a force range. When two particles i and j with radii R_i and R_j are close enough, an explicit force is added:

$$F^p = \frac{1}{\epsilon_p} (\boldsymbol{x}_i - \boldsymbol{x}_j) \left(R_i + R_j + \rho - d_{ij} \right)^2 \quad (6\text{-}2)$$

In the above equation, ρ is the force range above which no repulsion happens. $\boldsymbol{x}_i$ and $\boldsymbol{x}_j$ are the particles centers and ϵ_p is the minimum stiffness parameter. The closer the particles, the more repulsion force will happen. The repulsion force for the particle-wall interaction is

$$F^w = \frac{1}{\epsilon_w} (\boldsymbol{x}_i - \boldsymbol{x}_{ij}) \left(2R_i + \rho - d_{ij} \right)^2 \quad (6\text{-}3)$$

In Equation (6-3), subscript j stands for an imaginary particle with a similar size located on the other side of the wall. The center to center line of the particles is perpendicular to the wall surface while the imaginary particle touches the wall surface.

Even though the method is simple to implement, there exists several problems with it. Firstly, lack of physical reasoning for implementing the model can lead to unrealistic results [272]. While the method can prevent particles' overlapping, it can enforce extra repulsion leading to unphysical results. Therefore, the accuracy of the results highly hinges on choosing case dependent parameters [91, 134, 273]. Secondly, the method ignores energy dissipation due to material damping [272]. Thirdly, definition of potential for non-spherical shape particles can be difficult and limited to classical shapes such as ellipsoids [274].

A common treatment in the particulate systems relies on modeling forces using some form of spring and potentially a type of damper. Several methods are suggested to find the spring system characteristics. One of the common methods defines the coefficients based on the particle's solid structure characteristics. For the spherical particles Hertz theory defines the spring force as $k_{Hz}\delta^{3/2}$ where δ is the displacement [275-277]. k_{Hz} is the Hertz spring constant obtained from the two particles material and geometrical properties. The Hertz theory as an elastic collision model agrees well with the experiments in dry collisions [275, 278, 279] but in a wet collision it neglects the viscous dissipation of energy. A dashpot can enforce the dissipation of energy during the collision to coincide the physical behavior. The damping coefficient of the dashpot is suggested to be proportional to some exponent of displacement [280, 281]. Even though the theory easily includes the solid object characteristics in the calculations, the implementation of the method to model wet collision can be inefficient even for spherical particles. This is because the time scales related to the actual solid contact mechanics is usually several orders of magnitude smaller than the fluid due to very high spring coefficient values [268].

Decrease of spring coefficient avoids problem of time scale disparities s as it extends the collision time to a scale comparable to the flow scale. Consequently, the problem changes from high impulse

collision in the short time to low impulse one in a long time while the momentum exchange is preserved. This preservation is very helpful as it does not change the problem in the large time scale in addition to the fact that the problem becomes practically solvable. However, the question becomes how to set the spring and dashpot variables to reach the actual physical behavior.

Kempe and Fröhlich [272] proposed the adaptive collision model (ACM) by stretching the collision time to ten times of the flow solver time step size. The model inspired by a Hertz-like force definition for the spring, represents a second order ODE as the spring and dashpot system. Using each particle's rebound velocity from the solid dry coefficient of restitution, the ODE coefficients were obtained from an iterative solver. When the gap between two particles is small the viscous forces become significant. Therefore, the lubrication model of Ladd [282] empowered the model to account for the non-negligible viscous dissipation. By proposing an explicit formulation to find the ODE coefficient instead of an iterative approach, Ray et al [261] simplified the implementation of the ACM. Both approaches ignore the hydrodynamic forces on the particles when the particle is very close to the wall. To avoid the unphysical behaviors during the enduring contacts, Biegert et al [283] limited to neglecting of hydrodynamic forces by including a critical Stokes number below which the hydrodynamic forces should not be ignored.

The idea of preservation of momentum exchange not only can help to increase the minimum time scale, it can also justify the implementation of a linear spring. When the velocity of the bounced particle is important and not the way this velocity is achieved, a linear ODE as harmonic damped oscillator can also represent the collision. This concept inspired Izard et al. [284] and Costa et al. [285] and to use the idea of adjusting the spring and dashpot based on the contact duration. As suggested by Costa et al. [285] obtaining the contact during from the flow time scale softens the collision and saves the computational cost significantly. A modified lubrication force can enforce the dissipation [285]. Applying the dissipation through the lubrication as the way used in [272, 284, 285] forces can be problematic in two ways. Firstly, the implementation of lubrication forces requires resolved grid at the places near the contact place which

reduces the efficiency of the simulation. Secondly, as shown in [283] the dissipation can depend on the lubrication gap thickness. Biegert et al. [283] could decrease the dependency on the lubrication gap by using higher order sub-stepping for the particle motion. To avoid the complications related to implementation of a lubrication model, this chapter offers two collision model with simplified definition of collision parameters to make the study of collision physics easier. With no implementation of lubrication forces, the new model leads to having robust results with no case dependent parameters.

6.2. Collision of Non-Spherical Particles

Study of particle collision becomes more challenging when the particles' shapes are not spherical. Difficulties with studying these particles collision stems from the fact that finding the related collision parameters i.e. contact point and the collision forces is a tedious task. While for the spherical particles the contact point is located on the intersection of the particles' interface and the center to center connecting line, for non-spherical objects the contact point location depends also on the orientation and the more complex geometry. Moreover, the collision forces depend on the amount of overlapping and reduced radius of curvature which is also more difficult to find when the particles do not have a spherical shape.

When the particles have a classical shape e.g. ellipsoids and polygons, the geometrical features help finding the contact/collision point. There are several ways to find the collision point of the non-spherical particles which mostly require an iterative approach to find the contact point [286-293]. For ellipsoids, the collision point can be defined as the midpoint of the intersection volume [294] which can lead to ill conditioned quadratic formulations [287]. Therefore, Lin and Ng [286, 295] considered the midpoints of the line connecting the surface of the two particles as the collision point. The connection line can connect the deepest part of each particle into the other one's similar point [295, 296] or can be the points that the common normals of the two particles are located [286]. The collision point of the ellipsoids also could be obtained from the closest distance between two particles as described by [288,

297]. The method as an iterative approach sets up two balls inside each particle and tangent to the surface and updates the positions of the balls by sliding the balls to the intersection of the ellipsoids and the line connecting the ball centers. For the polygonal particles, Nezami et al. [289] used the common plane [290] between the particles to detect the collision point. Other contact point detection methods include other shapes e.g. polyhedrons [291, 292], superquadrics and hyperquadrics [293, 298], polar shapes [299] as well as "potential particles" [300, 301]. A potential particle forms the particles by defining a potential field which can morph from a sphere to cube. The resulted shape can have a shape of sphere, cube or a transition of sphere to cube. The method was extended to other classical shapes such as tetrahedral-shaped, prism and rounded tetrahedral-shapes.

For arbitrary particles, no special feature of the geometry can help to find the collision point. However, it is common to compose the particle from small geometric elements to form the particle. Thus, the original particle with arbitrary shape is a composite of the elements that are glued. The geometric elements can be spheres [302-309], cylinders [310] , ellipsoids [311] or a combination of several shapes [312]. The problem with combining different shapes is that the accuracy depends on the number of used elements. While fewer number of elements are easier and faster to form the final clumped geometry, the resulted surface will be rough and inaccurate and multiple collision points might be captured. To avoid this problem, recently use of "spherosimplices" for complex objects has gained popularity. Spherosimplices constructs the shapes by moving a cylinder or sphere over a frame named skeleton [313-317]. The method is shown to be faster than the composed particle method. However, the generation of the shape becomes complicated for the complex objects especially in 3D as it depends on how accurate the shape of skeleton is set up. Moreover, the sharp edges will be smoothed because of using a cylinder or sphere to generate a shape. (Virtual space method)

The other way to find the contact point of the arbitrary shape particles is to classify the simulation grid points into fluid and each individual particle. Wachs [127] implemented this concept by using a spatial algorithm to define the grid points in the context of fictitious domain method [318]. We believe

classification of grid point is the most general method in definition of arbitrary shape particles as no analytical representation will restrict the definition of the particles' shapes. Moreover, finding the contact point which is a challenging task for non-spherical particles becomes easy.

The method presented by Wachs [127] suggests a range for the spring/dashpot stiffness based on the problem and an initial estimation is required for the for their values . Moreover, the direction of normal forces needs to be defined clearly. To overcome the shortcoming of the current collision models, this study proposes two different soft collision model for the simulation of arbitrary shape particles by using a field variable to find the overlapping places. They helps us to avoid many difficulties related to finding the collision points, collision normals, local particle interface curvature and the amount of overlapping. Moreover, as non-iterative schemes, the methods save time in finding the collision parameters. Moreover, none of the methods need extra grid refinement at the collision places to find the lubrication forces.

The first model uses a novel spring method for the collision which facilitates implementation of the model significantly. As the method uses a simplified spring model for the collision we call it SSCM (Simplified Spring Collision Model). A particle tagging system is also presented to conduct the model efficiently for high particle numbers. The method does not include any case dependent parameters and can handle any particle shape. The second model uses a pseudo pressure which acts like a potential to apply the collision forces and we call it PPCM (Pseudo Pressure Collision Model). The benefit of this model is simplicity and the efficiency and the disadvantage is necessity of implementing a case dependent parameter.

6.3. Simplified Spring Collision Model (SSCM)

The remedy to implementation of very small time scales is engaged with one interesting feature of the wet collisions. In fact, in a wet collision the material properties do not act as the dominant parameter because the collision depends mostly on flow properties represented by the Stokes number [319, 320],

$St = \frac{\rho_p}{9\rho_f} Re_p$, where ρ_p, ρ_f and Re_p are particle and fluid densities and the particle's relative Reynolds number. $St \cong 10$ is the critical Stokes number below which no rebound happens [319, 321] and the particle move as a group which is compatible with the experiments [322]. When $St > 500$, the effect of fluid becomes negligible and dry collision models become applicable [321]. Having the correlation between the restitution coefficient, $e = \frac{u_{out}}{u_{in}}$, and the Stokes number established, the question now is how the spring-dashpot constants should be defined for a general shape particles to that can calculate the rebound velocity correctly.

The SSCM method starts with introducing a field variable i.e. overlapping function with values that vary like a potential based on the distance from the particle interface. The definition of the overlapping function depends on how the particles are defined. For arbitrary shapes the value of the particle level-set, the signed distance from the interface, can define the overlapping function. The overlapping function itself does not directly contribute to the collision forces; however, it helps with evaluating the forces. A cut off value for the overlapping function could be used because the far field grid points for each particle will not contribute to the calculations. One can also use a $tanh$ profile of the normalized distance variable to lift the necessity of using a cut off:

$$\psi_i(\boldsymbol{x}, t) = \frac{1}{2}\left[\tanh\left(\frac{d_i(\boldsymbol{x},t)}{\xi_i}\right) + 1\right] \tag{6-4}$$

where $d_i(\boldsymbol{x}, t)$ is the distance from the interface of particle i and ξ_i is the thickness of the interface that can be adjusted for each problem. We will discuss this variable later in results section. ψ_i in Equation (6-4), varies from zero outside the particle to one inside the particle. On the interface $\psi_i = 0.5$ and the transition between solid to fluid depends on the interface thickness. As the grid points far away from the interface do not contribute to the collision, use of a cut off value of ε for ψ_i leads to a significant saving in the computational cost without affecting the collision forces.

For classical particle shapes the overlapping function could be defined in an easier way by using the analytical definition of the particle. For example, for an elliptical particle, a new distance function could be defined as

$$d_i(\boldsymbol{x}, t) = 1 - \left(\frac{x^2}{a^2} + \frac{y^2}{b^2} + \frac{z^2}{c^2}\right) \tag{6-5}$$

Then the total overlapping function is the linear summation of each particle's overlapping function:

$$\psi(\boldsymbol{x}, t) = \sum_{i=1}^{N_p} \psi_i \tag{6-6}$$

Here N_P is the total number of particles. As long as the particles are far apart, their overlapping function fields does not overlap and $\psi_i = \psi$ on the related grid point. When two particles are close, their overlapping functions overlaps. The amount of overlapping signifies how much the particles are close. At each node near the vicinity of the particle interface, the overlapping amount is

$$d\psi_{ij}(\boldsymbol{x}, t) = \psi - \psi_i \tag{6-7}$$

Where the index ij denotes the overlapping between particle i and particle j. The volume of the region of overlapping is

$$V_{c,ij} = \int H(d\psi_{ij})\, dV \tag{6-8}$$

Here H is the step function. As we will discuss in the next section, ε has a small value close to zero. The coordinates of the center of collision then is measured as

$$\boldsymbol{X}_{cp,ij} = \frac{\int \boldsymbol{x} H(d\psi_{ij}) dV}{V_{c,ij}} \tag{6-9}$$

The algorithm proceeds by calculating the normal vector field using the gradient of the particle overlapping function.

$$\boldsymbol{n}_i(\boldsymbol{x}, t) = \frac{\nabla \psi_i}{|\nabla \psi_i|} \tag{6-10}$$

Integration of the normal vector field on the overlapping region leads to finding the collision normal vector and the unit normal vector:

$$\boldsymbol{N}_{cp,ij}(\boldsymbol{X}_{cp,ij}, \mathrm{t}) = \int \boldsymbol{n}_i\, H(d\psi_{ij}) dV \tag{6-11}$$

$$\widehat{\boldsymbol{N}}_{cp,ij}\left(\boldsymbol{X}_{cp,ij},t\right)=\frac{\boldsymbol{N}_{cp,ij}}{\left\|\boldsymbol{N}_{cp,ij}\right\|} \tag{6-12}$$

The volume of overlapping region also signifies the amount of overlapping or the overlapping distance vector as

$$\boldsymbol{\delta}_{N,ij}=\sqrt[3]{V_{c,ij}}\widehat{\boldsymbol{N}}_{cp,ij} \tag{6-13}$$

$\boldsymbol{\delta}_{N,ij}$ is the overlapping distance of the particle i in proximity with the particle j.

The next step is definition of a particle field velocity to determine a local velocity. For each particle, using the particle's velocity and angular velocity the particle field velocity $\widetilde{\boldsymbol{u}}_i^{k+1}$ is defined as

$$\widetilde{\boldsymbol{u}}_i\ (\boldsymbol{x},t)=\left(\boldsymbol{V}_i\ +\boldsymbol{\Omega}_i\ \times\left[\boldsymbol{x}-\boldsymbol{x}_i\ (t)\right]\right)\psi_i \tag{6-14}$$

Then the relative particle field velocity is obtained:

$$\widetilde{\boldsymbol{u}}_{ij}(\boldsymbol{x},t)=\widetilde{\boldsymbol{u}}_i\ -\sum_{j\neq i}^{N_P}\widetilde{\boldsymbol{u}}_j \tag{6-15}$$

This definition becomes computationally intensive when the number of particles increases because it requires $N_P(N_P-1)$ operations. The remedy for this is definition of a total particle field velocity as

$$\widetilde{\boldsymbol{u}}\ \ (\boldsymbol{x},t)=\sum_{i=1}^{N_p}\widetilde{\boldsymbol{u}}_i \tag{6-16}$$

Therefore, the relative particle field velocity becomes:

$$\widetilde{\boldsymbol{u}}_{ij}(\boldsymbol{x},t)=\widetilde{\boldsymbol{u}}\ \ -2\widetilde{\boldsymbol{u}}_i \tag{6-17}$$

This definition is helpful in saving the computational time by reducing the number of operations to $2N_P$. Then the relative velocity between particle i and particle j at the collision point $\widetilde{\boldsymbol{u}}_{ij}^{k+1}\left(\boldsymbol{X}_{cp,ij},t\right)$ is used to define the Stokes number.

$$St_{ij}=\frac{m_{ij}\,\widetilde{\boldsymbol{u}}_{ij}\left(\boldsymbol{X}_{cp,ij},t\right)}{6\pi\mu r_{ij}^2} \tag{6-18}$$

In equation (6-18), $m_{ij}=\left(\frac{1}{m_i}+\frac{1}{m_j}\right)^{-1}$ is the reduced mass and μ is the carrier fluid's viscosity. r_{ij} is the reduced radius obtained from the amplitude of curvature. Considering $\kappa_i=\nabla.\boldsymbol{n}_i(\boldsymbol{X}_{cp,ij},t)$ as the local

curvature of particle i, in 2D the reduced radius is $r_{ij} = \left(\kappa_i + \kappa_j\right)^{-1}$. In 3D $\kappa_{i1} + \kappa_{i2} = \nabla.\boldsymbol{n}_i(\boldsymbol{X}_{cp,ij}, t)$ and thus ($r_{ij} = 2\left(\kappa_{i1}+\kappa_{i2} + \kappa_{j1} + \kappa_{j2}\right)^{-1}$) is the reduced radius.

The Stokes number helps to define the restitution coefficient. At low Stokes numbers, hardly any rebound happens. On the other hand, at very high Stokes number values the collision becomes a dry collision with wet restitution coefficient equal to one. Based on [323], the following correlation could be used to calculate the restitution coefficient e_i for the entire range of the Stokes numbers:

$$e_{ij} = \begin{cases} 1 - 8.65St_{ij}^{-0.75} & \text{for} \quad St_{ij} > 18 \\ 0 & \text{for} \quad St_{ij} \leq 18 \end{cases} \tag{6-19}$$

Then, the normal coefficient of restitution $e_{N,ij}$ and tangential coefficient of restitution $e_{T,ij}$ become:

$$e_{N,ij} = \frac{\langle \tilde{\boldsymbol{u}}_{ij}(\boldsymbol{X}_{cp,ij},t).\boldsymbol{N}_{cp,ij}\rangle}{\left\|\tilde{\boldsymbol{u}}_{ij}(\boldsymbol{X}_{cp,ij},t)\right\|} e_{ij} \tag{6-20}$$

$$e_{T,ij} = \sqrt{e_{ij}^2 - e_{N,ij}^2} \tag{6-21}$$

6.3.1. Normal component of the collision forces

The collision force is applied by assuming a mass and spring system. The spring stiffness should stop the normal component of the particle motion in a course equal to the distance that the collision is detected and the physical particle interface. This distance is function of minimum cut off ε in Equation (6-4) which depends on the value of the interface thickness in Equation (6-8).

Unlike other collision models, we do not consider any dashpot effect here. Therefore, all of the kinetic energy of the particle in the normal direction should be transformed to the spring potential energy within the collision course by σ_{ij}:

$$\frac{1}{2}k_{N,ij}\sigma_{ij}^2 = \frac{1}{2}m_{ij}\left(\tilde{\boldsymbol{u}}_{ij}\left(\boldsymbol{X}_{cp,ij}, t\right)\right)^2 \tag{6-22}$$

Consequently, the spring stiffness in the normal direction $k_{N,i}$ is

$$k_{N,ij} = m_{ij}\left(\frac{\tilde{\boldsymbol{u}}_{ij}(\boldsymbol{X}_{cp,ij},t)}{\sigma_{ij}}\right)^2 \tag{6-23}$$

and the normal collision forces becomes

$$\boldsymbol{F}_{N,i}(\boldsymbol{X}_{cp,ij},t) = -k_{N,i}\boldsymbol{\delta}_{N,ij} \tag{6-24}$$

We will discuss the effect of σ_{ij} on the collision outcomes in the results.

To include the damping effect based on the restitution coefficient it is very common to use a dashpot as a damper. However, implementation of a dashpot is engaged with the challenge of the definition of the spring stiffness and the damping coefficient [272]. A new approach is suggested here to overcome the difficulties related to implementation of a dashpot model. In this approach to consider the damping effect after the particle reaches the final collision course, the spring's stiffness is reduced based on the normal restitution coefficient:

$$k_{N,ij,b} = \varepsilon^2 k_{N,ij} \tag{6-25}$$

where $k_{N,ij,b}$ is the spring stiffness during the bounce. The collision force as an external force is added to the forces applied to the particle in each time step until there is no overlapping between two particles. It should be mentioned that during the collision, $k_{N,ij}$ and $k_{N,ij,b}$ remain unchanged while $\boldsymbol{\delta}_{N,ij}$ changes at each time step.

6.3.2. Tangential component of the collision forces

The tangential component of the contact (friction) can happen in two modes. One mode is the rolling condition when no slip condition at the contact point in tangential direction is applied by assuming a zero relative velocity and using the static friction coefficient. The other mode, sliding motion, uses with kinetic friction coefficient to find tangential forces. Here we follow a scheme inspired by Biegert et al. [283] which chooses the friction coefficient based on the contact mode. At first, the vector in tangential direction of the collision forces is obtained by removing the normal component from the relative velocity:

$$\tilde{\boldsymbol{u}}_{ij,T}(\boldsymbol{X}_{cp,ij},t) = \tilde{\boldsymbol{u}}_{ij}(\boldsymbol{X}_{cp,ij},\mathrm{t}) - \langle\tilde{\boldsymbol{u}}_{ij}(\boldsymbol{X}_{cp,ij},\mathrm{t}).\hat{\boldsymbol{N}}_{cp,i}\rangle\hat{\boldsymbol{N}}_{cp,i} \tag{6-26}$$

Normalizing the tangential vector finds the unit tangential vector.

$$\widehat{\boldsymbol{T}}_{cp,i}\left(\boldsymbol{X}_{cp,ij}, t^{k+1}\right) = \frac{\widetilde{\boldsymbol{u}}_{ij,T}(\boldsymbol{X}_{cp,ij},t)}{\left\|\widetilde{\boldsymbol{u}}_{ij,T}(\boldsymbol{X}_{cp,ij},\mathrm{t})\right\|} \tag{6-27}$$

If $\left\|\widetilde{\boldsymbol{u}}_{ij}\left(\boldsymbol{X}_{cp,ij},\mathrm{t}\right)\right\| = 0$ then

$$\widehat{\boldsymbol{T}}_{cp,i}(1) = -\widehat{\boldsymbol{N}}_i(2) \text{ and } \widehat{\boldsymbol{T}}_{cp,i}(2) = \widehat{\boldsymbol{N}}_i(1) \tag{6-28}$$

We use the static friction coefficient μ_s to find friction mode in the rolling regime. Having the normal forces form a soft collision model leads to a soft collision model in tangential direction too. For the no slip mode, the friction force equals the tangential component of the hydrodynamic forces. If the sliding happens

$$\boldsymbol{F}_{T,i}\left(\boldsymbol{X}_{cp,ij},\mathrm{t}\right) = -\mu_k\, \boldsymbol{F}_{N,i}\left(\boldsymbol{X}_{cp,ij},\mathrm{t}\right) \tag{6-29}$$

where μ_k is the kinetic friction coefficient.

6.3.3. Data structure for colliding particles

Due to the very high number of particles and need for binary collision, it is very important to manage the data efficiently to minimize the computational cost. In the following description, a system of data communication is proposed to study the collision of flows laden with several particles. The benefit of this system is that for each particle, it does not require checking the entire list of particles to find the potential collision parameters. The following algorithm is based on the assumption that no more than two particles' overlapping functions occupy each grid point of the domain:

1- Each particle is tagged with an ID number. The walls also are tagged with a value of zero.

2- The reduced mass variable m_{ij} and a new field variable P_{id} is declared for each grid point of the domain. P_{id} or particle ID, is a two-dimensional array with the first argument representing the related cell and the second one with a size of two standing for ID number of the particle. These variables are applied to the grid points of the particle i with $\psi_i > \varepsilon$. Here, for simplicity we do not include the first dimension related to the cells.

3- At first $m_{ij} = \infty$ and $P_{id} = -1$ are set in the entire domain. Then, for the grid points nearby the walls $P_{id}(1) = 0$.

4- For each particle, the values of P_{id} in the cells with $\psi_i > \varepsilon$ is set to the particle ID number and also $m_{ij} = m_i$. If $P_{id} \neq -1$ for the first index, P_{id} of the second index is changed from -1 to the particle ID number. Moreover, for those cells, $m_{ij} = \left(\frac{1}{m_i} + \frac{1}{m_j}\right)^{-1}$ is used to update the reduced mass.

5- Particles with $P_{id}(2) \neq -1$ are in the process of collision and they are tagged to find the collision forces and moments. For these particles m_{ij} is obtained by using the data from grid points.

6.4. Pseudo Pressure Collision Model (PPCM)

The main problem of the SSCM is that since they are based on binary collision of many particles, it becomes so complicated when the number of particles increases to track the possible binary collisions. Therefore, still a more efficient collision model for arbitrary shape particles is still desirable. The Pseudo Pressure Collision Model (PPCM) like SSCM in sprit with SPM uses a field variable to find the possible collision spots and apply a repulsion force. In PPCM use of a field variable or the overlapping function, can suppress inclusion of complexities related to the extra parameters for non-symmetric shapes and bypass the requirement for the binary proximity check.

Like SSCM, when two particles are in proximity $d\psi(\boldsymbol{x}, t) = \psi - \psi_i > 0$. Since ψ is defined based on a $tanh$ function of distance to the interface, $tanh^{-1}$ will lead to a distance showing the amount of overlapping:

$$\eta(\boldsymbol{x}, t) = \frac{\xi}{2} ln\left(\frac{1+d\psi}{1-d\psi}\right) \tag{6-30}$$

The more overlapping, the higher values of η. The variable η is a field variable with a length dimension. The total overlapping distance is obtained by integrating $\eta(\boldsymbol{x}, t)$:

$$\delta = \int \eta(\boldsymbol{x}, t) dx \tag{6-31}$$

Hence, a repulsion pressure is added to the field pressure as

$$p_r = \begin{cases} 0 & for\ \rho > \delta \\ \varepsilon_P \delta^2 & for\ \delta > \rho \end{cases} \tag{6-32}$$

In the above equation, p_r is the repulsion pressure that is added to the field pressure temporarily to add the effect of other particles and ε_P is the stiffness parameter which depends on each case condition. ρ is the distance threshold above which no repulsion force is applied.

In order to add a repulsion force using the overlapping function, a temporary pressure variable is defined by adding the resulted particle repulsion pressure and the flow pressure. Then by using the projection step as Equation (3-8), the resulted temporary provisional velocity is used to find the particle forces as Equations (3-22) and (3-23). By saving the original values of velocity and pressure, the repulsion force only acts as an external force since it does not directly change the velocity and pressure fields. In this way, the deviation from physics and also calculation instabilities are avoided.

The main benefit of the above equation is that it does not need to check all particles one by one to find the overlapping pair particles. Since ψ is a field variable, it is defined in the whole domain and the overlapping places will be automatically captured and the repulsion pressure is applied. Moreover, PPCM does not need to directly find the collision contact point. In order to consider the wall collision, a similar overlapping function for the wall can be defined to apply repulsion whenever, the overlapping function of the wall overlap's the one from the particle.

PPCM unlike SSCM cannot model the tangential component of the collision and therefore, the collisions are frictionless. Moreover, the method contains a case dependent parameter ε_P which sometimes can be challenging to define.

6.5. Results

In this section at first the collision models are validated and then the capability of each model are presented in details.

6.5.1. Results for simplified spring collision model

In this section at first the collision model is validated by comparison with the experimental results for a particle wall collision. Then, the robustness of the method is studied for various cases of non-spherical particles including in collisions with friction and without friction and finally, the model is tested for the simulation of many particles.

6.5.1.1. Validation: particle-wall collision

In order to validate the method for the collision with a stationary wall, the experimental results of Gondret et al. [1] which were also implemented later in [283, 285] is used. A spherical particle made of steel with $d_p = 3\ mm,\ \rho_p = 7800\ kg/m^3$, $\nu = 0.3$ and $E = 2.4 \times 10^{11}$ is released for a free fall in silicon oil RV10 with $\mu = 0.01\ Pa.s$ and $\rho_f = 935\ kg/m^3$. Here, d_p, ρ_p, ν, E are respectively solid particle's diameter, density, Poisson's ratio, and Young modulus. ρ_f and μ are the fluid's density and viscosity. The simulation is performed in non-dimensional form by normalizing the distance with the particle diameter and the non-dimensional parameters $Re = 164$, $Fr = 11.8$ and $\gamma = \rho_p/\rho_f = 8.342$. The simulation is made in a $10 \times 10 \times 10$ domain with different minimum grid sizes to study the effect of grid refinement. The cut off value for the overlapping function is set to 10% of the particle diameter. Consequently, when a particle approaches the wall, the course of deceleration is $\sigma = 0.1$.

The particle starts to fall and reaches the final steady velocity before hitting the wall. It starts bouncing and losing the kinetic energy and finally it stays on the wall motionless. The very low or zero spring stiffness values related to the final stage of the collision means that the particle may not have enough collision force to hold it over the wall after ultimate reduction of spring coefficient. This happens when the bouncing height is so low that the particle cannot escape the area of overlapping. Therefore, the spring coefficient is not updated to higher values related to the next bounce as it still has the low bounce spring coefficient value. To avoid penetration of the particle to the wall in these cases, an extra upward force equal to negative of weight is applied.

The results are presented in Figure (6-1) and they show the overall agreement of the method with the experiment. Moreover, the independency of the results from the grid also is approved. There is a small discrepancy among the current results and the experiment which is more noticeable in the velocity after the second collision. The maximum velocity just after the collision is smaller in the simulation than the experiment. The reason is that the soft collision model transforms the actual collision to a softer collision which smoothes the sudden changes in the velocity. However, it is not apparent in the first collision because of the short duration of collision at high impact velocity which results in a harder collision. Consequently, the discrepancy grows in the subsequent collisions with diminution of the impact velocity and longer collision durations. Moreover, the accumulation of errors by time also is the other reason for increase in the discrepancy.

6.5.1.2. Effect of collision course

In the presented Simplified Spring Collision Method, the collision course is the only parameter that is not defined. We defined the collision course, σ, as the distance between the point with $d\psi_i(\boldsymbol{x},t)|_{cut\ off} = \varepsilon$ and the particle interface. This section studies the dependency of the results to σ. A problem like the one in section 6.5.1.1 is considered but with different collision courses (Figure (6-2)). The results are related to minimum grid size of $\Delta x = 0.075$ and $CFL = 0.25$.

For $\sigma = 0.3$, the error related to the simulation is not significant as it is mostly limited to the instants of impact. After the collision .i.e. when particle leaves the overlapping region, it reaches the actual path and the error is partially compensated. Variation of height with time for the first collision of the particle is represented in Figure (6-2c) for the particle using different collision courses. When $\sigma = 0.3$, the particle does not reach the wall completely leading to emerge of the related error.

For $\sigma = 0.05$, the difference between the simulation and experiment becomes noteworthy by showing a higher restitution coefficient for the collision. In this case, the collision duration is so short

that the simulation becomes sensitive to the small errors. As it could be observed in Figure (6-2c), even though the particle path is very close to the experiment, after the collision it bounces with higher velocity.

6.5.1.3. Collision of an elliptical particle with a frictionless wall

When a particle is not spherical, the rotation becomes important even if the walls are frictionless. Here, we consider collision of a free-falling ellipse on a frictionless wall. The ellipse with $D_p = (2.0,0.5)$ and $\rho_p/\rho_f = 10$ is located at (5.0,7.0) in a 10×10 channel with four no-slip walls. The particle is released and settled under the gravity. At Froude number $Fr = 0.51$, two Reynolds numbers of $Re = 20$ and $Re = 2000$ are studies respectively. The final Reynolds and Froude numbers are measured with respect to the major diameter. The initial angle of the particle is $\theta = \pi/4$ with respect to the horizontal wall. Due to high asymmetry of the problem, the particle should start to rotate after the start of motion. However, to avoid more complexities, the rotational motion of the particle is restricted until the collision time. Moreover, during this time the particle is set to move with a unit vertical downward velocity. The minimum grid size is $\Delta x = 0.0375$ and $CFL = 0.2$.

Figure (6-3) shows the sequence of the particle position in the channel. Due to the tilted placement of the particle at the time of impact, the particle reaches the wall on its sharp edge. Then it bounces slightly and rotates towards the final position of the particle with minimum gravitational potential on the flat side of the particle.

Figure (6-4) represents the time history of the particle kinematical variables. It is clear from Figures (6-3) and (6-4) that at $Re = 20$ after the impact of the particle with wall and a small vertical bounce, the particle settles down to the final vertical position very fast. This is because of the high dissipation at low Reynolds number. The other hand, the particle continues its motion in the horizontal direction by sliding over the frictionless wall after gaining a horizontal momentum. This momentum damps due to dissipation in the fluid. At $Re = 2000$, the lower dissipation of enery leads a number of subsequent collisions after the first collision as well as a horizontal motion in the other direction.

6.5.1.4. Tangential collision model

To validate the tangential collision model, we study a case similar to Biegert et al. [283]. A sphere with $D_p = 0.125$ and $\rho_p/\rho_f = 2.5$ is exposed to a linear shear flow in a $1 \times 1 \times 1$ domain. Two cases in different fluids with $\nu = 0.1$ and $\nu = 0.02$ are considered. The top wall is driven by with $u_w = 1$ leading to $Re_w = 10$ and $Re_w = 50$. Considering $g = 9.81$ and the static and dynamic friction coefficient as $\mu_s = 0.8$ and $\mu_k = 0.15$, the particle will be subject to rolling condition [283]. This friction coefficients are related to silicate materials. The linear velocity profile in the domain varies with height and is applied to all boundaries except the outlet which satisfies the condition of zero gradient for the variables. The particle is placed on the bottom wall. A minimum grid size of 0.05 is considered with $CFL = 0.5$.

The particle is placed on the wall and with the start of the simulation the collision is detected. It is held for $T = \frac{tu_w}{H} = 0.01\ s$ for the flow to develop slightly and avoid the spikes in the forces at the start of the simulation. Then the particle is released leading to acceleration and motion to reach the steady condition. We compared our results with Biegert et al. [283] in Figure (6-5). It shows that at similar to Biegert et al. [283], at $Re_w = 10$ the translational velocity (U) is more than the rolling velocity ($R_i w_i$); however, they are similar at $Re_w = 50$ which is not shown in the graph. While the results are very similar, there is a small discrepancy which is probably because of using a different diffuse interface solver.

6.5.1.5. Collision of rectangular particle with wall

To study the effect of tangential part of the collision in this section we consider a rectangular block of copper with 2×0.5 dimensions standing vertically on a wall. We consider the bottom wall in two situations: one case without friction and the other one with static and dynamic friction coefficients similar to copper on steel friction i.e. $\mu_s = 0.53$ and $\mu_k = 0.36$. A uniform unit velocity is applied for the input and the top wall in the x direction and the bottom wall no slip boundary condition. The particle

is located vertically at (3,1) in a 15×6 channel. With $\rho_p/\rho_f = 8.96$, $Re = \frac{U_\infty L}{\nu} = 100$ and $Fr = \frac{U_\infty^2}{gL} = 0.102$ related to $\nu = 0.01$, $g = 9.81$ and L as the average dimension of the rectangle. The rectangle is fixed at first until $T = 0.1$ to have the flow developed over the particle and avoid a sudden spike in force at the start of the simulation.

The sequence of particle motion is shown in Figure (6-6) for both friction and frictionless collisions. Figures (6-7) and (6-8) display the quantitative variation in particle's motion for the two cases. With friction, the particle shows a limited motion which leads to a final stop at about $T \sim 2.2$. Without friction, the particle continues to move to reach the end of the channel with a steady velocity of $u_{final} \sim 0.56$. Even though the contact is frictionless, the particle does not reach the freestream velocity because of the boundary layer on the wall. Moreover, the particle is losing momentum by time as it has less flow blockage in comparison with the start of the motion.

The differences between the two cases is not limited to the translational motions as the two particles have different rotational motions. With friction, the particle pivots around the front collision point and rotates until it contacts the wall on the length and becomes stable. On the other hand, without friction, the particle is free to rotate around any of the bottom edges. Therefore, when the applied moment on the particle is positive due to more blockage of the flow on the bottom, the particle rotates on the other direction leading a positive angular velocity. However, for both cases the rotation is restricted because after the particle reaches the long edge, the stabilizing effect of the weight does not allow to particle to rotate more.

The history of variation of angle is studied in Figures (6-6) to (6-9) and it shows when the wall is frictionless, the particle rotates on clockwise direction leading to negative angular velocities. This is because of the more blockage of the flow on the bottom region of the particle. However, when the particle, has friction, the tangential force causes the particle to pivot on the contact point leading to a positive angle with some fluctuations when the particle hits the wall on its new position.

Figures (6-10) and (6-11) display the contour plots of vorticity for the frictionless and frictional collision at different time instants. The evolution of vorticity from the tip of the rectangle is noticeable which in the case of the frictionless collision is attached to the tip and moves with the flow and the particle. For the frictional collision, it detaches the tip due to fast downward motion while another vorticity is generated on the other side of the particle.

6.5.2. Results for pseudo pressure collision model

Several of 2D and 3D cases are considered to study the PPCM in the context of SPM. For better comparison, the sharp interface method (SIM) with a repulsion force as defined in Equation (6-2) is defined. The diffuse interface of SPM causes the velocity fields near the interface be slightly different from the real value. Additionally, the particle pressure in SPM which is applied to consider the rigidity of the particle leads to a repulsion force which is intrinsic for SPM. Accordingly, it is expected that new collision model be different from Equation (6-2) if implemented with SIM. To investigate further, another case also is considered which is SPM but instead of the analytical equation for definition of the particles' shapes, like SIM level set method is implemented with a repulsion force as Equation (6-2) (we call it SPMLS).

6.5.2.1. Two moving circular cylinders at $Re = 20$

Two stationary particles are considered to start moving impulsively in a uniform flow at $T = 0.0$. When the particles start moving, the second particle is always in the wake of the first one. Hence, the second particle will have less velocity and collision happens. A 2D channel of size 32×10 is considered with two particles located at (4,5) and (6,5), namely the distance between two particles is 2.0. As the particles are at the centerline of the channel, the only reason to deviate from the centerline is instability due to numerical truncation error. The particles have diameters of one and the uniform velocity flow enters the channel from all boundaries except the outlet which has the zero gradient velocity. The base

grid size is 0.3333 but it refines two time based on the vorticity and vorticity gradient to have 12 grid points across the particles. The fluid to solid density ratio is 10.0 and the collision parameters in Equation (6-2) are $\epsilon_p = 0.001$ and $\rho = 0.12$. For SPM simulation with analytical shape definition, the Equation (6-32) is used by $\varepsilon_P = 0.3$ for $Re = 20$.

When the particles are able to rotate and one particle is at the wake of the other one, like the case of drafting, kissing, tumbling (DKT) [125, 200, 324], after the collision both particles drift from centerline toward the wall. Our experience with the current case is similar. Hence, we at first did not consider the rotation to make the study purely based on collision and avoid instabilities. The distance between two particles and the relative velocity among them are shown in Figure (6-12). The collision occurs when the relative velocity changes sign from positive to negative. At this low Re flow, the maximum relative velocity is about 0.11 and thus, $St \sim 5 < 10$ it is expected that the particles stick together and continue the motion with almost the same velocity. At the start of motion, the distance between two particles at first decrease at the same rate. Considering contact point as the minimum center to center distant of the two particles, the contact happens at $T = 12.71$, 12.82 and 14.83 at a minimum distance of 1.056, 1.036 and 1.027 for SIM, SPMLS and SPM. One reason for the late contact of the particles in SPMLS and SPM is that the particles need more time to reach the minimum distance as the minimum distance is smaller for SPM and SPMLS in comparison with SIM. The more important reason is that SPM, which has a diffuse interface and uses a different collision model, is affected by particle pressure to impose the rigidity of the solid. This pressure is prominent when the two particles' interfaces are thicker at low Re causing the discrepancy.

After the collision, there is a very small bounce in all models and they show damping behavior before reaching the final velocity. SPMLS and SIM which use the same collision model obey almost the same pattern. However, SPMLS shows a higher bounce after the collision and less damping. On the other hand, SPM shows the greatest amount of damping which is very close to the experiment. Therefore, it can be inferred that by using a same collision model, there would be less energy damping in SPMLS in

comparison with SPM which shows the highest amount of damping because of the new collision capturing method. SPM with the set up parameters shows a smoother collision than SPMLS. The final center to center distance of the particles are approximately1.10, 1.10 and 1.09 for SIM, SPMLS and SPM, respectively showing the co-moving translation of the particles after the collision.

Figure (6-13) displays the effect of mesh refinement on the behavior of the new collision model. The distance between two particles and the relative velocity varies almost the same way for different grids. With grid refinement there is a same trend toward the finest grid results. At coarse grids the diffuse interface of SPM is thicker, thus collision becomes smoother and higher energy damping happens before the first collision. It is necessary to mention that the overlapping function in all grids are identical; however, it is the effect of SPM interface to smooth the collision in coarse grids.

After collision, there is less bounce for finer grids. Since no ricochet is expected, the results of all grids agree with the experiment but the after collision distance between the particles decreases with grid refinement.

6.5.2.2. Two moving circular cylinders at $Re = 150$

Similar conditions as $Re = 20$ are applied for $Re = 150$ but here for SPM with analytical shape $\varepsilon_P = 0.08$ is applied. At this higher Re, the wake is more extended and stronger. Consequently, the two particles should have higher relative velocity in the first collisions. The results related to different methods are presented in Figure (6-14). One significant different is that in SIM instability leads to deviation of the particles from the centerline. SIM is more sensitive to numerical instability as it uses surface integral in order to find the force while in SPM forces on the particles are calculated with volumetric integration making the method, less sensitive to numerical instabilities. The numerical instabilities of SIM appears at $Re = 150$ when the 2D wake is unstable too and at the time of the collision, the relative velocity does not show a smooth pattern.

Having the maximum relative velocity as approximately 0.17, the resulted Stokes number is $St \cong 25.5$ and a rather strong bounce is expected. The coefficient of restitution that Yang and Hunt [320] used in their experiments ranged from 0.3 to 0.7 for different particle materials. Due to the broad range of coefficient of restitution, all of the methods in current study are within this range and it is not clear which method is better. SPMLS and SIM are very similar but changes in relative velocity of SPMLS are smoother leading to a reduction in the peaks and a lag in the collision time. SPM collision energy damps faster leading to smaller bounce and faster achievement of final steady conditions. After three bounces, the particles in SPM move at the same velocity but SPMLS tends to have more bounces to reach this condition.

Grid refinement study (Figure (6-15)) shows that similar to $Re = 20$, at coarse grids there is more damping and less restitution coefficient which is because of thicker SPM interface. Anyway, after enough refinements the results approach the same value and there is a consistent trend towards this value.

6.5.2.3. Two moving spheres at Re=20

Similar behavior as 2D cases is expected for the translation of spherical particles using SPM with overlapping function. In 3D, collision happens later due the less wake effect. After the collision, the particles almost stick together (Figure (6-16)) and grid refinement shows an approaching trend for finer grids. At coarse grid, the interface is thicker leading to earlier repulsion as a results of higher SPM particle pressure.

6.5.2.4. Two moving spheres at Re=150

As displayed in Figure (6-17), this case is very similar to 2D results. The particles bounce after the collision and the amount of bounce is more for finer grids. At course grids, there is more energy damping and consequently less bounce due to thicker interface. However, different grids follow a similar pattern in particle distance and relative velocity.

6.6. Conclusions

Two new wet particle collision methods were developed to model the collision of particles with arbitrary shapes. These can be applied to any particle shape as long as the distance to the interface can be obtained and the collision point is limited to one. They define an overlapping function as a field variable in the entire domain and find the collision parameters by using this field variable.

The Simplified Spring Collision Model (SSCM) uses the overlapping function to find the collision place and the collision forces and moments. To avoid complexities related to defining a mass and spring system, instead of using a dashpot, the spring coefficient is modified after the collision to reach the desired restitution coefficient. We show that the method is capable of finding the collision forces for arbitrary shape particles. The method is validated with the experiment and shown to be accurate over a wide range of Stokes numbers. Study of the effect of the collision course as the only unknown parameter shows that if $\sigma \cong \mathcal{O}(0.2d_p)$, the error in the results is not significant. With this collision capturing method there is no need for extra grid refinement to solve the lubrication forces during the collision. This results in significant saving in the cost of calculations. Moreover, the model is simple to implement and applicable for general shape particles.

The Pseudo Pressure Collision Model (PPCM), on the other hand, uses a pseudo pressure to apply the collision forces from the overlapping function. PPCM does not use binary collision and does not need to identify the contact point. While it is faster and easier to implement than SSCM, it requires defining a case sensitive parameter. Moreover, PPCM is restricted to normal forces and consideration of the tangential component of the collision forces is not included.

Using a collision capturing method, the next chapter studies flows containing multitude of particles. To reach the ability of modeling big data of particles, the particles' data structure is managed using a linked list. This concept is described in detail in the next chapter. Then, the results for the flow of the disk shape particles are presented. Finally, the flow of blood over a constricted region representing the hinge region of a mechanical heart valve is analyzed.

FIGURES

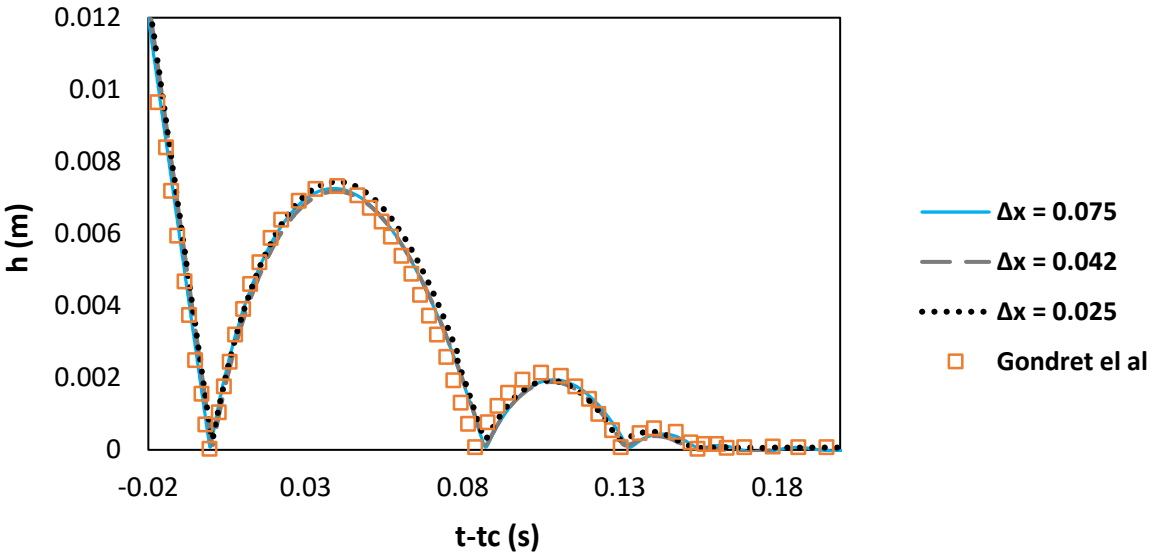

(a)

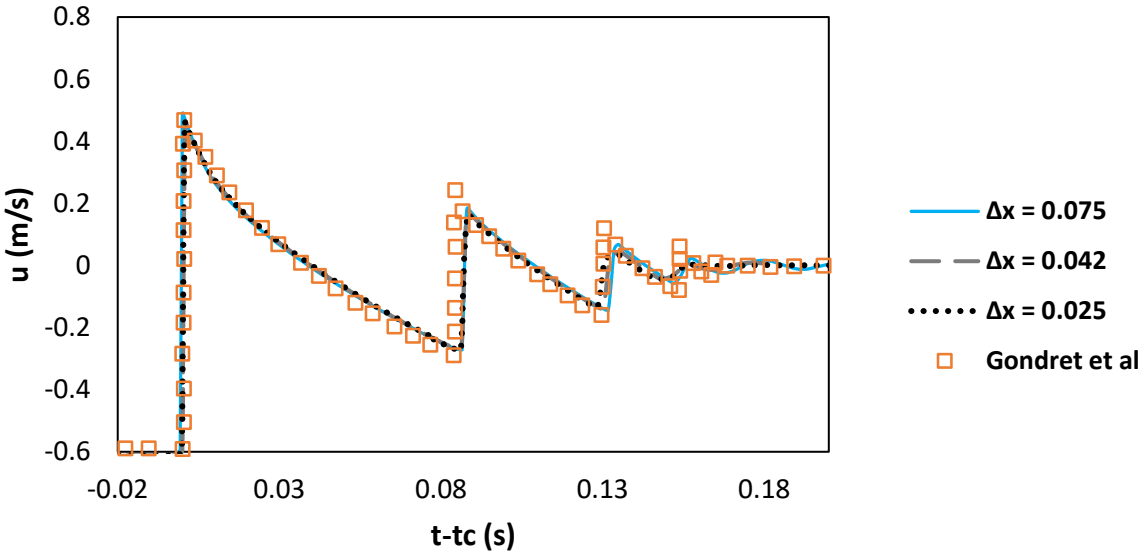

(b)

Figure 6-1- Collision of a spherical particle with a solid stationary wall at Re=164 and comparison with [1]. Variation of **(a)** height and **(b)** velocity with time which happens for a steel particle with $d_i = 3\ mm$ colliding with a glass wall in silicon oil RV10. For the first collision, $St_n = 152$.

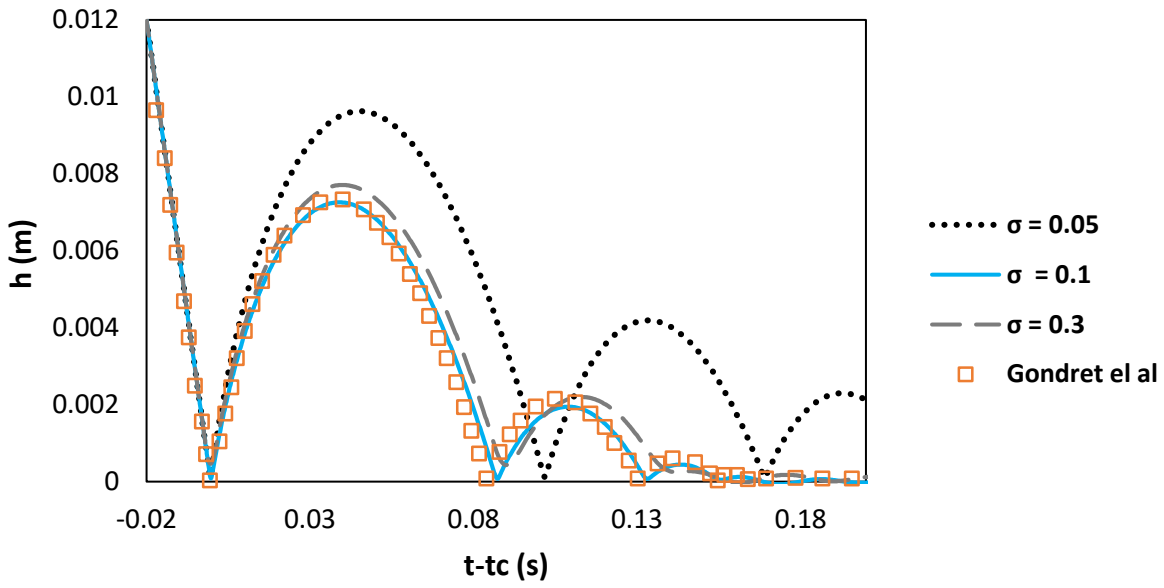

(a)

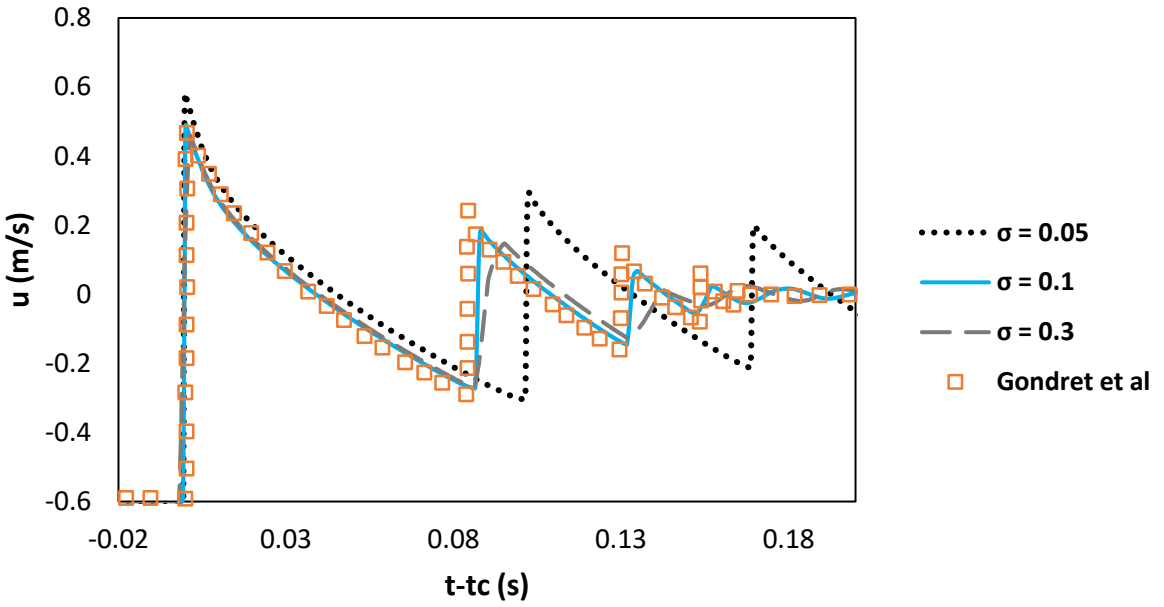

(b)

Figure 6-2- Effect of collision course on the collision of a spherical particle with a solid stationary wall at Re=164 and comparison with [1]. Variation of **(a)** height and **(b)** velocity with time which happens for a steel particle with $d_i = 3\ mm$ colliding with a glass wall in silicon oil RV10. **(c)** The zoomed view of height history which shows the high smoothing when $\sigma = 0.3$.

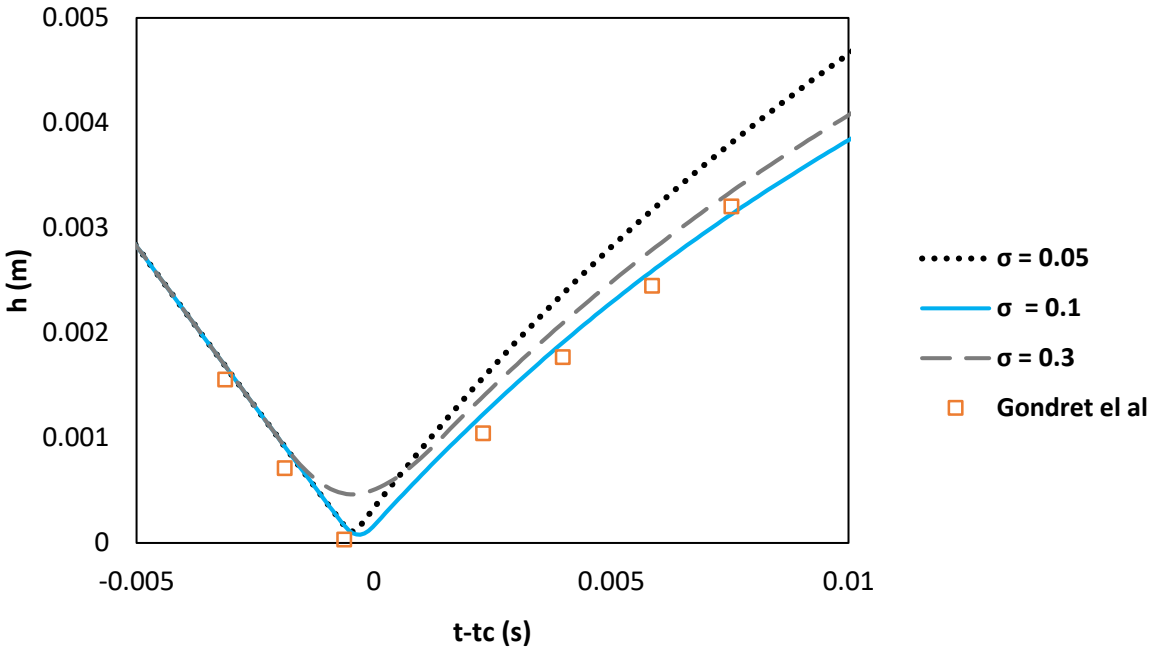

(c)

Figure 6-2 (continued)- Effect of collision course on the collision of a spherical particle with a solid stationary wall at Re=164 and comparison with [1]. Variation of **(a)** height and **(b)** velocity with time which happens for a steel particle with $d_i = 3\ mm$ colliding with a glass wall in silicon oil RV10. **(c)** The zoomed view of height history which shows the high smoothing when $\sigma = 0.3$.

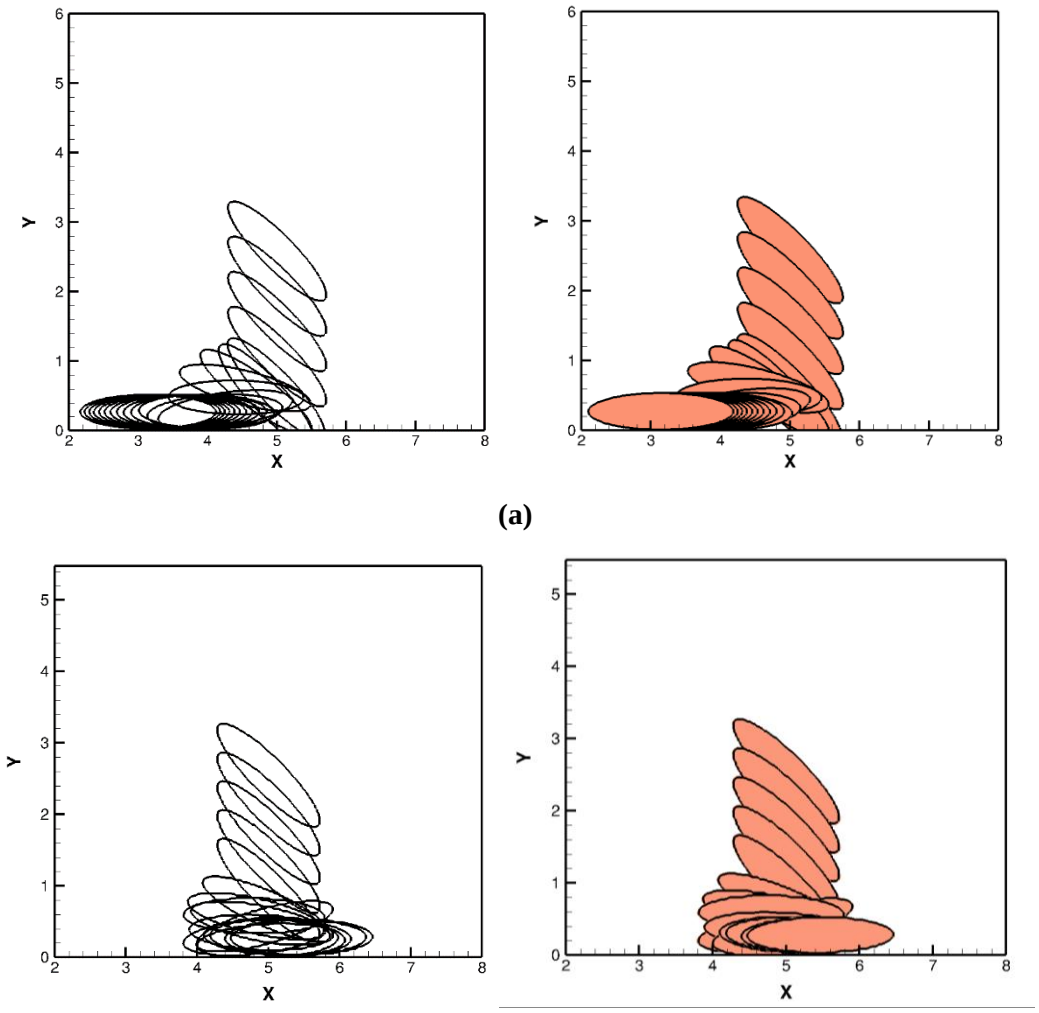

Figure 6-3- Sequences of the collision of a falling ellipse with frictionless wall at **(a)** $Re = 20$ and **(b)** $Re = 2000$. At the start of the collision $\theta = \frac{\pi}{4}$ with $\omega = 0$ and $V_p = (0, -1.0)$. After the collision, the elliptical particle rotates to reach its final position with minimum gravitational potential.

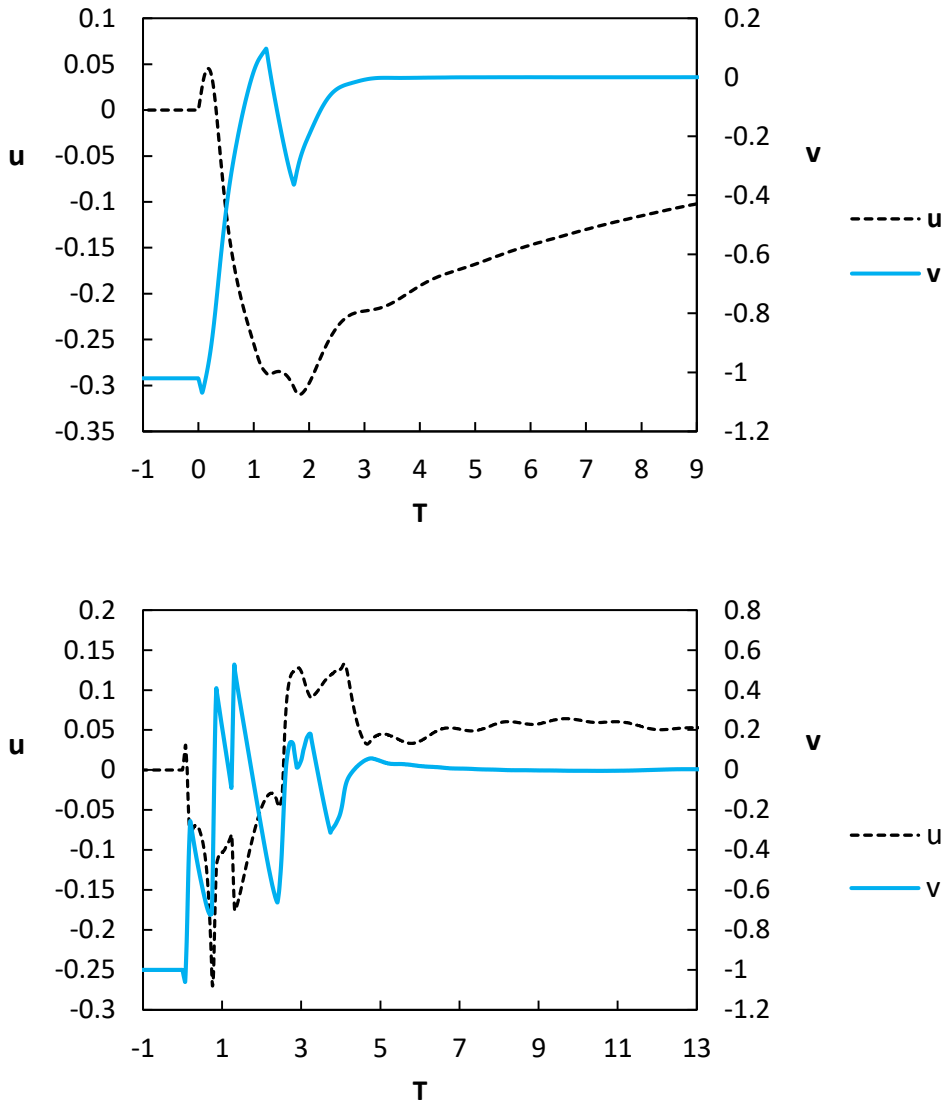

(a)

Figure 6-4- History of **(a)** velocity, **(b)** position **(c)** rotation parameters for an elliptical particle with $D_p =$ (2.0,0.5) and $\rho_p/\rho_f = 10$ at $Fr = 0.51$. The particle collides with a frictionless wall. The top and bottom figures show the results for $Re = 20$ and $Re = 2000$ respectively. $T = 0$ is the time that the particle starts the course of collision and is free to rotate.

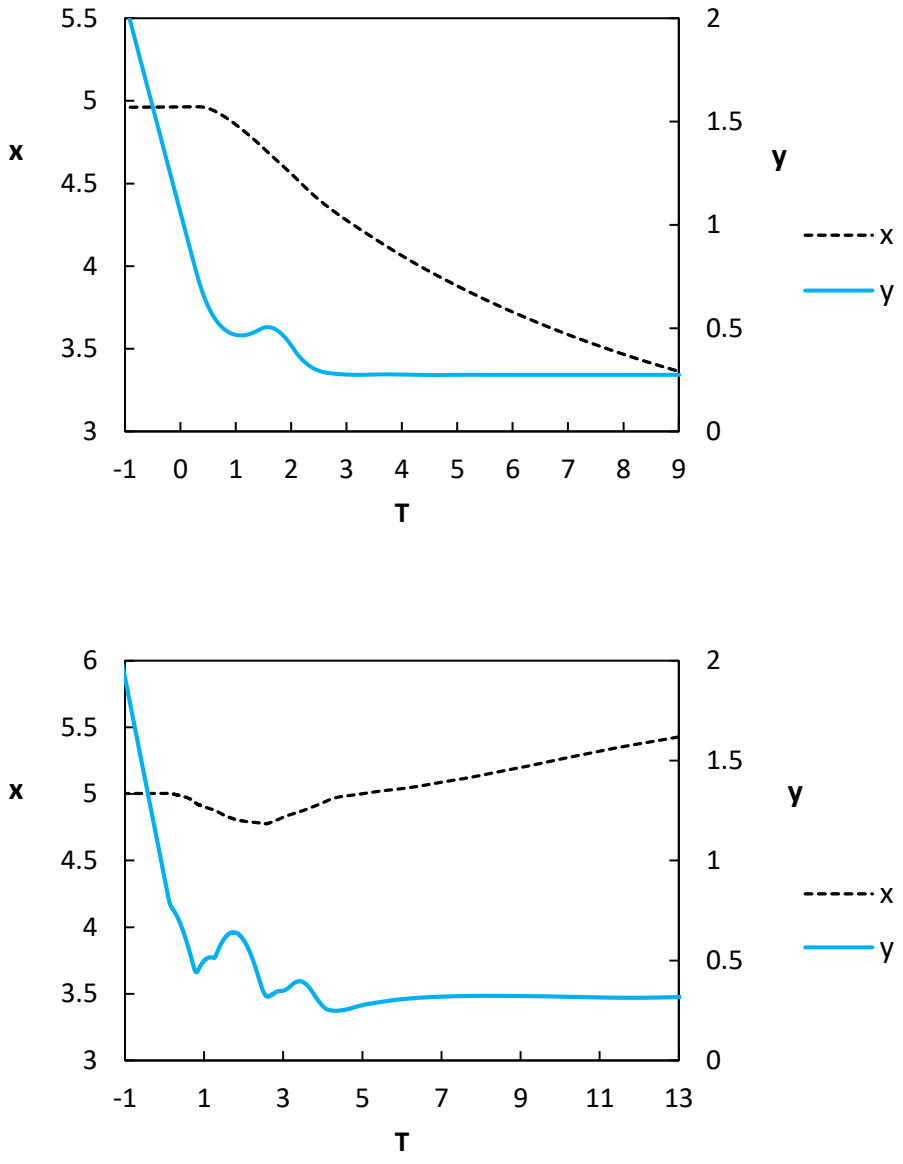

(b)

Figure 6-4 (continued)- History of **(a)** velocity, **(b)** position **(c)** rotation parameters for an elliptical particle with $D_p = (2.0,0.5)$ and $\rho_p/\rho_f = 10$ at $Fr = 0.51$. The particle collides with a frictionless wall. The top and bottom figures show the results for $Re = 20$ and $Re = 2000$ respectively. $T = 0$ is the time that the particle starts the course of collision and is free to rotate.

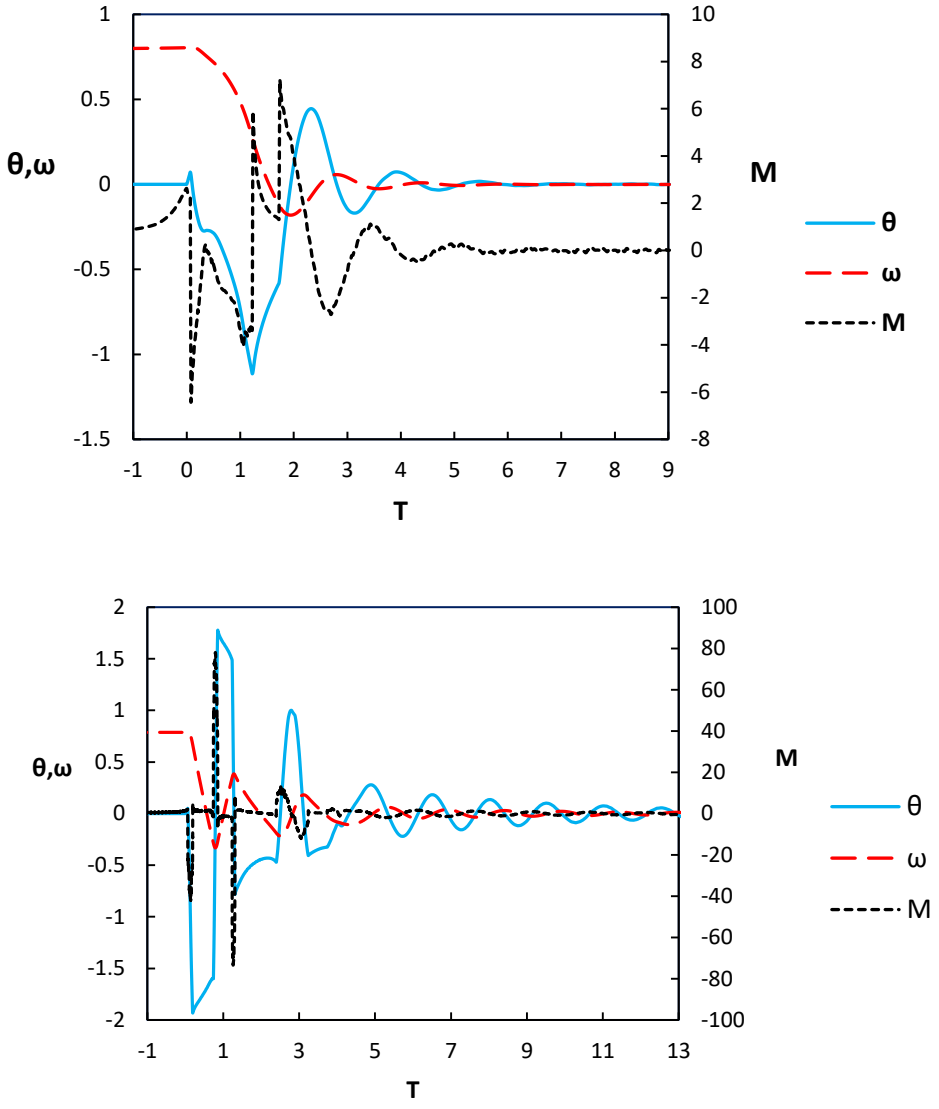

(c)

Figure 6-4 (continued)- History of **(a)** velocity, **(b)** position **(c)** rotation parameters for an elliptical particle with $D_p = (2.0,0.5)$ and $\rho_p/\rho_f = 10$ at $Fr = 0.51$. The particle collides with a frictionless wall. The top and bottom figures show the results for $Re = 20$ and $Re = 2000$ respectively. $T = 0$ is the time that the particle starts the course of collision and is free to rotate.

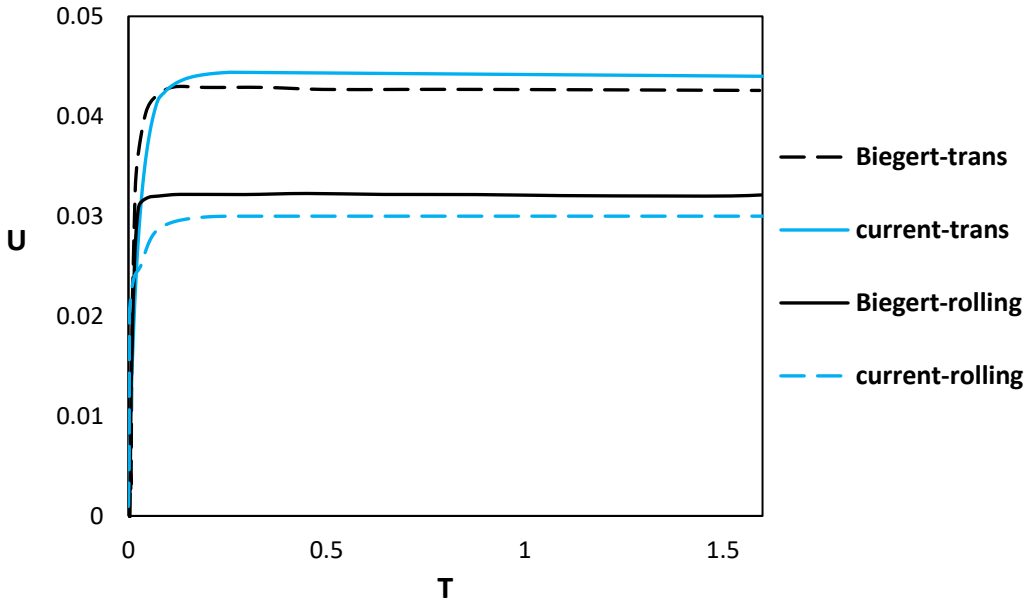

(a)

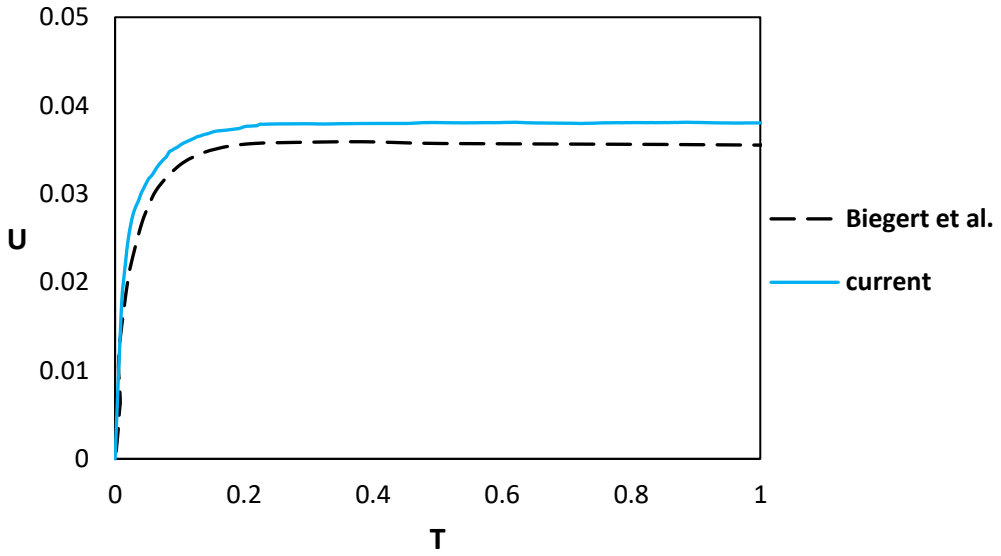

(b)

Figure 6-5- The translational velocity of a spherical particle subject to a Couette flow at **(a)** $Re_w = 10$ and **(b)** $Re_w = 50$. The particle starts to move at T=0.01 and shows a rolling motion. At $Re_w = 10$ the rolling velocity is different from the translating velocity showing a slip velocity for the particle and wall. At $Re_w = 50$ there is no difference between the rolling and translating velocities (Not shown due to similarity).

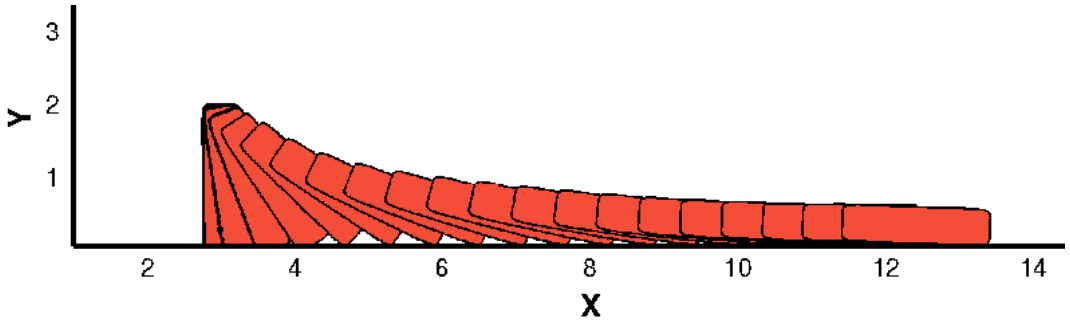

(a)

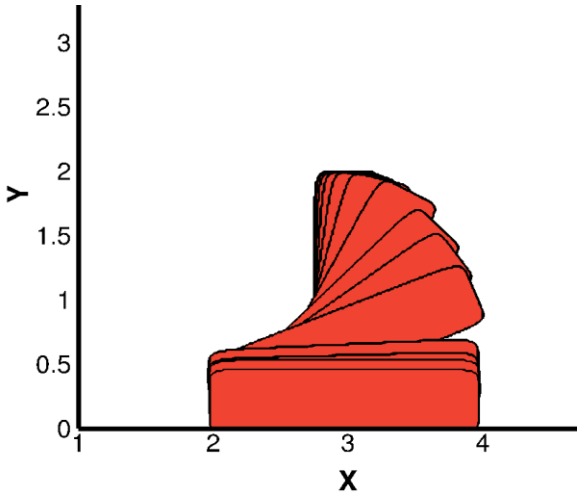

(b)

Figure 6-6- Sequence of particle motion for the collision of a 2×0.5 rectangular copper particle exposed to a unit freestream velocity and contact with a steel wall at $Re = 100$ and $Fr = 0.102$. **(a)** Frictionless collision **(b)** Frictional collision.

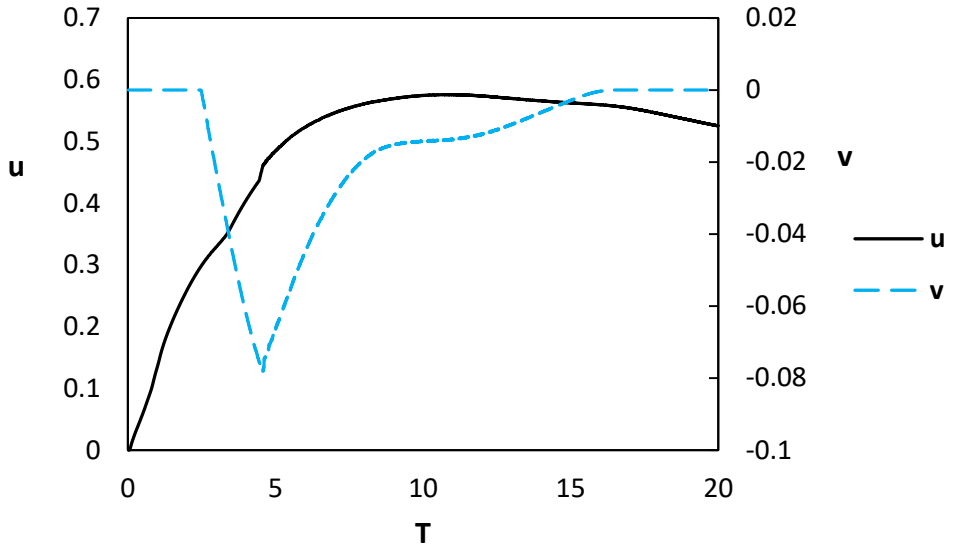

(a)

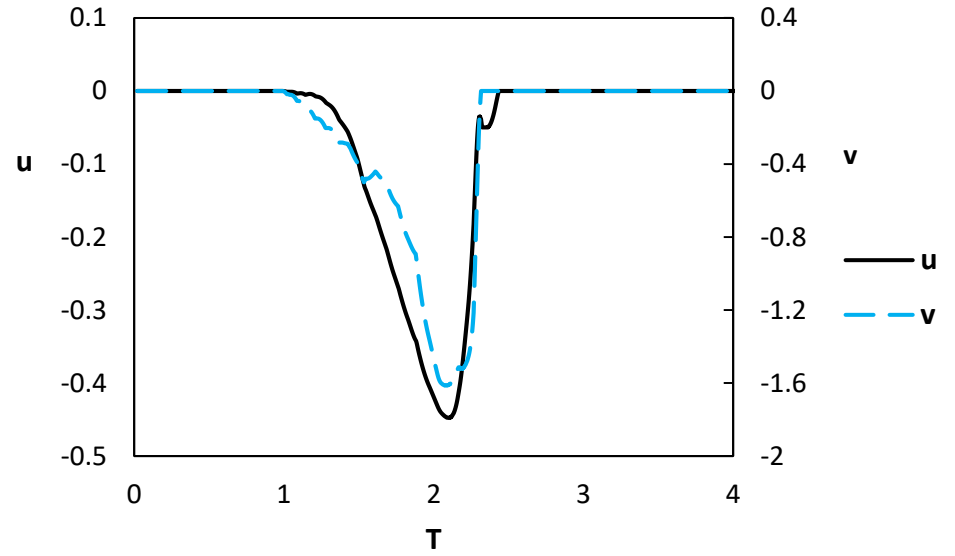

(b)

Velocity

Figure 6-7- Motion of 2×0.5 rectangular copper particle exposed to uniform freestream unit velocity and collision with a steel wall at $Re = 100$ and $Fr = 0.102$. **(a)** Frictionless collision **(b)** Frictional collision.

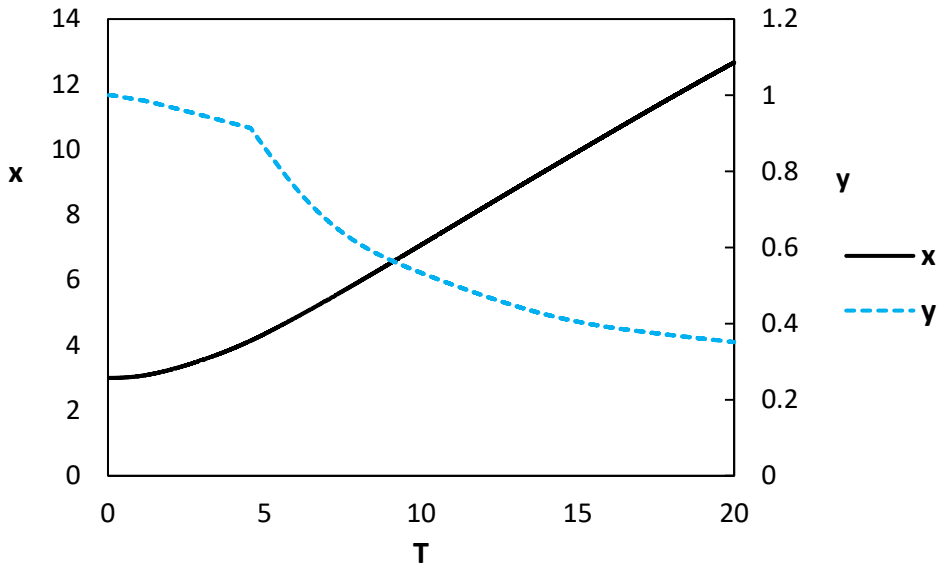

(a)

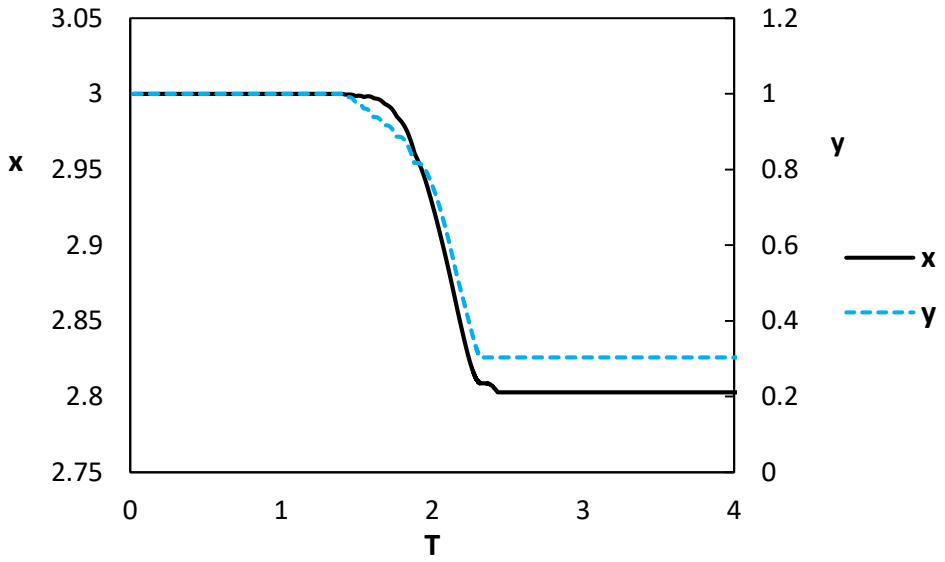

(b)

Position

Figure 6-7 (continued)- Motion of 2×0.5 rectangular copper particle exposed to uniform freestream unit velocity and collision with a steel wall at $Re = 100$ and $Fr = 0.102$. **(a)** Frictionless collision **(b)** Frictional collision.

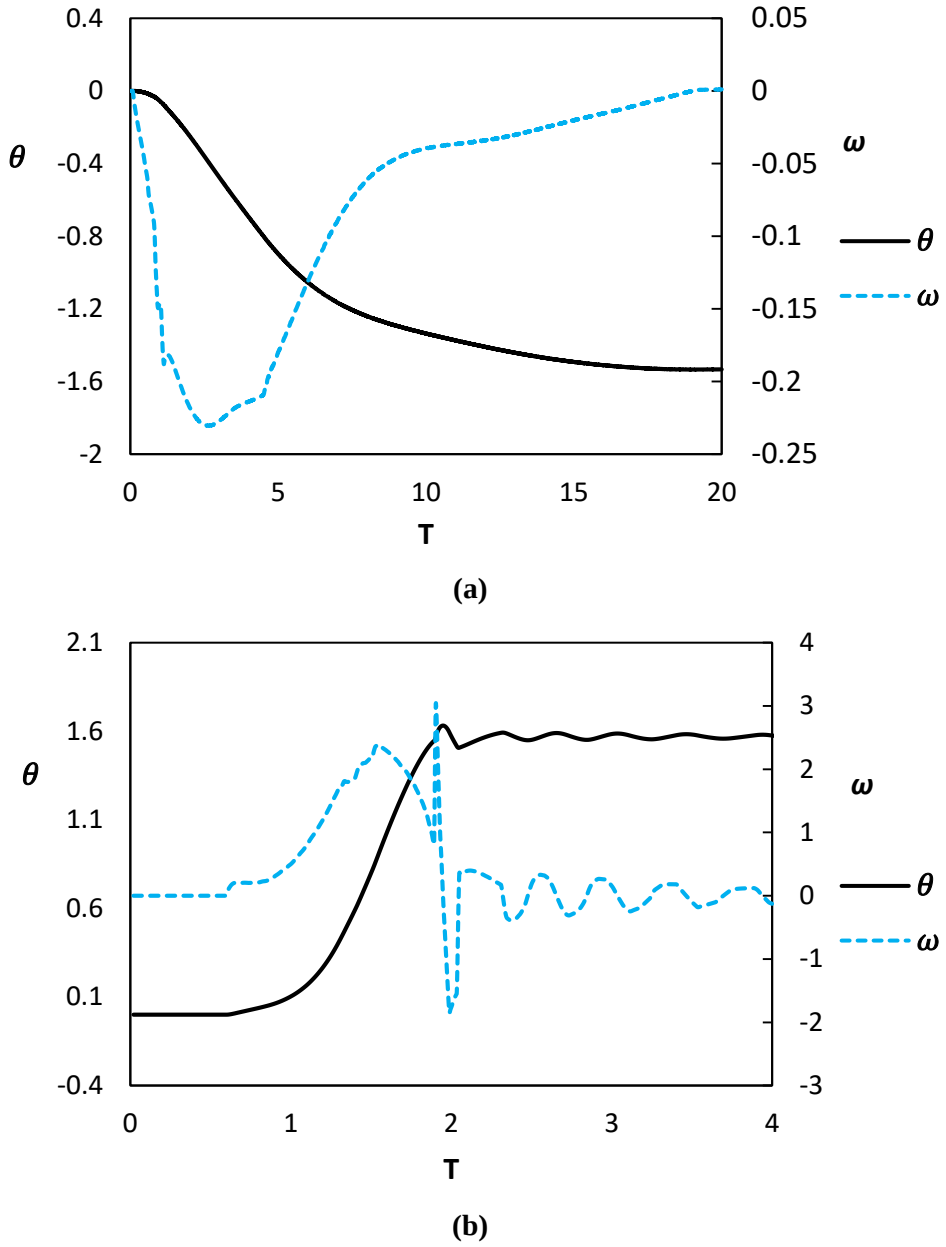

Figure 6-7 (continued)- Motion of 2×0.5 rectangular copper particle exposed to uniform freestream unit velocity and collision with a steel wall at $Re = 100$ and $Fr = 0.102$. **(a)** Frictionless collision **(b)** Frictional collision.

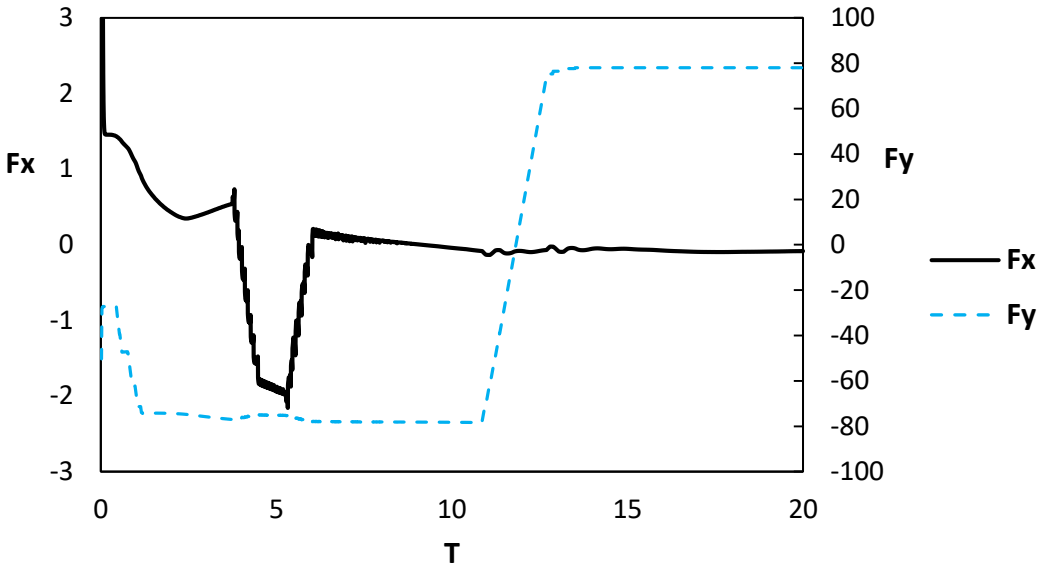

(a)

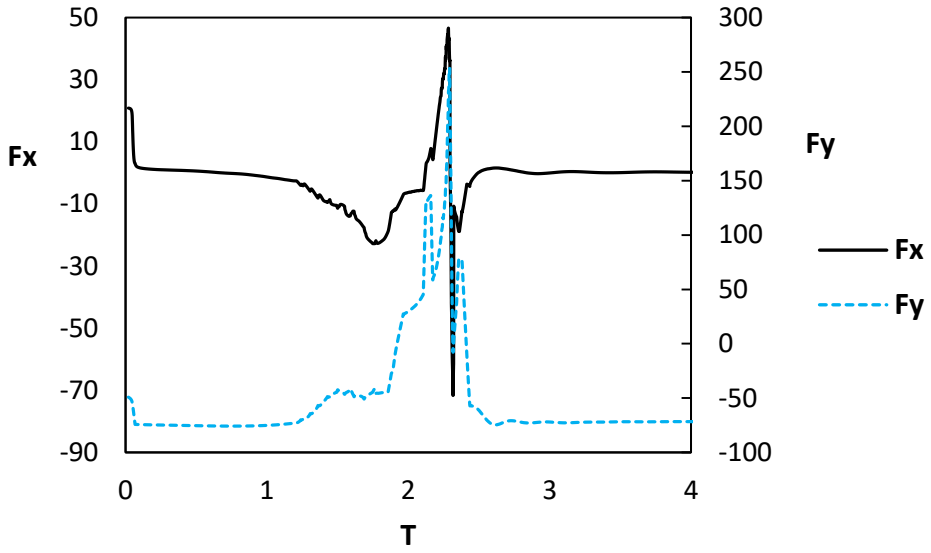

(b)

Force

Figure 6-8- History of force components and moment for the motion of 2×0.5 rectangular copper particle exposed to uniform freestream unit velocity and collision with a steel wall at $Re = 100$ and $Fr = 0.102$. **(a)** Frictionless collision **(b)** Frictional collision.

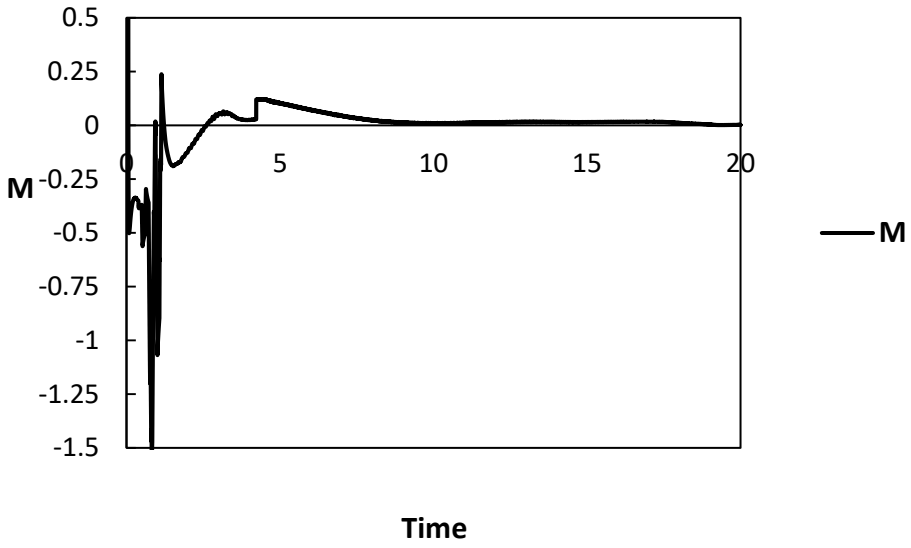

(a)

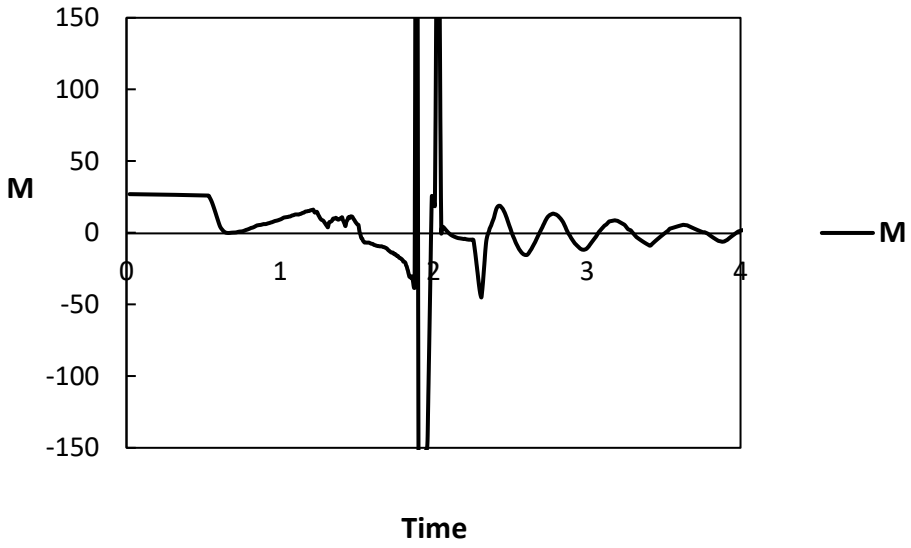

(b)

Moment

Figure 6-8 (continued)- History of force components and moment for the motion of 2×0.5 rectangular copper particle exposed to uniform freestream unit velocity and collision with a steel wall at $Re = 100$ and $Fr = 0.102$. **(a)** Frictionless collision **(b)** Frictional collision.

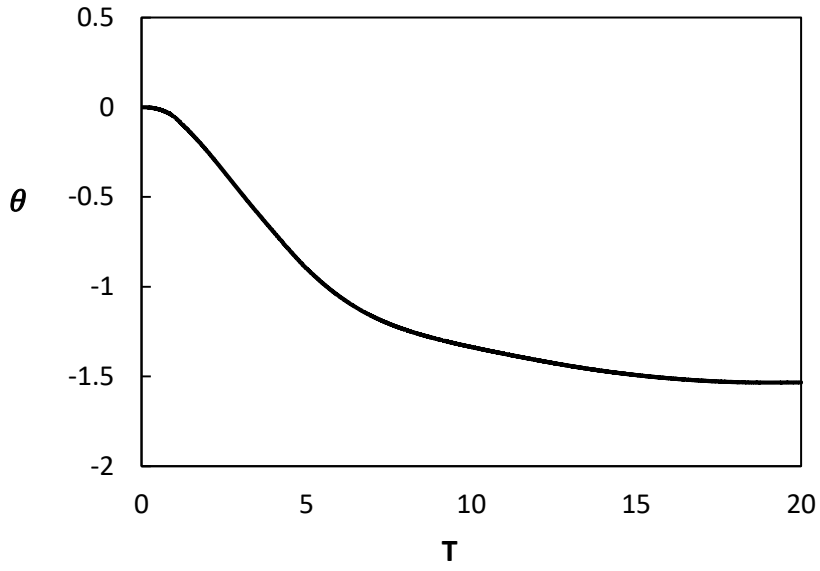

(a)

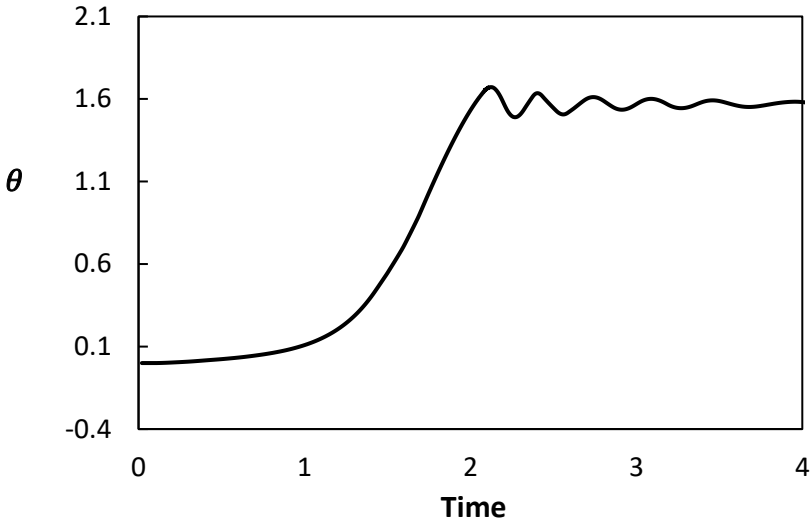

(b)

Figure 6-9- Variation of angle for the motion of a 2×0.5 rectangular copper particle exposed to uniform freestream unit velocity and collision with a steel wall at $Re = 100$ and $Fr = 0.102$. **(a)** Frictionless collision **(b)** Frictional collision.

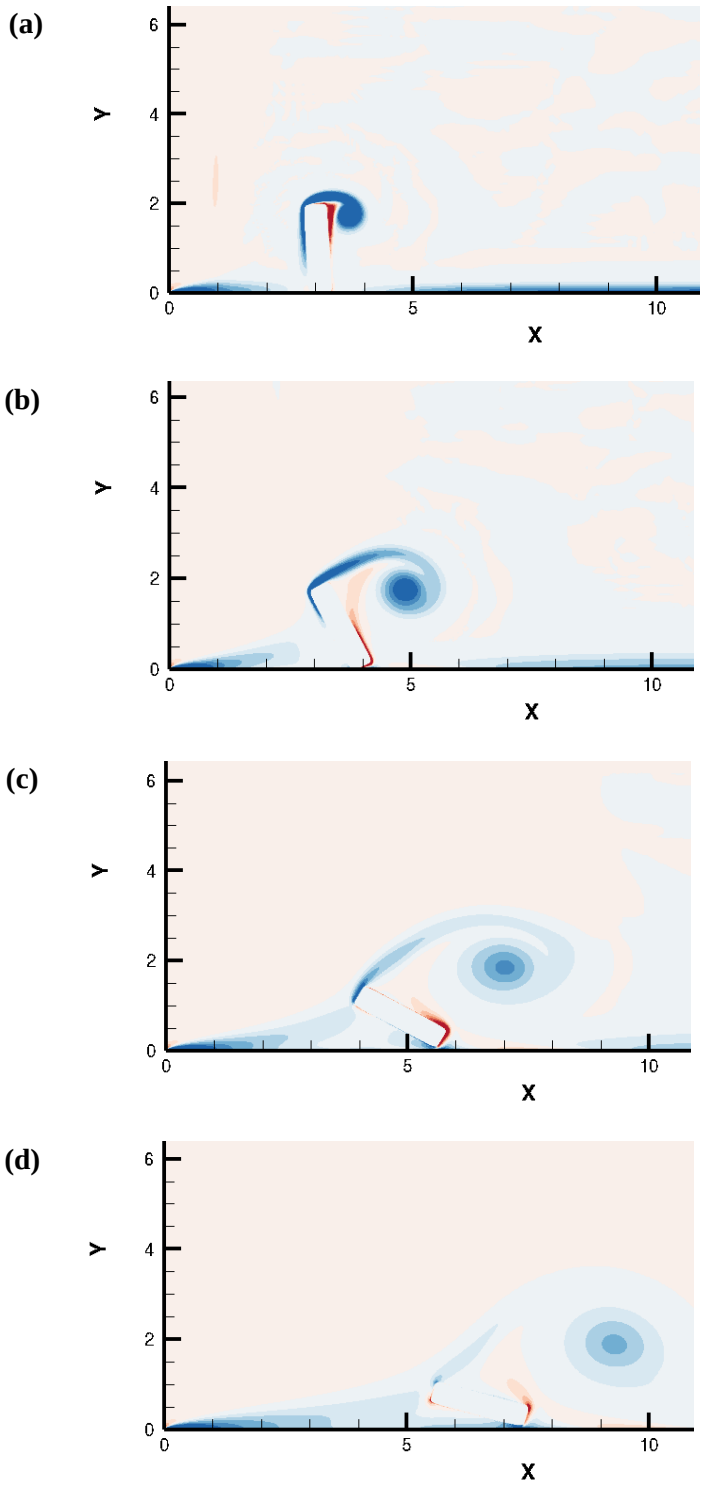

Figure 6-10- Contour plots of vorticity for the frictionless collision of motion of a 2×0.5 rectangular copper particle exposed to uniform freestream unit velocity and collision with a steel wall at $Re = 100$ and $Fr = 0.102$ at **(a)** $T = 1.0$, **(b)** $T = 3.0$, **(c)** $T = 6.0$ and **(d)** $T = 9.0$.

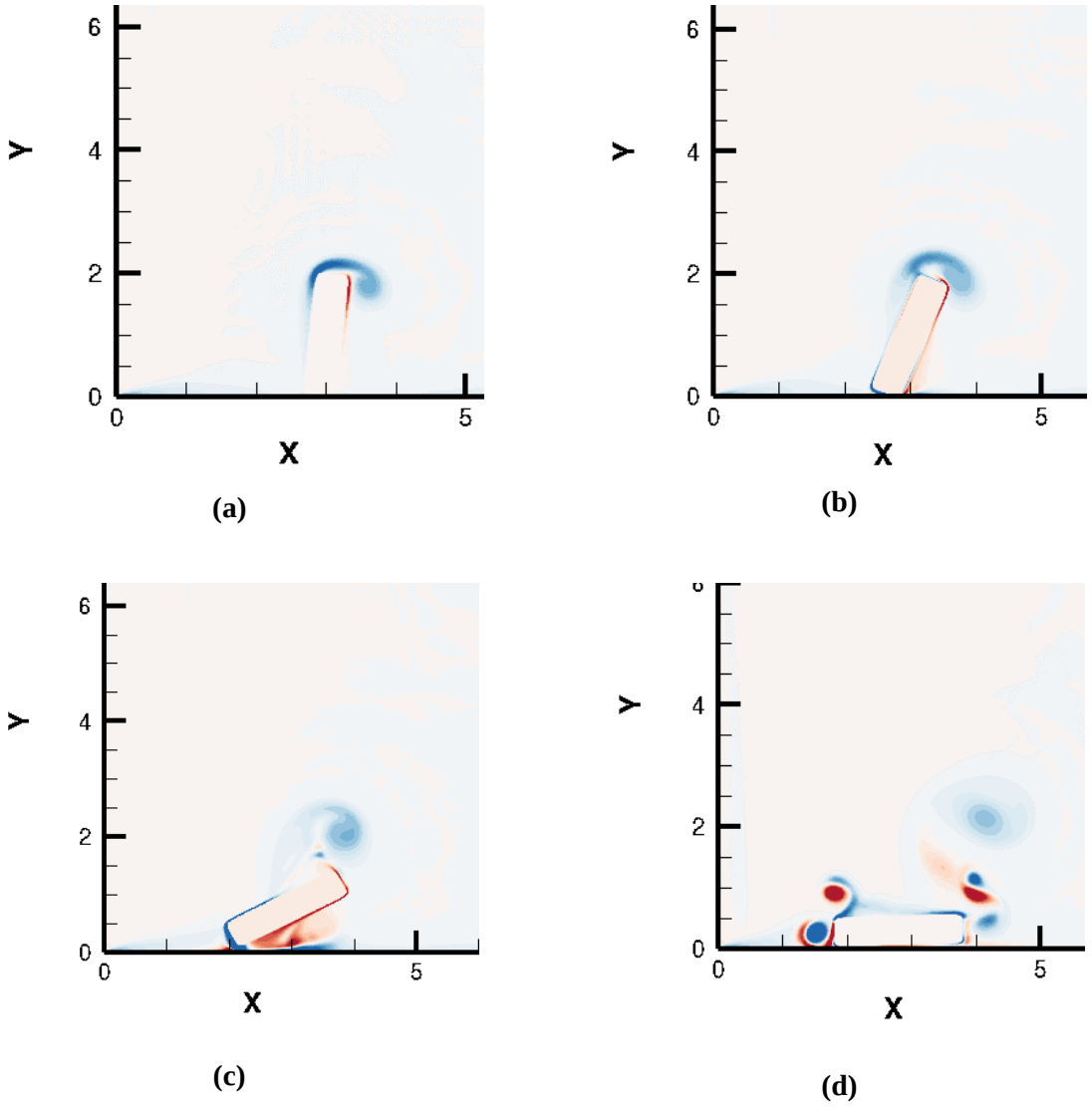

Figure 6-11- Contour plots of vorticity for the frictional collision of motion of a 2×0.5 rectangular copper particle exposed to uniform freestream unit velocity and collision with a steel wall at $Re = 100$ and $Fr = 0.102$ at **(a)** $T = 1.0$, **(b)** $T = 1.5$, **(c)** $T = 2.0$ and **(d)** $T = 2.5$.

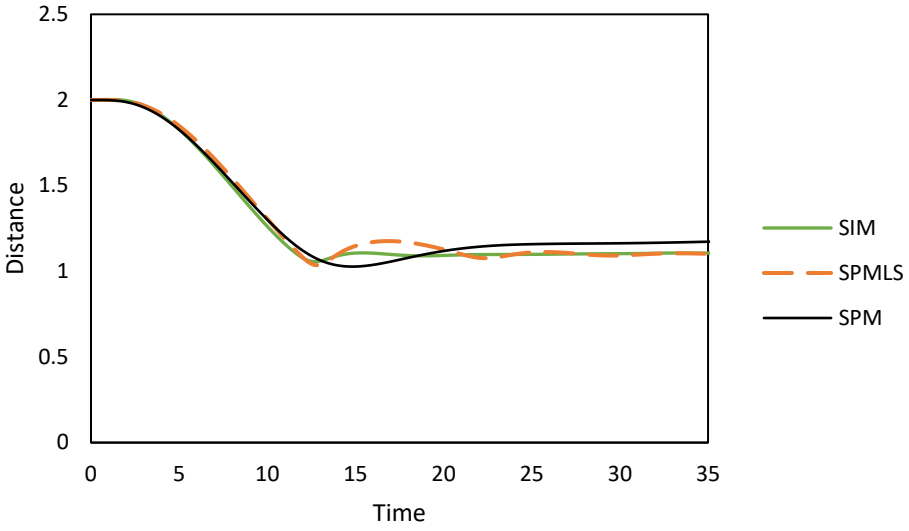

(a)

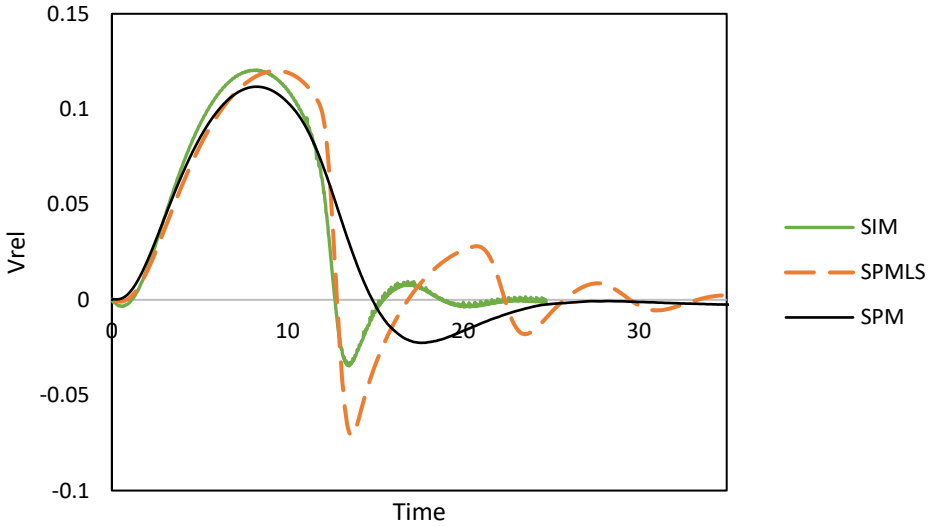

(b)

Figure 6-12- Translation and collision of two circular cylinder particles at the $Re = 20$ for various cases of SIM, SPM with level set (SPMLS) and analytical definition of shape in SPM (SPM): **(a)** Distance between two particles; **(b)** Relative velocity between two particles.

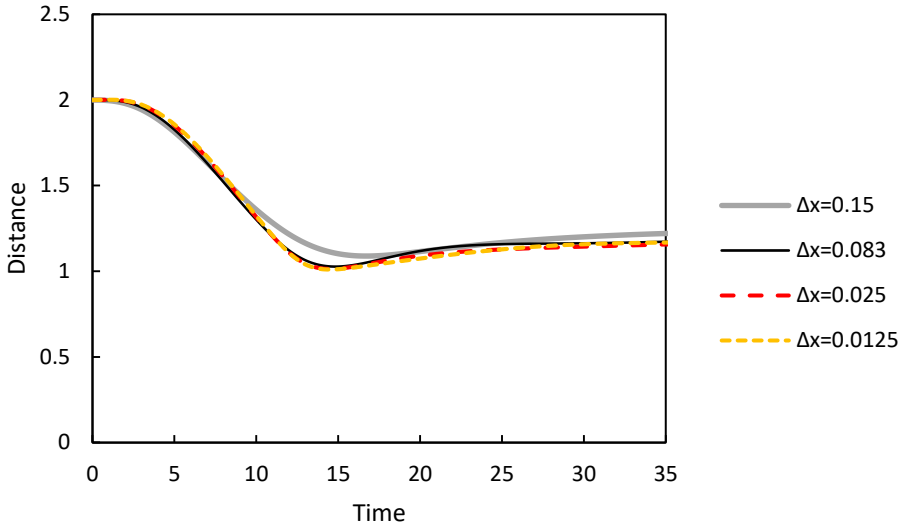

(a)

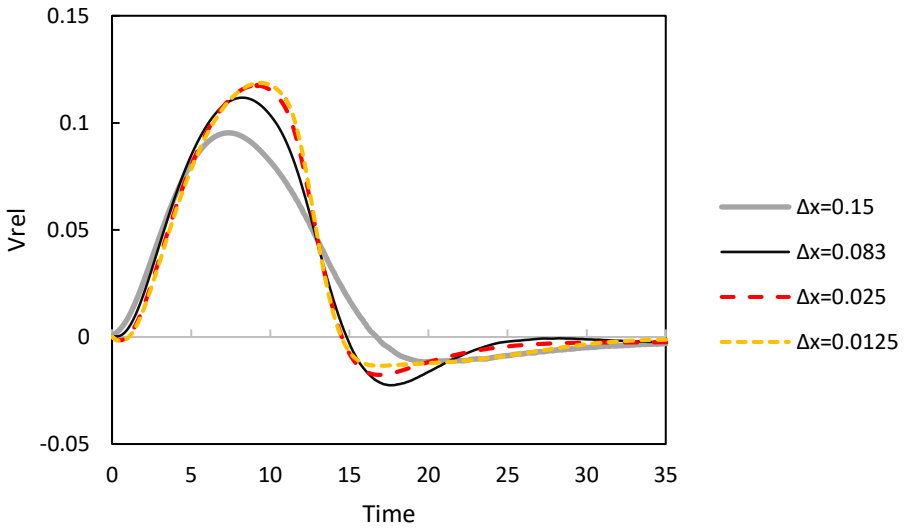

(b)

Figure 6-13- SPM collision model for two circular cylinder particles at the $\mathrm{Re} = 20$ at various grid sizes: **(a)** Distance between two particles; **(b)** Relative velocity between two particles.

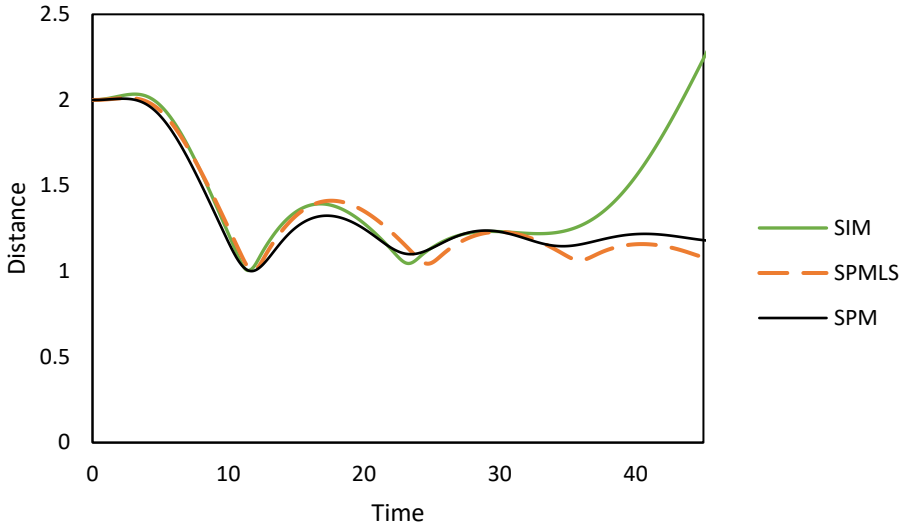

(a)

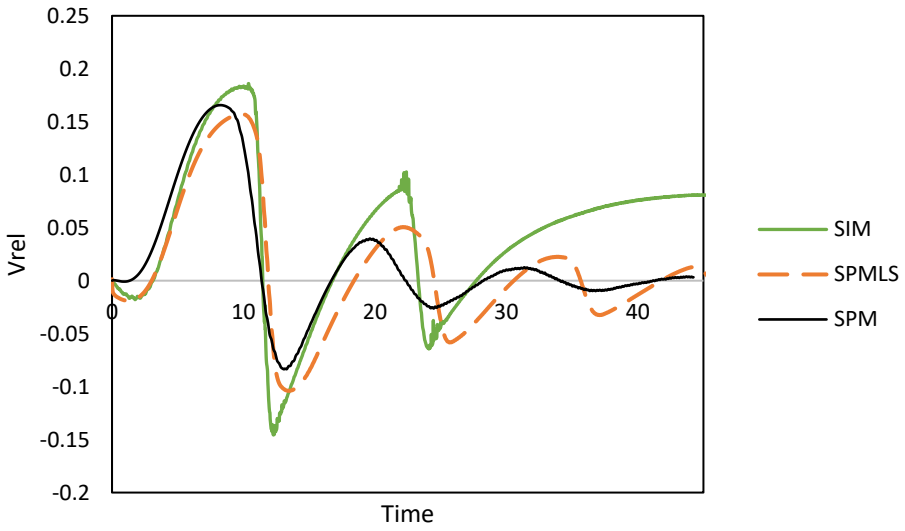

(b)

Figure 6-14- Translation and collision of two circular cylinder particles at the $Re = 150$ for various cases of SIM, SPM with level set (SPMLS) and analytical definition of shape in SPM (SPM): **(a)** Distance between two particles; **(b)** Relative velocity between two particles.

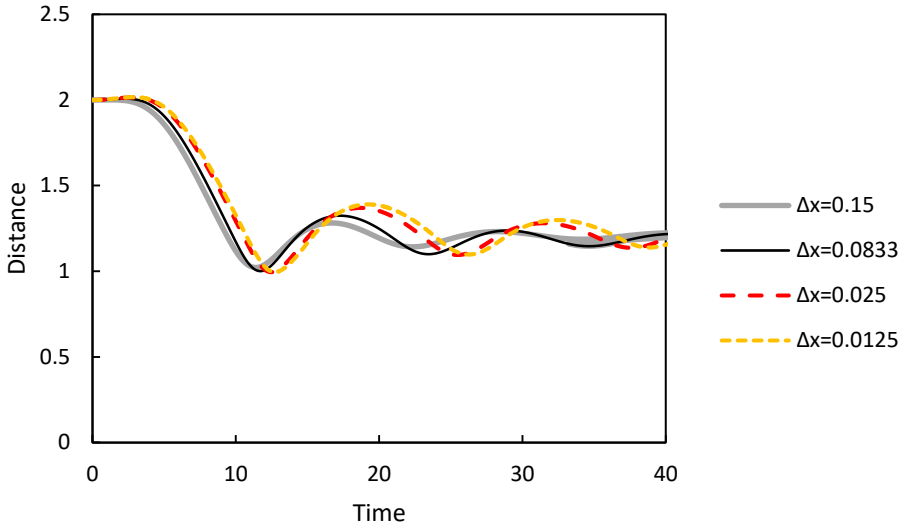

(a)

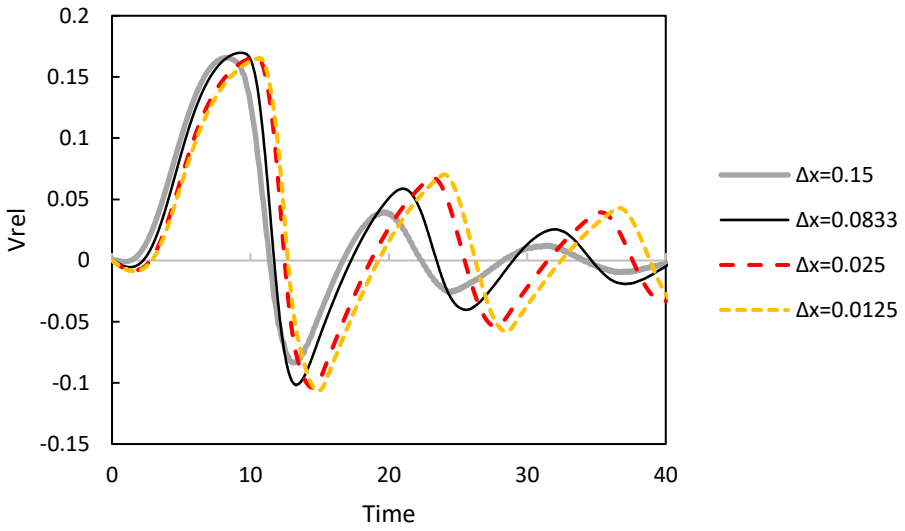

(b)

Figure 6-15- SPM collision model for two circular cylinder particles at the $Re = 150$ at various grid sizes: **(a)** Distance between two particles; **(b)** Relative velocity between two particles.

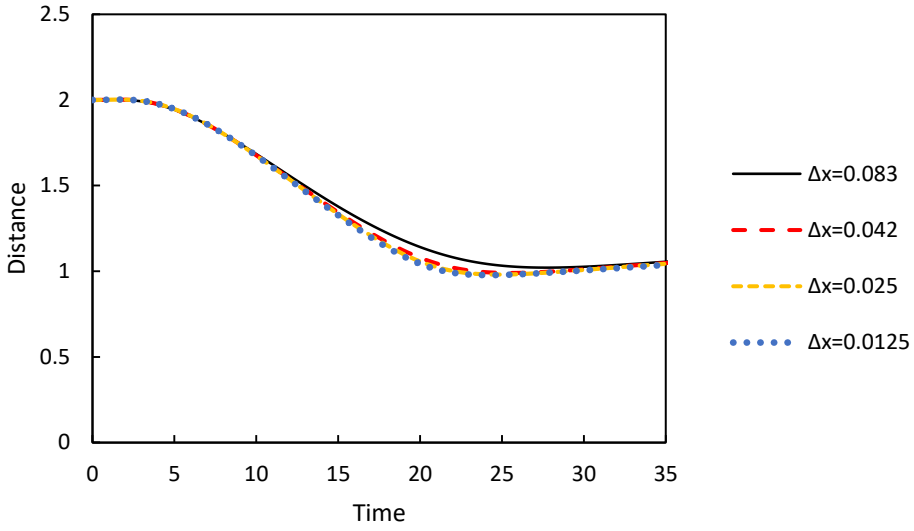

(a)

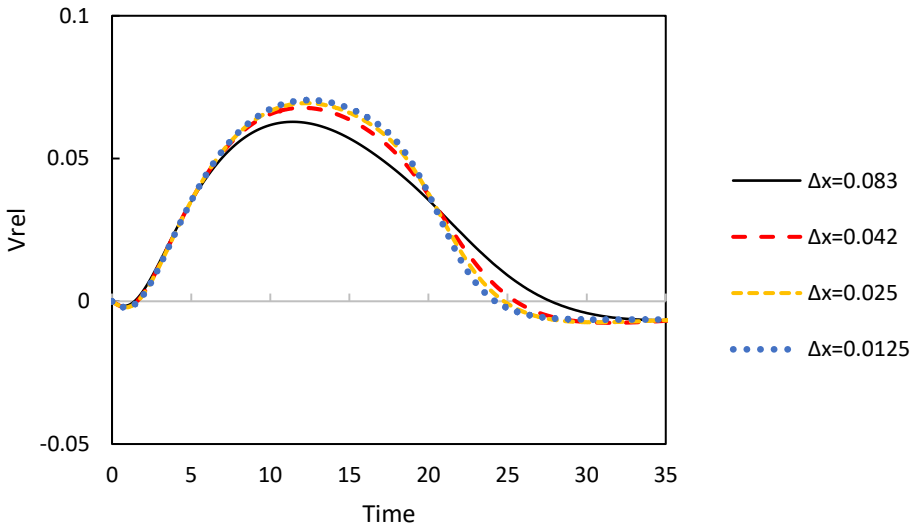

(b)

Figure 6-16- SPM collision model for two spherical particles at the $Re = 20$ at various grid sizes: **(a)** Distance between two particles; **(b)** Relative velocity between two particles.

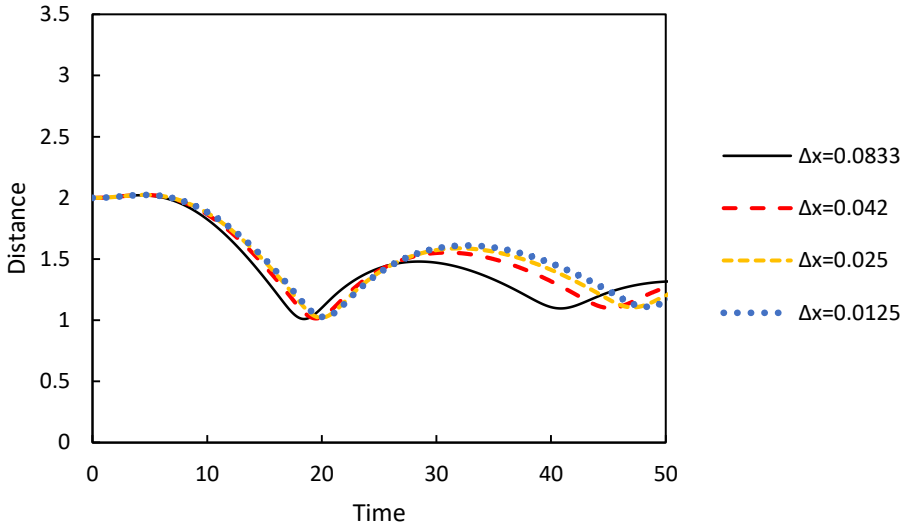

(a)

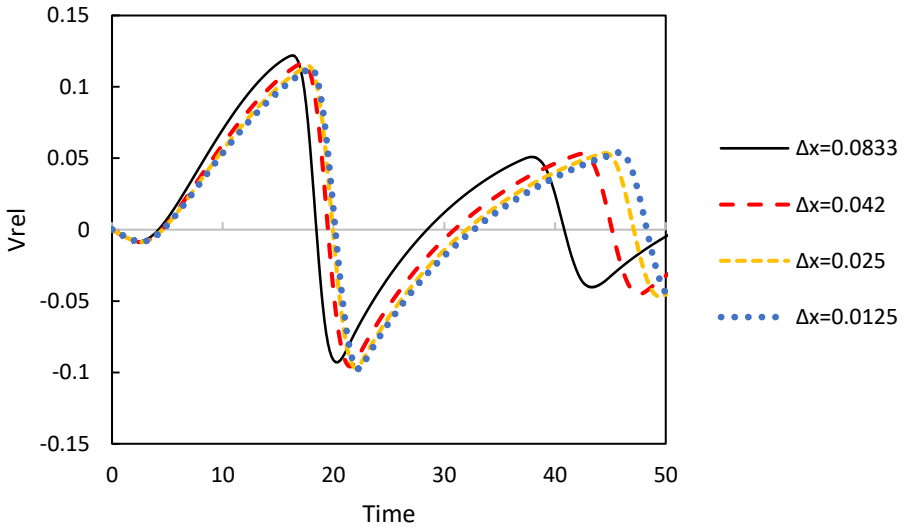

(b)

Figure 6-17- SPM collision model for two spherical particles at the $Re = 150$ at various grid sizes: **(a)** Distance between two particles; **(b)** Relative velocity between two particles.

CHAPTER 7

SIMULATION OF PARTICLE LADEN FLOWS

This chapter describes the study of a channel flow containing multitude of particles. Due to the very high number of the particles, the required memory to store the particle data increases significantly. This chapter discusses the particle data structure and then displays the results for the blood flow over a constricted region.

7.1. Data Management of Large Ensembles of Particles

Since blood contains a large number of different types of cells, management of the associated data for each cell as the computational object is very problematic. While storing the cells information data in an array of derived types is possible, it is not efficient for the following reasons:

1- If a particle moves out of the domain the occupied memory related to that particle is not released. Thus, a memory leak occurs which means that the associated part of computer memory is not accessible anymore. Although, it is not a problem when only a few particles are removed from the domain, over a long term this memory leak reduces the efficiency of the hardware and eventually results in insufficient memory for the simulation.

2- It is not possible to add a particle to the domain after constructing the array because the static array size is not changeable. It is possible to add new particles' data by defining a large enough array. However, there are two disadvantages defining the arrays this way: first, most of the time the used memory is significantly higher than the required one. Secondly, there will be not enough space if more particles needed to be defined during the run.

The remedy for this is use of a linked list instead of an array to define the particles' properties which will be described in the next session.

7.1.1. Linked list concept

Unlike arrays, linked lists do not store the data in one series of consecutive blocks of memory and memory does not need to be allocated at the start of the program run. Instead, a linked list features a dynamic data structure, which means that the memory is able to change without limitation during the run. This feature is possible by using pointers. A pointer can allocate and deallocate memory to each particle's data during the run. Having the ability to define the same variable types as an arrays instead of an array index, the properties are defined on each "node" of the linked list in a way that each node represents a particle data such as position, velocity and so on. In addition to the data information related to each particle, each node includes a pointer which is the address to the next node. The address is used to reference to the next node and "link" the list of nodes which is helpful in traversing across the nodes (Figure (7-1)).

7.1.2. Implementation of the linked list

The definition of the linked list starts with allocating a head node, the first node, which does not have any data except for specifying an address to the next node i.e. the first particle node. Namely, the head node only contains a pointer or a "link" to the first node that contains actual data. A head node helps with the process of adding the particles to the linked list. After allocation of the head node, the rest of the nodes are allocated one by one based on the initial number of particles and form a list. In order to move through the linked list, the current node pointer starts by pointing to the head node and by using the link of each node the current pointer moves through the linked list to reach the desired node. Then the associated data is defined as the pointer attribute. The end of the list is identified by either a node that does not point to any extra point or by number of the nodes in the linked list.

Insertion of a node to a linked list is like the construction of the linked list. The new node can be added to anywhere in the list but it is easier to add it after the head node because otherwise, in order to reach a node within the list, a scan over the nodes should be performed. In addition, the sequence of the particles is not important and insertion of the node to anywhere in the linked list is legitimate. The node is inserted by allocating memory dynamically and changing the head node pointer address to point to the new node. Then the pointer of the new node is set to point to the rest of the linked list i.e., the linked list before adding the new node.

To delete a node from the linked list, first the position of the node to be deleted node is spotted in the linked list. Next, the previous node's pointer is assigned to the next one to preserve the continuity of the list. By deallocating the memory associated with the deleting node, memory leak is prevented.

7.1.3. Particle generation from in the input file

One benefit of SPM is that the method does not need implementation of level sets in order to define the object. Level sets use a surface mesh to define the geometry of the object. Interpolations help to define the value of the normal to the surface. In contrast, analytical definition of the particle in the SPM object is easier and more efficient as no interpolation or surface mesh file is required. The SPM object can be defined analytically or with level sets.

To preserve efficiency only one input file is created for SPM in which the number of particles, type of SPM object creation (analytical vs level set), the initial position of the first particle, distances among the particles and their velocities are defined. One option that is useful in setting up the SPM is the random particle generator. If necessary, particles are placed randomly in a domain at the start of the simulation. After the particles start to move in the channel, a space is formed at the entrance for generation of new particles. Particle generation during the simulation also can be random. The issue is that when a new particle is placed in the domain, overlapping may occur. To avoid the particle-particle overlapping, a flag is set for each generated particle. If $\psi - \psi_i > \varepsilon$ and $\psi_i > \varepsilon$ i.e., when the overlapping function

fields have an overlapping more than a certain threshold, ε, the newly generated particle will be removed from the domain.

7.2. Results

In this section, first we investigate the ability of the code to handle a large number of particles by using a linked list data structure with variable number of nodes (particles). Then, we focus on modeling blood as a particle laden flow moving over a constricted region.

7.2.1 Channel flow laden with cylindrical particles

So far the simulation of only one or two particles in a channel has been studied. In this section, the translation of 2D circular cylinder (disk) particles in a channel is considered to investigate the capabilities of the code. The particles have the same density as the fluid which results in a high added mass effect situation and thus the need to use a strongly coupled FSI. The channel which as dimensions of 30×12 is subject to a uniform inlet velocity and the slip wall boundary conditions. There is an initial random placement of the particles as shown in Figure (7-2a). All generated particles have unit diameter and the initial velocity of the particles is $(1.0 \pm 0.2\sigma_1, 0.2\sigma_2)$ with initial angular velocity of $0.01\sigma_3$ where σ_i is a random number between zero and one. The initial number of particles is 30 but this number is changing in the domain due to the linked list feature. Figure (7-2b) represents $T = 4.35$ when the particle on the right of the domain is going out. At the time of removal every related running memory is deallocated. At $T = 4.5$ a particle is added to the domain through the entrance (Figure (7-2c)).

This case shows that the code is capable of handling a large number of particles and updating the linked list when a particle is added or removed from the domain. Since the particles' densities are similar to the fluid, particles reach the flow velocity very fast and at the entrance of the domain. Moreover, because there is no significant disturbance to the flow, the number of collisions is not significant for this case.

7.2.2. Blood flow over a constriction

A channel of 55×16 is subject to uniform unit flow at the entrance at $Re_H = 1600$ based on the channel height. The flow has RBCs and platelets with non-dimensional diameters $D_{RBC} = (2.0,0.5)$ and $D_{platelet} = 1.0$. The average number density of platelet to RBC is set to be $1/15$ with a maximum of $1/8$. All particles and the carrier fluid have the same density. The particles' type, location, angle, velocity and angular velocity at the start of placement in the domain is random and based on Table (7-1). The variable σ_i is a random number used to generate the desired random parameter for the initial particle placement and H is the height of the channel.

The smoothed profile method is used to construct a constriction region with a bump. We use a Gaussian distribution formulation for the bump as

$$f = 10\ exp(-0.2\ x^2) - y \qquad (7\text{-}1)$$

In the above formulation 10 is the height of the bump and the factor 0.2 controls the width. The bump is located at $(18.5, -1)$ and this location is achieved by transferring the axes. The horizontal wings of the Gaussian distribution are located underneath the wall because the walls already have the repulsive forces. Otherwise, the particles do not enter the regions close to the bottom wall due to extra collision forces in the region.

The collision parameters are $\xi_i = 0.1$, $\epsilon_p = 0.5$ and the cut off value for ψ_i is 0.0055 leading to a halo of size 0.26 around each particle. Similar values are defined for the bump and the walls. The simulation ran until $T = 300$. Figure (7-3) show the results for this case at $T = 200$ and it demonstrates that almost uniform distribution of the particles before the constriction and the non-uniform distribution after it. When the particles move over the bump they accelerate. The particles on the top move faster and tent exit from the domain faster. However, the particles that get trapped in the recirculation zone are separated from the top particles. Consequently, there is a small region between these two zones that has fewer particles. As it is clear in the figures, while the soft sphere model used here allows a small amount

of overlapping, the overlapping between the particles is almost negligible. Here, the bump that is defined using SPM formulation also acts as a big fixed particle. It is also clear from the figure that the particles are almost randomly placed in the region, which means almost no particle sorting and alignment occurs.

The velocity contour (Figure (7-4)) shows higher velocity regions over the bump and on the top zone of channel after the bump. The uniform velocity at the entrance accelerates over the bump to satisfy the mass conservation of the incompressible flow. After the bump, the high velocity region decelerates and detaches from the top wall in contact with the low velocity flow behind the bump and the top wall. The perturbations in the velocity occurs because of the rigidity of the particles. They might be more noticeable when two particles collide with high relative velocity.

One important issue for the blood flow over a constricted region is the activation of platelets due to high exposure time to high shear stresses. As shown in Figure (7-5), high shear stress occurs locally when particles collide but because of the very short collision time, the platelets do not activate. Activation of a particle is more likely to happen if it stays in the borders of the recirculation zone. Especially, particles that go through the lower border of the recirculation zone move more slowly and therefore will have more exposure to the high shear stresses. Consequently, particles that that pass through the middle of upper bump zone are more likely to be activated.

Now, we study the probability density function (PDF) or time integral of particles' presence in the domain. The PDF contour at each grid point of the domain signifies the total time the particles stay on each part of the domain. It is represented as

$$PDF = \frac{1}{T_{total}} \sum_{i=1}^{N_{total}} \int \int \varphi_i dx\, dt \qquad (7\text{-}2)$$

where N_{total} is the total number of particles in the domain and T_{total} is the total simulation time. As shown in Figure (7-6), the PDF of particles before reaching the bump is almost uniform. There is an elevated PDF for the lower parts of the upper bump region which is because of the accumulation of particles behind the constriction. After the constriction, the particles disperse again and most of the particles exit the domain from the middle region in the outlet with high velocities. Therefore, even though

most of the particles exit from almost the same region, their high velocity leads to low PDF. On the other hand, the particles trapped behind the bump have very low velocities, leading to higher PDF near the bottom wall behind the bump.

The probability density function (PDF) for the platelets (Figure (7-7)) shows high residence time for platelets close to the lower walls behind the bump where the flow velocity is low. The RBCs tend to push the platelets into the low velocity regions near the bottom wall or the top right corner.

7.3. Suggestions for The Future work

There is still a lot of room for modeling of particle laden flows using SPM. It what follows, I suggest some of cases that might be more relevant to this work:

7.3.1. 3D simulation of particles:

3D simulation of Simulation of particles is more challenging than 2D because in 2D the translation is restricted in one direction and the rotation is restricted in two directions. Changing the particle degree of freedom from three to six may trigger more instabilities related to the added mass. Moreover, 3D simulation has a huge computational cost that might require extra modifications in parallel processing.

7.3.2. Implementation of other FSI relaxation techniques:

Aitken acceleration is implemented in the subiterative process and helps to stabilize the simulation; however, other methods such as steepest descent relaxation [225, 226] or vector extrapolation [228] can be used in an iterative scheme designed to avoid instability issues related to high added mass effects. These methods can lead to higher stability in these cases.

7.3.3. Revision of SPM to allow overlapping interfaces:

The no slip and no penetration boundary condition on the particle surface is satisfied if the indicator function of the two nearby particles are not overlapping. If overlapping occurs violation of the boundary condition can lead to unphysical results and instability. Therefore, if the method is modified in a way that with the overlapping of two particles' indicator functions, the boundary conditions are still satisfied, the problem can be solved. However, developing the formulation in this way might not be feasible as changing this intrinsic mathematical feature of the method may cause other difficulties.

7.3.4. Unsteady flow in a constriction

As a more realistic case, unsteady flow in a constricted region could be studied. A pulsatile flow based on systole and diastole time can be applied to the entrance and the unsteady effects on the interaction of the particles is studied. The differences between this case and the steady case can be the different formation of the recirculation zone, and different shear stress time, and PDF for the particles.

7.3.5. Implementation of SSCM

As SSCM can capture the tangential component of a collision, it is more accurate than PPCM. While SSCM is more complicated, it will lead to more comprehensive results. Therefore, use of SSCM for studying a flow in a constriction can have substantial benefits.

7.4. Conclusions

We simulated motion of blood cells in a constricted region using a random pattern for particle generation at the inlet. The concept of using a linked list to represent the dynamic data structure of the particles was useful in handling a large number of particles. We studied the motion and the interaction of the particles with each other the enclosing surfaces and showed the effectiveness of PPCM.

It shown that the platelets' activation is more likely to happen for the particles that pass from the middle of the upper bump region because those particles will have longer exposure time to the high shear flow behind the bump. PDF contour of particles' presence show the more concentrated presence of the particles near the bump. Moreover, the interaction of RBCs and platelets pushes the platelets toward the wall after the bottom wall.

TABLES

Table 7-1- The initial random placement characteristics of the particles.

Variable	Formulation
Initial location	$(1 \pm 0.1\sigma_1, (H-1)\sigma_2 + 0.5)$
Initial velocity	$1 \pm 0.1\sigma_3$
Initial angle	$\pi\sigma_4$
Initial angular velocity	$0.1\sigma_5$

FIGURES

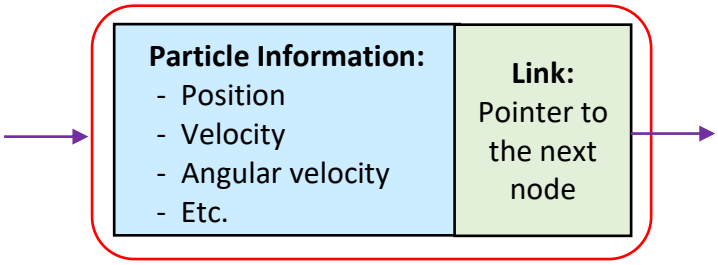

Particle i

(a)

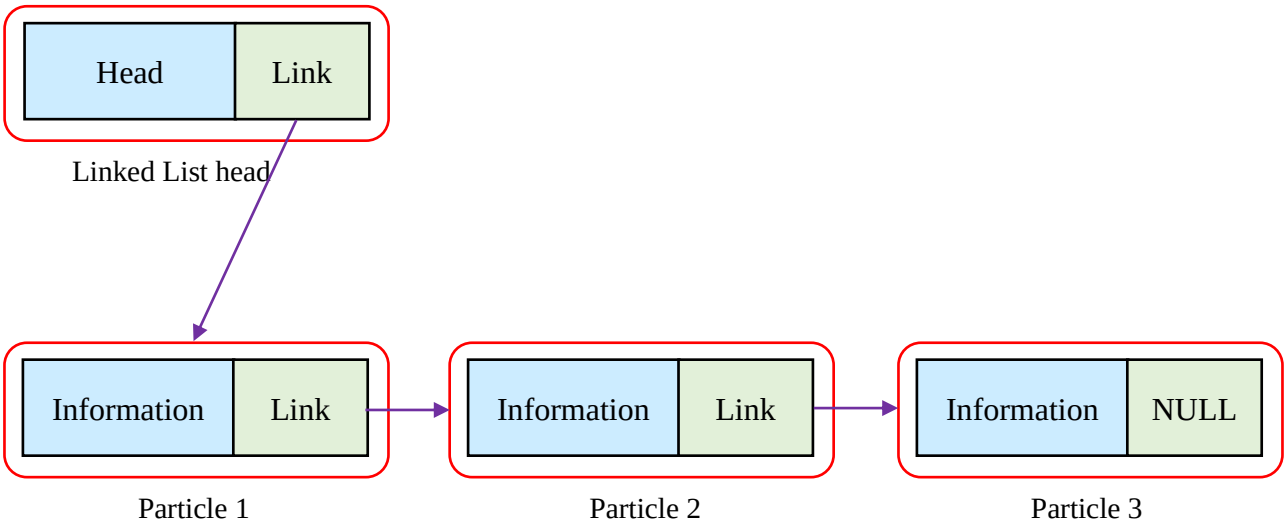

(b)

Figure 7-1- A schematic for the linked list. (a) A node on the linked list to describe particle i. (b) A linked list of three particles.

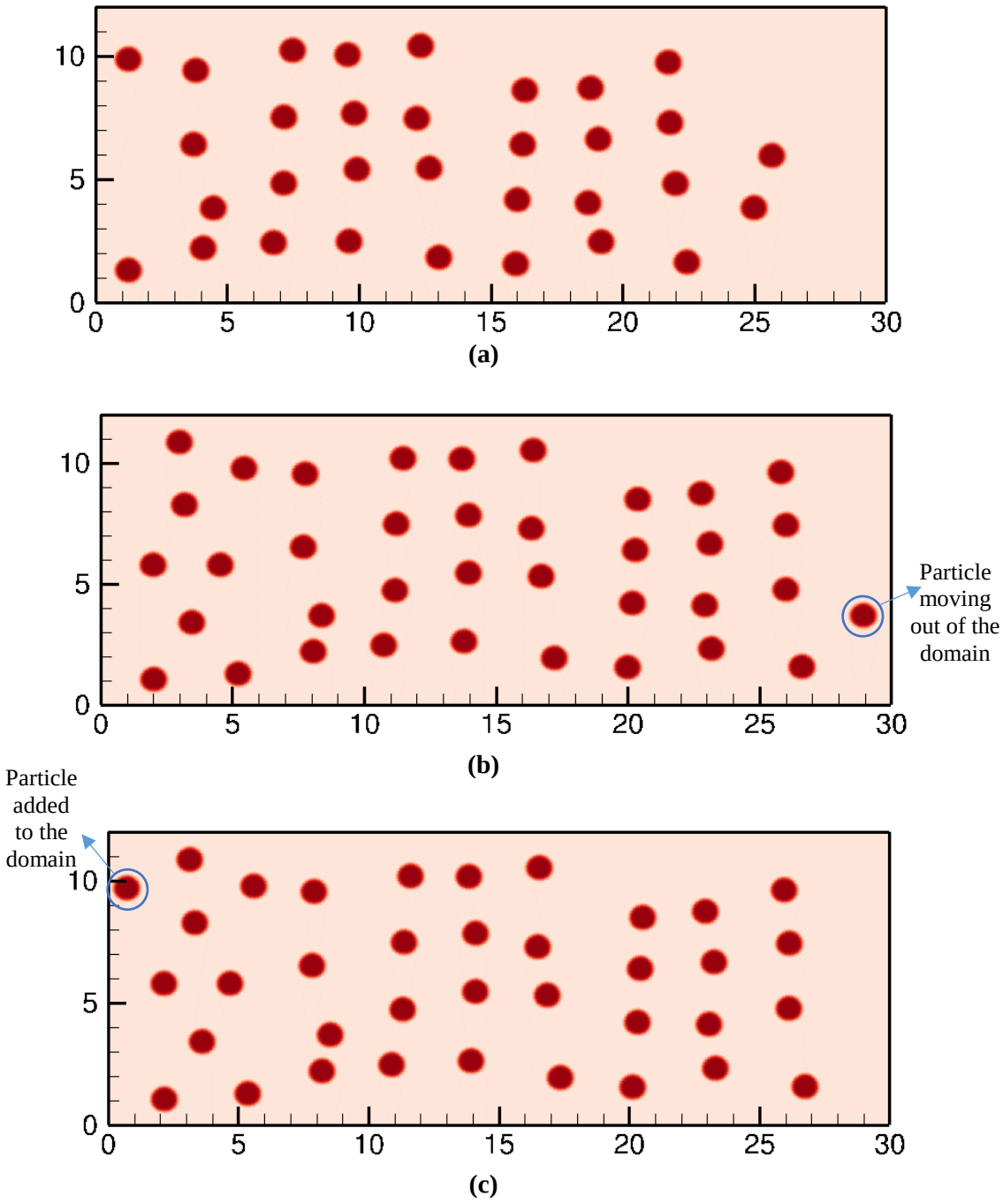

Figure 7-2- Motion of cylindrical particles in a 2D channel. **(a)** The Initial configuration of particles in the channel. **(b)** Configuration of the particles at $T = 4.35$ before removal of one particle from the domain and adding a particle to the domain. **(c)** Configuration of the particles at $T = 4.5$ after removal of one particle from the domain and adding a particle to the domain.

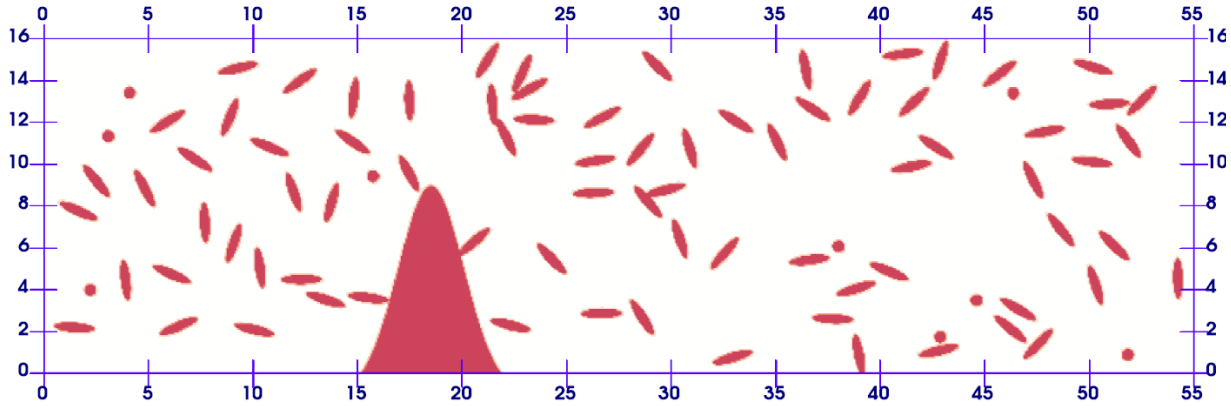

Figure 7-3- A snapshot of the position of blood cells in the flow over a constricted region. The particles are randomly placed at the entrance of the domain and move over the bump. A soft collision capturing method for the collision of general shape particles is used to avoid particles' overlapping.

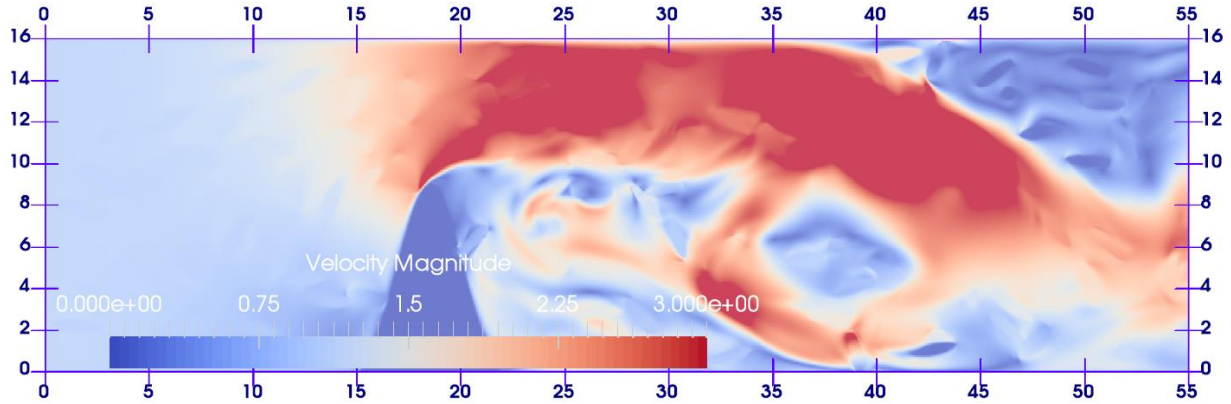

Figure 7-4- A snapshot of the velocity for the flow over a constricted region. There is a high velocity region over the bump and a low velocity region behind the bump. The perturbations in the average flow are because of the presence of rigid particles in the domain and their collision.

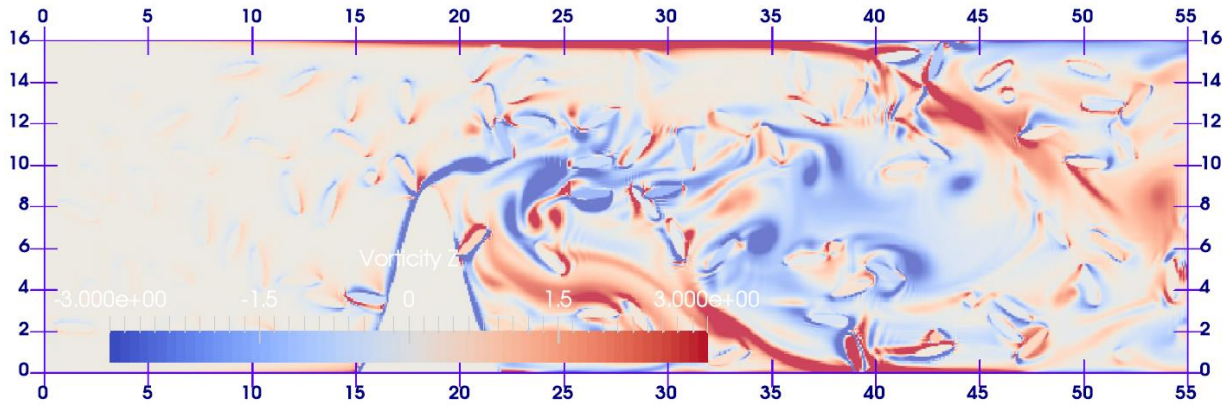

Figure 7-5- A snapshot of shear stress in the domain. Long time exposure to high shear stresses leads to platelet activation. Therefore, while the rigid particles during the collision times have very high shear stress values, the platelets do not activate due to the short collision period. However, at the high shear regions behind the bump, the activation is more likely to happen.

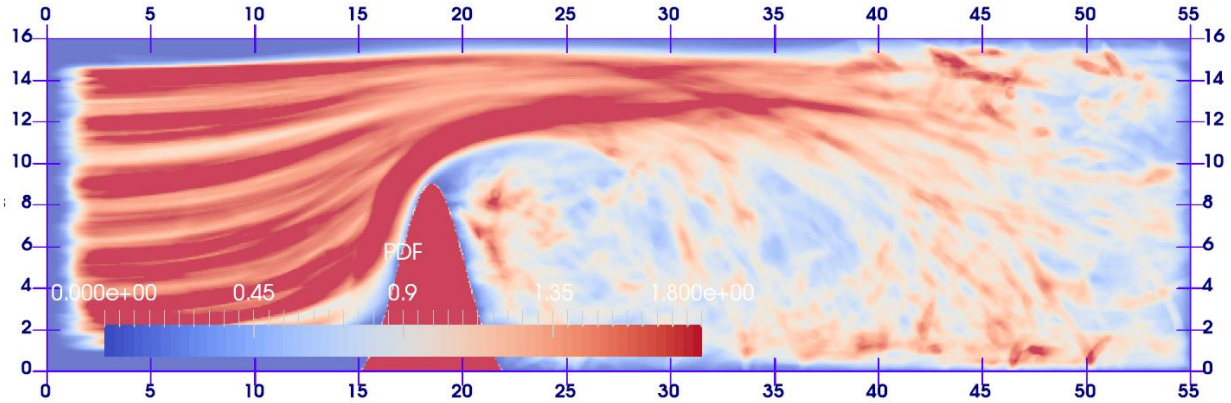

Figure 7-6- The probability density function (PDF) displays the time integral of particles' presence in the domain. It shows that the particles have low presence in the low velocity region behind the bump. This is because the majority of the particles tend to exit the domain from the middle region in the outlet with very high velocities.

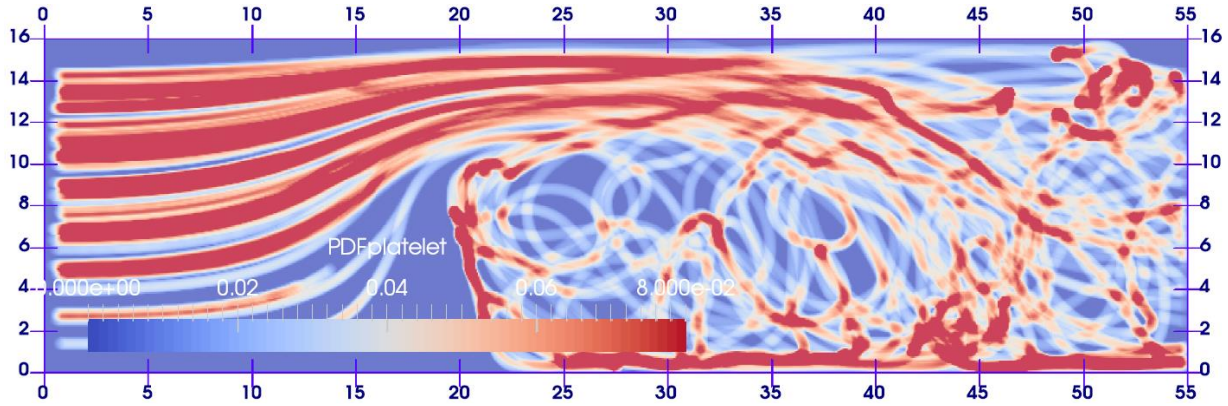

Figure 7-7- The probability density function (PDF) for the platelets shows the high residence time of platelets close to the lower walls behind the bump where the flow velocity is low. The RBCs tend to push the platelets to the low velocity regions near the bottom wall.

REFERENCES

1. Gondret, P., M. Lance, and L. Petit, *Bouncing motion of spherical particles in fluids.* Physics of Fluids (1994-present), 2002. **14**(2): p. 643-652.
2. Arias, E., et al., *National vital statistics reports.* Deaths: Final data for 2001, 2013. **52**.
3. Nkomo, V.T., et al., *Burden of valvular heart diseases: a population-based study.* The Lancet, 2006. **368**(9540): p. 1005-1011.
4. Pibarot, P. and J.G. Dumesnil, *Prosthetic heart valves selection of the optimal prosthesis and long-term management.* Circulation, 2009. **119**(7): p. 1034-1048.
5. Yacoub, M. and J. Takkenberg, *Will heart valve tissue engineering change the world?* Nature clinical practice cardiovascular medicine, 2005. **2**(2): p. 60-61.
6. Cheng, R., Y.G. Lai, and K.B. Chandran, *Three-dimensional fluid-structure interaction simulation of bileaflet mechanical heart valve flow dynamics.* Annals of biomedical engineering, 2004. **32**(11): p. 1471-1483.
7. Waite, L., *Biofluid mechanics in cardiovascular systems*. 2005: McGraw Hill Professional.
8. Dasi, L.P., et al., *Fluid mechanics of artificial heart valves.* Clinical and experimental pharmacology and physiology, 2009. **36**(2): p. 225-237.
9. Simon, H.A., et al., *Simulation of the three-dimensional hinge flow fields of a bileaflet mechanical heart valve under aortic conditions.* Annals of biomedical engineering, 2010. **38**(3): p. 841-853.
10. Yoganathan, A.P., Z. He, and S. Casey Jones, *Fluid mechanics of heart valves.* Annu. Rev. Biomed. Eng., 2004. **6**: p. 331-362.
11. Körfer, R., et al., *The worldwide mid-term experience with the Medtronic ADVANTAGE bileaflet mechanical heart valve.* The Journal of heart valve disease, 2006. **15**(3): p. 404-12; discussion 413.
12. Bluestein, D., Y. Li, and I. Krukenkamp, *Free emboli formation in the wake of bi-leaflet mechanical heart valves and the effects of implantation techniques.* Journal of biomechanics, 2002. **35**(12): p. 1533-1540.
13. Hedayat, M., H. Asgharzadeh, and I. Borazjani, *Platelet activation of mechanical versus bioprosthetic heart valves during systole.* Journal of Biomechanics, 2017. **56**: p. 111-116.
14. Simon, H.A., et al., *Numerical investigation of the performance of three hinge designs of bileaflet mechanical heart valves.* Annals of biomedical engineering, 2010. **38**(11): p. 3295-3310.
15. Wurzinger, L., et al., *" Shear induced platelet activation"--a critical reappraisal.* Biorheology, 1984. **22**(5): p. 399-413.
16. Hellums, J.D., *1993 Whitaker Lecture: biorheology in thrombosis research.* Annals of biomedical engineering, 1994. **22**(5): p. 445-455.
17. Ellis, J., et al., *Velocity measurements and flow patterns within the hinge region of a Medtronic Parallel bileaflet mechanical valve with clear housing.* The Journal of heart valve disease, 1996. **5**(6): p. 591-599.
18. Leo, H.-L., et al., *Microflow fields in the hinge region of the CarboMedics bileaflet mechanical heart valve design.* The Journal of thoracic and cardiovascular surgery, 2002. **124**(3): p. 561-574.

19. Saxena, R., et al., *An in vitro assessment by means of laser Doppler velocimetry of the medtronic advantage bileaflet mechanical heart valve hinge flow.* The Journal of thoracic and cardiovascular surgery, 2003. **126**(1): p. 90-98.
20. Ellis, J.T. and A.P. Yoganathan, *A comparison of the hinge and near-hinge flow fields of the St Jude medical hemodynamic plus and regent bileaflet mechanical heart valves.* The Journal of thoracic and cardiovascular surgery, 2000. **119**(1): p. 83-93.
21. Simon, H.A., et al., *Comparison of the hinge flow fields of two bileaflet mechanical heart valves under aortic and mitral conditions.* Annals of biomedical engineering, 2004. **32**(12): p. 1607-1617.
22. Nobili, M., et al., *Numerical simulation of the dynamics of a bileaflet prosthetic heart valve using a fluid–structure interaction approach.* Journal of biomechanics, 2008. **41**(11): p. 2539-2550.
23. Dumont, K., et al., *Comparison of the hemodynamic and thrombogenic performance of two bileaflet mechanical heart valves using a CFD/FSI model.* Journal of Biomechanical Engineering, 2007. **129**(4): p. 558-565.
24. Ciarlet, P.G., *The finite element method for elliptic problems*. Vol. 40. 2002: Siam.
25. Sui, Y., et al., *Dynamic motion of red blood cells in simple shear flow.* Physics of Fluids (1994-present), 2008. **20**(11): p. 112106.
26. Zarda, P., S. Chien, and R. Skalak, *Elastic deformations of red blood cells.* Journal of biomechanics, 1977. **10**(4): p. 211-221.
27. Dao, M., C. Lim, and S. Suresh, *Mechanics of the human red blood cell deformed by optical tweezers.* Journal of the Mechanics and Physics of Solids, 2003. **51**(11): p. 2259-2280.
28. Eggleton, C.D. and A.S. Popel, *Large deformation of red blood cell ghosts in a simple shear flow.* Physics of Fluids (1994-present), 1998. **10**(8): p. 1834-1845.
29. Wang, C.-H. and A.S. Popel, *Effect of red blood cell shape on oxygen transport in capillaries.* Mathematical biosciences, 1993. **116**(1): p. 89-110.
30. Han, K.-H. and A.B. Frazier, *Continuous magnetophoretic separation of blood cells in microdevice format.* Journal of Applied Physics, 2004. **96**(10): p. 5797-5802.
31. Tan, Y., et al., *Mechanical characterization of human red blood cells under different osmotic conditions by robotic manipulation with optical tweezers.* Biomedical Engineering, IEEE Transactions on, 2010. **57**(7): p. 1816-1825.
32. Secomb, T.W., B. Styp-Rekowska, and A.R. Pries, *Two-dimensional simulation of red blood cell deformation and lateral migration in microvessels.* Annals of biomedical engineering, 2007. **35**(5): p. 755-765.
33. AlMomani, T., et al., *Micro-scale dynamic simulation of erythrocyte–platelet interaction in blood flow.* Annals of biomedical engineering, 2008. **36**(6): p. 905-920.
34. Zhang, L., et al., *Immersed finite element method.* Computer Methods in Applied Mechanics and Engineering, 2004. **193**(21): p. 2051-2067.
35. Liu, W.K., et al., *Immersed finite element method and its applications to biological systems.* Computer Methods in Applied Mechanics and Engineering, 2006. **195**(13): p. 1722-1749.
36. Liu, Y. and W.K. Liu, *Rheology of red blood cell aggregation by computer simulation.* Journal of Computational Physics, 2006. **220**(1): p. 139-154.
37. Banerjee, P.K. and R. Butterfield, *Boundary element methods in engineering science*. Vol. 17. 1981: McGraw-Hill London.
38. Ramanujan, S. and C. Pozrikidis, *Deformation of liquid capsules enclosed by elastic membranes in simple shear flow: large deformations and the effect of fluid viscosities.* Journal of Fluid Mechanics, 1998. **361**: p. 117-143.

39. Chen, S. and G.D. Doolen, *Lattice Boltzmann method for fluid flows.* Annual review of fluid mechanics, 1998. **30**(1): p. 329-364.
40. Dupin, M., et al., *Lattice Boltzmann modelling of blood cell dynamics.* International Journal of Computational Fluid Dynamics, 2008. **22**(7): p. 481-492.
41. Dupin, M.M., et al., *Modeling the flow of dense suspensions of deformable particles in three dimensions.* Physical Review E, 2007. **75**(6): p. 066707.
42. Zhang, J., P.C. Johnson, and A.S. Popel, *Red blood cell aggregation and dissociation in shear flows simulated by lattice Boltzmann method.* Journal of biomechanics, 2008. **41**(1): p. 47-55.
43. Zhang, J., P.C. Johnson, and A.S. Popel, *An immersed boundary lattice Boltzmann approach to simulate deformable liquid capsules and its application to microscopic blood flows.* Physical biology, 2007. **4**(4): p. 285.
44. Krüger, T., et al., *Numerical simulations of complex fluid-fluid interface dynamics.* The European Physical Journal Special Topics, 2013. **222**(1): p. 177-198.
45. Bagchi, P., P.C. Johnson, and A.S. Popel, *Computational fluid dynamic simulation of aggregation of deformable cells in a shear flow.* Journal of biomechanical engineering, 2005. **127**(7): p. 1070-1080.
46. Doddi, S.K. and P. Bagchi, *Three-dimensional computational modeling of multiple deformable cells flowing in microvessels.* Physical Review E, 2009. **79**(4): p. 046318.
47. Peskin, C.S., *Numerical analysis of blood flow in the heart.* Journal of computational physics, 1977. **25**(3): p. 220-252.
48. Piegl, L. and W. Tiller, *The NURBS book*. 2012: Springer Science & Business Media.
49. Lu, J., *Isogeometric contact analysis: Geometric basis and formulation for frictionless contact.* Computer Methods in Applied Mechanics and Engineering, 2011. **200**(5): p. 726-741.
50. Chivukula, V.K., *Development of a NURBS-based particulate dynamics framework for modeling circulating cells.* 2014.
51. Freund, J.B., *Numerical simulation of flowing blood cells.* Annual Review of Fluid Mechanics, 2014. **46**: p. 67-95.
52. Groot, R.D. and P.B. Warren, *Dissipative particle dynamics: Bridging the gap between atomistic and mesoscopic simulation.* Journal of Chemical Physics, 1997. **107**(11): p. 4423.
53. Fedosov, D.A., et al., *Blood Flow and Cell ‐Free Layer in Microvessels.* Microcirculation, 2010. **17**(8): p. 615-628.
54. Imai, Y., et al., *Modeling of hemodynamics arising from malaria infection.* Journal of biomechanics, 2010. **43**(7): p. 1386-1393.
55. Sun, C. and L.L. Munn, *Particulate nature of blood determines macroscopic rheology: a 2-D lattice Boltzmann analysis.* Biophysical journal, 2005. **88**(3): p. 1635-1645.
56. Fåhræus, R. and T. Lindqvist, *The viscosity of the blood in narrow capillary tubes.* American Journal of Physiology--Legacy Content, 1931. **96**(3): p. 562-568.
57. Goldsmith, H.L., G.R. Cokelet, and P. Gaehtgens, *Robin Fahraeus: evolution of his concepts in cardiovascular physiology.* American Journal of Physiology-Heart and Circulatory Physiology, 1989. **257**(3): p. H1005-H1015.
58. Tokarev, A., et al., *Finite platelet size could be responsible for platelet margination effect.* Biophysical journal, 2011. **101**(8): p. 1835-1843.
59. Zhang, J., P.C. Johnson, and A.S. Popel, *Effects of erythrocyte deformability and aggregation on the cell free layer and apparent viscosity of microscopic blood flows.* Microvascular research, 2009. **77**(3): p. 265-272.
60. Vahidkhah, K., S.L. Diamond, and P. Bagchi, *Platelet dynamics in three-dimensional simulation of whole blood.* Biophysical journal, 2014. **106**(11): p. 2529-2540.

61. Zhao, H., et al., *A spectral boundary integral method for flowing blood cells.* Journal of Computational Physics, 2010. **229**(10): p. 3726-3744.
62. Rahimian, A., et al. *Petascale direct numerical simulation of blood flow on 200k cores and heterogeneous architectures*. in *Proceedings of the 2010 ACM/IEEE International Conference for High Performance Computing, Networking, Storage and Analysis*. 2010. IEEE Computer Society.
63. Chandran, K.B., H. Udaykumar, and J.M. Reinhardt, *Image-Based Computational Modeling of the Human Circulatory and Pulmonary Systems*. 2011: Springer.
64. Ku, D.N., *Blood flow in arteries.* Annual Review of Fluid Mechanics, 1997. **29**(1): p. 399-434.
65. Sotiropoulos, F., et al., *Computational techniques for biological fluids: from blood vessel scale to blood cells*, in *Image-Based Computational Modeling of the Human Circulatory and Pulmonary Systems*. 2011, Springer. p. 105-155.
66. Krishnan, S., et al., *Two-dimensional dynamic simulation of platelet activation during mechanical heart valve closure.* Annals of biomedical engineering, 2006. **34**(10): p. 1519-1534.
67. Lai, Y.G., K.B. Chandran, and J. Lemmon, *A numerical simulation of mechanical heart valve closure fluid dynamics.* Journal of Biomechanics, 2002. **35**(7): p. 881-892.
68. Vierendeels, J., et al., *Analysis and stabilization of fluid-structure interaction algorithm for rigid-body motion.* AIAA journal, 2005. **43**(12): p. 2549-2557.
69. Mousel, J.A., *A massively parallel adaptive sharp interface solver with application to mechanical heart valve simulations.* 2012.
70. Borazjani, I., L. Ge, and F. Sotiropoulos, *Curvilinear immersed boundary method for simulating fluid structure interaction with complex 3D rigid bodies.* Journal of Computational physics, 2008. **227**(16): p. 7587-7620.
71. Borazjani, I., L. Ge, and F. Sotiropoulos, *High-resolution fluid–structure interaction simulations of flow through a bi-leaflet mechanical heart valve in an anatomic aorta.* Annals of biomedical engineering, 2010. **38**(2): p. 326-344.
72. Ge, L. and F. Sotiropoulos, *A numerical method for solving the 3D unsteady incompressible Navier–Stokes equations in curvilinear domains with complex immersed boundaries.* Journal of computational physics, 2007. **225**(2): p. 1782-1809.
73. De Hart, J., et al., *A three-dimensional computational analysis of fluid–structure interaction in the aortic valve.* Journal of biomechanics, 2003. **36**(1): p. 103-112.
74. Nakayama, Y. and R. Yamamoto, *Simulation method to resolve hydrodynamic interactions in colloidal dispersions.* Physical Review E, 2005. **71**(3): p. 036707.
75. Luo, X., M.R. Maxey, and G.E. Karniadakis, *Smoothed profile method for particulate flows: Error analysis and simulations.* Journal of Computational Physics, 2009. **228**(5): p. 1750-1769.
76. Kim, J. and P. Moin, *Application of a fractional-step method to incompressible Navier-Stokes equations.* Journal of computational physics, 1985. **59**(2): p. 308-323.
77. Perot, J.B., *An analysis of the fractional step method.* Journal of Computational Physics, 1993. **108**(1): p. 51-58.
78. Butany, J., et al., *Mechanical heart valve prostheses:: identification and evaluation (erratum).* Cardiovascular pathology, 2003. **12**(6): p. 322-344.
79. Russel, W.B., D.A. Saville, and W.R. Schowalter, *Colloidal dispersions*. 1992: Cambridge university press.
80. Ladd, A.J., *Numerical simulations of particulate suspensions via a discretized Boltzmann equation. Part 1. Theoretical foundation.* Journal of Fluid Mechanics, 1994. **271**: p. 285-309.
81. Nabian, M.A., *An efficient mesh-free particle method for modeling of free surface and multiphase flows*. 2015, The George Washington University.

82. Nabian, M.A. and L. Farhadi, *Multiphase Mesh-Free Particle Method for Simulating Granular Flows and Sediment Transport.* Journal of Hydraulic Engineering, 2016. **143**(4): p. 04016102.
83. Hinds, W.C., *Aerosol technology: properties, behavior, and measurement of airborne particles*. 2012: John Wiley & Sons.
84. MacMECCAN, R.M., et al., *Simulating deformable particle suspensions using a coupled lattice-Boltzmann and finite-element method.* Journal of Fluid Mechanics, 2009. **618**: p. 13-39.
85. Kim, I., S. Elghobashi, and W.A. Sirignano, *Three-dimensional flow over two spheres placed side by side.* Journal of Fluid Mechanics, 1993. **246**: p. 465-488.
86. Kim, D. and H. Choi, *Laminar flow past a sphere rotating in the streamwise direction.* Journal of Fluid Mechanics, 2002. **461**: p. 365-386.
87. Schlatter, P., *Spectral Methods.* Lecture Notes KTH, 2009.
88. Bagchi, P. and S. Balachandar, *Shear versus vortex-induced lift force on a rigid sphere at moderate Re.* Journal of Fluid Mechanics, 2002. **473**: p. 379-388.
89. Uhlmann, M. and J. Dušek, *The motion of a single heavy sphere in ambient fluid: a benchmark for interface-resolved particulate flow simulations with significant relative velocities.* International Journal of Multiphase Flow, 2014. **59**: p. 221-243.
90. Fischer, P.F., G.K. Leaf, and J.M. Restrepo, *Forces on particles in oscillatory boundary layers.* Journal of Fluid Mechanics, 2002. **468**: p. 327-347.
91. Prosperetti, A. and G. Tryggvason, *Computational methods for multiphase flow*. 2007: Cambridge university press.
92. Johnson, A.A. and T.E. Tezduyar, *3D simulation of fluid-particle interactions with the number of particles reaching 100.* Computer Methods in Applied Mechanics and Engineering, 1997. **145**(3): p. 301-321.
93. Hu, H.H., *Direct simulation of flows of solid-liquid mixtures.* International Journal of Multiphase Flow, 1996. **22**(2): p. 335-352.
94. Hu, H.H., N.A. Patankar, and M. Zhu, *Direct numerical simulations of fluid–solid systems using the arbitrary Lagrangian–Eulerian technique.* Journal of Computational Physics, 2001. **169**(2): p. 427-462.
95. Riemslagh, K., J. Vierendeels, and E. Dick, *An arbitrary Lagrangian–Eulerian finite-volume method for the simulation of rotary displacement pump flow.* Applied numerical mathematics, 2000. **32**(4): p. 419-433.
96. Arienti, M., et al., *A level set approach to Eulerian–Lagrangian coupling.* Journal of Computational Physics, 2003. **185**(1): p. 213-251.
97. Al Quddus, N., W.A. Moussa, and S. Bhattacharjee, *Motion of a spherical particle in a cylindrical channel using arbitrary Lagrangian–Eulerian method.* Journal of colloid and interface science, 2008. **317**(2): p. 620-630.
98. Chayantrakom, K., *Mathematical modelling of particle-fluid flows in microchannels*. 2009: Curtin University of Technology.
99. Ai, Y., et al., *Pressure-driven transport of particles through a converging-diverging microchannel.* Biomicrofluidics, 2009. **3**(2): p. 022404.
100. Ai, Y., et al., *Electrokinetic motion of a deformable particle: Dielectrophoretic effect.* Electrophoresis, 2011. **32**(17): p. 2282-2291.
101. Ai, Y., Z. Zeng, and S. Qian, *Direct numerical simulation of AC dielectrophoretic particle–particle interactive motions.* Journal of colloid and interface science, 2014. **417**: p. 72-79.
102. Mittal, R. and G. Iaccarino, *Immersed boundary methods.* Annu. Rev. Fluid Mech., 2005. **37**: p. 239-261.

103. Udaykumar, H., W. Shyy, and M. Rao, *Elafint: a mixed Eulerian–Lagrangian method for fluid flows with complex and moving boundaries.* International journal for numerical methods in fluids, 1996. **22**(8): p. 691-712.
104. Udaykumar, H., R. Mittal, and W. Shyy, *Computation of solid–liquid phase fronts in the sharp interface limit on fixed grids.* Journal of computational physics, 1999. **153**(2): p. 535-574.
105. Udaykumar, H., et al., *A sharp interface Cartesian grid method for simulating flows with complex moving boundaries.* Journal of Computational Physics, 2001. **174**(1): p. 345-380.
106. Marella, S., et al., *Sharp interface Cartesian grid method I: an easily implemented technique for 3D moving boundary computations.* Journal of Computational Physics, 2005. **210**(1): p. 1-31.
107. Seo, J.H. and R. Mittal, *A sharp-interface immersed boundary method with improved mass conservation and reduced spurious pressure oscillations.* Journal of computational physics, 2011. **230**(19): p. 7347-7363.
108. Ye, T., W. Shyy, and J.N. Chung, *A fixed-grid, sharp-interface method for bubble dynamics and phase change.* Journal of Computational Physics, 2001. **174**(2): p. 781-815.
109. Sussman, M., et al., *A sharp interface method for incompressible two-phase flows.* Journal of computational physics, 2007. **221**(2): p. 469-505.
110. Ye, T., et al., *An accurate Cartesian grid method for viscous incompressible flows with complex immersed boundaries.* Journal of computational physics, 1999. **156**(2): p. 209-240.
111. Ohta, M., et al., *The sensitivity of drop motion due to the density and viscosity ratio.* Physics of Fluids (1994-present), 2010. **22**(7): p. 072102.
112. Fedkiw, R.P., et al., *A non-oscillatory Eulerian approach to interfaces in multimaterial flows (the ghost fluid method).* Journal of computational physics, 1999. **152**(2): p. 457-492.
113. Sethian, J. and P. Smereka, *Level set methods for fluid interfaces.* Annual Review of Fluid Mechanics, 2003. **35**(1): p. 341-372.
114. Hong, J.-M. and C.-H. Kim, *Discontinuous fluids.* ACM Transactions on Graphics (TOG), 2005. **24**(3): p. 915-920.
115. Kim, B., et al. *Simulation of bubbles in foam with the volume control method*. in *ACM Transactions on Graphics (TOG)*. 2007. ACM.
116. Van Poppel, B., O. Desjardins, and J. Daily, *A ghost fluid, level set methodology for simulating multiphase electrohydrodynamic flows with application to liquid fuel injection.* Journal of Computational Physics, 2010. **229**(20): p. 7977-7996.
117. Ménard, T., S. Tanguy, and A. Berlemont, *Coupling level set/VOF/ghost fluid methods: Validation and application to 3D simulation of the primary break-up of a liquid jet.* International Journal of Multiphase Flow, 2007. **33**(5): p. 510-524.
118. Peskin, C.S., *Flow patterns around heart valves: a numerical method.* Journal of computational physics, 1972. **10**(2): p. 252-271.
119. Bandringa, H., *Immersed boundary methods.* MasterΓs thesis, University of Groningen, 2010. **9700**.
120. Fogelson, A.L. and C.S. Peskin, *A fast numerical method for solving the three-dimensional Stokes' equations in the presence of suspended particles.* Journal of Computational Physics, 1988. **79**(1): p. 50-69.
121. Höfler, K. and S. Schwarzer, *Navier-Stokes simulation with constraint forces: Finite-difference method for particle-laden flows and complex geometries.* Physical Review E, 2000. **61**(6): p. 7146.
122. Bagchi, P., *Mesoscale simulation of blood flow in small vessels.* Biophysical journal, 2007. **92**(6): p. 1858-1877.

123. Kempe, T. and J. Fröhlich, *An improved immersed boundary method with direct forcing for the simulation of particle laden flows.* Journal of Computational Physics, 2012. **231**(9): p. 3663-3684.
124. Glowinski, R., et al., *A fictitious domain approach to the direct numerical simulation of incompressible viscous flow past moving rigid bodies: application to particulate flow.* Journal of Computational Physics, 2001. **169**(2): p. 363-426.
125. Uhlmann, M., *An immersed boundary method with direct forcing for the simulation of particulate flows.* Journal of Computational Physics, 2005. **209**(2): p. 448-476.
126. Wang, Z., J. Fan, and K. Luo, *Combined multi-direct forcing and immersed boundary method for simulating flows with moving particles.* International Journal of Multiphase Flow, 2008. **34**(3): p. 283-302.
127. Wachs, A., *A DEM-DLM/FD method for direct numerical simulation of particulate flows: Sedimentation of polygonal isometric particles in a Newtonian fluid with collisions.* Computers & Fluids, 2009. **38**(8): p. 1608-1628.
128. Feng, Z.-G. and E.E. Michaelides, *The immersed boundary-lattice Boltzmann method for solving fluid–particles interaction problems.* Journal of Computational Physics, 2004. **195**(2): p. 602-628.
129. Guo, Z., C. Zheng, and B. Shi, *Discrete lattice effects on the forcing term in the lattice Boltzmann method.* Physical Review E, 2002. **65**(4): p. 046308.
130. Feng, Z.-G. and E.E. Michaelides, *Proteus: a direct forcing method in the simulations of particulate flows.* Journal of Computational Physics, 2005. **202**(1): p. 20-51.
131. Zhang, H., et al., *PIBM: Particulate immersed boundary method for fluid–particle interaction problems.* Powder Technology, 2015. **272**: p. 1-13.
132. Glowinski, R., et al., *A distributed Lagrange multiplier/fictitious domain method for particulate flows.* International Journal of Multiphase Flow, 1999. **25**(5): p. 755-794.
133. Patankar, N.A., et al., *A new formulation of the distributed Lagrange multiplier/fictitious domain method for particulate flows.* International Journal of Multiphase Flow, 2000. **26**(9): p. 1509-1524.
134. Apte, S.V., M. Martin, and N.A. Patankar, *A numerical method for fully resolved simulation (FRS) of rigid particle–flow interactions in complex flows.* Journal of Computational Physics, 2009. **228**(8): p. 2712-2738.
135. Singh, P., T. Hesla, and D. Joseph, *Distributed Lagrange multiplier method for particulate flows with collisions.* International Journal of Multiphase Flow, 2003. **29**(3): p. 495-509.
136. Zhang, L. and M. Gay, *Immersed finite element method for fluid-structure interactions.* Journal of Fluids and Structures, 2007. **23**(6): p. 839-857.
137. Wang, X. and W.K. Liu, *Extended immersed boundary method using FEM and RKPM.* Computer Methods in Applied Mechanics and Engineering, 2004. **193**(12): p. 1305-1321.
138. Liu, Y., et al., *Coupling of Navier-Stokes equations with protein molecular dynamics and its application to hemodynamics.* International Journal for Numerical Methods in Fluids, 2004. **46**(12): p. 1237-1252.
139. Lee, L. and R.J. LeVeque, *An Immersed Interface Method for Incompressible Navier--Stokes Equations.* SIAM Journal on Scientific Computing, 2003. **25**(3): p. 832-856.
140. Li, Z., *The immersed interface method using a finite element formulation.* Applied Numerical Mathematics, 1998. **27**(3): p. 253-267.
141. Leveque, R.J. and Z. Li, *The immersed interface method for elliptic equations with discontinuous coefficients and singular sources.* SIAM Journal on Numerical Analysis, 1994. **31**(4): p. 1019-1044.

142. Vigmostad, S.C. and H. Udaykumar, *Algorithms for fluid–structure interaction*, in *Image-Based Computational Modeling of the Human Circulatory and Pulmonary Systems*. 2011, Springer. p. 191-234.
143. Le, D.-V., B.C. Khoo, and J. Peraire, *An immersed interface method for viscous incompressible flows involving rigid and flexible boundaries.* Journal of Computational Physics, 2006. **220**(1): p. 109-138.
144. Xu, S. and Z.J. Wang, *An immersed interface method for simulating the interaction of a fluid with moving boundaries.* Journal of Computational Physics, 2006. **216**(2): p. 454-493.
145. Lomholt, S. and M.R. Maxey, *Force-coupling method for particulate two-phase flow: Stokes flow.* Journal of Computational Physics, 2003. **184**(2): p. 381-405.
146. Fadlun, E., et al., *Combined immersed-boundary finite-difference methods for three-dimensional complex flow simulations.* Journal of Computational Physics, 2000. **161**(1): p. 35-60.
147. Angot, P., C.-H. Bruneau, and P. Fabrie, *A penalization method to take into account obstacles in incompressible viscous flows.* Numerische Mathematik, 1999. **81**(4): p. 497-520.
148. Khadra, K., et al., *Fictitious domain approach for numerical modelling of Navier–Stokes equations.* International journal for numerical methods in fluids, 2000. **34**(8): p. 651-684.
149. Yamamoto, R., K. Kim, and Y. Nakayama, *Strict simulations of non-equilibrium dynamics of colloids.* Colloids and Surfaces A: Physicochemical and Engineering Aspects, 2007. **311**(1): p. 42-47.
150. Yamamoto, R., Y. Nakayama, and K. Kim, *Smoothed profile method to simulate colloidal particles in complex fluids.* International Journal of Modern Physics C, 2009. **20**(09): p. 1457-1465.
151. Kang, S., *Two-dimensional dipolophoretic motion of a pair of ideally polarizable particles under a uniform electric field.* European Journal of Mechanics-B/Fluids, 2013. **41**: p. 66-80.
152. Luo, X., A. Beskok, and G.E. Karniadakis, *Modeling electrokinetic flows by the smoothed profile method.* Journal of computational physics, 2010. **229**(10): p. 3828-3847.
153. Iwashita, T., Y. Nakayama, and R. Yamamoto, *A numerical model for Brownian particles fluctuating in incompressible fluids.* Journal of the Physical Society of Japan, 2008. **77**(7): p. 074007.
154. Kang, S. and Y. Suh, *Direct simulation of flows with suspended paramagnetic particles using one-stage smoothed profile method.* Journal of Fluids and Structures, 2011. **27**(2): p. 266-282.
155. Luo, X., et al., *Comparison of Turbulence Models for Simulating Flow in Waterjets.* 2011.
156. Nakayama, Y., K. Kim, and R. Yamamoto, *Direct simulation of flowing colloidal dispersions by smoothed profile method.* Advanced Powder Technology, 2010. **21**(2): p. 206-211.
157. Hamid, A. and R. Yamamoto, *Direct numerical simulations of anisotropic diffusion of spherical particles in sedimentation.* Physical Review E, 2013. **87**(2): p. 022310.
158. Grinberg, L., D.A. Fedosov, and G.E. Karniadakis, *Parallel multiscale simulations of a brain aneurysm.* Journal of computational physics, 2013. **244**: p. 131-147.
159. Zayernouri, M., et al., *Stochastic smoothed profile method for modeling random roughness in flow problems.* Computer Methods in Applied Mechanics and Engineering, 2013. **263**: p. 99-112.
160. Tatsumi, R. and R. Yamamoto, *Direct numerical simulation of dispersed particles in a compressible fluid.* Physical Review E, 2012. **85**(6): p. 066704.
161. Molina, J.J., Y. Nakayama, and R. Yamamoto, *Hydrodynamic interactions of self-propelled swimmers.* Soft Matter, 2013. **9**(19): p. 4923-4936.

162. Rad, M.T. and C. Beckermann, *Validation of A Model for the Columnar to Equiaxed Transition with Melt Convection.* CFD Modeling and Simulation in Materials Processing 2016: p. 83-92.
163. Mohaghegh, F., H. SM, and M. Doustdar, *Parametric Study of Fuel Vapor Concentration Due to Vaporization of Fuel Droplets in Free Atmosphere* 2009.
164. Choi, H. and P. Moin, *Effects of the computational time step on numerical solutions of turbulent flow.* Journal of Computational Physics, 1994. **113**(1): p. 1-4.
165. Yang, J. and F. Stern, *Sharp interface immersed-boundary/level-set method for wave–body interactions.* Journal of Computational Physics, 2009. **228**(17): p. 6590-6616.
166. Yang, J. and F. Stern, *A simple and efficient direct forcing immersed boundary framework for fluid–structure interactions.* Journal of Computational Physics, 2012. **231**(15): p. 5029-5061.
167. Karniadakis, G. and S. Sherwin, *Spectral/hp element methods for computational fluid dynamics*. 2013: Oxford University Press.
168. Guermond, J., P. Minev, and J. Shen, *An overview of projection methods for incompressible flows.* Computer methods in applied mechanics and engineering, 2006. **195**(44): p. 6011-6045.
169. Timmermans, L., P. Minev, and F. Van De Vosse, *An approximate projection scheme for incompressible flow using spectral elements.* International journal for numerical methods in fluids, 1996. **22**(7): p. 673-688.
170. Brown, D.L., R. Cortez, and M.L. Minion, *Accurate projection methods for the incompressible Navier–Stokes equations.* Journal of computational physics, 2001. **168**(2): p. 464-499.
171. Guermond, J. and J. Shen, *On the error estimates for the rotational pressure-correction projection methods.* Mathematics of Computation, 2004. **73**(248): p. 1719-1737.
172. Shen, J., T. Tang, and L.-L. Wang, *Spectral methods: algorithms, analysis and applications*. Vol. 41. 2011: Springer Science & Business Media.
173. Emmrich, E., *Stability and error of the variable two-step BDF for semilinear parabolic problems.* Journal of Applied Mathematics and Computing, 2005. **19**(1-2): p. 33-55.
174. Mittal, R., et al., *A versatile sharp interface immersed boundary method for incompressible flows with complex boundaries.* Journal of computational physics, 2008. **227**(10): p. 4825-4852.
175. Sambasivan, S.K. and H. UdayKumar, *Sharp interface simulations with Local Mesh Refinement for multi-material dynamics in strongly shocked flows.* Computers & Fluids, 2010. **39**(9): p. 1456-1479.
176. Causon, D.M., et al., *Calculation of shallow water flows using a Cartesian cut cell approach.* Advances in water resources, 2000. **23**(5): p. 545-562.
177. Meinke, M., et al., *A cut-cell method for sharp moving boundaries in Cartesian grids.* Computers & Fluids, 2013. **85**: p. 135-142.
178. Hartmann, D., M. Meinke, and W. Schröder, *A strictly conservative Cartesian cut-cell method for compressible viscous flows on adaptive grids.* Computer Methods in Applied Mechanics and Engineering, 2011. **200**(9): p. 1038-1052.
179. Günther, C., et al., *A Cartesian cut-cell method for sharp moving boundaries.* AIAA Paper, 2011. **3387**: p. 27-30.
180. Gibou, F. and R. Fedkiw, *A fourth order accurate discretization for the Laplace and heat equations on arbitrary domains, with applications to the Stefan problem.* Journal of Computational Physics, 2005. **202**(2): p. 577-601.
181. Luo, H., et al., *On the numerical oscillation of the direct-forcing immersed-boundary method for moving boundaries.* Computers & Fluids, 2012. **56**: p. 61-76.
182. Cheng, N.-S., *Comparison of formulas for drag coefficient and settling velocity of spherical particles.* Powder Technology, 2009. **189**(3): p. 395-398.

183. Johnson, T. and V. Patel, *Flow past a sphere up to a Reynolds number of 300.* Journal of Fluid Mechanics, 1999. **378**: p. 19-70.
184. Sakamoto, H. and H. Haniu, *The formation mechanism and shedding frequency of vortices from a sphere in uniform shear flow.* Journal of Fluid Mechanics, 1995. **287**: p. 151-171.
185. Gushchin, V. and R. Matyushin, *Vortex formation mechanisms in the wake behind a sphere for 200< Re< 380.* Fluid Dynamics, 2006. **41**(5): p. 795-809.
186. Lee, J., et al., *Sources of spurious force oscillations from an immersed boundary method for moving-body problems.* Journal of computational physics, 2011. **230**(7): p. 2677-2695.
187. Schneiders, L., et al., *An accurate moving boundary formulation in cut-cell methods.* Journal of Computational Physics, 2013. **235**: p. 786-809.
188. Yang, J. and E. Balaras, *An embedded-boundary formulation for large-eddy simulation of turbulent flows interacting with moving boundaries.* Journal of Computational Physics, 2006. **215**(1): p. 12-40.
189. Aslam, T.D., *A partial differential equation approach to multidimensional extrapolation.* Journal of Computational Physics, 2004. **193**(1): p. 349-355.
190. Dütsch, H., et al., *Low-Reynolds-number flow around an oscillating circular cylinder at low Keulegan–Carpenter numbers.* Journal of Fluid Mechanics, 1998. **360**: p. 249-271.
191. Fernández, M.A., J.F. Gerbeau, and C. Grandmont, *A projection semi‐implicit scheme for the coupling of an elastic structure with an incompressible fluid.* International Journal for Numerical Methods in Engineering, 2007. **69**(4): p. 794-821.
192. Piperno, S., C. Farhat, and B. Larrouturou, *Partitioned procedures for the transient solution of coupled aroelastic problems Part I: Model problem, theory and two-dimensional application.* Computer methods in applied mechanics and engineering, 1995. **124**(1): p. 79-112.
193. Farhat, C., M. Lesoinne, and P. Le Tallec, *Load and motion transfer algorithms for fluid/structure interaction problems with non-matching discrete interfaces: Momentum and energy conservation, optimal discretization and application to aeroelasticity.* Computer methods in applied mechanics and engineering, 1998. **157**(1): p. 95-114.
194. Causin, P., J.-F. Gerbeau, and F. Nobile, *Added-mass effect in the design of partitioned algorithms for fluid–structure problems.* Computer methods in applied mechanics and engineering, 2005. **194**(42): p. 4506-4527.
195. Mohaghegh, F., J. Mousel, and H. Udaykumar, *Comparison of Sharp Interface and Smoothed Profile Methods for Laminar Flow Analysis Over Stationary and Moving Boundaries*, in *ASME 2014 4th Joint US-European Fluids Engineering Division Summer Meeting collocated with the ASME 2014 12th International Conference on Nanochannels, Microchannels, and Minichannels*. 2014, American Society of Mechanical Engineers: Chicago, IL.
196. Aland, S., et al., *Quantitative comparison of Taylor flow simulations based on sharp‐interface and diffuse‐interface models.* International Journal for Numerical Methods in Fluids, 2013. **73**(4): p. 344-361.
197. Thornton, K., J. Ågren, and P. Voorhees, *Modelling the evolution of phase boundaries in solids at the meso-and nano-scales.* Acta Materialia, 2003. **51**(19): p. 5675-5710.
198. Ettrich, J., *Fluid flow and heat transfer in cellular solids*. Vol. 39. 2014: KIT Scientific Publishing.
199. Park, K., C. Felippa, and J. DeRuntz, *Stabilization of staggered solution procedures for fluid-structure interaction analysis.* Computational methods for fluid-structure interaction problems, 1977: p. 95-124.
200. Hu, H.H., D.D. Joseph, and M.J. Crochet, *Direct simulation of fluid particle motions.* Theoretical and Computational Fluid Dynamics, 1992. **3**(5): p. 285-306.

201. Barker, A.T. and X.-C. Cai, *Scalable parallel methods for monolithic coupling in fluid–structure interaction with application to blood flow modeling.* Journal of computational physics, 2010. **229**(3): p. 642-659.
202. Küttler, U., et al., *Coupling strategies for biomedical fluid‐structure interaction problems.* International Journal for Numerical Methods in Biomedical Engineering, 2010. **26**(3‐4): p. 305-321.
203. Heil, M., *An efficient solver for the fully coupled solution of large-displacement fluid–structure interaction problems.* Computer Methods in Applied Mechanics and Engineering, 2004. **193**(1): p. 1-23.
204. Ryzhakov, P., et al., *A monolithic Lagrangian approach for fluid–structure interaction problems.* Computational mechanics, 2010. **46**(6): p. 883-899.
205. Idelsohn, S.R., et al., *Fluid‐structure interaction problems with strong added‐mass effect.* International journal for numerical methods in engineering, 2009. **80**(10): p. 1261-1294.
206. Fernández, M.Á. and M. Moubachir, *A Newton method using exact Jacobians for solving fluid–structure coupling.* Computers & Structures, 2005. **83**(2): p. 127-142.
207. Degroote, J., et al., *Stability of a coupling technique for partitioned solvers in FSI applications.* Computers & Structures, 2008. **86**(23): p. 2224-2234.
208. Badia, S., F. Nobile, and C. Vergara, *Robin–Robin preconditioned Krylov methods for fluid–structure interaction problems.* Computer Methods in Applied Mechanics and Engineering, 2009. **198**(33): p. 2768-2784.
209. Degroote, J., K.-J. Bathe, and J. Vierendeels, *Performance of a new partitioned procedure versus a monolithic procedure in fluid–structure interaction.* Computers & Structures, 2009. **87**(11): p. 793-801.
210. Van Brummelen, E., *Added mass effects of compressible and incompressible flows in fluid-structure interaction.* Journal of Applied mechanics, 2009. **76**(2): p. 021206.
211. Kuhl, E., S. Hulshoff, and R. De Borst, *An arbitrary Lagrangian Eulerian finite-element approach for uid–structure interaction phenomena.* Int. J. Numer. Meth. Engng, 2003. **57**: p. 117-142.
212. Baek, H. and G.E. Karniadakis, *A convergence study of a new partitioned fluid–structure interaction algorithm based on fictitious mass and damping.* Journal of Computational Physics, 2012. **231**(2): p. 629-652.
213. Süli, E. and D.F. Mayers, *An introduction to numerical analysis*. 2003: Cambridge university press.
214. Dong, S., *BDF-like methods for nonlinear dynamic analysis.* Journal of Computational physics, 2010. **229**(8): p. 3019-3045.
215. Celaya, E. and J. Anza, *BDF-α: A multistep method with numerical damping control.* Universal Journal of Computational Mathematics, 2013. **1**(3): p. 96-108.
216. Heard, A., *Scale and modify for the second and third order BDF methods.* Numerical Algorithms, 2010. **53**(2-3): p. 261-280.
217. Swaminathan, T., K. Mukundakrishnan, and H.H. Hu, *Sedimentation of an ellipsoid inside an infinitely long tube at low and intermediate Reynolds numbers.* Journal of fluid mechanics, 2006. **551**: p. 357-385.
218. Goldstein, H., *Classical mechanics*. 1965: Pearson Education India.
219. Blaser, S., *Forces on the surface of small ellipsoidal particles immersed in a linear flow field.* Chemical Engineering Science, 2002. **57**(3): p. 515-526.
220. Yin, C., et al., *Modelling the motion of cylindrical particles in a nonuniform flow.* Chemical Engineering Science, 2003. **58**(15): p. 3489-3498.

221. Fukushima, T., *Simple, regular, and efficient numerical integration of rotational motion.* The Astronomical Journal, 2008. **135**(6): p. 2298.
222. Fan, F.-G. and G. Ahmadi, *Wall deposition of small ellipsoids from turbulent air flows—a Brownian dynamics simulation.* Journal of aerosol science, 2000. **31**(10): p. 1205-1229.
223. Hughes, P.C., *Spacecraft attitude dynamics*. 2012: Courier Corporation.
224. Bungartz, H.-J. and M. Schäfer, *Fluid-structure interaction: modelling, simulation, optimisation*. Vol. 1. 2006: Springer Science & Business Media.
225. Mok, D. and W. Wall, *Partitioned analysis schemes for the transient interaction of incompressible flows and nonlinear flexible structures.* Trends in computational structural mechanics, Barcelona, 2001.
226. Wall, W.A., S. Genkinger, and E. Ramm, *A strong coupling partitioned approach for fluid–structure interaction with free surfaces.* Computers & Fluids, 2007. **36**(1): p. 169-183.
227. Asgharzadeh, H. and I. Borazjani, *A Newton–Krylov method with an approximate analytical Jacobian for implicit solution of Navier–Stokes equations on staggered overset-curvilinear grids with immersed boundaries.* Journal of computational physics, 2017. **331**: p. 227-256.
228. Küttler, U. and W.A. Wall, *Vector extrapolation for strong coupling fluid-structure interaction solvers.* Journal of Applied Mechanics, 2009. **76**(2): p. 021205.
229. Küttler, U. and W.A. Wall, *Fixed-point fluid–structure interaction solvers with dynamic relaxation.* Computational Mechanics, 2008. **43**(1): p. 61-72.
230. Irons, B.M. and R.C. Tuck, *A version of the Aitken accelerator for computer iteration.* International Journal for Numerical Methods in Engineering, 1969. **1**(3): p. 275-277.
231. Baek, H. and G.E. Karniadakis, *Sub-iteration leads to accuracy and stability enhancements of semi-implicit schemes for the Navier–Stokes equations.* Journal of Computational Physics, 2011. **230**(12): p. 4384-4402.
232. Fischer, P.F., et al., *Simulation of high-Reynolds number vascular flows.* Computer methods in applied mechanics and engineering, 2007. **196**(31): p. 3049-3060.
233. Koumoutsakos, P. and A. Leonard, *High-resolution simulations of the flow around an impulsively started cylinder using vortex methods.* Journal of Fluid Mechanics, 1995. **296**: p. 1-38.
234. Prahl, L., A. Jadoon, and J. Revstedt, *Interaction between two spheres placed in tandem arrangement in steady and pulsating flow.* International Journal of Multiphase Flow, 2009. **35**(10): p. 963-969.
235. Mohaghegh, F. and H. Udaykumar, *Comparison of sharp and smoothed interface methods for simulation of particulate flows I: Fluid structure interaction for moderate reynolds numbers.* Computers & Fluids, 2016. **140**: p. 39-58.
236. Mohaghegh, F., J. Mousel, and H. Udaykumar, *Effect of Interface Thickness on Smoothed Profile Modeling of Flow over a Stationary Sphere in Re< 300*, in *21st AIAA Computational Fluid Dynamics Conference* 2013, AIAA: San Diego, CA.
237. Muijres, F., et al., *Leading-edge vortex improves lift in slow-flying bats.* Science, 2008. **319**(5867): p. 1250-1253.
238. Taylor, G.K., R.L. Nudds, and A.L. Thomas, *Flying and swimming animals cruise at a Strouhal number tuned for high power efficiency.* Nature, 2003. **425**(6959): p. 707-711.
239. Warrick, D.R., B.W. Tobalske, and D.R. Powers, *Lift production in the hovering hummingbird.* Proceedings of the Royal Society of London B: Biological Sciences, 2009. **276**(1674): p. 3747-3752.
240. Janechek, M., *Numerical Investigation of a Plunging Airfoil*. 2017: The University of Iowa.

241. Panah, A.E., J.M. Akkala, and J.H. Buchholz, *Vorticity transport and the leading-edge vortex of a plunging airfoil.* Experiments in Fluids, 2015. **56**(8): p. 160.
242. Doligalski, T., C. Smith, and J. Walker, *Vortex interactions with walls.* Annual Review of Fluid Mechanics, 1994. **26**(1): p. 573-616.
243. Lewin, G.C. and H. Haj-Hariri, *Modelling thrust generation of a two-dimensional heaving airfoil in a viscous flow.* Journal of Fluid Mechanics, 2003. **492**: p. 339-362.
244. Visbal, M.R., *High-fidelity simulation of transitional flows past a plunging airfoil.* AIAA journal, 2009. **47**(11): p. 2685-2697.
245. Wojcik, C.J. and J.H. Buchholz, *Vorticity transport in the leading-edge vortex on a rotating blade.* Journal of Fluid Mechanics, 2014. **743**: p. 249-261.
246. Akkala, J., *Understanding and controlling vorticity transport in unsteady, separated flows.* 2015.
247. Brunton, S.L. and C.W. Rowley, *Empirical state-space representations for Theodorsen's lift model.* Journal of Fluids and Structures, 2013. **38**: p. 174-186.
248. Meagher, D., *Geometric modeling using octree encoding.* Computer graphics and image processing, 1982. **19**(2): p. 129-147.
249. Burstedde, C., L.C. Wilcox, and O. Ghattas, *p4est: Scalable algorithms for parallel adaptive mesh refinement on forests of octrees.* SIAM Journal on Scientific Computing, 2011. **33**(3): p. 1103-1133.
250. Losasso, F., F. Gibou, and R. Fedkiw. *Simulating water and smoke with an octree data structure*. in *ACM Transactions on Graphics (TOG)*. 2004. ACM.
251. Mohaghegh, F. and H. Udaykumar, *Comparison of sharp and smoothed interface methods for simulation of particulate flows II: Inertial and added mass effects.* Computers & Fluids, 2017. **143**: p. 103-119.
252. Balay, S., et al., *Petsc users manual revision 3.5*. 2014, Technical report, Argonne National Laboratory (ANL).
253. Sleijpen, G.L. and H.A. Van der Vorst, *An overview of approaches for the stable computation of hybrid BiCG methods.* Applied numerical mathematics, 1995. **19**(3): p. 235-254.
254. Sundar, H., et al. *Parallel geometric-algebraic multigrid on unstructured forests of octrees*. in *Proceedings of the International Conference on High Performance Computing, Networking, Storage and Analysis*. 2012. IEEE Computer Society Press.
255. BCCS-Bristol, *Modelling Environmental Interactions*, in *iGEM 2010 Jamboree*. November 6 - 8, 2010: Massachusetts Institute of Technology.
256. Davis, R.H., *Elastohydrodynamic collisions of particles.* PhysicoChem. Hydrodyn, 1987. **9**: p. 41-52.
257. Ardekani, A.M., S. Dabiri, and R.H. Rangel, *Collision of multi-particle and general shape objects in a viscous fluid.* Journal of Computational Physics, 2008. **227**(24): p. 10094-10107.
258. Ardekani, A. and R. Rangel, *Numerical investigation of particle–particle and particle–wall collisions in a viscous fluid.* Journal of fluid mechanics, 2008. **596**: p. 437-466.
259. Van der Hoef, M., et al., *Numerical simulation of dense gas-solid fluidized beds: a multiscale modeling strategy.* Annu. Rev. Fluid Mech., 2008. **40**: p. 47-70.
260. Guo, Y. and J.S. Curtis, *Discrete element method simulations for complex granular flows.* Annual Review of Fluid Mechanics, 2015. **47**: p. 21-46.
261. Ray, S., T. Kempe, and J. Fröhlich, *Efficient modelling of particle collisions using a non-linear viscoelastic contact force.* International Journal of Multiphase Flow, 2015. **76**: p. 101-110.
262. Luding, S., *About contact force-laws for cohesive frictional materials in 2d and 3d.* Behavior of granular media, 2006. **9**: p. 137-147.

263. Ding, J. and D. Gidaspow, *A bubbling fluidization model using kinetic theory of granular flow.* AIChE Journal, 1990. **36**(4): p. 523-538.
264. Hoomans, B., et al., *Discrete particle simulation of bubble and slug formation in a two-dimensional gas-fluidised bed: a hard-sphere approach.* Chemical Engineering Science, 1996. **51**(1): p. 99-118.
265. Foerster, S.F., et al., *Measurements of the collision properties of small spheres.* Physics of Fluids (1994-present), 1994. **6**(3): p. 1108-1115.
266. Schwarzer, S., *Sedimentation and flow through porous media: Simulating dynamically coupled discrete and continuum phases.* Physical Review E, 1995. **52**(6): p. 6461.
267. Xu, B. and A. Yu, *Numerical simulation of the gas-solid flow in a fluidized bed by combining discrete particle method with computational fluid dynamics.* Chemical Engineering Science, 1997. **52**(16): p. 2785-2809.
268. Feng, Z.-G., E.E. Michaelides, and S. Mao, *A three-dimensional resolved discrete particle method for studying particle-wall collision in a viscous fluid.* Journal of Fluids Engineering, 2010. **132**(9): p. 091302.
269. Walton, O.R. and R.L. Braun, *Viscosity, granular ‐ temperature, and stress calculations for shearing assemblies of inelastic, frictional disks.* Journal of Rheology (1978-present), 1986. **30**(5): p. 949-980.
270. Thornton, C., *Coefficient of restitution for collinear collisions of elastic-perfectly plastic spheres.* Journal of Applied Mechanics, 1997. **64**(2): p. 383-386.
271. Wan, D. and S. Turek, *Direct numerical simulation of particulate flow via multigrid FEM techniques and the fictitious boundary method.* International Journal for Numerical Methods in Fluids, 2006. **51**(5): p. 531-566.
272. Kempe, T. and J. Fröhlich, *Collision modelling for the interface-resolved simulation of spherical particles in viscous fluids.* Journal of Fluid Mechanics, 2012. **709**: p. 445-489.
273. Uhlmann, M., *Interface-resolved direct numerical simulation of vertical particulate channel flow in the turbulent regime.* Physics of Fluids (1994-present), 2008. **20**(5): p. 053305.
274. Perram, J.W., et al., *Ellipsoid contact potential: Theory and relation to overlap potentials.* Physical Review E, 1996. **54**(6): p. 6565.
275. Stevens, A. and C. Hrenya, *Comparison of soft-sphere models to measurements of collision properties during normal impacts.* Powder Technology, 2005. **154**(2): p. 99-109.
276. Johnson, K., *Contact Mechanics Cambridge University Press London*. 1985, UK.
277. Marshall, J., *Discrete-element modeling of particulate aerosol flows.* Journal of Computational Physics, 2009. **228**(5): p. 1541-1561.
278. Kruggel-Emden, H., et al., *Review and extension of normal force models for the discrete element method.* Powder Technology, 2007. **171**(3): p. 157-173.
279. Walton, O.R., *Numerical simulation of inelastic, frictional particle-particle interactions*. 1993, chap.
280. Antypov, D. and J. Elliott, *On an analytical solution for the damped Hertzian spring.* EPL (Europhysics Letters), 2011. **94**(5): p. 50004.
281. Tsuji, Y., T. Tanaka, and T. Ishida, *Lagrangian numerical simulation of plug flow of cohesionless particles in a horizontal pipe.* Powder technology, 1992. **71**(3): p. 239-250.
282. Ladd, A.J., *Sedimentation of homogeneous suspensions of non-Brownian spheres.* Physics of Fluids (1994-present), 1997. **9**(3): p. 491-499.
283. Biegert, E., B. Vowinckel, and E. Meiburg, *Grain-resolving simulations of flows over dense, mobile, multidisperse granular sediment beds: an Immersed Boundary approach.* arXiv preprint arXiv:1608.03566, 2016.

284. Izard, E., T. Bonometti, and L. Lacaze, *Modelling the dynamics of a sphere approaching and bouncing on a wall in a viscous fluid.* Journal of Fluid Mechanics, 2014. **747**: p. 422-446.
285. Costa, P., et al., *Collision model for fully resolved simulations of flows laden with finite-size particles.* Physical Review E, 2015. **92**(5): p. 053012.
286. Lin, X. and T.T. Ng, *Contact detection algorithms for three‐dimensional ellipsoids in discrete element modelling.* International Journal for Numerical and Analytical Methods in Geomechanics, 1995. **19**(9): p. 653-659.
287. Ting, J.M., *A robust algorithm for ellipse-based discrete element modelling of granular materials.* Computers and Geotechnics, 1992. **13**(3): p. 175-186.
288. Lin, A. and S.-P. Han, *On the distance between two ellipsoids.* SIAM Journal on Optimization, 2002. **13**(1): p. 298-308.
289. Nezami, E.G., et al., *A fast contact detection algorithm for 3-D discrete element method.* Computers and Geotechnics, 2004. **31**(7): p. 575-587.
290. Cundall, P.A. *Formulation of a three-dimensional distinct element model—Part I. A scheme to detect and represent contacts in a system composed of many polyhedral blocks*. in *International Journal of Rock Mechanics and Mining Sciences & Geomechanics Abstracts*. 1988. Elsevier.
291. Zhao, D., et al., *Three-dimensional discrete element simulation for granular materials.* Engineering Computations, 2006. **23**(7): p. 749-770.
292. Jiménez, J.J. and R.J. Segura, *Collision detection between complex polyhedra.* Computers & Graphics, 2008. **32**(4): p. 402-411.
293. Williams, J.R. and A.P. Pentland, *Superquadrics and modal dynamics for discrete elements in interactive design.* Engineering Computations, 1992. **9**(2): p. 115-127.
294. Lu, G., J. Third, and C. Müller, *Discrete element models for non-spherical particle systems: From theoretical developments to applications.* Chemical Engineering Science, 2015. **127**: p. 425-465.
295. Lin, X. and T.-T. Ng, *A three-dimensional discrete element model using arrays of ellipsoids.* Geotechnique, 1997. **47**(2): p. 319-329.
296. Baram, R.M. and P.G. Lind, *Deposition of general ellipsoidal particles.* Physical Review E, 2012. **85**(4): p. 041301.
297. Ardekani, M.N., et al., *Numerical Study of the Sedimentation of Spheroidal Particles.* arXiv preprint arXiv:1602.05769, 2016.
298. Jaklic, A., A. Leonardis, and F. Solina, *Segmentation and recovery of superquadrics*. Vol. 20. 2013: Springer Science & Business Media.
299. Hogue, C. and D. Newland, *Efficient computer simulation of moving granular particles.* Powder Technology, 1994. **78**(1): p. 51-66.
300. Boon, C.W., G. Houlsby, and S. Utili, *A new contact detection algorithm for three-dimensional non-spherical particles.* Powder technology, 2013. **248**: p. 94-102.
301. Houlsby, G., *Potential particles: a method for modelling non-circular particles in DEM.* Computers and Geotechnics, 2009. **36**(6): p. 953-959.
302. Weigler, F. and J. Mellmann, *Investigation of grain mass flow in a mixed flow dryer.* Particuology, 2014. **12**: p. 33-39.
303. Tong, L. and Y.-H. Wang, *DEM simulations of shear modulus and damping ratio of sand with emphasis on the effects of particle number, particle shape, and aging.* Acta Geotechnica, 2015. **10**(1): p. 117-130.
304. Pei, C., et al., *Contact electrification and charge distribution on elongated particles in a vibrating container.* Chemical Engineering Science, 2015. **125**: p. 238-247.

305. Majidi, B., et al., *Simulation of vibrated bulk density of anode-grade coke particles using discrete element method.* Powder Technology, 2014. **261**: p. 154-160.
306. Kruggel‐Emden, H. and F. Elskamp, *Modeling of Screening Processes with the Discrete Element Method Involving Non‐Spherical Particles.* Chemical Engineering & Technology, 2014. **37**(5): p. 847-856.
307. Bertei, A., et al., *Modified collective rearrangement sphere-assembly algorithm for random packings of nonspherical particles: Towards engineering applications.* Powder Technology, 2014. **253**: p. 311-324.
308. He, T., W. ZHONG, and J. Baosheng, *Comparison of construction method for DEM simulation of ellipsoidal particles.* Chinese Journal of Chemical Engineering, 2013. **21**(7): p. 800-807.
309. Tao, H., et al. *DEM simulation of non-spherical granular segregation in hopper*. in *7TH INTERNATIONAL SYMPOSIUM ON MULTIPHASE FLOW, HEAT MASS TRANSFER AND ENERGY CONVERSION*. 2013. AIP Publishing.
310. Ketchel, J. and P. Larochelle. *Collision detection of cylindrical rigid bodies for motion planning*. in *Proceedings 2006 IEEE International Conference on Robotics and Automation, 2006. ICRA 2006.* 2006. IEEE.
311. Munjiza, A., et al., *A poly-ellipsoid particle for non-spherical discrete element method.* Engineering Computations, 2009. **26**(6): p. 645-657.
312. Kodam, M., et al., *Cylindrical object contact detection for use in discrete element method simulations. Part I–Contact detection algorithms.* Chemical Engineering Science, 2010. **65**(22): p. 5852-5862.
313. Galindo-Torres, S., et al., *Molecular dynamics simulation of complex particles in three dimensions and the study of friction due to nonconvexity.* Physical Review E, 2009. **79**(6): p. 060301.
314. Galindo-Torres, S., J. Muñoz, and F. Alonso-Marroquin, *Minkowski-Voronoi diagrams as a method to generate random packings of spheropolygons for the simulation of soils.* physical review E, 2010. **82**(5): p. 056713.
315. Galindo-Torres, S. and D. Pedroso, *Molecular dynamics simulations of complex-shaped particles using Voronoi-based spheropolyhedra.* Physical Review E, 2010. **81**(6): p. 061303.
316. Pournin, L. and T.M. Liebling. *A generalization of distinct element method to tridimensional particles with complex shapes*. in *Powders and Grains 2005*. 2005. AA Balkema Publishers.
317. Alonso-Marroquín, F. and Y. Wang, *An efficient algorithm for granular dynamics simulations with complex-shaped objects.* Granular Matter, 2009. **11**(5): p. 317-329.
318. Glowinski, R., *Finite element methods for incompressible viscous flow.* Handbook of numerical analysis, 2003. **9**: p. 3-1176.
319. Joseph, G., et al., *Particle–wall collisions in a viscous fluid.* Journal of Fluid Mechanics, 2001. **433**: p. 329-346.
320. Yang, F.-L. and M. Hunt, *Dynamics of particle-particle collisions in a viscous liquid.* Physics of Fluids (1994-present), 2006. **18**(12): p. 121506.
321. Gondret, P., et al., *Experiments on the motion of a solid sphere toward a wall: From viscous dissipation to elastohydrodynamic bouncing.* Physics of Fluids (1994-present), 1999. **11**(9): p. 2803-2805.
322. Li, X., M.L. Hunt, and T. Colonius, *A contact model for normal immersed collisions between a particle and a wall.* Journal of Fluid Mechanics, 2012. **691**: p. 123-145.
323. Ruiz-Angulo, A. and M. Hunt, *Measurements of the coefficient of restitution for particle collisions with ductile surfaces in a liquid.* Granular matter, 2010. **12**(2): p. 185-191.

324. Fortes, A.F., D.D. Joseph, and T.S. Lundgren, *Nonlinear mechanics of fluidization of beds of spherical particles.* Journal of Fluid Mechanics, 1987. **177**: p. 467-483.